UNIVERSITÉ DE LILLE

Ecole doctorale Sciences de l'Ingénierie et des Systèmes

IEMN - Institut d'électronique de microélectronique et de nanotechnologie

Thèse soutenue par **Huu Thoai NGO**

Soutenue le **17 septembre 2024**

Devenir Docteur à **l'Université de Lille**

Domaine académique: Electronique, microélectronique, nanoélectronique

et micro-ondes

UNIVERSITÉ DE GAND

Faculté des Sciences

Devenir docteur à **l'Université de Gand**

Domaine académique: Physique

Propriétés optiques et électroniques des nanoplaquettes colloidales de CdSe et des hétérostructures associées

---

La thèse encadrée par

Dr. Louis BIADALA	Directeur de thèse
Prof. Iwan MOREELS	Co-superviseur
Dr. Gang JI	Co-superviseur

Membres du comité

Dr. Amandine BELLEC	Rapporteure	
Prof. Sandrine ITHURRIA	Rapporteure	
Dr. Bruno GRANDIDIER	Examinateur	**President du jury**
Dr. Benoit MAHLER	Examinateur	
Prof. Jean-Pierre HERMIER	Examinateur	
Prof. Jolien DENDOOVEN	Examinateure	

UNIVERSITY OF LILLE

Graduate School Engineering and System Sciences

IEMN - Institute of Electronics, Microelectronics and Nanotechnology

Thesis defended by **Huu Thoai NGO**

Defended on **17th September 2024**

To become a Doctor at the **University of Lille**

Academic field: Electronics, microelectronics, nanoelectronics, and microwaves

GHENT UNIVERSITY

Faculty of Sciences

To become a Doctor at **Ghent University**

Academic field: Physics

Optical and electronic properties of colloidal CdSe nanoplatelets and related heterostructures

The thesis supervised by

Dr. Louis BIADALA	Director of the thesis	
Prof. Iwan MOREELS	Co-supervisor	
Dr. Gang JI	Co-supervisor	

Committee member

Dr. Amandine BELLEC	Referee	
Prof. Sandrine ITHURRIA	Referee	
Dr. Bruno GRANDIDIER	Examiner	**Committee President**
Dr. Benoit MAHLER	Examiner	
Prof. Jean-Pierre HERMIER	Examiner	
Prof. Jolien DENDOOVEN	Examiner	

Committee member

Referees
Dr. Amandine BELLEC
(Senior Researcher at MPQ – CNRS, Paris Cité University)
Prof. Sandrine ITHURRIA
(Professor at ESPCI-Paris, PSL Research University, Sorbonne University)

Examiners
Dr. Bruno GRANDIDIER   Committee President
(Senior Researcher at IEMN – CNRS, University of Lille)

Dr. Benoit MAHLER
(Senior Researcher at ILM – Claude Bernard Lyon 1 University)

Prof. Jean-Pierre HERMIER
(Professor at University of Versailles St-Quentin-en-Yvelines)

Prof. Jolien DENDOOVEN
(Professor at Department of Solid State Sciences – Ghent University)

Supervisors
Dr. Louis BIADALA   Main supervisor
(Senior Researcher at IEMN – CNRS, University of Lille)
Prof. Iwan MOREELS   Co-supervisor
(Professor at Department of Chemistry – Ghent University)
Dr. Gang JI   Co-supervisor
(Senior Researcher at UMET – CNRS, University of Lille)

Contents

Abstract

Acknowledgements

Contents

Abstract

Advances in colloidal chemistry have enabled the synthesis of various types of colloidal nanocrystals (NCs), such as quantum dots (QDs), quantum rings (QRs), nanoplatelets (NPLs), and nanorods (NRs), which are characterized by quantum confinement effects. Among them, colloidal NPLs (e.g., CdSe, PbSe, etc.) have attracted considerable attention due to the combination of their distinct shape with tunable optoelectronic properties. To exploit NPLs in optoelectronic devices requires a deep understanding of their structural and electronic properties at the scale of single nanocrystals.

In this thesis, we propose scanning tunneling microscopy (STM) to investigate the structural and electronic properties of CdSe NPLs. STM is a powerful tool commonly used to study the material's surface and electronic characteristics at the atomic scale. To begin with, we performed STM measurements on individual NPLs at low temperatures (T = 77 K). The resulting STM images revealed the truncated edges, which expose atomic terraces at the side facets of NPLs. The truncated edges contain structural defects and dangling bonds, favoring the formation of surface traps. To demonstrate that, we measured the spatial distribution of the tunneling current on the surface of a single NPL. As a result, we observed strong fluctuations in the tunneling current at the NPL edges, implying the dense presence of surface traps on the NPL side facets. By probing the density of states (DOS) of single NPLs using scanning tunneling spectroscopy (STS), we observed in-gap states corresponding to electron (at positive bias) and hole trap states (at negative bias) within the band gap energy of the NPLs. The trapping mechanism was then investigated by recording the blinking traces of the tunneling current in real time (feedback loop: OFF). By analyzing the blinking effects with a power spectral density (PSD), we demonstrated that a single electron trap behaves as a stochastic two-level system in NPLs.

In addition to the structural and electronic properties, the thesis delves into the magneto-optical properties of CdSe and CdSe/CdS core/crown NPLs using magneto-photoluminescence (PL) spectroscopy. Magneto-optical effects relate to the changes in the optical properties of materials under internal or external magnetic fields. By

analyzing the degree of circular polarization (DCP) of the dark exciton, we elucidated the influence of surface dangling bond (DB) spins on the polarized emission in CdSe NPLs. Meanwhile, we did not observe the effect of DB spins on the exciton DCP in the core/large crown NPLs. This leads to two conclusions: (1) Surface traps on the side facets of CdSe NPLs have completely been passivated by the CdS crown, and (2) Surface DB spins on the side facets interact strongly with the dark excitons in NPLs. These findings indicate surface DB spins can change the optical and magnetic properties of CdSe NPLs.

Based on the comprehensive investigation of CdSe NPLs, the scope of the thesis was extended to investigate the structural and electronic properties of ultrathin PbSe NPLs using the STM/STS technique. By analyzing STM topographic images, we confirm the presence of NPLs with various thicknesses in the same sample. Measuring the DOS of the 0.45 nm, 0.8 nm, and 1.6 nm thick NPLs, we found the decreasing electronic band gap with increasing thickness, implying the quantum confinement effect along the NPL thickness. Tight-binding calculations were employed to predict the influence of the NPL lateral size on their band gap (thickness is constant). As a result, we observed that the band gap energy of NPLs decreases as the lateral size increases. The experimental and simulation results show the ability to tune the optoelectronic properties of NPL for telecom and optoelectronic applications.

Résumé

Les avancées en chimie colloïdale ont permis la synthèse de divers types de nanocristaux colloïdaux (NCs) tels que les points quantiques (QDs), les anneaux quantiques (QRs), les nanoplaquettes (NPLs) et les nanobâtonnets (NRs), caractérisés par des effets de confinement quantique. Parmi eux, les NPLs colloïdaux (par exemple, CdSe, PbSe, etc.) ont attiré une attention considérable en raison de la combinaison de leur forme distincte et de leurs propriétés optoélectroniques modulables. Pour exploiter les NPLs dans les dispositifs optoélectroniques, il est nécessaire de comprendre en profondeur leurs propriétés structurales et électroniques à l'échelle des nanocristaux individuels.

Dans cette thèse, nous proposons l'utilisation de la microscopie à effet tunnel (STM) pour étudier les propriétés structurales et électroniques des NPLs de CdSe. La STM est un outil puissant couramment utilisé pour étudier les caractéristiques de surface et électroniques des matériaux à l'échelle atomique. Pour commencer, nous avons effectué des mesures STM sur des NPLs individuels à basse température (T = 77 K). Les images STM obtenues ont révélé les bords tronqués qui exposent des terrasses atomiques sur les facettes latérales des NPLs. Les bords tronqués contiennent des défauts structuraux et des liaisons pendantes favorisant la formation de pièges de surface. Pour démontrer cela, nous avons mesuré la distribution spatiale du courant tunnel sur la surface d'un seul NPL. En conséquence, nous avons observé de fortes fluctuations du courant tunnel aux bords des NPLs, ce qui implique une présence dense de pièges de surface sur les facettes latérales des NPLs. En sondant la densité d'états (DOS) des NPLs individuels à l'aide de la spectroscopie par effet tunnel (STS), nous avons observé des états dans la bande interdite correspondant aux pièges à électrons (à polarisation positive) et aux pièges à trous (à polarisation négative) dans l'énergie de la bande interdite des NPLs. Le mécanisme de piégeage a ensuite été étudié en enregistrant les traces de clignotement du courant tunnel en temps réel (boucle de rétroaction : OFF). En conséquence, nous avons démontré qu'un seul piège à électrons se comporte comme un système stochastique à deux niveaux dans les NPLs.

En plus des propriétés structurales et électroniques, la thèse explore les propriétés magnéto-optiques des NPLs de CdSe et CdSe/CdS core/crown en utilisant la spectroscopie magnéto-photoluminescente (PL). Les effets magnéto-optiques se rapportent aux changements des propriétés optiques des matériaux sous des champs magnétiques internes ou externes. En analysant le degré de polarisation circulaire (DCP) de l'exciton noir, nous avons élucidé l'influence des spins des liaisons pendantes (DB) de surface sur l'émission polarisée dans les NPLs de CdSe. Pendant ce temps, nous n'avons pas observé l'effet du spin DB sur le DCP de l'exciton dans les NPLs core/crown. Cela conduit à deux conclusions : (1) Les pièges de surface sur les facettes latérales des NPLs de CdSe ont été complètement passivés par la couronne de CdS, et (2) le spin des DB de surface sur les facettes latérales interagit fortement avec les excitons noirs dans les NPLs. Ces résultats indiquent que les spins des DB de surface peuvent modifier les propriétés optiques et magnétiques des NPLs de CdSe.

Sur la base de l'étude complète des NPLs de CdSe, le champ d'investigation de la thèse a été étendu à l'étude des propriétés structurales et électroniques des NPLs ultra-minces de PbSe en utilisant la technique STM/STS. En analysant les images topographiques STM, nous confirmons la présence de NPLs de diverses épaisseurs dans le même échantillon. En mesurant la DOS des NPLs de 0,45 nm, 0,8 nm et 1,6 nm d'épaisseur, nous avons constaté que la bande interdite électronique diminue avec l'augmentation de l'épaisseur, ce qui implique l'effet de confinement quantique le long de l'épaisseur des NPLs. Des calculs par liaison forte ont été utilisés pour prédire l'effet de la taille latérale des NPLs sur leur bande interdite (sans changer l'épaisseur). En conséquence, nous avons observé que l'énergie de la bande interdite des NPLs diminue à mesure que la taille latérale augmente. Les résultats expérimentaux et de simulation montrent la capacité de moduler les propriétés optoélectroniques des NPLs pour des applications dans les télécommunications et l'optoélectronique.

Overzicht

Vooruitgang in de colloïd chemie hebben de synthese van verschillende soorten colloïdale nanokristallen mogelijk gemaakt, zoals kwantum stippen, kwantum ringen, nanoplaatjes (NPLs) en nanostaafjes, die allen gekenmerkt worden door kwantum opsluitingseffecten. Colloïdale NPLs (gemaakt uit CdSe, PbSe, enz.) hebben aanzienlijke aandacht getrokken vanwege de combinatie van hun unieke vorm met varieerbare opto-elektronische eigenschappen. Om NPLs in opto-elektronische toepassing te kunnen gebruiken, is een diepgaand begrip van hun structurele en elektronische eigenschappen, op de schaal van individuele nanokristallen, vereist.

In deze scriptie stellen we scanning tunneling microscopie (STM) voor om de structurele en elektronische eigenschappen van CdSe NPLs te onderzoeken. STM is een krachtig instrument dat veel wordt gebruikt voor het bestuderen van de oppervlak- en elektronische kenmerken van materialen op atomair niveau. Om te beginnen hebben we STM-metingen uitgevoerd bij lage temperatuur ($T = 77$ K) op individuele NPLs. De resulterende STM-beelden tonen afgeknotte randen aan de zijkanten van de NPLs, met atomaire terrassen. De afgeknotte randen bevatten structurele defecten en gebroken bindingen, die de vorming van oppervlakdefecten bevorderen. Om dit expliciet aan te tonen, hebben we de ruimtelijke verdeling van de tunnelstroom op het oppervlak van een individuele NPL gemeten. We zagen sterke fluctuaties in de tunnelstroom aan de randen van de NPL, wat wijst op de aanwezigheid van oppervlakdefecten aan de zijkanten van de NPL. Door de toestandsdichtheid van enkele NPLs te onderzoeken met behulp van scanning tunneling spectroscopie (STS), observeerden we toestanden in de bandkloof die overeenkomen met elektron- (bij positieve bias) en gatdefecten (bij negatieve bias). Het vangmechanisme werd vervolgens onderzocht door de knipperende tunnelstroom in reële tijd op te nemen (d.w.z. zonder terugkoppelingslus). Door de knipperende stroom te analyseren met een vermogensspectrale dichtheid, toonden we aan dat een enkele elektronval zich gedraagt als een stochastisch tweeniveausysteem in NPLs.

Naast de structurele en elektronische eigenschappen, gaat de scriptie ook in op de magneto-optische eigenschappen van CdSe en CdSe/CdS kern/kroon NPLs, opgemeten met behulp van magneto-fotoluminescentie spectroscopie. Magneto-optische effecten hebben betrekking op de veranderingen in de optische eigenschappen van materialen onder interne of externe magnetische velden. Door de mate van circulaire polarisatie (DCP) van het donkere exciton te analyseren, hebben we de invloed van de spin van de oppervlak-gebroken bindingen (DBs) op de gepolariseerde emissie in CdSe NPLs kunnen begrijpen. Terzelfdertijd observeerden we geen effect van DB-spins op de exciton DCP in kern/kroon NPLs met een grote kroon. Dit leidt tot twee conclusies: (1) Oppervlakdefecten aan de zijkanten van CdSe NPLs zijn volledig gepassiveerd door de CdS kroon, en (2) Oppervlak-DB-spins aan de zijkanten interageren sterk met de donkere excitonen in NPLs. Deze bevindingen geven aan dat oppervlak-DB-spins de optische en magnetische eigenschappen van CdSe NPLs kunnen wijzigen.

Naast het uitgebreide onderzoek op CdSe NPLs, werd de scriptie uitgebreid tot het onderzoek van de structurele en elektronische eigenschappen van PbSe NPLs met behulp van de STM/STS-techniek. Door topografische STM beelden te analyseren, bevestigden we de aanwezigheid van NPLs met verschillende diktes in hetzelfde monster. Door de toestandsdichtheid van de 0.45 nm, 0.8 nm en 1.6 nm dikke NPLs te meten, ontdekten we een vermindering van de elektronische bandkloof met toenemende dikte, wat wijst op het kwantum opsluitingseffect in de richting van de dikte van de NPLs. Daarnaast werden tight-binding berekeningen gebruikt om het effect van de laterale grootte van de NPLs op de bandkloof te voorspellen. Als resultaat observeerden we dat de bandkloofenergie van NPLs afneemt naarmate de laterale grootte toeneemt. De experimentele en simulatieresultaten tonen de mogelijkheid om de opto-elektronische eigenschappen van NPLs af te stemmen voor telecommunicatie- en opto-elektronische toepassingen.

Acknowledgments

The Ph.D. degree was a long and challenging journey that could not have been completed without the support of my supervisors, friends, and family, in addition to my tireless efforts. First, I would like to express my deepest gratitude to my primary supervisor, Dr. Louis Biadala, for giving me this fantastic opportunity. Louis taught me profound knowledge of STM and the optoelectronic properties of colloidal nanocrystals, which are important for my future academic career. In addition to sharing his extensive scientific knowledge, Louis has a unique approach to sharing his views and experiences about life and the academic world with me. While supervising my work, Louis asked me interesting questions regarding my Ph.D. This sparked my creativity, curiosity, and passion for materials science. Thank you so much for being my wonderful mentor – Dr. Louis Biadala.

I would like to thank Dr. Bruno Grandidier, whose expertise, patience, and encouragement were valuable throughout my Ph.D thesis. Bruno taught me an intensive knowledge of scanning tunneling microscopy (STM), which is essential for developing my academic career in nanosciences. During the working process, Bruno not only asked questions but also offered incredible ideas, providing great support for my thesis and upcoming manuscripts. A friendly thank you for your teaching and support - Dr. Bruno Grandidier.

I would like to express my intense appreciation to Dr. Nemanja Peric, my great mentor and nice friend. Nemanja shared his hands-on experience with STM, colloidal nanocrystals, and data treatment with me for the first time in my thesis. His sharing is valuable and important for completing my thesis. On top of sharing scientific knowledge, I also received advice about life and academic careers from Nemanja. A big thank you for being my mentor and friend – Dr. Nemanja Peric.

To Dr. Maxime Berthe – Thank you for your support and teaching me about the technical issues at our laboratory. STM is a modern and complex system with various electrical and mechanical components. Maxime taught me technical problems that I

may encounter operating an STM system. Most importantly, he gives me the confidence to work with complex scientific equipment during my thesis. A big thank you to Dr. Maxime Berthe.

I want to express my gratitude to Prof. Iwan Moreels (co-supervisor) for allowing me to work at his chemical laboratory. He taught me an intensive knowledge of material synthesis, particularly the colloidal synthesis of semiconductor nanoplatelets. This knowledge is essential for extending my research from pure to chemical physics. Importantly, Iwan gave me the motivation to learn colloidal chemistry further, and I learned carefulness and perseverance from chemists at Iwan's laboratory. His expertise, patience, and encouragement were invaluable throughout my research. A big thank you for being my supervisor – Prof. Iwan Moreels.

To Dr. Gang Ji (co-supervisor) and Dr. Ahmed Addad – Thank you for your support. They taught me about scanning transmission electronic microscopy (STEM), a powerful tool for studying the structural properties of materials. The results obtained from STEM contribute significantly to our upcoming manuscript. Thank you for the great collaboration.

I would like to thank prof. Dmitri R Yakovlev and Dr. Elena V Shornikova for allowing me to work at the laboratory of Experimental Physics II – Technical University of Dortmund, Germany. Their teaching and guidance in magneto-PL spectroscopy are very valuable for my thesis and important for my future career. A big thank you for the great collaboration.

My heart left thanks to my colleagues at the Physics of Nanostructures & Quantum Devices team (IEMN-CNRS). A big thank you to Dr. Yevheniia Chernukha, Dr. Fatima Léa Hussein, Dr. Houda Koussir, and Zeinab Issa at IEMN-CNRS. In addition, I would like to thank all the members of the Physics and Chemistry of Nanostructures group – Ghent University, Belgium.

I am profoundly grateful to my mother for her unconditional love and encouragement. To Mrs. Tham Thi Ngo, my great mother, thank you for giving me life and brainpower. Mother, you are my light and motivation, and I will provide you with everything I have. Additionally, I would like to thank Hao Pham, My Nghe, Manh Nguyen, and Suvajit Mukherjee.

<div align="right">Thank you very much!!</div>

Huu Thoai Ngo

We can overcome life's difficulties if we have enough motivation. With enough determination, we can break through obstacles and achieve our goals.

<div align="center">(Career – Love – Money – Happiness)</div>

Just like electrons from the STM tip can tunnel through a barrier to the substrate. As a result, atomic-resolution STM images can be acquired.

<div align="center">Don't give up on every situation!!</div>

Introduction

Cadmium selenide (CdSe) nanoplatelets (NPLs) are an interesting class of colloidal nanocrystals, with distinct advantages and potential applications due to their anisotropic shape and outstanding electronic characteristics. Specifically, CdSe NPLs exhibit a strong quantum confinement effect along their thickness, resulting in tunable optoelectronic properties [1]. Not only that, the two-dimensional (2D) shape of NPLs can be controlled during colloidal synthesis, offering the possibility of tuning the fluorescence polarization [2], and absorption/emission area [3]. Despite these advantages, CdSe NPLs contain many surface traps which strongly reduce their quantum efficiency. Moreover, surface traps seriously affect charged carrier transport in NPL-based heterostructures (HNs) such as core/crown, and core/shell NPLs. In NPLs, surface traps originate from structural imperfections and unsuccessful ligand passivations during colloidal synthesis [4], [5]. However, the surface characteristics and the true shape of NPLs have not been fully studied at the nanoscale. This will restrict establish effective solutions for improving the optoelectronic properties of NPLs.

On the other hand, the surface of CdSe NPLs contains dangling bonds that are not passivated by organic ligands. Dangling bond spins (DBSs) have been demonstrated to induce surface magnetism in non-magnetic CdSe NPLs [6]. Surface DB spins can interact with an electron spin localized in NPLs, leading to changes in the degree of circular polarization of the dark exciton [7]. Because the NPLs have well-defined surfaces upon their orientation, the nature and number of dangling bonds differ on each surface, e.g., surface DBs originate from Se and Cd atoms. Therefore, the surface DB-electron spin interactions differ on each specific surface.

In this thesis, we employ low-temperature scanning tunneling microscopy (LT-STM) and spectroscopy (LT-STS) to investigate the structural and electronic properties of NPLs at the nanoscale. Meanwhile, the magneto-optical effects in CdSe/CdS core/crown NPLs are studied with magneto-photoluminescence (PL) spectroscopy at cryogenic temperatures. To present the obtained results smoothly, the thesis is divided into four chapters as follows:

The first chapter mainly introduces materials and basic concepts of fundamental properties. The first part will present the theory of structural, electronic, and optical properties of CdSe nanocrystals. For electronic properties, the focus is to clarify the band structure, quantum, and dielectric confinement effects in CdSe NCs. Meanwhile, optical properties focus on optical transitions, exciton binding energy, and exciton fine structure in NCs. Then, we shift to present the review of synthetic approaches of colloidal semiconductor NCs, among which the hot-injection synthesis of CdSe nanoplatelets stands out. The second part briefly introduces the electronic and optical properties of CdSe NPLs, focusing on the shape and the electronic band structure probed by the STM/STS technique. The final part of the first chapter will present possible types of electronic band alignment in CdSe NPLs-heterostructures, with attention placed on the band structure of CdSe/CdS core/crown NPLs.

The second chapter will present the material synthesis and the experimental techniques used in this work. The detailed protocol for the synthesis of 4.5 ML CdSe NPLs and CdSe/CdS core/crown NPLs with different crown sizes is provided in the first part of the chapter. Meanwhile, the theoretical background of STM (STS) and magneto-photoluminescence (PL) spectroscopy techniques is provided in the second part. This part begins with a description of tunnel effects, microscopy, and STS measurements. Then, the working principle of absorption and PL spectra are also presented, particularly the magneto-PL spectroscopy technique.

The third chapter focuses on exploring the structural and electronic properties of 4.5 ML CdSe NPLs. The NPLs are checked with high–angle annular dark–field transmission electron microscopy (HAADF-TEM) to determine the crystal structure, lateral size, thickness, and shape of NPLs. The STM/STS technique was performed on individual NPLs to investigate their surface and electronic characteristics. STM topographic images reveal evidence of the truncated edges, which expose atomic terraces on the side facets of NPLs. Tunneling dI/dV spectra (STS) are employed to probe the density of states (DOS) of NPLs. STS results provide insight into the electronic band structure of NPLs, especially the presence of electron and hole trap states in the band gap. The trapping mechanism in NPLs was studied by recording the tunneling current in real time (feedback loop: OFF). The current-time (I (t))

measurements exhibit the blinking effects caused by electron traps. Power spectral density (PSD) was used to characterize the blinking traces in the tunneling current. As a result, PSD curves follow a power law dependency with an exponent of 2, implying that a single electron trap behaves as a stochastic two-level system (TLS) in individual CdSe NPLs.

The fourth chapter focuses on investigating magneto-optical effects in 4.5 ML CdSe and CdSe/CdS core/crown NPLs using magneto-photoluminescence (PL) spectroscopy at 4.2 K. The first part will summarize the recombination mechanisms of dark excitons via phonons and surface DB spins in CdSe NCs, followed by CdSe NPLs. The second part presents the low-temperature emission properties of CdSe NPLs, focusing on the polarized emission under external magnetic fields. By analyzing the degree of circular polarization (DCP) of the exciton emission, we observed the non-monotonous DCP behavior caused by the surface DB-dark exciton spins interaction in low magnetic fields. To clarify the contribution of DB spins on each specific surface, we synthesized CdSe/CdS core/crown NPLs with various crown sizes. The formation of the CdS crown part is determined by energy dispersive X-ray (EDX), and absorption/emission spectra. Similarly, we also investigate the exciton DCP as a function of external magnetic fields in core/crown NPLs. As a result, we found the non-monotonous DCP behavior in CdSe/CdS core/smallest crown (5 mins) like the exciton DCP in CdSe NPLs but with a larger magnitude. Meanwhile, the non-monotonous DCP of the exciton vanishes as the lateral size of the CdS crown part is increased. This indicates that the DB spins on the side facets of CdSe NPLs are the main responsibility for the non-monotonous DCP behavior of the dark exciton. In addition, we also investigate the exciton spin dynamics in the bare NPLs and the core/crown NPLs (30 min) via polarization-resolved PL decay measurements. The bare NPLs exhibit the ultrafast spin relaxation process supported by surface DB spins in low magnetic fields. In contrast, the core/crown NPLs (30 min) show the linear dependency of the spin relaxation rate on magnetic fields.

In addition to the above chapters, the thesis is extended to investigate the structural and electronic properties of ultrathin PbSe NPLs by the LT-STM/STS technique. The first part will present the chemical composition and structural properties of NPLs analyzed using the EDX spectroscopy and HAADF-STEM technique. As a result, we determined

the formation of rock-salt PbSe NPLs with an average lateral size of 3.5 nm × 4.8 nm. The second part presents STM/STS measurements on individual PbSe NPLs. We analyzed STM topographic images and found the NPLs with various thicknesses, typically 0.4 nm, 0.8 nm, and 1.6 nm-thick NPLs. The electronic properties of these NPLs were checked with STS at 77 K. The STS results show the increasing electronic band gap with decreasing thickness of NPLs, implying the 1D quantum confinement effect in NPLs. Particularly, the 1.6 nm thick-NPL has an electronic band gap of 1.0 eV, approximately equal to the optical gap (0.95 eV). Therefore, the emission properties of PbSe NPLs are dominated by the population of 1.6 nm thick-NPLs. The final part presents theoretical predictions of the effect of lateral size on the electronic properties of NPLs. Tight-binding calculations demonstrated that the electronic band gap of NPLs depends on their lateral size, particularly the 1.6 nm thick-NPLs that can achieve the telecom wavelengths (e.g., S-, E-, O-bands).

Chapter I: Theoretical Background

This chapter will present the theoretical concept of structural, electronic, and optical properties of CdSe nanocrystals (NCs), followed by an exploration of the specific properties of CdSe nanoplatelets (NPLs).

1.1. Crystal structure of CdSe

In materials science, the crystal structure plays a critical role in determining the characteristics of materials. For example, Titanium dioxide (TiO_2) semiconductors, exhibit differences in the electronic band structure among the anatase, rutile, and brookite phases [8]. Indeed, the arrangement of atoms in a crystal lattice creates the periodic potential that interacts with electrons, leading to the formation of energy bands. These bands consist of allowed energy levels, separated by a band gap. Therefore, any change in the crystal structure regularly influences the electronic properties of semiconductors.
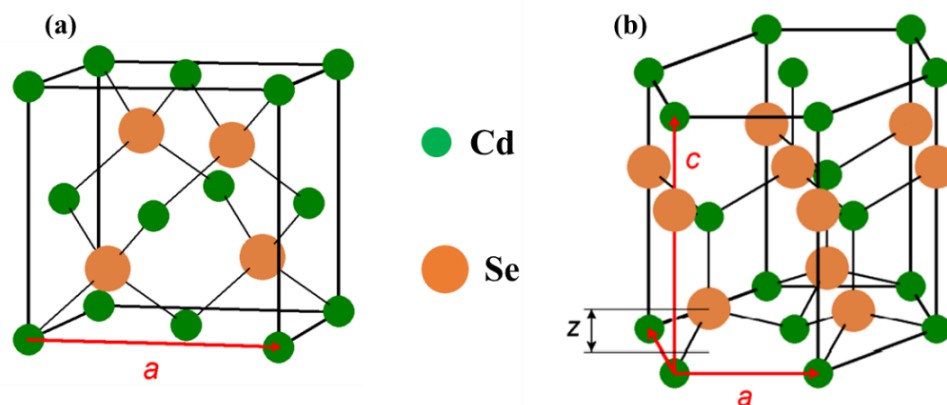
Figure 1: Structure of bulk CdSe semiconductors with **(a)** cubic zinc-blende (ZB) structure, and **(b)** hexagonal wurtzite (WZ) structure. Reproduced from reference [9].

Bulk CdSe is a direct band gap semiconductor characterized by a zinc-blende (ZB) or wurtzite (WZ) structure, resulting in different physical chemistry. The ZB structure consists of two interpenetrating face-centered cubic sublattices distanced from each other by 1/4 of the lattice constant (Figure 1a). Meanwhile, the WZ structure includes the two hexagonal close-packed sublattices displaced from each other by 3/8 of the

lattice constant along the c-axis (Figure 1b). This difference leads to two different stacking styles of Cadmium (Cd) and Selenium (Se) atoms. In the ZB structure, Cd and Se atoms are arranged above each other in an ABCABC arrangement along the [111] direction, while the arrangement of atoms is ABAB along the [0001] direction in the WZ structure [10]. The electronic band structure of CdSe differs between the WZ and ZB structures [11]. In the allowed scope of the thesis, we only discuss the electronic and optical properties of the ZB structure.

1.2. Electronic band structure of CdSe

Semiconductors are widely recognized as materials with electrical conductivity between an insulator and a conductor. They are typically characterized by an electronic band gap (≤ 3 eV) that lies between the valence and conduction bands, influencing electronic and optical properties. Therefore, we must comprehend the motion of charge carriers (electron and hole) in the electronic band structure of semiconductors. In solid-state physics, the Bloch theorem describes the wave function of electrons and holes in a bulk crystal under periodic boundary conditions.

$$\psi_{\text{nk}}(\vec{r}) = u_{nk}(\vec{r}) \exp(i\vec{k}\vec{r}) \tag{1.1}$$

Where $u_{nk}(\vec{r})$ is the Bloch function. k is the wavevector associated with the particle and the set of k-values is called the first Brillouin zone [12]. The index n is associated with the energy levels of the wave functions described by the Bloch theorem, forming the band structure. To compute these energies, E (k), the effective mass (EM) approximation is used to simplify the band structure by modeling the behavior of electrons and holes as free quasi-particles with different masses. Under these conditions, the energies of these wavefunctions are approximated as parabolic bands at the same k-vector. The energy dispersion for the valence band (VB) and conduction band (CB) are mathematically expressed as:

$$E_c(\text{k}) = \frac{\hbar^2 k^2}{2m_c^*} + E_g \; ; \; E_v(\text{k}) = \frac{-\hbar^2 k^2}{2m_v^*} \tag{1.2}$$

Where m_c^* and m_v^* are the effective mass of the electron in the conduction band and the valence band, respectively. E_g is the electronic band gap where no charge carriers can exist.

The electronic band structure of CdSe arises from the interplay of orbitals between Cd and Se atoms. Specifically, the conduction band is formed from the s-orbital of the Cd atom ([Kr] $4d^{10}5s^2$), while the valence band is constructed from the p-orbital of the Se atom ([Ar] $3d^{10}4s^24p^4$). The electronic band structure can be theoretically calculated through various methods, including tight-binding calculations (TBC) [13], density functional theory (DFT) [14], and ab initio calculations [11]. Voisin and co-workers [13] recently reported the calculated band structure of CdSe NPLs using tight-binding calculation (Figure 2a). Since the s- and p-orbitals are deep, a very intense region appears in the CB and the VB at the Γ-point (the red rectangle). The band gap energy (E_g) is determined as the energy distance from the HOMO level in the VB and the LUMO level in the CB.
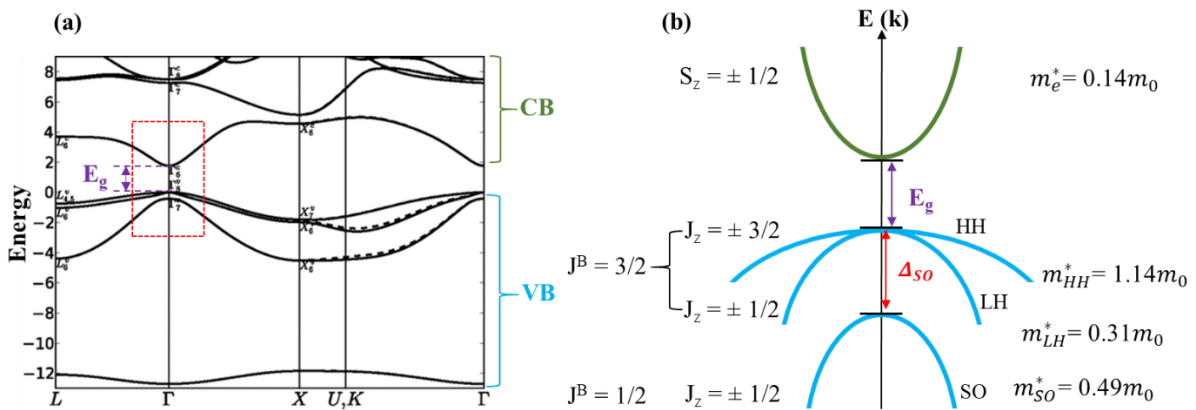
Figure 2: Zinc-blende CdSe NPLs. (**a**) Calculated band structure [13]. (**b**) A simplified view of the band edges in the parabolic approximation. The in-plane effective mass of the heavy hole (HH), light hole (LH), and split-off hole (SO) (in m_0 unit) are quoted from the reference [15].

If the conduction band can be effectively approximated using the EM approximation, the valence band proves more intricate due to the inherent sixfold (p_x, p_y, p_z) degeneracy (including spin) of the p-orbital at $k = 0$ (Figure 2a). Consequently, the electron spin will interact relatively with its orbital moment in a potential, resulting in the splitting of

energy levels. This relativistic interaction is called the spin-orbit interaction (or the spin-orbit coupling). In this case, the total angular momentum (J) is a conserved quantity, expressed as: $J = L + S$, where L is the orbital angular momentum and S is the spin angular momentum. Figure 2b shows a simplified band structure (ZB CdSe structure) in the parabolic approximation, including the band edges of the CB (green bands) and the VB (blue bands). When the spin-orbit interaction becomes strong, the sixfold degeneracy of the p orbital is split into a fourfold degenerated band ($J^B = 3/2$) at the Γ_8-point and a "split-off" twofold degenerated band ($J^B = 1/2$) at the Γ_7-point with the split-off coupling constant of 0.42 eV [15]. The $J = 3/2$ band still degenerates into two sub-bands differing in the projection of the total angular momentum (J_z) at $k \neq 0$. As a result, the $J_z = \pm 3/2$ represents the heavy hole (HH), and the $J_z = \pm 1/2$ is the light hole (LH) (Figure 2b). The splitting between the LH and HH bands does not occur because no intrinsic crystal field is induced in the ZB structure comparable to the WZ structure. In summary, understanding the electronic band structure is very important and necessary to further study the optoelectronic properties of semiconductors.

1.3. Quantum confinement effect

Quantum confinement is one of the important physical effects in semiconductors. When the dimension of a semiconductor reduces to the nanoscale, the motion of charge carriers is thus spatially confined in the remaining dimensions, resulting in the modification of the density of state (DOS), band edge, and bandgap energy. This phenomenon is called the quantum confinement effect. Depending on the material dimension, the quantum confinement effect is divided into three different types, including quantum wells (2D confinement), quantum wires (1D confinement), and quantum dots (0D confinement) (Figure 3).
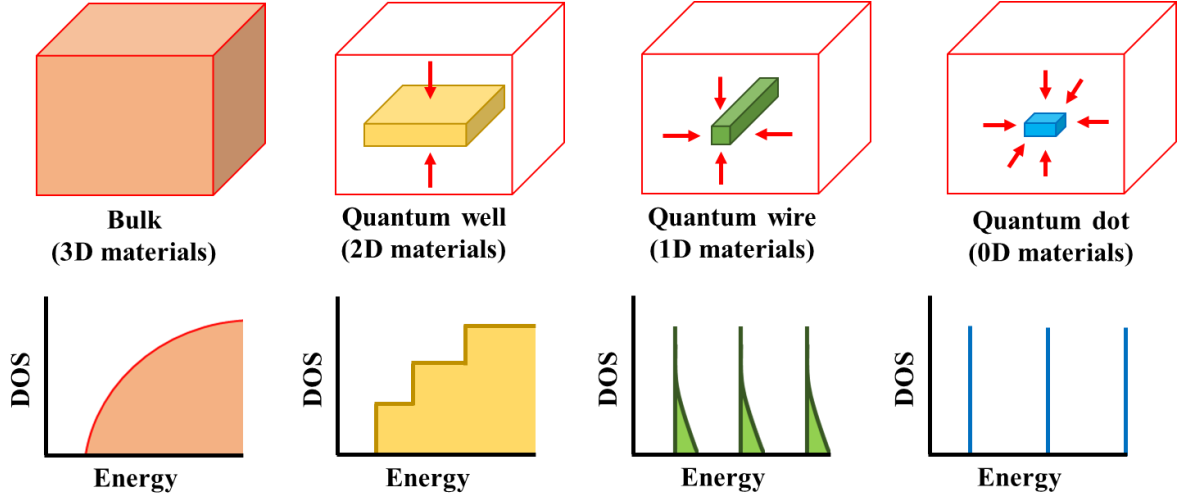
Figure 3: Schematic illustration of three different types of quantum confinement in semiconductors.

In bulk semiconductors, the electronic band structure is approximated as parabolic bands using the effective mass (EM) approximation. This approximation depends on the condition that the crystal size sufficiently exceeds the lattice constant. Given the lattice constant of zinc-blende CdSe NCs as p = 6.08 Å, the EM approximation is still consistent in describing the electronic band structure of these nanocrystals [16]. Therefore, the wavefunction of an electron and hole can be expressed as a linear combination of Bloch functions.

$$\psi_n(\vec{r}) = \sum_k F_{n\vec{k}} u_{n\vec{k}}(\vec{r}) \exp(i\vec{k}\vec{r}) \tag{1.3}$$

Where F_{nk} is the expansion coefficient satisfying the limit conditions for the infinite well. The Bloch functions (u_{nk}) weakly vary under the function of the k-vector such that the wavefunction can be simplified as:

$$\psi_n(\vec{r}) \sim u_{n\vec{0}}(\vec{r}) \, \phi_n(\vec{r}) \tag{1.4}$$

With $\phi_n(\vec{r})$ is the envelop function expressed as:

$$\phi_n(\vec{r}) = \Sigma C_{n\vec{k}} \, exp(i\vec{k}\vec{r}) \tag{1.5}$$

Since the nanocrystal size (R) is larger than the lattice constant (p), the Bloch function and the envelope function vary on distinct spatial scales. In this case, the envelope

function will comply with the Schrödinger equation and can describe the quantum confinement effect.

1.3.1. The electron confinement in the conduction band

The electronic states in 2D nanostructures can be described as the movement of an electron in an infinite potential well. The Schrödinger equation can be written as follows.

$$[H_0 + U_0(r)]\psi(r) = E\psi(r) \tag{1.6}$$

where H_0 is the Hamiltonian for the unperturbed crystal and $U_0(r)$ is the unperturbed potential. Inserting the electron wavefunction into equation (**1.6**), we will obtain a new form of the Schrödinger equation as follows:

$$\left[-\frac{\hbar^2}{2m_e^*}\nabla_e^2(r) + V_e(r)\right]\phi_e(r) = E\phi_e(r) \tag{1.7}$$

With the infinite potential barrier $V_e(r)$: $V_e(r) = 0$ if $r < R$ and $V_e(r) = \infty$ if $r > R$. Solving equation (**1.7**) under these above conditions, we obtain the corresponding energy levels as follows:

$$E_e^{nlm} = \frac{\hbar k_{nl}^2}{2m_e^*} \tag{1.8}$$

The electron wavefunction solutions are referred to as hydrogen-like atomic orbitals with the principal quantum number (n = 1, 2, 3,...), the angular momentum quantum number (l = 0, 1, 2,...n-1), and the magnetic quantum number (m = 0, ±1, ±2,...±l). These quantum numbers describe the size, shape, and orientation of the orbital in space, respectively. The condition $k = \frac{n\pi}{R}$ is set up to prevent the wave function from being zero, so the first quantized electronic state (n = 1) can be written as follows:

$$E_e^{1s} = \frac{\hbar\pi^2}{2m_e^*R^2} \tag{1.9}$$

Chapter I: Theoretical Background

In terms of physics, the electronic state of an atom can be expressed as nL_e, in which, L represents each specific orbital (S, P, D,...) and e is electrons. The 1S electronic state has a twofold degenerated band with the total spin angular momentum equal to zero.

1.3.2. The hole confinement in the valence band

If the conduction band is unique, the valence band is more complicated because it is constructed from the p-orbital originating from the Se atom, which has six degenerate states. As a result, the valence band is split into three first subbands with different effective masses, including the HH, LH, and SO bands (see Figure 2b). These sub-bands are created by a mixture of various states; therefore, the hole wavefunctions include contributions from different envelope functions with L_h and L_{h+2}, which is called the "S-D" mixing [17]. Consequently, the calculation of the hole energy levels becomes complicated and must be based on the Luttinger Hamiltonian [18], [19], [20]. In this case, a new quantum number is introduced to the system, which is the total momentum: $\vec{F} = \vec{L_h} + \vec{J_h}$, where $\vec{L_h}$ is the orbital angular momentum for the hole envelope function, and $\vec{J_h}$ is the projection of the total angular momentum on the quantization axis [19]. The hole energy level (E_h) can be determined through the following equation [20]:

$$j_0(k)j_2\left(\sqrt{\beta}k\right) + j_2(k)j_0\left(\sqrt{\beta}k\right) = 0 \tag{1.10}$$

Where $k = R\sqrt{2m^*_{HH}E_h}/\hbar$, j_i is the Bessel function, and $\beta = m^*_{LH}/m^*_{HH}$ is the ratio of the light- and heavy-hole effective mass in the valance band. The energy level of holes can be deduced as follows:

$$E_h = \frac{\hbar^2 k^2}{2m^*_{HH}R^2} \tag{1.11}$$

When $m^*_{LH} \ll m^*_{HH}$, the lowest energy level of holes is given by:

$$E_h^{\frac{3}{2}}(\beta) = \frac{\hbar^2 \varphi^2(\beta)}{2m^*_{HH}R^2} \tag{1.12}$$

With $\varphi = 5.76$ taken from reference [20]. Like the electrons in the conduction band, the hole states are also denoted as nL_F with the total momentum F ($F = 1/2, 3/2,...$). The first hole state is $1S_{3/2}$ which is fourfold degenerate with the corresponding projection

F (F_z = -3/2, -1/2, 1/2, 3/2). A summary of relevant quantum numbers is presented in Figure 4.
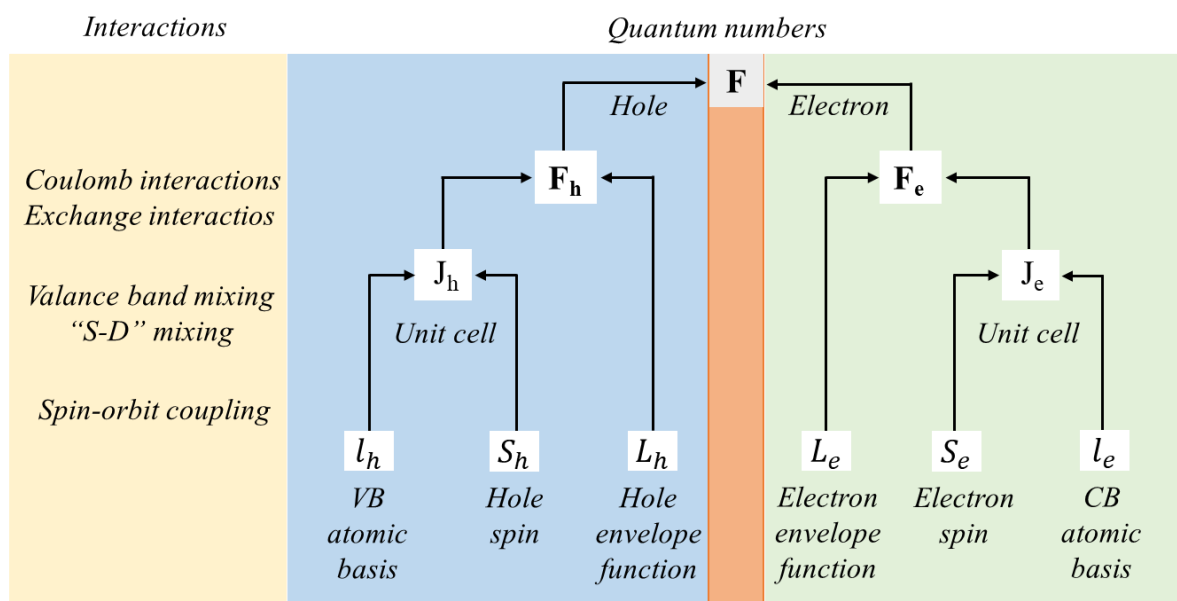
Figure 4: Summary of relevant quantum numbers for the wave functions in nanocrystals. Reproduced from reference [17].

1.4. Dielectric confinement effect

In addition to quantum confinement, colloidal semiconductor NCs are also affected by dielectric confinement caused by the difference in the dielectric constant inside the semiconductor (ε_{in}) and the surrounding media (ε_{out}). In bulk semiconductors, the dielectric confinement is very weak because the $\varepsilon_{in}/\varepsilon_{out}$ ratio is close to 1 [21]. In contrast, the dielectric confinement becomes strong in colloidal NCs due to the penetration of the electric field of the charge carriers into the surrounding media with a smaller dielectric constant ($\varepsilon_{in} > \varepsilon_{out}$). Figure 5 shows the dielectric confinement effect occurring in $(HOCH_2CH_2NH_3)_2PbI_4$ perovskite single crystals (2D) surrounded by ethanolamine (EA, ε_{out} = 37.7) and phenethylamine (PEA, ε_{out} = 3.3) ligands. In this case, the excitonic binding energy was estimated to be 13 meV for 2D–EA perovskite and 250 meV for 2D-PEA perovskite [22]. This example indicates that the dielectric confinement effect has a strong influence on the electron-hole Coulomb interactions, thus affecting the binding energy of the exciton. Experimentally, the quantum and dielectric confinement effect can be detected through the excitonic resonance signals in

absorption and PL spectroscopy [22]. However, the separation of the influence of these effects is very difficult by experimental methods compared to computational simulations [23]. In colloidal CdSe nanoplatelets (NPLs), the dielectric confinement effect has been investigated experimentally [24] and theoretically [25]. For example, the excitonic binding energy is 315 meV for 3.5 ML CdSe NPLs surrounded by oleic acid (OA) ligands ($\varepsilon_{in}= 6$, $\varepsilon_{out}= 2$) [25] while this value is 15 meV for bulk CdSe [26]. Therefore, understanding dielectric confinement offers the possibility of tuning the excitonic binding energy in colloidal NCs [21], [27].
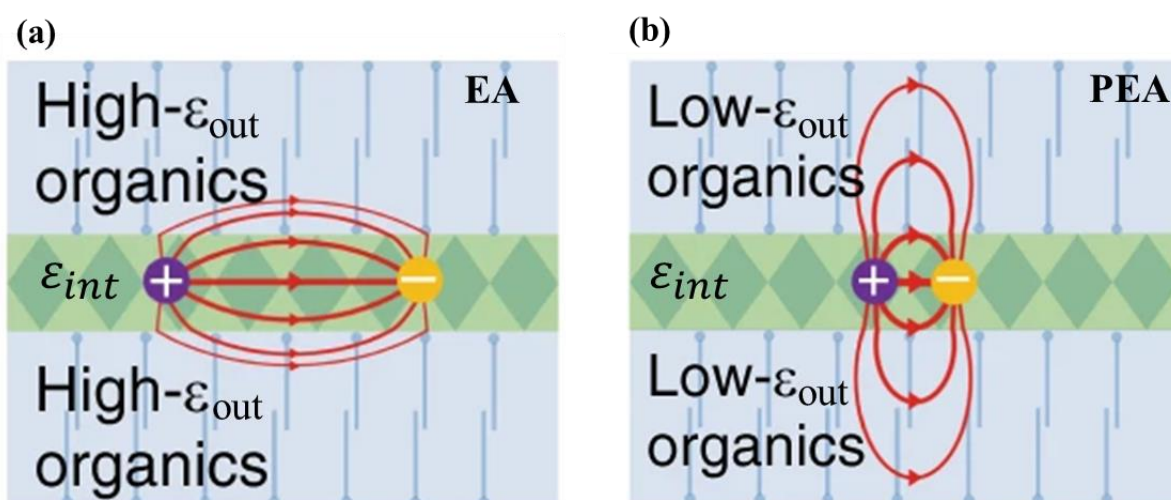
Figure 5: Schematic of the dielectric confinement effect in $(HOCH_2CH_2NH_3)_2PbI_4$ perovskite single crystals surrounded by two different types of organic ligands. **(a)** Ethanolamine (EA, $\varepsilon_{out} = 37.7$). **(b)** Phenethylamine (PEA, $\varepsilon_{out} = 3.3$). Note that the inside dielectric constant is larger than the dielectric constant of organic ligands in both cases ($\varepsilon_{in} > \varepsilon_{out}$). Reproduced from reference [22].

1.5. Optical properties

The arrangement of energy levels in the electronic band structure of a semiconductor forms the electronic properties that dictate its optical properties. Therefore, any changes in the electronic band structure can also influence the optical properties of semiconductors. This section will present basic concepts of optical transition and exciton (e.g., exciton binding energy, exciton fine structure), which are necessary to understand the optical properties of CdSe.

1.5.1. Optical transition in CdSe nanocrystals

Semiconductors are characterized by a band gap where no charge carriers can exist. Therefore, most of the electrons will occupy the energy levels in the valence band at room temperature. However, if an electron can absorb a high-energy photon, it will leave its initial state to an excited state. This process is called an optical transition. There are two possible types of optical transitions in semiconductors: interband transitions (where an excited electron leaves its initial state in an energy band to another state in another energy band) and intraband transitions (where an excited electron leaves its initial state to another state in the same energy band). However, only the interband transitions are allowed within semiconductors because they satisfy the three optical selection rules: $\Delta n = 0$; $\Delta L = 0, \pm 2$; $\Delta F = 0, \pm 1$ [28]. These optical transitions represent the absorption and emission of photons in semiconductors.

Optical spectroscopy techniques have widely been used to probe the optical transitions in colloidal NCs, such as static absorption [29], [30], and ultrafast transient absorption spectra [31]. Figure 6a shows the absorption and PL spectra of CdSe NCs measured at room temperature [29]. The absorption spectroscopy exhibits four main absorption lines corresponding to four allowed optical transitions originating from band-to-band electronic transitions. Figure 6b shows a simple schematic of allowed optical transitions in CdSe NCs. The conduction band is quite simple and consists of the electron state (1S, 1P). The valence band consists of four first-hole states, such as $1S_{3/2}$ (heavy-hole), $1P_{3/2}$, $2S_{3/2}$ (light-hole), and $2S_{1/2}$ (split-off) states. The first absorption line corresponds to the $1S_{3/2}$ (h) $\rightarrow$ 1S (e) transition (red arrow), which is the clearest peak. The second absorption line corresponds to the $2S_{3/2}$ (h) $\rightarrow$ 1S (e) transition (orange arrow). The third absorption line corresponds to the $1P_{3/2}$ (h) $\rightarrow$ 1P transition (green arrow), which is quasi-degenerate [32]. The fourth absorption line represents the $2S_{1/2}$ (h) $\rightarrow$ 1S (e) transition (blue arrow). The optical transition from the $1S_{3/2}$ (h) state to the 1S (e) state is also called the exciton, representing the emission peak observed in the PL spectroscopy (black dashed curve).
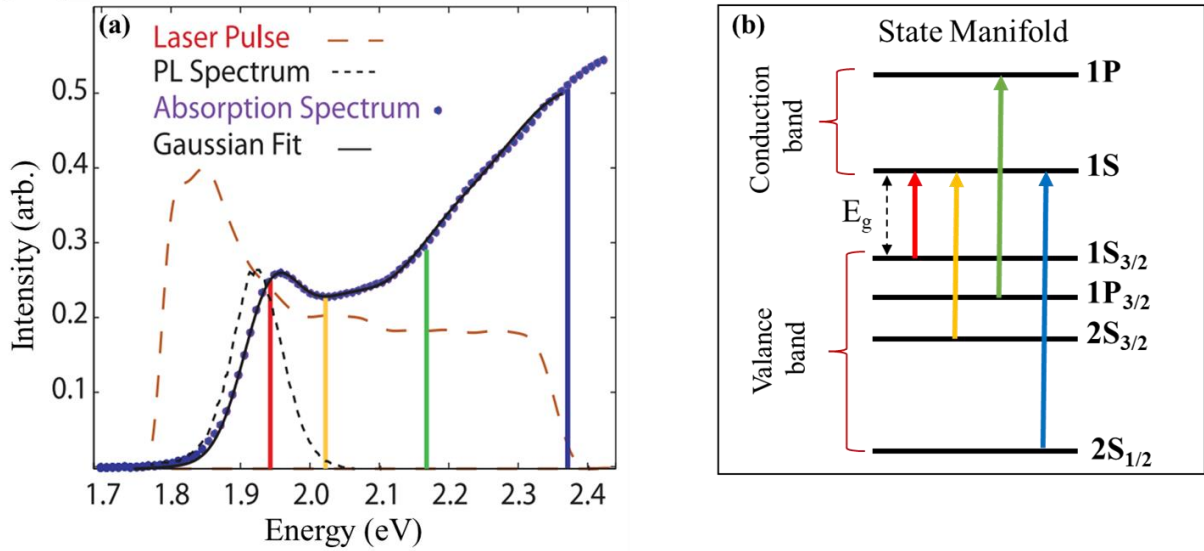
Figure 6: (a) Absorption and PL spectra of zinc-blende CdSe NCs. The ultrafast pulse spectrum used to interrogate the system is plotted with the absorption spectrum. **(b)** Schematic illustration of the allowed optical transitions in the NCs. Reproduced from reference [37].

1.5.2. Exciton in semiconductors

1.5.2.1. Definition of exciton

When a semiconductor undergoes a photoexcitation process, electrons are excited to the conduction band, leaving corresponding holes in the valence band. As a result, electron-hole pairs are formed, which are called "exciton" (Figure 7a). In a simple term, the excitons are hydrogen-like quasiparticles. Therefore, the exciton is characterized by the Bohr radius (a_0), which is written as follows:

$$a_0 = \frac{4\pi\varepsilon\varepsilon_0\hbar^2}{m_0 e\mu} \tag{1.13}$$

Where ε_0 is the vacuum permittivity, ε is the relative dielectric constant of the semiconductor, e is the charge of an electron, $\mu = 1/m_e^* + 1/m_h^*$ is the reduced mass of the electron/hole pair, and m_0 is the rest mass of an electron. In an exciton, an electron will interact with a hole through the attractive Coulomb force, also known as a bound state. The average physical separation between the electron and hole is referred to as the Bohr radius (or the exciton Bohr radius). Every semiconductor has a characteristic

Bohr radius. For example, such a semiconductor as monolayer WS_2 has $a_0 = 2.6$ nm [33], ZnO has $a_0 = 2.34$ nm [34], and CdSe NCs has $a_0 = 5.3$ nm [35]. To better understand the excitonic properties in semiconductor NCs, it is important to clarify the relation between the Coulomb exchange interaction and the quantum confinement effect. The influence of the quantum confinement effect on the exciton characteristic is typically evaluated by comparing the nanocrystal size (R) to the exciton Bohr radius (a_0).

Weak confinement regime: occurs when the nanocrystal size (R) is larger than the exciton Bohr radius (a_0). In this regime, the Coulomb exchange interaction is dominant in an exciton while the quantum confinement is considered perturbation. The exciton energy states are shifted by confinement

Moderated confinement regime: is typically observed in II-VI semiconductor NCS with a size equal to the exciton Bohr radius ($R \approx a_0$), and the following conditions should be satisfied: $a_h < R < a_e$ (where a_e and a_h are respectively the electron and hole Bohr radiuses) [34].

Strong confinement regime: To observe this confinement regime, the nanocrystal size (R) should be smaller than the exciton Bohr radius (a_0). In this regime, the quantum confinement effect is very important while the Coulomb interaction is neglective (Figure 7b). Experimentally, the strong confinement regime is found in quantum dots (QDs) where its electronic band structure consists of a series of discrete peaks [36].
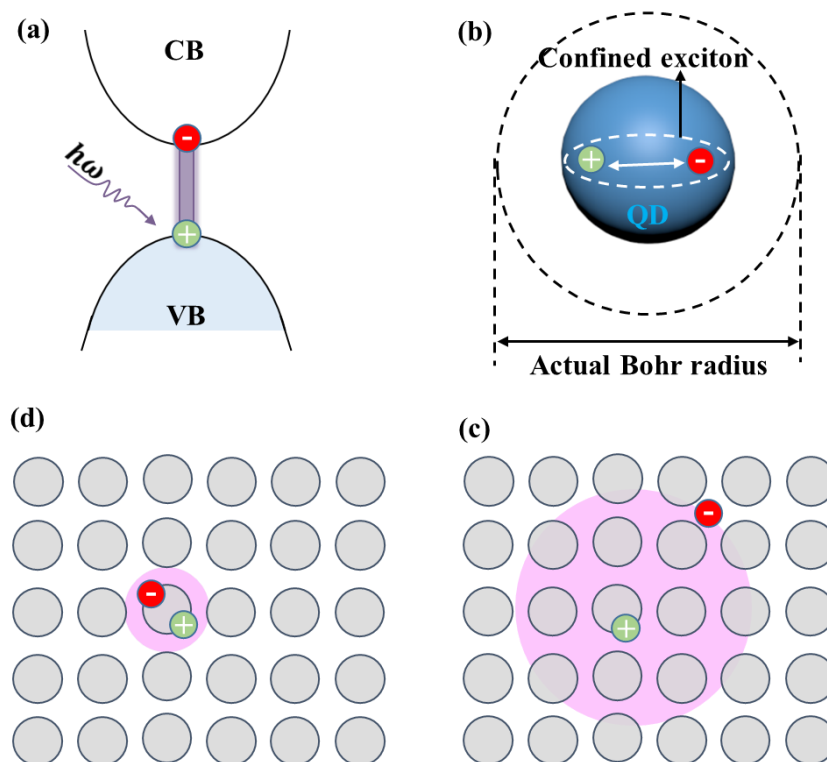
Figure 7: (a) Formation of an exciton in a semiconductor. **(b)** Schematic illustration of the strong confinement regime in quantum dots which have a smaller radius than the exciton Bohr radius. **(c)** Wannier-Mott exciton. **(d)** Frenkel exciton.

The excitons are typically classified into two following categories: (1) Wannier-Mott excitons which have a larger excitonic radius, the relative motion of the electron and the hole thus covering many unit cells in the crystal structure (Figure 7c). This type of exciton is considered a hydrogen-like quasiparticle, characterized by its Bohr radius (as mentioned in the previous content). (2) Frenkel excitons which are tightly bound excitons where the average distance between the electron and the hole is equal to one or a few nearest unit cells (Figure 7d).

1.5.2.2. Exciton binding energy

The exciton binding energy is the energy that is required to dissociate an exciton into a free electron and hole [37]. The binding energy is one of the most important physical parameters that characterize the exciton. For instance, an exciton with a high binding energy will imply a more stable exciton with a longer lifetime, which can dominate the optical properties of materials. Therefore, the binding energy of excitons always attracts attention when studying the optical properties of semiconductors, especially in the case

of colloidal semiconductor NCs. In 3D semiconductors with high principal quantum numbers (n), the Wannier–Mott exciton is normally called the Rydberg exciton, characterized by its Rydberg energy ($R_y = 13.6$ eV). The exciton binding energy (E_b) in bulk semiconductors can be written as:

$$E_b^{3D}(n) = \frac{\mu}{n^2 m_0 \varepsilon^2} R_y \qquad (1.14)$$

When reducing one of the semiconductor dimensions, the quantum confinement effect occurs in the direction perpendicular to the material plane, leading to the reduction of the Bohr radius as compared to 3D semiconductors. Therefore, the exciton binding energy is enhanced in 2D semiconductors, the relationship that can be expressed as [38]:

$$E_b^{2D}(n) = \frac{\mu}{(n - 0.5)^2 m_0 \varepsilon^2} R_y \qquad (1.15)$$

The above equation shows that the exciton binding energy is affected by various factors, including the effective mass of the charge carriers (electron and hole), the dielectric constant, and the quantum confinement effect. Experimentally, the binding energy of exciton in colloidal NCs can be measured by optical spectroscopic methods (e.g., one- and two-photon absorption [25], and photoacoustic spectroscopy [39]), and low-temperature scanning tunneling microscopy (LT-STM) [24].

1.5.3. Exciton fine structure in CdSe nanocrystals

In zinc-blende CdSe NCs, the $1S_{3/2} \rightarrow 1S$ band edge exciton has an eightfold degeneracy that is split into five energy levels due to the electron-hole interaction, intrinsic crystal field, and shape asymmetry [40]. This splitting results in the exciton fine (EF) structure. Each fine structure is described by its total angular momentum F; in particular, the state with $F = 1$ has three projections ($F_z = 0, \pm 1$), and the state with $F = 2$ has five projections ($F_z = 0, \pm 1, \pm 2$). The letters (U, L) are used to distinguish between the upper states ($F_z = 0^U, \pm 1^U$) and the lower states ($F_z = 0^L, \pm 1^L$). The states with $F_z = 0, 0^L$ and $F_z = \pm 2$ are optically passive within the electric dipole approximation, whereas $F_z = \pm 1$ are optically bright states (Figure 8). The EF structure plays a critical role in understanding the optical properties of colloidal NCs. For example, the bright-

dark exciton splitting leads to the dependency of PL decays on temperatures in CdSe NPLs [41]. Given the importance of exciton fine structure, many efforts have been made to investigate its effect on the optoelectronic properties of colloidal NCs, both theoretically [42], [43] and experimentally [44], [45].
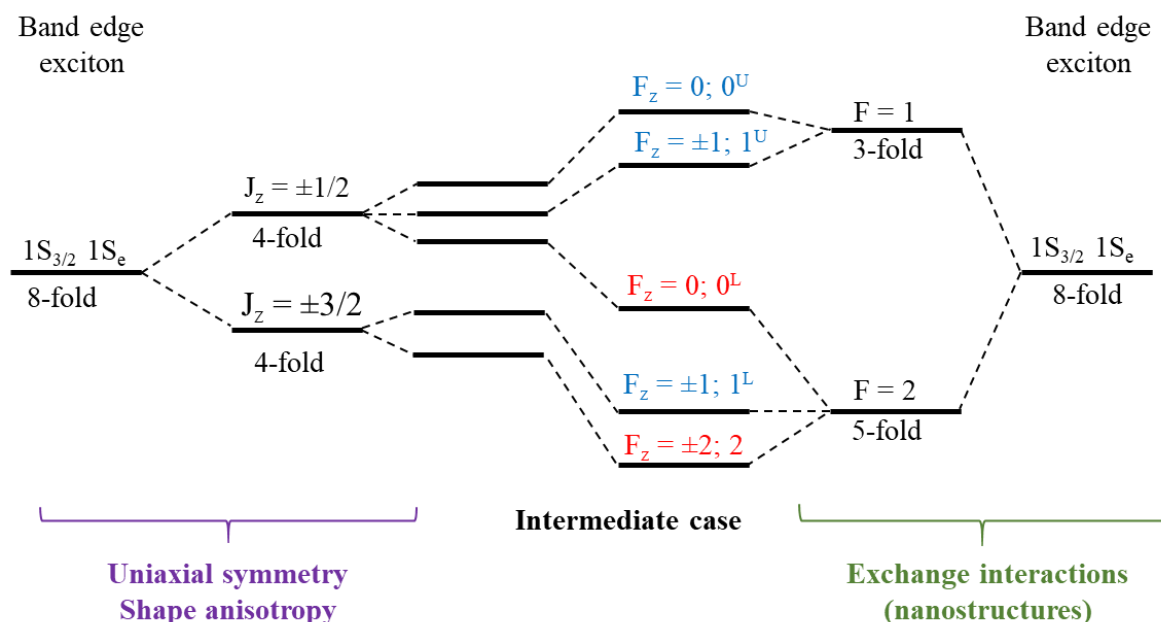
Figure 8: The exciton fine (EF) structure in semiconductors originates from the uniaxial symmetry, shape anisotropy, and electron-hole exchange interactions. In bulk semiconductors, the EF structure is dominated by uniaxial symmetry or shape anisotropy (the left part, purple). In contrast, the EF structure is dominated by electron-hole exchange interactions due to the quantum confinement effect in colloidal NCs (the right part, green). Reproduced from reference [40].

1.6. Synthesis of CdSe nanocrystals

Over the past decades, various types of CdSe NCs have been successfully prepared by different synthetic methods. Each method offers advantages for controlling the shape and size of NCs. In the scope of the thesis, we would like to present a summary of the synthetic methods for CdSe NCs, followed by CdSe nanoplatelets and their heterostructures.

Solvothermal synthesis is a method used for preparing nanomaterials such as metals, semiconductors, and ceramics. A solvothermal process involves the decomposition or

chemical reactions between precursors in the presence of a solvent. The synthesis proceeds in a closed reaction vessel under moderate to high pressure at a high temperature. This process has been used to prepare various semiconductor nanocrystals such as CdS [46], CdTe [47], and CdSe [48]. The morphology of nanomaterials can be controlled by manipulating the solvent supersaturation, concentration of precursors, and kinetics of chemical reactions [49].
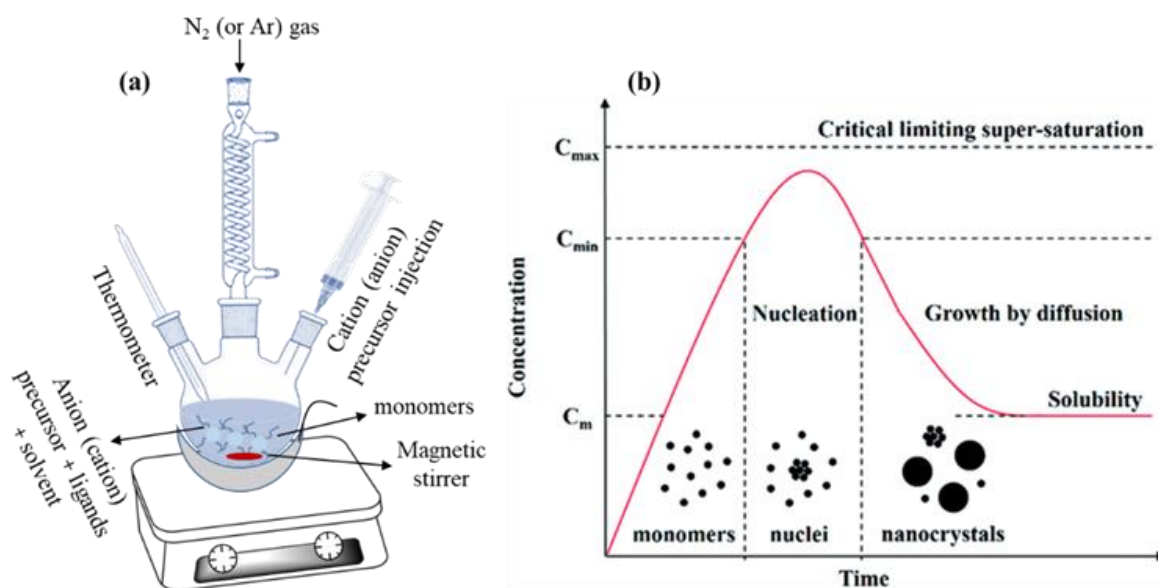
Figure 9 : **(a)** A typical hot-injection synthesis for colloidal NCs**. (b)** The LaMer model describes the growth of colloidal NCs as a function of reaction time and concentration of monomers. Reproduced from reference [50].

One-pot synthesis (non-injection synthesis) is a widely used method for the synthesis of organic compounds in which all the reactants used are mixed in the same reaction vessel. This method is quite simple because it does not require to inject precursors rapidly, and decreases the reaction temperature in a very short time. On the other hand, the shape and size of nanomaterials are also controlled by adjusting the reaction time during the synthesis. This method has also been applied for synthesizing semiconductor NCs such as CdS [51], CdSe [52], [53], and CdSe-based heterostructures [54], [55].

Hot-injection synthesis was initially introduced by Murray and co-workers in the synthesis of CdE (E = S, Se, Te) nanocrystals [56]. Since that time, this method has been widely used to synthesize colloidal NCs with various shapes and sizes. In this

thesis, we also synthesized colloidal CdSe NPLs by the hot injection method. The detailed protocol for this synthesis is presented in Chapter II. Typically, a hot-injection synthesis will proceed in a three-neck flask at the temperature range of 100 – 300 ℃ (Figure 9a). According to the model of LaMer [50], the formation of NCs involves the nucleation and growth process (Figure 9b). Firstly, all the necessary precursors are dispersed or dissolved in a proper solvent. Subsequently, the entire mixture is heated to a reaction temperature that allows monomers to be generated from chemical reactions between the initial precursors. The monomer concentration increases rapidly in the solution and reaches the supersaturation level after a certain time. At this point, nuclei are formed by the self-nucleation and aggregation of monomers. The growth process of NCs occurs on these pre-existing nuclei until the monomer concentration drops below the critical level. This stage enables us to control the size of NCs by adjusting the reaction parameters, including (i) the reaction time and temperature, (ii) the ratio of precursors, and (iii) the effect of solvent [57].

1.7. Colloidal CdSe nanoplatelets

The previous part provided basic theories of structural, electronic, and optical properties of CdSe NCs. These theories are very important and necessary to understand the optoelectronic properties of CdSe semiconductors, followed by colloidal CdSe and CdSe/CdS core/crown nanoplatelets. In addition, some synthetic methods for CdSe NCs were also presented, providing an overview of the formation of CdSe NCs. The next part will present information on the self-assembly, structural, and optoelectronic properties of CdSe nanoplatelets.

1.7.1. Definition of CdSe nanoplatelets

Nanoplatelets (NPLs), known as colloidal quantum wells (QWs), are atomically flat materials with well-defined surfaces upon their orientation. In 2006, wurtzite-CdSe nanoplatelets (NPLs) with a thickness of 1.4 nm were first synthesized by Jin Joo and co-workers [58]. Two years later, Ithurria and Dubertret successfully synthesized zinc-blende CdSe NPLs via a hot injection process [59]. Structurally, CdSe NPLs are quasi-two-dimensional (2D) nanostructures composed of alternating atomic layers of Cd and

Se elements in the [001] direction, forming the NPL thickness (d) and distinct geometry (Figure 10a) [60]. The shape and size of NPLs can be controlled with high precision by carefully adjusting the injection, the ratios between precursors, the reaction time, and temperature during the hot-injection synthesis [59]. For example, Yoon and co-workers successfully synthesized 4.5 monolayer (ML)-thick CdSe NPLs with various shapes by increasing the ratio of $Cd(ac)_2$/Se during a typical hot injection process [60]. Here, the n ML thickness of CdSe NPL corresponds to n Se layers sandwiched between $(n + 1)$Cd layers [61]. The high-resolution transmission electron microscopy (HR-TEM) image in Figure 10b shows rectangular CdSe NPLs with a thickness of 2 nm [62].
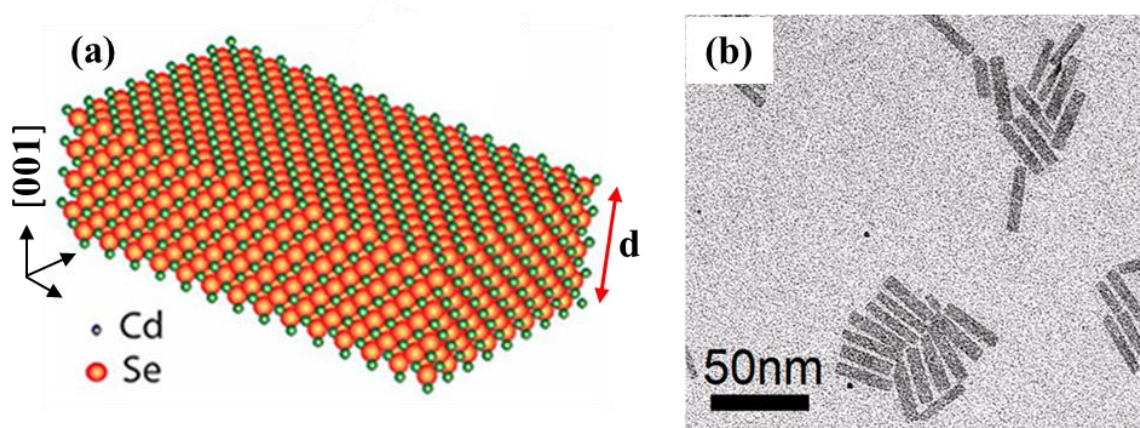
Figure 10: (a) Simulated structure of CdSe NPLs (the NPL thickness is denoted as d). **(b)** Transmission electron microscopy (TEM) image of CdSe NPLs with a thickness of 2 nm. Reproduced from reference [62].

1.7.2. Tunable emission wavelength of CdSe nanoplatelets

One of the most interesting characteristics of CdSe NPLs is their thickness-dependent optical properties. For example, Christodoulou et al reported the dependence of the emission wavelength of CdSe NPLs on their thickness [63]. The authors first synthesized 4.5 ML NPLs by injecting $Cd(Ac)_2$ into a mixture of Cd-myristate and Se in ODE solvent at 220 °C (Figure 11a). The 4.5 ML NPLs give a green emission under UV illumination, as shown in Figure 11b. Thicker NPLs can be synthesized by adding a mixture of $CdCl_2$, CdO, and oleic acid (OA) to the 4.5 ML CdSe NPL solution, and combining the control of the reaction temperature (280 – 320 °C) and time (2 – 5 hours). As a result, 5.5 ML, 6.5 ML, 7.5 ML, and 8.5 ML thick NPLs can be acquired according

to the above synthetic protocol (Figure 11a). The emission properties of NPLs were investigated with PL spectroscopy at room temperature. Figure 11c shows that the emission peak is shifted towards larger wavelengths as the NPL thickness is increased. Such spectral shift is attributed to the strong quantum confinement effect that occurred along the NPL thickness. With this unique characteristic, CdSe NPLs have become a promising semiconductor for optoelectronic devices, such as light-emitting diodes (LEDs) [64], and photodetectors [65]. Moreover, colloidal NPLs can easily be deposited on substrates by simple methods such as drop-casting, spin-coating, dip-coating, or inkjet printing [66]. This is beneficial for fabricating low-cost optoelectronic devices.
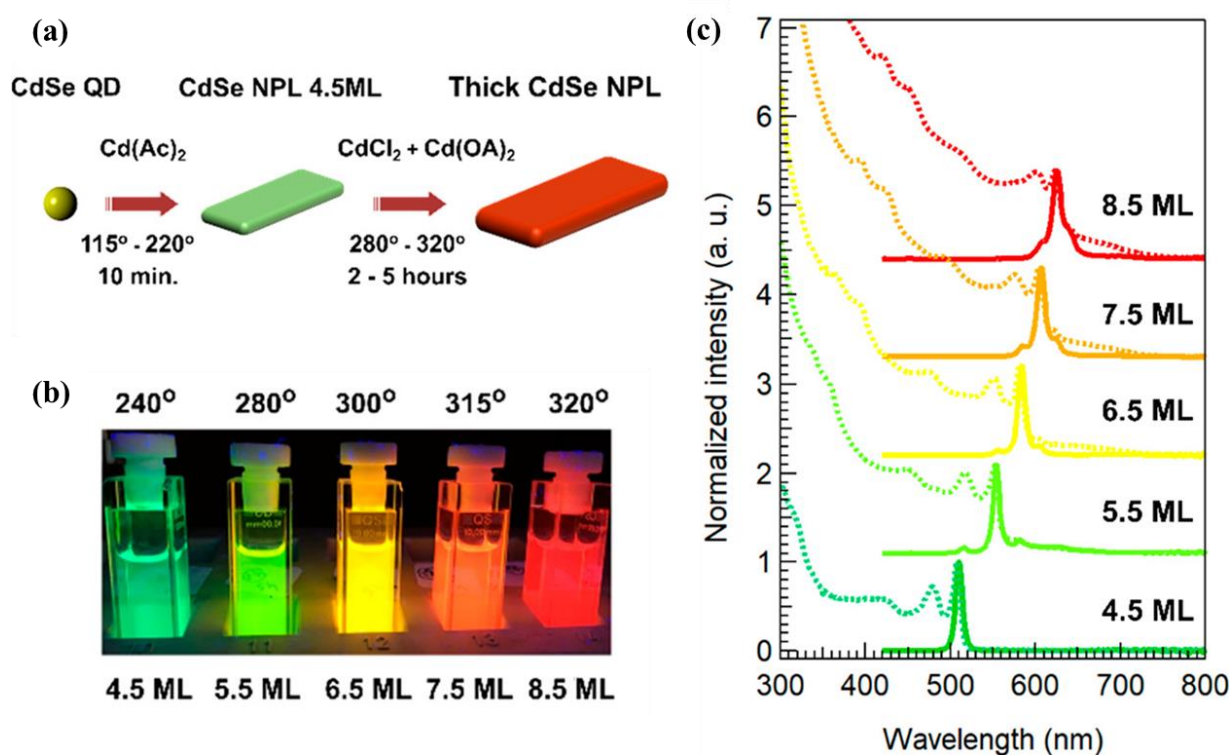
Figure 11: (a) Schematic illustration of the chemical reactions during the colloidal synthesis of CdSe NPLs. **(b)** Photography of different NPL samples under UV illumination. **(c)** Room temperature PL spectra of NPLs with various thicknesses. Reproduced from reference [63].

1.7.3. Quantum confinement effect in CdSe nanoplatelets probed by scanning tunneling microscopy

The unique shape of CdSe NPLs implies interesting physical phenomena governing their optoelectronic properties. The dependency of emission wavelength on the NPL thickness is evidence of the one-dimensional (1D) quantum confinement effect which strongly modifies the electronic band structure of NPLs. To probe this effect, some techniques have been employed such as optical spectroscopy and scanning tunneling spectroscopy (STS). Optical spectroscopy techniques (e.g., absorption and emission spectra) have been used to determine the quantum confinement effects in CdSe NPLs. These optical spectra are quite simple and beneficial to operating time and cost. For example, it is possible to quickly determine the band gap energy of NPLs based on their absorption and emission spectra measured at room temperature. Despite these, optical spectroscopy techniques do not provide the electronic band structure that is important and necessary to understand quantum confinement effects in NPLs. In contrast, scanning tunneling spectroscopy (STS) directly probes the electronic band structure of single NPLs. Here, we introduce low-temperature scanning tunneling microscopy (LT-STM) which is one of the powerful techniques for studying the electronic properties of materials, including colloidal CdSe NPLs.

Figure 12a shows a schematic illustration of STM/STS measurements on an isolated and flat-lying CdSe NPL. There are two main measurements in an STM system: (1) STM topographic measurement which is used to investigate the morphological properties (shape, size, and surface characteristics) of materials, and (2) STS measurement which directly probes the density of states (DOS) of materials. The detailed information on the STM/STS measurements is presented in Chapter II. Figure 12b exhibits the topography of two CdSe NPLs (5.5 ML) in the flat-lying geometry. To characterize their electronic properties, the STM tip is posited over an individual NPL to probe its density of state. Figure 12c presents tunneling dI/dV spectra (STS) measured on 5.5 ML (red) and 7.5 ML CdSe (black) NPLs (note that the STM topographic image of 7.5 ML CdSe NPLs is not presented in Figure 12). For 5.5 ML CdSe NPL, the dI/dV spectroscopy exhibits resonant peaks at both sides of the zero-

conductance region (ZCR). Specifically, the peak observed at a positive bias corresponds to the first electronic state in the CB while two separated peaks at negative bias voltages represent the heavy-hole (hh) and light-hole/spin-off (lh/so) states in the VB. The band gap energy is defined as the spacing between the first peaks in the CB and VB. The estimated band gap energy is 2.97 eV for 5.5 ML CdSe NPLs. Meanwhile, the STS measured on an individual 7.5 ML CdSe NPL shows a narrow band gap energy (2.17 eV). The decrease in the band gap energy implies the strong quantum confinement effect occurring along the NPL thickness [67].
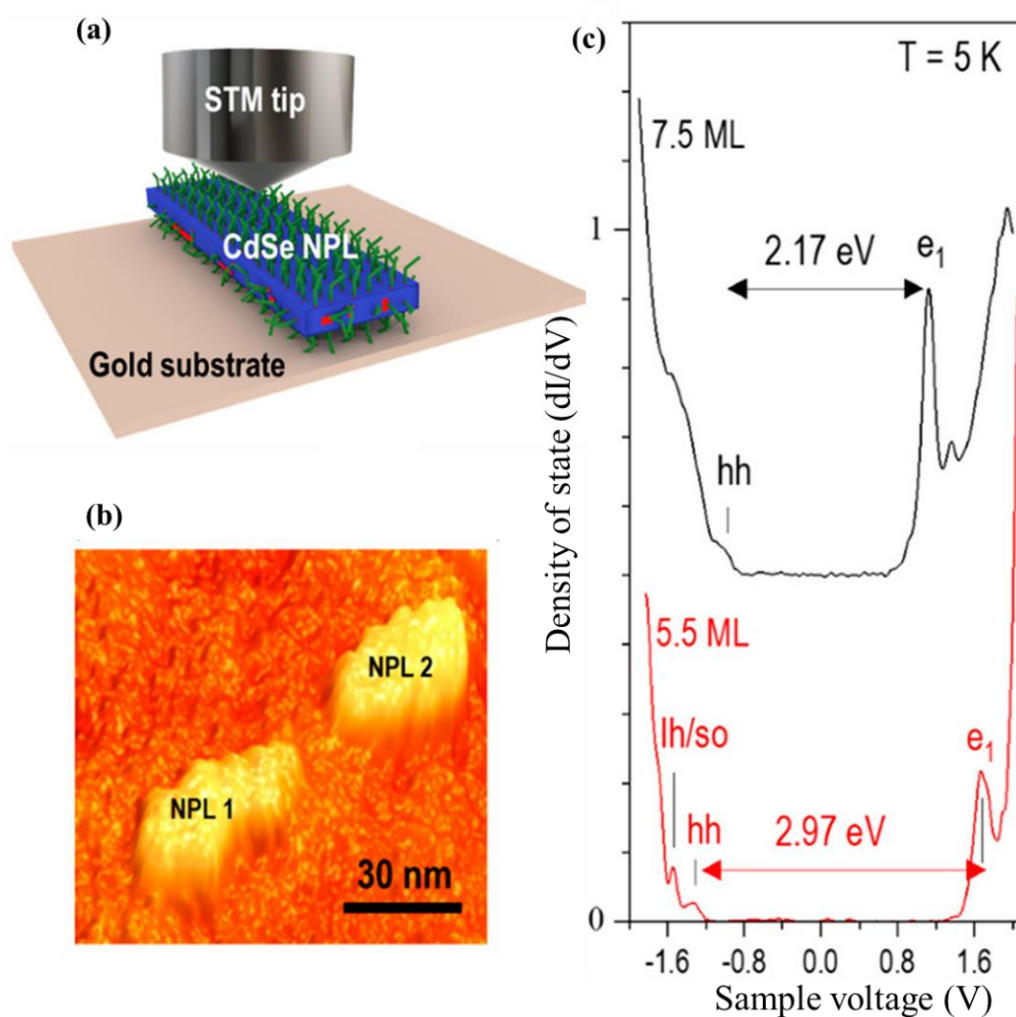
Figure 12: (a) Schematic illustration of STM/STS measurements on individual CdSe NPLs. **(b)** STM topographic images of two flat-lying NPLs (5.5 ML) measured at the following conditions: $V_s = -1.5$ V, $I_t = 5$ pA. **(c)** Tunneling dI/dV spectra were measured on individual 5.5 ML (red) and 7.5 ML (black) NPLs (T = 5 K). Reproduced from reference [67].

1.7.4. Self-assembly of CdSe nanoplatelets

Colloidal CdSe NPLs are 2D semiconductor nanostructures surrounded by organic ligands. These ligands play a critical role in controlling the surface characteristics of NPLs, particularly passive surface traps that strongly reduce the overall quantum efficiency of NPLs. In addition, ligands are beneficial to the stability of the crystalline structure and the chemical stability of NPLs. In solution, NPLs can interact with themselves or their surrounding media, resulting in two self-assemblies: flat-lying and stacked styles. The NPL-NPL interactions are typically physical forces such as van der Waals, electrostatic, and steric forces [68]. These interactions are affected by ligands surrounding NPLs [69], [70]. Antanovich and co-workers reported the influences of ligands on the self-assembly of 4.5 ML CdSe NPLs [68]. Figure 13a presents the TEM image of the NPL surrounded by oleic acid (OA) ligands, showing flat-lying and stacked NPLs. This NPL sample was treated with cadmium acetate ($Cd(OAc)_2$) and then checked with the TEM technique. Figure 13b shows the crowded presence of flat-lying NPLs compared to stacked NPLs. This difference is because of the interaction between ligands. Stacked NPL chains are primarily driven by the van der Waals attraction force between two flat plates and stabilized by ligand interchain interactions. Indeed, OA ligands surrounding the NPLs can interpenetrate each other due to the Brownian motion of NPLs, resulting in the attractive interaction between ligands through dispersive forces (Figure 13a, bottom panel) [69], [71]. These attractive interactions enhance the stability of stacked NPL chains in polar solvents. Furthermore, the NPLs have a high surface area that increases the number of dispersive contacts between the ligands, thus contributing to enhanced ligand chain interactions. In contrast, the number of dispersive contacts is significantly reduced after the treatment with $Cd(OAc)_2$ because acetate ions replaced surface-bound OA ions (Figure 13b, bottom panel) [68]. This decreases the ligand chain interactions, which weakens the stabilization of the stacked NPLs.
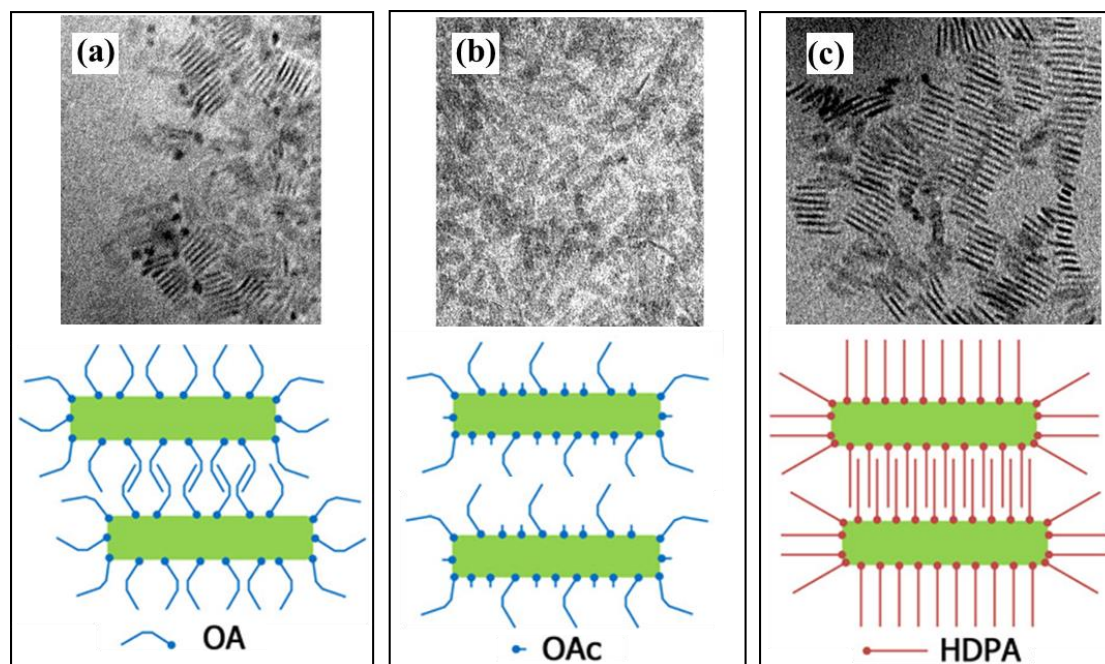
Figure 13: TEM images of 4.5 ML CdSe NPLs (upper) and schematic illustration of the ligand interactions (bottom). The NPLs are surrounded by oleic acid (OA) and stored in chloroform solvent. **(a)** before and **(b)** after treating with $Cd(OAc)_2$. **(c)** the NPLs capped with OA and OAc ligands carry out a ligand exchange with n-hexadecylphosphonic acid (HDPA). Reproduced from reference [68].

The NPLs capped with OA ligands treated with $Cd(OAc)_2$ carried out a ligand exchange with n-hexadecylphosphonic acid (HDPA). Figure 13c presents the TEM image of the NPLs capped with HDPA ligands, indicating that most nanoplatelets appear as long stacked chains. After the ligand exchange, OA ligands are entirely replaced by HDPA because oleic acid ($pK_a \approx 5$) is weaker than HDPA ($pK_a = 2.6$). The footprint of HDPA ligands is much shorter than OA ligands, thus the HDPA ligand chain interaction is tighter than the interaction between OA ligand chains [68], [72], [73]. This significantly enhances the stabilization of the stacked NPLs. In summary, ligands play a critical role in creating stacked NPLs in addition to enhancing the chemical stability of NPLs. Long-stacked NPLs have been demonstrated to create unique optical phenomena such as fast Förster resonance energy transfer (FRET) [74], [75], and giant oscillator strength [76], which could be exploited in NPL-based optoelectronic devices in the future.

1.7.5. Chiral shape of CdSe nanoplatelets

In addition to thickness, the 2D shape of NPLs also plays an important role in shaping their optical properties. For example, rectangular NPLs exhibit a higher fluorescence polarization than square NPLs at the same thickness [2]. Recently, increasing studies reported the chiral shape of NPLs (scrolls, helices, and twist) which may induce peculiar optical properties, such as circularly polarized light [77], [78], [79]. Such chiral shapes mainly originate from the interactions between organic ligands and nanoplatelet surfaces [80], [81]. In the scope of this thesis, we only focus on clarifying the origin of twisted CdSe NPLs surrounded by oleic acid (OA) ligands.

Experimentally, the shape of NPLs can be investigated with transmission electron microscopy (TEM) or other TEM modes. Figure 14d shows a high-angle annular dark-field scanning transmission electron microscopy (HAADF-STEM) image of CdSe NPLs surrounded by OA ligands, showing the presence of flat-laying and twisted NPLs. Figure 14e displays two types of twisted NPLs including edge-twisted and middle-twisted NPLs. The schematic illustration of twisted NPLs is presented in Figures 14b and 14c. Because twisted 2D NPLs typically relate to their Gaussian curvature, it is necessary to understand the concept of curvature. According to Guillemeney et al [70], a surface always has a curvature along two orthogonal directions at any point on the surface, called principal directions. The Gaussian curvature is defined as the product of two principal directions. The CdSe NPLs in Figure 14d were twisted by an angle of 45° along their long edge [77]. In this case, the twisted NPLs have a non-zero Gaussian curvature. According to Jana et al [77], twisted NPLs are formed due to three following causes: (1) the ligand absorption at the surface of the NPLs strains their 2D geometry, (2) the ligand self-assembly can induce surface stress in NPLs due to a mismatch between the crystalline and ligand lattices [78], [82], and (3) the elastic strain at the surfaces can also induce the twist of NPLs [83], [84]. The authors also calculated that only 140 ligands per NPL are needed to match the twist energy.
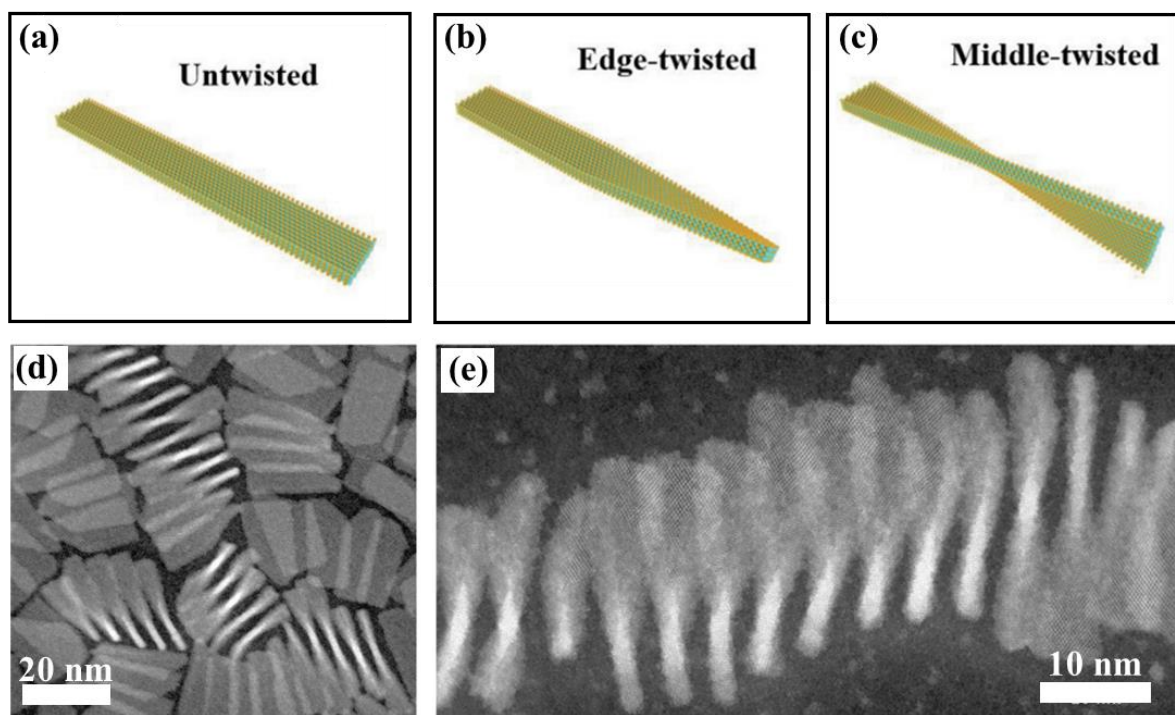
Figure 14: (a-c) Schematic illustration of twisted modes of CdSe NPLs [85]. **(d-e)** HAADF-STEM images of 5 ML CdSe NPLs [77].

In addition, the formation of twisted NPLs can also relate to structural defects. According to Nazir et al [85], any structural defects formed during the synthesis process can cause internal trapped stresses around the edges of NPLs. These internal stresses tend to be released at elevated temperatures, resulting in twist or rolling NPLs. By combining experiments and computational simulations (DFT), the authors pointed out that NPLs are easily twisted if their length exceeds 30 nm. In summary, the interactions between the ligands and the surfaces are responsible for the twist of CdSe NPLs, which has been discussed in previous studies [77], [80], [81]. However, we are interested in the role and impact of structural defects on the formation of twisted NPLs. This is because the true topography and shape of NPLs are still unknown at the atomic scale.

1.8. CdSe NPL-based heterostructures

1.8.1. Introduction

Despite possessing outstanding optoelectronic properties CdSe NPLs contain many surface traps caused by structural imperfections and unsuccessful ligand passivation [4]. These surface traps provide the pathway for non-radiative recombination, strongly reducing the quantum efficiency of NPLs [86]. One of the strategies for reducing the number of surface traps is the growth of CdSe NPL-based heterostructures such as core/shell and core/crown NPLs. These heterostructures (HSs) have proven their efficiency in improving chemical stability [87] and quantum efficiency [88] compared to bare CdSe NPLs. Therefore, CdS NPL-based heterostructures became ideal materials for applications in photocatalysis [89], and optoelectronic devices such as lasers [90], light-emitting diodes (LEDs) [91], [92], and photodetectors [93]. The optoelectronic applications of CdSe NPL-based heterostructures are presented in Figure 15.
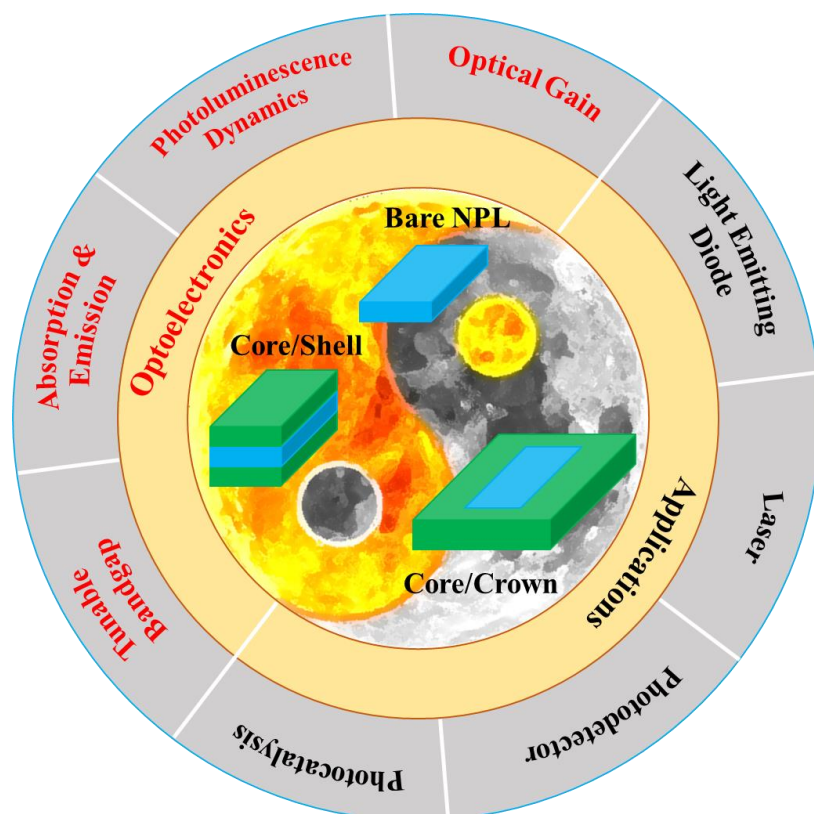
Figure 15: Summary of optical and electronic properties and applications of CdSe NPL-based heterostructures.

1.8.2. Electronic band alignment in CdSe NPL-based heterostructures

CdSe NPL-based heterostructures are 2D nanostructures formed by combining CdSe NPLs with another semiconductor. This combination leads to three possible band alignments in the heterostructures due to the difference in the electronic properties of semiconductors.

The type I band alignment typically forms when combining a wide band gap semiconductor (material A) with a narrow bandgap semiconductor (material B) into a nanostructure. As a result, both the electron and hole are confined in material B, while material A acts as a potential barrier (Figure 16a). Therefore, the optical properties of the heterostructure are mainly dominated by material B (narrow band gap semiconductor). For example, CdSe/CdS, and CdSe/ZnS core/shell NCs typically have the type-I band structure, where the excitonic properties of the whole structure are governed by the core material (CdSe) [87], [94].
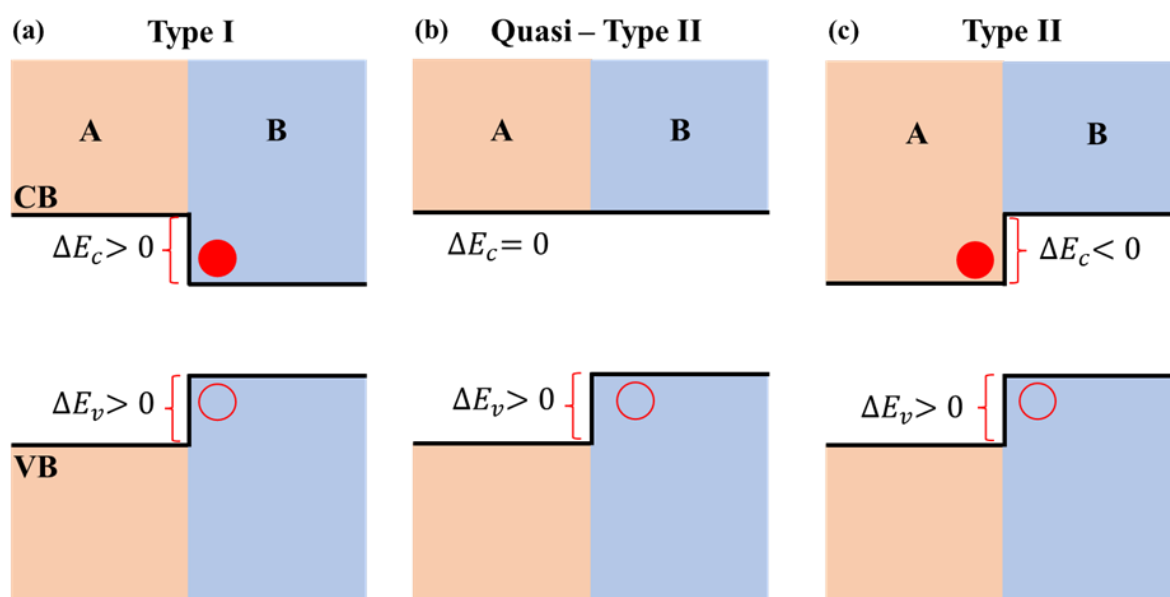
Figure 16: Schematic diagram of three possible band alignments in heterostructures. **(a)** Type I structure. **(b)** Quasi-type II structure. **(c)** Type II structure.

The type II band alignment is formed when the conduction and the valence band edges of material A are at lower energies than those of material B, so that ΔE_c and ΔE_v have an opposite sign (Figure 16c). In this band alignment, the electron and hole wavefunction are spatially separated and confined on each material, forming the

heterostructure. For example, CdSe/CdTe core/crown NPLs exhibit the type II band structure, where the electron and electron wavefunction are confined in the conduction band of the core (CdSe) and the valence band of the crown (CdTe), respectively. Therefore, exciton recombination allowed the formation of the spatially indirect exciton [95].

Colloidal heterostructures can also form the quasi-type II band alignment, as described in Figure 16b. In this band alignment, one of the charge carriers is only confined in one region of the heterostructure, while the other carrier is delocalized over the whole structure. The quasi-type II structure is found in CdTe/CdSe core/shell [96] and CdSe/CdS core/thick-shell NCs [97].

1.8.3. Synthesis of CdSe NPL-based heterostructures

CdSe NPL-based heterostructures have successfully been prepared by various methods such as c-ALD [98], one-pot synthesis [99], and hot-injection synthesis [97], [100]. Generally, the growth of CdSe-based heterostructures (e.g., core/shell, and core/crown NCs) can consist of two steps: the growth of CdSe NPLs, and the epitaxial growth of another material on CdSe NPLs. The formation of CdSe-based heterostructures requires that (1) CdSe NPLs provide favorable sites for the growth of the second material, and (2) the nucleation of the second material can be controlled [101]. In this work, our CdSe/CdS core/crown nanoplatelets were prepared by a hot-injection synthesis. The detailed synthetic process is presented in Chapter II.

1.9. Conclusion

In summary, we have provided the theory on the structural, electronic, and optical properties, and the synthesis methods of CdSe NCs, followed by CdSe NPLs and their heterostructures.

For the electronic properties, the Bloch theorem and effective mass approximation provide a basic background to understand the formation of energy levels in the band structure of CdSe NCs. These theories are necessary to understand the confinement of charge carriers in the NC dimensions, known as the quantum confinement effect. This effect strongly modifies the electronic band structure (e.g., band edges, and band gap energy), which opens the pathways for adjusting the optical properties of NCs.

For the optical properties, the absorption spectroscopy showed the main optical transitions in CdSe NCs, where the $1S_{3/2} - 1S$ band edge is split into five sub-energy levels, forming the exciton fine (EF) structure. Understanding the EF structure is very important in explaining the low-temperature optical properties of CdSe NCs, particularly in the case of CdSe NPLs**.**

For CdSe NPLs, this material exhibits unique optoelectronic properties that can be regulated by controlling their shape and size. For example, the emission wavelength of NPLs strongly depends on their thickness, known as the 1D quantum confinement effect. In particular, scanning tunneling spectroscopy (STS) was employed to probe the density of states (DOS) of CdSe NPL at the nanoscale, providing detailed information on the electronic band structure and the quantum confinement effect.

Finally, the synthetic methods of CdSe NPLs and their heterostructures were also provided in this chapter. Particularly, the hot injection synthesis offers the ability to control the NPL shape and size by carefully adjusting the reaction parameters such as the ratios between precursors, temperature, and time.

Bibliography

[1]   S. Ithurria, M. D. Tessier, B. Mahler, R. P. S. M. Lobo, B. Dubertret, and A. L. Efros, "Colloidal nanoplatelets with two-dimensional electronic structure," *Nat. Mater.*, vol. 10, no. 12, pp. 936–941, 2011, doi: 10.1038/nmat3145.

[2]   D.-E. Yoon *et al.*, "Origin of Shape-Dependent Fluorescence Polarization from CdSe Nanoplatelets," *J. Phys. Chem. C*, vol. 121, no. 44, pp. 24837–24844, Nov. 2017, doi: 10.1021/acs.jpcc.7b07216.

[3]   G. H. V Bertrand, A. Polovitsyn, S. Christodoulou, A. H. Khan, and I. Moreels, "Shape control of zincblende CdSe nanoplatelets," *Chem. Commun.*, vol. 52, no. 80, pp. 11975–11978, 2016, doi: 10.1039/C6CC05705E.

[4]   S. O. M. Hinterding *et al.*, "Single Trap States in Single CdSe Nanoplatelets," *ACS Nano*, vol. 15, no. 4, pp. 7216–7225, 2021, doi: 10.1021/acsnano.1c00481.

[5]   S. Pokrant and K. B. Whaley, "Tight-binding studies of surface effects on electronic structure of CdSe nanocrystals: the role of organic ligands, surface reconstruction, and inorganic capping shells," *Eur. Phys. J. D - At. Mol. Opt. Plasma Phys.*, vol. 6, no. 2, pp. 255–267, 1999, doi: 10.1007/s100530050307.

[6]   R. W. Meulenberg *et al.*, "Evidence for Ligand-Induced Paramagnetism in CdSe Quantum Dots," *J. Am. Chem. Soc.*, vol. 131, no. 20, pp. 6888–6889, May 2009, doi: 10.1021/ja8098454.

[7]   E. V Shornikova *et al.*, "Surface spin magnetism controls the polarized exciton emission from CdSe nanoplatelets," *Nat. Nanotechnol.*, vol. 15, no. 4, pp. 277–282, 2020, doi: 10.1038/s41565-019-0631-7.

[8]   M. Landmann, E. Rauls, and W. G. Schmidt, "The electronic structure and optical response of rutile, anatase and brookite TiO2," *J. Phys. Condens. Matter*, vol. 24, no. 19, p. 195503, 2012, doi: 10.1088/0953-8984/24/19/195503.

[9]   A. I. Lebedev, "Negative thermal expansion in CdSe quasi-two-dimensional nanoplatelets," *Phys. Rev. B*, vol. 100, no. 3, p. 35432, Jul. 2019, doi: 10.1103/PhysRevB.100.035432.

[10] S. Datta, T. Saha-Dasgupta, and D. D. Sarma, "Wannier function study of the relative stability of zinc-blende and wurtzite structures in the CdX (X = S, Se, Te) series," *J. Phys. Condens. Matter*, vol. 20, no. 44, p. 445217, Oct. 2008, doi: 10.1088/0953-8984/20/44/445217.

[11] A. Abbassi, Z. Zarhri, C. Azahaf, H. Ez-Zahraouy, and A. Benyoussef, "Boltzmann equations and ab initio calculations: comparative study of cubic and wurtzite CdSe," *Springerplus*, vol. 4, no. 1, p. 543, 2015, doi: 10.1186/s40064-015-1321-z.

[12] H. Haug and S. W. Koch, *Quantum Theory of the Optical and Electronic Properties of Semiconductors*, 5th ed. WORLD SCIENTIFIC, 2009. doi: 10.1142/7184.

[13] R. Benchamekh *et al.*, "Tight-binding calculations of image-charge effects in colloidal nanoscale platelets of CdSe," *Phys. Rev. B*, vol. 89, no. 3, p. 35307, Jan. 2014, doi: 10.1103/PhysRevB.89.035307.

[14] M. R. Ashwin Kishore, K. Larsson, and P. Ravindran, "Two-Dimensional CdX/C2N (X = S, Se) Heterostructures as Potential Photocatalysts for Water Splitting: A DFT Study," *ACS Omega*, vol. 5, no. 37, pp. 23762–23768, Sep. 2020, doi: 10.1021/acsomega.0c02804.

[15] D. J. Norris and M. G. Bawendi, "Measurement and assignment of the size-dependent optical spectrum in CdSe quantum dots," *Phys. Rev. B*, vol. 53, no. 24, pp. 16338–16346, Jun. 1996, doi: 10.1103/PhysRevB.53.16338.

[16] L. Liu *et al.*, "Shape Control of CdSe Nanocrystals with Zinc Blende Structure," *J. Am. Chem. Soc.*, vol. 131, no. 45, pp. 16423–16429, Nov. 2009, doi: 10.1021/ja903633d.

[17] V. I. Klimov and J. A. Hollingsworth, "Nanocrystals Quantum Dots." pp. 1–62, 2010. [Online]. Available: https://doi.org/10.1201/9781420079272

[18] J. M. Luttinger and W. Kohn, "Motion of Electrons and Holes in Perturbed Periodic Fields," *Phys. Rev.*, vol. 97, no. 4, pp. 869–883, Feb. 1955, doi:

10.1103/PhysRev.97.869.

[19]   A. I. Ekimov *et al.*, "Absorption and intensity-dependent photoluminescence measurements on CdSe quantum dots: assignment of the first electronic transitions," *J. Opt. Soc. Am. B*, vol. 10, no. 1, pp. 100–107, Jan. 1993, doi: 10.1364/JOSAB.10.000100.

[20]   A. L. Efros, "Luminescence polarization of CdSe microcrystals," *Phys. Rev. B*, vol. 46, no. 12, pp. 7448–7458, Sep. 1992, doi: 10.1103/PhysRevB.46.7448.

[21]   A. V Rodina and A. L. Efros, "Effect of dielectric confinement on optical properties of colloidal nanostructures," *J. Exp. Theor. Phys.*, vol. 122, no. 3, pp. 554–566, 2016, doi: 10.1134/S1063776116030183.

[22]   B. Cheng *et al.*, "Extremely reduced dielectric confinement in two-dimensional hybrid perovskites with large polar organics," *Commun. Phys.*, vol. 1, no. 1, p. 80, 2018, doi: 10.1038/s42005-018-0082-8.

[23]   R. Chakraborty and A. Nag, "Dielectric confinement for designing compositions and optoelectronic properties of 2D layered hybrid perovskites," *Phys. Chem. Chem. Phys.*, vol. 23, no. 1, pp. 82–93, 2021, doi: 10.1039/D0CP04682E.

[24]   B. Ji *et al.*, "Dielectric Confinement and Excitonic Effects in Two-Dimensional Nanoplatelets," *ACS Nano*, vol. 14, no. 7, pp. 8257–8265, Jul. 2020, doi: 10.1021/acsnano.0c01950.

[25]   E. V Shornikova *et al.*, "Exciton Binding Energy in CdSe Nanoplatelets Measured by One- and Two-Photon Absorption," *Nano Lett.*, vol. 21, no. 24, pp. 10525–10531, 2021, doi: 10.1021/acs.nanolett.1c04159.

[26]   Y. S. Park and D. C. Reynolds, "Exciton Structure in Photoconductivity of CdS, CdSe, and CdS: Se Single Crystals," *Phys. Rev.*, vol. 132, no. 6, pp. 2450–2457, Dec. 1963, doi: 10.1103/PhysRev.132.2450.

[27]   M. Kumagai and T. Takagahara, "Excitonic and nonlinear-optical properties of dielectric quantum-well structures," *Phys. Rev. B*, vol. 40, no. 18, pp. 12359–12381, Dec. 1989, doi: 10.1103/PhysRevB.40.12359.

[28]   N. C. Gerhardt and M. R. Hofmann, "Spin-Controlled Vertical-Cavity Surface-Emitting Lasers," *Adv. Opt. Technol.*, vol. 2012, p. 268949, 2012, doi: 10.1155/2012/268949.

[29]   J. R. Caram *et al.*, "Exploring size and state dynamics in CdSe quantum dots using two-dimensional electronic spectroscopy," *J. Chem. Phys.*, vol. 140, no. 8, p. 84701, Feb. 2014, doi: 10.1063/1.4865832.

[30]   D. Xiang, Y. Li, L. Wang, T. Ding, J. Wang, and K. Wu, "Electron and Hole Spin Relaxation in CdSe Colloidal Nanoplatelets," *J. Phys. Chem. Lett.*, vol. 12, no. 1, pp. 86–93, Jan. 2021, doi: 10.1021/acs.jpclett.0c03257.

[31]   C. Zhang, T. N. Do, X. Ong, Y. Chan, and H.-S. Tan, "Understanding the features in the ultrafast transient absorption spectra of CdSe quantum dots," *Chem. Phys.*, vol. 481, pp. 157–164, 2016, doi: https://doi.org/10.1016/j.chemphys.2016.08.027.

[32]   M. Cadirci *et al.*, "Ultrafast exciton dynamics in Type II ZnTe–ZnSe colloidal quantum dots," *Phys. Chem. Chem. Phys.*, vol. 14, no. 39, pp. 13638–13645, 2012, doi: 10.1039/C2CP41978E.

[33]   E. J. Sie *et al.*, "Observation of Exciton Redshift–Blueshift Crossover in Monolayer WS2," *Nano Lett.*, vol. 17, no. 7, pp. 4210–4216, Jul. 2017, doi: 10.1021/acs.nanolett.7b01034.

[34]   V. Babentsov and F. Sizov, "Defects in quantum dots of IIB–VI semiconductors," *Opto-Electronics Rev.*, vol. 16, no. 3, pp. 208–225, 2008, doi: 10.2478/s11772-008-0025-0.

[35]   K. Kyhm, J. H. Kim, S. M. Kim, and H. Yang, "Gain dynamics and excitonic transition in CdSe colloidal quantum dots," *Opt. Mater. (Amst).*, vol. 30, no. 1, pp. 158–160, 2007, doi: https://doi.org/10.1016/j.optmat.2006.11.036.

[36]   B. Alperson, I. Rubinstein, G. Hodes, D. Porath, and O. Millo, "Energy level tunneling spectroscopy and single electron charging in individual CdSe quantum dots," *Appl. Phys. Lett.*, vol. 75, no. 12, pp. 1751–1753, Sep. 1999, doi:

10.1063/1.124808.

[37] J.-C. Lee, J.-D. Chai, and S.-T. Lin, "Assessment of density functional methods for exciton binding energies and related optoelectronic properties," *RSC Adv.*, vol. 5, no. 123, pp. 101370–101376, 2015, doi: 10.1039/C5RA20085G.

[38] A. Chernikov *et al.*, "Exciton Binding Energy and Nonhydrogenic Rydberg Series in Monolayer ${\mathrm{WS}}_{2}$," *Phys. Rev. Lett.*, vol. 113, no. 7, p. 76802, Aug. 2014, doi: 10.1103/PhysRevLett.113.076802.

[39] S. J. Zelewski, K. C. Nawrot, A. Zak, M. Gladysiewicz, M. Nyk, and R. Kudrawiec, "Exciton Binding Energy of Two-Dimensional Highly Luminescent Colloidal Nanostructures Determined from Combined Optical and Photoacoustic Spectroscopies," *J. Phys. Chem. Lett.*, vol. 10, no. 12, pp. 3459–3464, Jun. 2019, doi: 10.1021/acs.jpclett.9b00591.

[40] M. Nirmal and L. Brus, "Luminescence Photophysics in Semiconductor Nanocrystals," *Acc. Chem. Res.*, vol. 32, no. 5, pp. 407–414, May 1999, doi: 10.1021/ar9700320.

[41] L. Biadala, F. Liu, M. D. Tessier, D. R. Yakovlev, B. Dubertret, and M. Bayer, "Recombination Dynamics of Band Edge Excitons in Quasi-Two-Dimensional CdSe Nanoplatelets," *Nano Lett.*, vol. 14, no. 3, pp. 1134–1139, Mar. 2014, doi: 10.1021/nl403311n.

[42] H. Bui, A. Karpulevich, and G. Bester, "Excitonic fine structure of zinc-blende and wurtzite colloidal CdSe nanocrystals and comparison to effective mass results," *Phys. Rev. B*, vol. 101, no. 11, p. 115414, Mar. 2020, doi: 10.1103/PhysRevB.101.115414.

[43] M. Korkusinski, O. Voznyy, and P. Hawrylak, "Fine structure and size dependence of exciton and biexciton optical spectra in CdSe nanocrystals," *Phys. Rev. B*, vol. 82, no. 24, p. 245304, Dec. 2010, doi: 10.1103/PhysRevB.82.245304.

[44] S. Vezzoli *et al.*, "Exciton Fine Structure of CdSe/CdS Nanocrystals Determined by Polarization Microscopy at Room Temperature," *ACS Nano*, vol. 9, no. 8, pp.

7992–8003, Aug. 2015, doi: 10.1021/acsnano.5b01354.

[45] E. V Shornikova *et al.*, "Addressing the exciton fine structure in colloidal nanocrystals: the case of CdSe nanoplatelets," *Nanoscale*, vol. 10, no. 2, pp. 646–656, 2018, doi: 10.1039/C7NR07206F.

[46] F. W. Guicun Li and Z. Zhang, "Synthesis of High Quality CdS Nanorods by Solvothermal Process and their Photoluminescence," *J. Nanoparticle Res.*, vol. 7, no. 6, pp. 685–689, 2005, doi: 10.1007/s11051-005-7521-7.

[47] B. Zhong, W. Kang, Z. Zhang, L. Zhang, and B. Ma, "Facile one-pot solvothermal synthesis of CdTe nanorods and their photoelectrical properties," *CrystEngComm*, vol. 22, no. 23, pp. 3927–3932, 2020, doi: 10.1039/D0CE00459F.

[48] T. Wang, J. Wang, Y. Zhu, F. Xue, J. Cao, and Y. Qian, "Solvothermal synthesis and characterization of CdSe nanocrystals with controllable phase and morphology," *J. Phys. Chem. Solids*, vol. 71, no. 7, pp. 940–945, 2010, doi: https://doi.org/10.1016/j.jpcs.2010.04.001.

[49] G. Demazeau, "Review. Solvothermal Processes: Definition, Key Factors Governing the Involved Chemical Reactions and New Trends," vol. 65, no. 8, pp. 999–1006, 2010, doi: doi:10.1515/znb-2010-0805.

[50] J. Chang and E. R. Waclawik, "Colloidal semiconductor nanocrystals: controlled synthesis and surface chemistry in organic media," *RSC Adv.*, vol. 4, no. 45, pp. 23505–23527, 2014, doi: 10.1039/C4RA02684E.

[51] K.-T. Yong, Y. Sahoo, M. T. Swihart, and P. N. Prasad, "Shape Control of CdS Nanocrystals in One-Pot Synthesis," *J. Phys. Chem. C*, vol. 111, no. 6, pp. 2447–2458, Feb. 2007, doi: 10.1021/jp066392z.

[52] S. Das and S. Paul, "Optimized one-pot synthesis of CdSe quantum dot capped with 3-mercaptopropionic acid as an efficient fluorescent probe for selective detection of Hg (II)," *Water Environ. J.*, vol. 36, no. 3, pp. 541–552, Aug. 2022, doi: https://doi.org/10.1111/wej.12785.

[53]   X. Liu *et al.*, "One-pot synthesis of CdSe magic-sized nanocrystals using selenium dioxide as the selenium source compound," *Chem. Eng. J.*, vol. 230, pp. 466–474, 2013, doi: https://doi.org/10.1016/j.cej.2013.06.116.

[54]   I. Mekis, D. V Talapin, A. Kornowski, M. Haase, and H. Weller, "One-Pot Synthesis of Highly Luminescent CdSe/CdS Core−Shell Nanocrystals via Organometallic and 'Greener' Chemical Approaches," *J. Phys. Chem. B*, vol. 107, no. 30, pp. 7454–7462, Jul. 2003, doi: 10.1021/jp0278364.

[55]   H. Zhan *et al.*, "One-pot aqueous-phase synthesis of ultra-small CdSe/CdS/CdZnS core–shell–shell quantum dots with high-luminescent efficiency and good stability," *J. Nanoparticle Res.*, vol. 15, no. 6, p. 1680, 2013, doi: 10.1007/s11051-013-1680-8.

[56]   C. B. Murray, D. J. Norris, and M. G. Bawendi, "Synthesis and characterization of nearly monodisperse CdE (E = sulfur, selenium, tellurium) semiconductor nanocrystallites," *J. Am. Chem. Soc.*, vol. 115, no. 19, pp. 8706–8715, Sep. 1993, doi: 10.1021/ja00072a025.

[57]   M. G. Burt, J. H. Harding, A. M. Stoneham, E. C. Scher, L. Manna, and A. P. Alivisatos, "Shape control and applications of nanocrystals," *Philos. Trans. R. Soc. London. Ser. A Math. Phys. Eng. Sci.*, vol. 361, no. 1803, pp. 241–257, Dec. 2002, doi: 10.1098/rsta.2002.1126.

[58]   J. Joo, J. S. Son, S. G. Kwon, J. H. Yu, and T. Hyeon, "Low-Temperature Solution-Phase Synthesis of Quantum Well Structured CdSe Nanoribbons," *J. Am. Chem. Soc.*, vol. 128, no. 17, pp. 5632–5633, May 2006, doi: 10.1021/ja0601686.

[59]   S. Ithurria and B. Dubertret, "Quasi 2D Colloidal CdSe Platelets with Thicknesses Controlled at the Atomic Level," *J. Am. Chem. Soc.*, vol. 130, no. 49, pp. 16504–16505, Dec. 2008, doi: 10.1021/ja807724e.

[60]   D.-E. Yoon *et al.*, "Atomistics of Asymmetric Lateral Growth of Colloidal Zincblende CdSe Nanoplatelets," *Chem. Mater.*, vol. 33, no. 12, pp. 4813–4820, 2021, doi: 10.1021/acs.chemmater.1c00563.

[61]   W. Cho *et al.*, "Direct Synthesis of Six-Monolayer (1.9 nm) Thick Zinc-Blende CdSe Nanoplatelets Emitting at 585 nm," *Chem. Mater.*, vol. 30, no. 20, pp. 6957–6960, Oct. 2018, doi: 10.1021/acs.chemmater.8b02489.

[62]   M. D. Tessier, C. Javaux, I. Maksimovic, V. Loriette, and B. Dubertret, "Spectroscopy of Single CdSe Nanoplatelets," *ACS Nano*, vol. 6, no. 8, pp. 6751–6758, 2012, doi: 10.1021/nn3014855.

[63]   S. Christodoulou *et al.*, "Chloride-Induced Thickness Control in CdSe Nanoplatelets," *Nano Lett.*, vol. 18, no. 10, pp. 6248–6254, 2018, doi: 10.1021/acs.nanolett.8b02361.

[64]   A. G. Vitukhnovsky, V. S. Lebedev, A. S. Selyukov, A. A. Vashchenko, R. B. Vasiliev, and M. S. Sokolikova, "Electroluminescence from colloidal semiconductor CdSe nanoplatelets in hybrid organic–inorganic light emitting diode," *Chem. Phys. Lett.*, vol. 619, pp. 185–188, 2015, doi: https://doi.org/10.1016/j.cplett.2014.12.002.

[65]   A. Dutta *et al.*, "Hybrid Nanostructures of 2D CdSe Nanoplatelets for High-Performance Photodetector Using Charge Transfer Process," *ACS Appl. Nano Mater.*, vol. 3, no. 5, pp. 4717–4727, May 2020, doi: 10.1021/acsanm.0c00728.

[66]   P. Bai, A. Hu, Y. Liu, Y. Jin, and Y. Gao, "Printing and In Situ Assembly of CdSe/CdS Nanoplatelets as Uniform Films with Unity In-Plane Transition Dipole Moment," *J. Phys. Chem. Lett.*, vol. 11, no. 11, pp. 4524–4529, Jun. 2020, doi: 10.1021/acs.jpclett.0c00748.

[67]   N. Peric *et al.*, "Van Hove Singularities and Trap States in Two-Dimensional CdSe Nanoplatelets," *Nano Lett.*, vol. 21, no. 4, pp. 1702–1708, Feb. 2021, doi: 10.1021/acs.nanolett.0c04509.

[68]   A. Antanovich, A. Prudnikau, A. Matsukovich, A. Achtstein, and M. Artemyev, "Self-Assembly of CdSe Nanoplatelets into Stacks of Controlled Size Induced by Ligand Exchange," *J. Phys. Chem. C*, vol. 120, no. 10, pp. 5764–5775, 2016, doi: 10.1021/acs.jpcc.5b12139.

[69] M. A. Boles and D. V Talapin, "Self-Assembly of Tetrahedral CdSe Nanocrystals: Effective 'Patchiness' via Anisotropic Steric Interaction," *J. Am. Chem. Soc.*, vol. 136, no. 16, pp. 5868–5871, Apr. 2014, doi: 10.1021/ja501596z.

[70] L. Guillemeney, L. Lermusiaux, G. Landaburu, B. Wagnon, and B. Abécassis, "Curvature and self-assembly of semi-conducting nanoplatelets," *Commun. Chem.*, vol. 5, no. 1, p. 7, 2022, doi: 10.1038/s42004-021-00621-z.

[71] L. Salem, "Attractive Forces between Long Saturated Chains at Short Distances," *J. Chem. Phys.*, vol. 37, no. 9, pp. 2100–2113, Nov. 1962, doi: 10.1063/1.1733431.

[72] J. R. Kanicky and D. O. Shah, "Effect of Degree, Type, and Position of Unsaturation on the pKa of Long-Chain Fatty Acids," *J. Colloid Interface Sci.*, vol. 256, no. 1, pp. 201–207, 2002, doi: https://doi.org/10.1006/jcis.2001.8009.

[73] G. H. Woehrle, L. O. Brown, and J. E. Hutchison, "Thiol-Functionalized, 1.5-nm Gold Nanoparticles through Ligand Exchange Reactions: Scope and Mechanism of Ligand Exchange," *J. Am. Chem. Soc.*, vol. 127, no. 7, pp. 2172–2183, Feb. 2005, doi: 10.1021/ja0457718.

[74] J. Liu, L. Guillemeney, B. Abécassis, and L. Coolen, "Long Range Energy Transfer in Self-Assembled Stacks of Semiconducting Nanoplatelets," *Nano Lett.*, vol. 20, no. 5, pp. 3465–3470, May 2020, doi: 10.1021/acs.nanolett.0c00376.

[75] C. E. Rowland *et al.*, "Picosecond energy transfer and multiexciton transfer outpaces Auger recombination in binary CdSe nanoplatelet solids," *Nat. Mater.*, vol. 14, no. 5, pp. 484–489, 2015, doi: 10.1038/nmat4231.

[76] B. Abécassis, M. D. Tessier, P. Davidson, and B. Dubertret, "Self-Assembly of CdSe Nanoplatelets into Giant Micrometer-Scale Needles Emitting Polarized Light," *Nano Lett.*, vol. 14, no. 2, pp. 710–715, Feb. 2014, doi: 10.1021/nl4039746.

[77] S. Jana, M. de Frutos, P. Davidson, and B. Abécassis, "Ligand-induced twisting

of nanoplatelets and their self-assembly into chiral ribbons," *Sci. Adv.*, vol. 3, no. 9, p. e1701483, Nov. 2023, doi: 10.1126/sciadv.1701483.

[78] C. Bouet *et al.*, "Two-Dimensional Growth of CdSe Nanocrystals, from Nanoplatelets to Nanosheets," *Chem. Mater.*, vol. 25, no. 4, pp. 639–645, Feb. 2013, doi: 10.1021/cm304080q.

[79] E. M. Hutter *et al.*, "Conformal and Atomic Characterization of Ultrathin CdSe Platelets with a Helical Shape," *Nano Lett.*, vol. 14, no. 11, pp. 6257–6262, Nov. 2014, doi: 10.1021/nl5025744.

[80] D. Monego *et al.*, "Ligand-induced incompatible curvatures control ultrathin nanoplatelet polymorphism and chirality," *Proc. Natl. Acad. Sci.*, vol. 121, no. 9, p. e2316299121, Feb. 2024, doi: 10.1073/pnas.2316299121.

[81] H. Po *et al.*, "Chiral Helices Formation by Self-Assembled Molecules on Semiconductor Flexible Substrates," *ACS Nano*, vol. 16, no. 2, pp. 2901–2909, Feb. 2022, doi: 10.1021/acsnano.1c09982.

[82] F. Bertolotti *et al.*, "Crystal symmetry breaking and vacancies in colloidal lead chalcogenide quantum dots," *Nat. Mater.*, vol. 15, no. 9, pp. 987–994, 2016, doi: 10.1038/nmat4661.

[83] R. Ghafouri and R. Bruinsma, "Helicoid to Spiral Ribbon Transition," *Phys. Rev. Lett.*, vol. 94, no. 13, p. 138101, Apr. 2005, doi: 10.1103/PhysRevLett.94.138101.

[84] S. Armon, E. Efrati, R. Kupferman, and E. Sharon, "Geometry and Mechanics in the Opening of Chiral Seed Pods," *Science (80-.).*, vol. 333, no. 6050, pp. 1726–1730, Sep. 2011, doi: 10.1126/science.1203874.

[85] Z. Nazir *et al.*, "Breaking the symmetry of colloidal 2D nanoplatelets: Twist induced quantum coupling," *Nano Res.*, vol. 16, no. 7, pp. 10522–10529, 2023, doi: 10.1007/s12274-023-5529-x.

[86] Z. Hu, A. Singh, S. V Goupalov, J. A. Hollingsworth, and H. Htoon, "Influence of morphology on the blinking mechanisms and the excitonic fine structure of

single colloidal nanoplatelets," *Nanoscale*, vol. 10, no. 48, pp. 22861–22870, 2018, doi: 10.1039/C8NR06234J.

[87]   A. Polovitsyn *et al.*, "Synthesis of Air-Stable CdSe/ZnS Core–Shell Nanoplatelets with Tunable Emission Wavelength," *Chem. Mater.*, vol. 29, no. 13, pp. 5671–5680, Jul. 2017, doi: 10.1021/acs.chemmater.7b01513.

[88]   C. Rodà *et al.*, "Colloidal CdSe/CdS Core/Crown Nanoplatelets for Efficient Blue Light Emission and Optical Amplification," *Nano Lett.*, vol. 23, no. 8, pp. 3224–3230, 2023, doi: 10.1021/acs.nanolett.2c05061.

[89]   Y. Liu, C. Guo Sun, J. Feng, J. Zhu, and Y. Shen, "CdSe nanoplatelets as photocatalyst for organic photochemistry: Synthesis of amino acid derivatives by decarboxylative alkylation of aldimines," *Tetrahedron Lett.*, vol. 123, p. 154551, 2023, doi: https://doi.org/10.1016/j.tetlet.2023.154551.

[90]   B. Guzelturk, Y. Kelestemur, M. Olutas, S. Delikanli, and H. V. Demir, "Amplified Spontaneous Emission and Lasing in Colloidal Nanoplatelets," *ACS Nano*, vol. 8, no. 7, pp. 6599–6605, Jul. 2014, doi: 10.1021/nn5022296.

[91]   T. K. Kormilina, S. A. Cherevkov, A. V Fedorov, and A. V Baranov, "Cadmium Chalcogenide Nano-Heteroplatelets: Creating Advanced Nanostructured Materials by Shell Growth, Substitution, and Attachment," *Small*, vol. 13, no. 41, p. 1702300, Nov. 2017, doi: https://doi.org/10.1002/smll.201702300.

[92]   Z. Wen *et al.*, "High-Performance Ultrapure Green CdSe/CdS Core/Crown Nanoplatelet Light-Emitting Diodes by Suppressing Nonradiative Energy Transfer," *Adv. Electron. Mater.*, vol. 7, no. 7, p. 2000965, Jul. 2021, doi: https://doi.org/10.1002/aelm.202000965.

[93]   N. T. Shelke, S. C. Karle, and B. R. Karche, "Photoresponse properties of CdSe thin film photodetector," *J. Mater. Sci. Mater. Electron.*, vol. 31, no. 18, pp. 15061–15069, 2020, doi: 10.1007/s10854-020-04069-0.

[94]   A. Dutta, A. Medda, S. Ghosh, S. Sain, and A. Patra, "2D CdSe/CdS Core–Shell Nanoplatelets for High-Performance Photodetectors," *ACS Appl. Nano Mater.*,

vol. 5, no. 8, pp. 11679–11688, Aug. 2022, doi: 10.1021/acsanm.2c02663.

[95] S. Pedetti, S. Ithurria, H. Heuclin, G. Patriarche, and B. Dubertret, "Type-II CdSe/CdTe Core/Crown Semiconductor Nanoplatelets," *J. Am. Chem. Soc.*, vol. 136, no. 46, pp. 16430–16438, Nov. 2014, doi: 10.1021/ja509307m.

[96] C. de Mello Donegá, "Formation of nanoscale spatially indirect excitons: Evolution of the type-II optical character of CdTe/CdSe heteronanocrystals," *Phys. Rev. B*, vol. 81, no. 16, p. 165303, Apr. 2010, doi: 10.1103/PhysRevB.81.165303.

[97] L. Wang, K. Nonaka, T. Okuhata, T. Katayama, and N. Tamai, "Quasi-Type II Carrier Distribution in CdSe/CdS Core/Shell Quantum Dots with Type I Band Alignment," *J. Phys. Chem. C*, vol. 122, no. 22, pp. 12038–12046, Jun. 2018, doi: 10.1021/acs.jpcc.7b11684.

[98] S. Ithurria and D. V Talapin, "Colloidal Atomic Layer Deposition (c-ALD) using Self-Limiting Reactions at Nanocrystal Surface Coupled to Phase Transfer between Polar and Nonpolar Media," *J. Am. Chem. Soc.*, vol. 134, no. 45, pp. 18585–18590, Nov. 2012, doi: 10.1021/ja308088d.

[99] A. H. Khan *et al.*, "CdSe/CdS/CdTe Core/Barrier/Crown Nanoplatelets: Synthesis, Optoelectronic Properties, and Multiphoton Fluorescence Upconversion," *ACS Nano*, vol. 14, no. 4, pp. 4206–4215, Apr. 2020, doi: 10.1021/acsnano.9b09147.

[100] M. D. Tessier, P. Spinicelli, D. Dupont, G. Patriarche, S. Ithurria, and B. Dubertret, "Efficient Exciton Concentrators Built from Colloidal Core/Crown CdSe/CdS Semiconductor Nanoplatelets," *Nano Lett.*, vol. 14, no. 1, pp. 207–213, Jan. 2014, doi: 10.1021/nl403746p.

[101] H. Zhong, Y. Zhou, Y. Yang, C. Yang, and Y. Li, "Synthesis of Type II CdTe−CdSe Nanocrystal Heterostructured Multiple-Branched Rods and Their Photovoltaic Applications," *J. Phys. Chem. C*, vol. 111, no. 17, pp. 6538–6543, May 2007, doi: 10.1021/jp0709407.

Chapter I: Theoretical Background

Chapter II: Experimental Method

In CdSe NPLs, structural defects and dangling bonds of surface atoms cause surface traps which strongly reduce the overall quantum efficiency of NPLs [1], [2]. Moreover, surface traps are responsible for the formation of trion emissions at low temperatures, reducing the fluorescent purity of CdSe NPL-based optoelectronic devices [3]. In this context, understanding the surface characteristics and overall shape of NPLs is very important for optoelectronic research. This requires that measurements provide the 3D images of the NPL shape. One of the possible approaches is low-temperature scanning tunneling microscopy (LTS-STM), which provides 3D-STM topographic images at the nanoscale. Here, we performed STM measurements on individual CdSe NPLs at 77 K. In addition, the STM technique also offers the possibility to probe the electronic band structure of NPLs at the sub-nanometer resolution, known as scanning tunneling spectroscopy (STS). The LT-STM/STS measurements will provide insight into the correlation between the trap distribution and the surface characteristics of NPLs.

On the other hand, CdSe/CdS core/crown NPLs have been demonstrated efficient in improving the quantum efficiency compared to the bare NPL [4]. To demonstrate the efficiency of the CdS crown, one typically compares the absorption/emission spectra of the bare NPLs and core/crown NPLs at the same measuring conditions. However, these optical spectra are steady-state measurements that provide information on the emission intensity, wavelength, and quantum efficiency of NPLs. In fact, after laser excitation, charge carriers are excited to the conduction band of a semiconductor, and a series of processes can then occur such as carrier cooling, relaxation to band edge, trapping, and radiative recombination [5]. In colloidal NPLs, these optical processes are quite complex due to the exciton fine structure. To better understand the mentioned optical processes, it is necessary to investigate the optical properties of NPLs at low temperatures and in magnetic fields. Therefore, our CdSe and CdSe/CdS core/crown NPLs were investigated with magneto PL spectroscopy. This spectroscopy technique allows us to conduct polarized PL spectroscopy and time-resolved polarized PL measurements at various temperatures. For the above targets, this chapter will

present the material synthesis, followed by detailed information on the LT-STM/STS and magneto PL spectroscopy techniques such as the structure, and the working principle.

2.1. Materials synthesis

2.1.1. The synthesis of 4.5 ML CdSe NPLs

In this thesis, we synthesized two different CdSe NPL samples at the same 4.5 ML thickness via a typical hot injection process. The synthesis was slightly adjusted from the reported protocol by H. V. Bertrand and co-workers [6]. The bare CdSe NPL solution (sample 1) was then used to synthesize 4.5 ML CdSe/CdS core/crown NPLs. The detailed protocol for each CdSe NPL sample is presented in the content below.

Sample 1: $Cd(myr)_2$ (0.6 mmol), Se powder (0.6 mmol), and ODE (30 mL) were mixed in a three-neck round-bottom flask (50 mL) which was equipped with a magnetic stirring bar, temperature sensor, and heating mantle. The reaction flask was connected to a Schlenk line through a condenser. The suspension was degassed under a vacuum for 30 minutes at 110 °C. After the degassing, the suspension was heated to 140 °C under a nitrogen atmosphere and kept at this temperature for 20 minutes. Subsequently, the temperature was increased to 240 °C, and when the suspension turned deep orange (around 215 °C), $Cd(Ac)_2.2H_2O$ (0.3 mmol) was swiftly injected into the reaction bath. The reaction occurred at 240 °C for 8 minutes, and after removing the heating mantle, the Cd-oleate/ODE mixture (2 g) was added to the flask to quench the reaction. The suspension was cooled by cold water to 80 °C and collected to proceed with purification.

Sample 2: This sample was slightly adjusted from the above protocol. Briefly, $Cd(myr)_2$ (0.6 mmol), Se powder (0.25 mmol), and ODE (25 mL) were mixed in the 50 mL three-neck round-bottom. The suspension was degassed under a vacuum for 30 minutes at 80°C. Afterward, the temperature was set to 240 °C under a nitrogen atmosphere, and when the suspension became deep orange (around 215 °C), 0.3 mmol of $Cd(Ac)_2.2H_2O$ was swiftly injected into the reaction bath. The reaction was kept at 240 °C for 8 minutes and, after removing the heating mantle, 0.8 g of the Cd-

oleate/ODE mixture was added to quench the reaction. The suspension was cooled down to 80 °C and collected to proceed with purification.

2.1.2. Purification protocol for CdSe NPLs

Purification of sample 1: 30 mL of n-hexane, 8.4 mL of acetonitrile (ACN), and 25.2 mL of isopropanol (IPA) were respectively added to the centrifuge tube containing the crude products of the above synthesis. The suspension was centrifuged for 12 minutes at 4800 rpm. After centrifugation, NPLs precipitated into the solid phase were retained, while the byproducts (dots, clusters) in the liquid phase were discarded. The solid was redispersed in n-hexane, ACN, and IPA, and then centrifuged at 4800 rpm for 12 minutes to remove unreacted carboxylates. The obtained solid was redispersed in 10 ml of n-hexane, and 1 mL of OA. The mixture was then centrifuged for 8 minutes at 2800 rpm. The solid was discarded, and the supernatant containing CdSe NPLs was centrifuged for 5 minutes at 5000 rpm to remove 3.5 ML NPLs. Finally, 4.5 ML CdSe NPLs were collected and stored in the n-hexane solvent.

Purification of sample 2: This NPL sample was purified according to the protocol reported by Di Giacomo and co-workers [7]. Briefly, the crude product obtained was mixed with 20 mL of n-hexane, and 15 mL of an IPA/EtOH 1:5 (v/v) solution in a centrifuge tube. The suspension was then centrifuged for 10 minutes at 4300 rpm. The liquid phase containing impurities was discarded, and NPLs precipitated into the solid phase were redispersed in n-hexane. Subsequently, the mixture was centrifuged at 4200 rpm for 10 minutes to remove unreacted carboxylates. Finally, the solid was discarded, and the supernatant containing NPLs was collected and stored in n-hexane.

2.1.3. The synthesis of 4.5 ML CdSe/CdS core/crown NPLs

The CdS crown solution has been prepared based on the reported protocol by C. Rodà and co-workers [4]. To initiate the growth process of core/crown NPLs, we determined the concentration of CdSe NPLs (core) based on the absorption coefficient reported by Achtstein et al [8] and rescaled the amount of the CdS (crown) solution accordingly. Specifically, 6 nmol of CdSe NPLs (Sample 1, the average lateral size: 15 nm × 5 nm) dispersed in n-hexane was added to a three-neck round-bottom flask.

Then, 20 mL ODE, 30 μL oleic acid, and $Cd(OAc)_2.2H_2O$ (0.6 mmol) were also added to the flask. The resulting mixture was degassed under a vacuum at 60º C for 1 hour. After degassing, the temperature was set at 200 ºC under a nitrogen atmosphere. When the temperature reached 150 ºC, 6 mL of CdS (crown) solution was manually injected into the reaction flask at an injection rate of 0.2 mL/min. After each reaction time (5, 12, 20, 27, and 30 min), 1 mL of the reaction solution was collected and mixed with 1 mL of oleic acid (OA) to measure optical absorbance and PL spectroscopy. After the reaction ended (30 min), the heating mantle was removed, and the mixture of $Cd(OAc)_2$/ODE (0.9 g) was added to the flask to quench the reaction. The flask was cooled down to 80 ºC, then the obtained product was transferred to centrifugation tubes for purification.

2.1.4. Purification protocol for CdSe/CdS core/crown NPLs

The crude synthesis product was mixed with toluene (15 mL), ACN (4 mL), and IPA (6 mL) solution. The mixture was centrifuged at 4500 rpm for 10 minutes. This purification process was repeated two times. After that, the supernatant was discarded, and NPLs precipitated into the solid phase were redispersed in n-hexane. The mixture was centrifuged at 4200 rpm for 10 minutes to remove impurities. The solid was discarded, and the liquid phase containing core/crown NPLs was dispersed in n-hexane for further use.

The above protocol was also applied to purify CdSe/CdS core/crown NPLs with different crown sizes (aliquot), however, the amount of toluene, ACN, and IPA must be rescaled accordingly.

2.2. Scanning Tunneling Microscopy (STM)

4.5 ML CdSe NPL and CdSe/CdS core/crown NPLs were studied with scanning tunneling microscopy (STM), and magneto-PL spectroscopy. Specifically, the structure and electronic properties of CdSe NPLs were investigated with the STM technique at low temperatures (T = 77 K). Meanwhile, magneto-PL spectroscopy was employed to investigate the optical properties of CdSe/CdS core/crown NPLs in an external magnetic field (up to 15 T) and at low temperatures (T = 4.2 K). Therefore,

the next part will present detailed information on the STM technique (theory, STM structures, and working principle), followed by magneto-PL spectroscopy (structure, spectrometers, and working principle).

2.2.1. Introduction

Scanning tunneling microscopy (STM) was developed by Gerd Binnig and Heinrich Rohrer at IBM Zurich Research Laboratories (Switzerland), which is the most powerful tool for studying the surface and electronic properties of semiconductors at atomic resolution. Moreover, this technique also provides researchers with an unprecedented tool to investigate the quantum confinement effect and manipulate materials at the atomic scale. Due to the breakthrough achieved through this invention, Rohrer and Binnig were awarded a Nobel Prize in 1986 [9]. Until now, the invention of the STM system remains an important breakthrough in nanoscience and nanotechnology.

A precise understanding of the influence of the structural properties (e.g., shape, size, structural defects) on the electronic properties of colloidal NCs is very important for optoelectronic research. For this target, we employed the low-temperature STM technique to investigate the structural and electronic properties of 4.5 ML CdSe NPLs at the nanoscale. Therefore, the next section will present the working principle of scanning tunneling microscopy (STM), starting with the theoretical basis of the tunnel effect. Then, detailed information on the structure and the operation of an STM system at low temperatures is also introduced to understand the formation of STM topographic images at atomic resolution. In addition, we also give more information on scanning tunneling spectroscopy (STS) for studying the electronic properties of materials.

2.2.2. Quantum mechanical tunneling

To understand the working principle of an STM system, we will consider the tunneling effect between two conductive electrodes in a vacuum. In this case, a particle of energy E can cross a vacuum gap, described as a potential barrier in quantum mechanics. Suppose that the potential barrier of constant height U_0 can be

extended between 0 and d on the x-axis, and the particle of energy ($E < U_0$) has mass m. According to classical physics, the particle of energy ($E < U_0$) is always reflected by the potential barrier. In contrast, the quantum wave function (A_1) of the particle still has a finite possibility to tunnel through the barrier to the other side (A_3) (Figure 17). The propagation of the particle wave function through the potential barrier is called the "tunnel" effect.
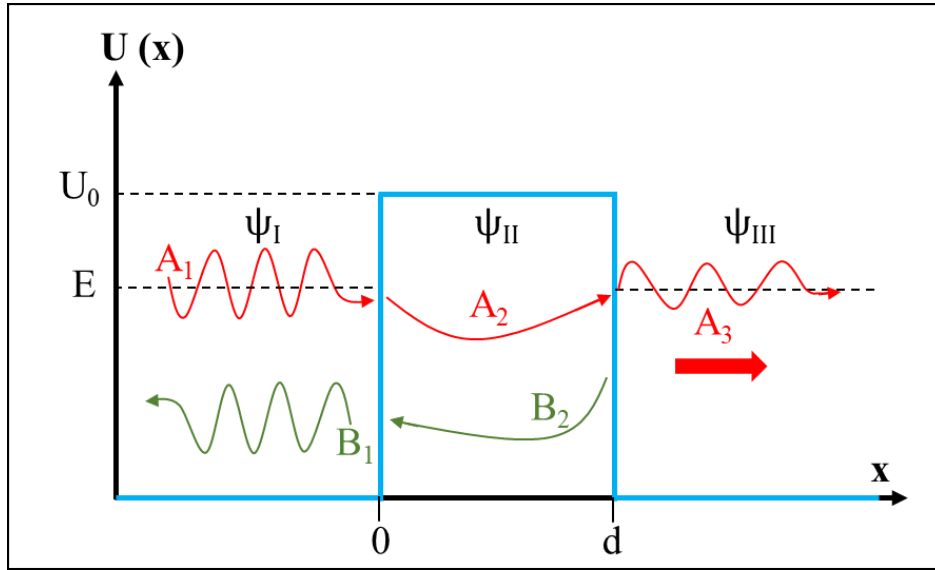
Figure 17: Schematic illustration of one-dimensional (1D) tunnel barrier along the x-axis. A particle of energy ($E < U_0$) described by a quantum wave function of an amplitude A_1 propagates to the potential barrier. This wave function is reflected by the barrier resulting in the reflected wave function of an amplitude B_1. The transmitted wave function (A_2) is reflected again by the barrier resulting in the reflected wave B_2. A small possibility for a particle to tunnel the barrier to the other side (A_3).

Quantum mechanics have made it possible to predict the effect of particle penetration through the potential barrier. The 1D stationary single-particle Schrödinger equations are written as follows:

$$\psi_n(x) = \begin{cases} \dfrac{-\hbar^2}{2mE}\dfrac{\partial^2\psi_1}{\partial x^2} & x < 0 \\[2mm] \dfrac{-\hbar^2}{2m(E-U_0)}\dfrac{\partial^2\psi_2}{\partial x^2} & 0 < x < d \\[2mm] \dfrac{-\hbar^2}{2mE}\dfrac{\partial^2\psi_3}{\partial x^2} & x > d \end{cases} \tag{2.1}$$

Chapter II: Experimental Method

Resolving these above equations, we will obtain the solutions that can be written as follows:

$$\psi_n = \begin{cases} A_1 e^{ikx} + B_1 e^{-ikx} & x < 0 \\ A_2 e^{\alpha x} + B_2 e^{-\alpha x} & 0 < x < d \\ A_3 e^{i\alpha x} & x > d \end{cases} \tag{2.2}$$

Where, $k = \frac{\sqrt{2mE}}{\hbar}$ and $\alpha = \frac{\sqrt{2m(U_0 - E)}}{\hbar}$. A_n and B_n are the incident and reflected part in the different regions (n = 1, 2, 3,...). The boundary conditions between the different regions of the system are written as follows: $\psi_I(0) = \psi_{II}(0)$ and $\psi_{II}(d) = \psi_{III}(d)$. Under these conditions, the wave function and its derivative have to be continuous at two interfaces of the system, $x = 0$ and $x = d$. Therefore, we obtain a system of four equations:

$$A_1 + B_1 = A_2 + B_2$$

$$A_2 e^{-\alpha d} + B_2 e^{\alpha d} = A_3 e^{ikd} \tag{2.3}$$

$$ik(A_1 - B_1) = -\alpha(B_2 - A_2)$$

$$\alpha(B_2 e^{\alpha d} - A_2 e^{-\alpha d}) = ikA_3 e^{ikd}$$

To resolve these equations, we will divide each of the above equations by A_1. Only four coefficients are thus unknown $\frac{B_1}{A_1}, \frac{A_2}{A_1}, \frac{B_2}{A_1}, \frac{A_3}{A_1}$. Among them, the coefficient $c = \frac{A_3}{A_1}$ leads to the transmission probability that we would like to find. By resolving these above equations, we will obtain the transmission probability $T(E)$ as follows:

$$T(E) = |c|^2 = \frac{1}{1 + \frac{U_0^2}{4E(U_0 - E)} \sinh^2(\alpha d)} \approx 16 \frac{E}{U_0}\left(1 - \frac{E}{U_0}\right) e^{-2\alpha d} \tag{2.4}$$

The above equation shows that the transmission coefficient is inversely proportional to the potential height (U_0), while it depends exponentially on the barrier width (d). The plot of equation (2.4) is presented in Figure 18. The transmission probability describes the likelihood of an electron passing through the potential barrier. Therefore, the transmission coefficient decreases with increasing the barrier width.
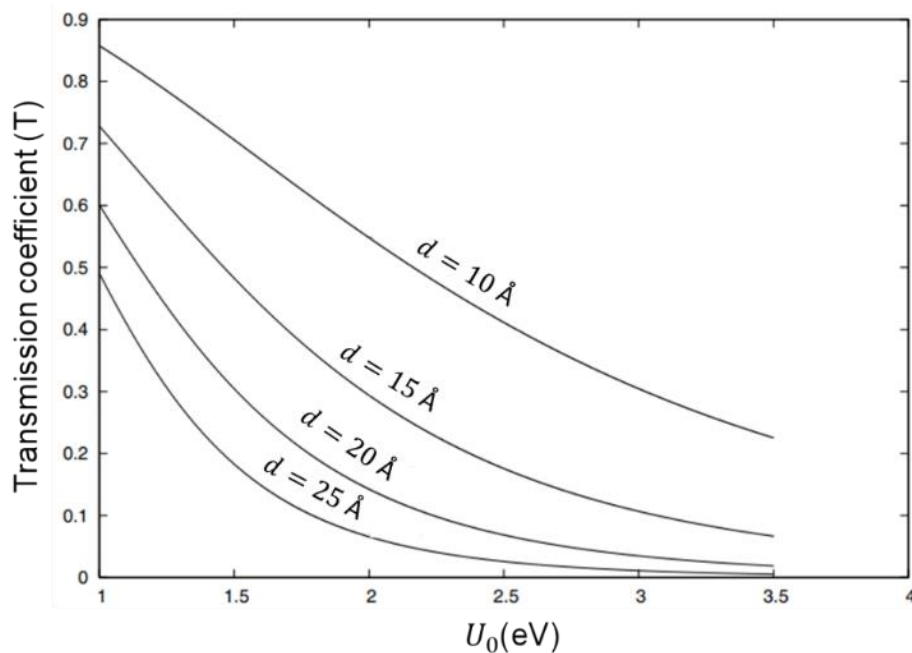
Figure 18: The transmission coefficient as a function of the potential height (U_0) and the barrier width (d). Reproduced from reference [10].

The above knowledge of quantum mechanics describes the probability for the particle with energy (E) to tunnel through a 1D potential barrier. In the case of STM, the tunneling effect will occur between the sample and the STM tip in a vacuum.

2.2.3. Tunneling current

Tunneling current is one of the important physical parameters that determines the resolution of STM measurements. The questions are how the tunneling current is generated in an STM system, and how to calculate the tunneling current. To address these questions, we will consider a junction in STM created by bringing an STM (Tungsten) tip close to the sample on a conductive substrate in a vacuum. When applying a positive bias voltage ($V_b > 0$) between the tip and sample, the Fermi level of the sample is shifted down by eV_b, allowing electrons to tunnel from the occupied states in the tip to the unoccupied states in the sample, forming a tunneling current (Figure 19). We now determine the height of the potential barrier (U_0) between the tip and sample. Because the potential barrier established in the STM junction is not rectangular, thus calculating the potential height is quite challenging. However, if we consider the condition ($eV_b \ll U_0$), the considered barrier can be approximated as a

Chapter II: Experimental Method

rectangular barrier. Therefore, the potential height (U_0) is determined through the work functions of the tip (Φ_t) and sample (Φ_s):

$$U_0 = \frac{\Phi_t + \Phi_s - eV_b}{2} \tag{2.5}$$

The transmission probability for an electron with energy E and applied bias V_b to cross the barrier is expressed as follows:

$$T(E, eV, d) = \exp\left\{-2d\sqrt{\frac{2m}{\hbar^2}(U_0 - E + eV_b)}\right\} \tag{2.6}$$

Where d is the tip-sample distance corresponding to the barrier width. Therefore, the transmission coefficient depends exponentially on the tip-sample distance.
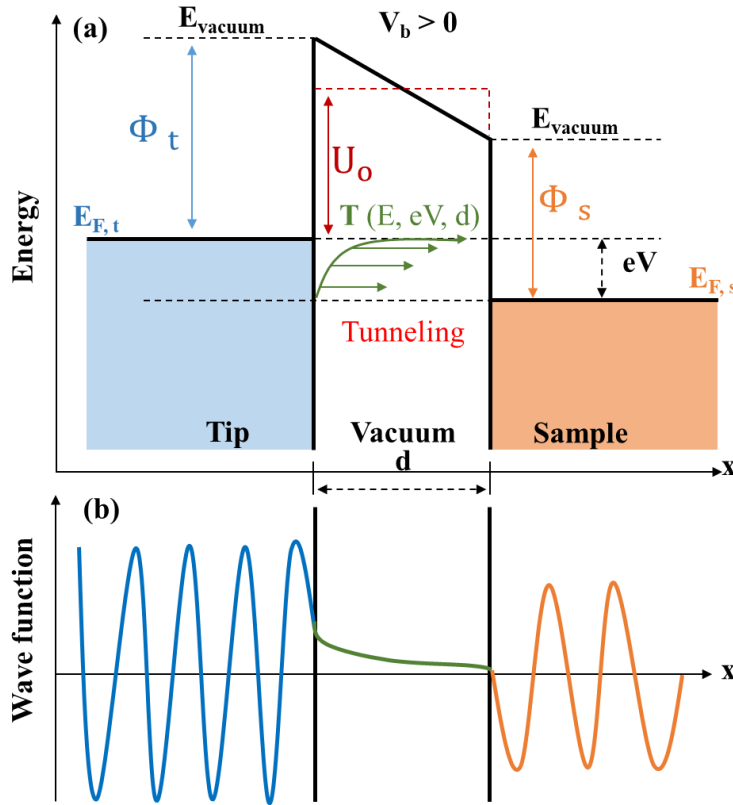
Figure 19: **(a)** Schematic energy diagram of an STM junction. When applying bias voltage ($V_b > 0$) between the system, electrons tunnel from the tip to the sample, forming a tunneling current. U_0 is the potential height, and $E_{F,t}$ and $E_{F,S}$ are the Fermi levels of the tip and sample, respectively. **(b)** The wave function of electrons passing through the potential barrier. Note that: only a simplified wave function is shown in the figure.

Chapter II: Experimental Method

The tunneling effect was theoretically studied by Bardeen in 1961 [11], predating the invention of STM. He developed a theory for calculating the tunneling probability through the tunneling matrix element. Considering two sides of the potential barrier as two electrodes, with the barrier broad enough to assume weak coupling between two electrodes. Bardeen demonstrated that the two electrodes can be treated separately using a time-dependent perturbation theory formalism. According to Bardeen, the tunneling matrix element M_{uv} from a state u, described a wave function ψ_u on the left side, to another state v with a wave function ψ_v on the right side, is written as follows:

$$M_{uv} = -\frac{\hbar^2}{2m} \int (\psi_u^* \nabla \psi_v - \psi_v \nabla \psi_u^*) d(S) \tag{2.7}$$

Where the integral is performed over any surfaces (S) lying between the two electrodes. The transmission rate is given by $|M_{uv}|^2$. Since the two metallic electrodes are characterized by a continuum of electronic states, the net tunneling current is thus calculated from the transmission rate $|M_{uv}|^2$ by summing up all states in both electrodes. Moreover, the $|M_{uv}|^2$ must be multiplied by the average number of unoccupied states (f_u) on the left electrode and by the average number of available states $[1 - f_u]$ on the right electrode. Therefore, the total tunneling current is written as follows:

$$I = \left(\frac{2\pi e}{\hbar}\right) \int_u^v f(E_u)[1 - f(E_v + eV_b)] - f(E_v + eV_b)[1 - f(E_u)] |M_{uv}|^2 \delta(E_u - E_v)$$

$$\tag{2.8}$$

Where $f(E)$ is the Fermi function, V_b is the applied bias voltage, E_u and E_v are the energies of the wave functions ψ_u and ψ_v. The delta function $\delta(E_u - E_v)$ describes the conservation of energy of the elastic tunneling. The calculation of the tunneling current is difficult due to the complication of unknown variables in equation (2.8). In 1983, Tersoff and Hamann [12] extended Bardeen's description to simplify the calculation of the tunneling current. At room temperature (or below), and a small voltage (~10 meV), Tersoff and Hamann rewrote the expression of tunneling current as follows:

Chapter II: Experimental Method

$$I = \left(\frac{2\pi e^2}{\hbar}\right) V \int_t^s |M_{ts}|^2 \delta(E_s - E_F)\delta(E_t - E_F) \tag{2.9}$$

Where E_t and E_s are the energies of the unperturbed wave functions of the tip and sample. E_F is the Fermi energy level. The main obstacle in the above equation is the presence of the tunneling matrix element M_{ts} between the occupied states of the tip and the unoccupied states of the sample. To evaluate the matrix M_{ts}, Tersoff and Hamann expanded the surface wave function of the sample ψ_s in the form.

$$\psi_s = (\Omega_s)^{-\frac{1}{2}} \Sigma_G a_G \exp\left(\left[k^2 + |\vec{k}_G|^2\right]z\right) exp(i\vec{k}_G\vec{x}) \tag{2.10}$$

Where Ω_s is the sample volume, $k = \hbar^{-1}\sqrt{2m\phi}$ represents the decay constant for the wave functions in a vacuum, ϕ is the work function, and the first few a_G are typically of order unity. $\vec{k}_G = \vec{k}_{\mathrm{II}} + \vec{G}$, where $\vec{k}_{\mathrm{II}}$ is the Bloch wave vector of the surface, and $\vec{G}$ is a reciprocal-lattice vector.

According to Tersoff and Hamann, the tip was modeled as a locally spherical potential well with a s-wave function ψ_t (Figure 20a). Therefore, the tip wave function can be written as follows:

$$\psi_t = (\Omega_t)^{-\frac{1}{2}}c_t kRe^{kR}(k|\vec{r} - \vec{r_0}|)^{-1}e^{-k|\vec{r}-\vec{r_0}|} \tag{2.11}$$

Where Ω_t is the volume of the tip, and $c_t \approx 1$ is the normalization parameter. R and r_0 are the local radius and the center position of the curvature of the tip, respectively. Under these assumptions, the tunneling matrix M_{ts} is written as follows:

$$M_{ts} = \frac{\hbar^2}{2m} 4\pi k^{-1}(\Omega_t)^{-\frac{1}{2}}kRe^{kR}\psi_s(\vec{r_0}) \tag{2.12}$$

Inserting the matrix M_{ts} into equation (2.12), we obtain the tunneling current as follows:

$$I = 32\pi^3 \hbar^{-1}e^2 V_b\phi^2 D_t(E_F)R^2k^{-4}e^{2kR} \times \sum_s |\psi_s(\vec{r_0})|^2\delta(E_s - E_F) \tag{2.13}$$

Here, D_t is the density of states (DOS) per unit volume of the tip and it can be defined as:

$$\rho(\vec{r}_0, E_F) \equiv \sum_s |\psi_s(\vec{r}_0)|^2 \delta(E_s - E_F) \tag{2.14}$$

Where $\rho(\vec{r}_0, E_F)$ is the surface local density of state (LDOS) at the Fermi level, and the position of the tip ($\vec{r}$). $\vec{r}_0$ is the center position of the tip. At constant current, the tip follows a contour of the LDOS, $\rho(\vec{r}_0, E_F)$. In an ideal STM, the tip apex can be visualized as a single atom (Figure 20a), and therefore the tunneling current is reduced to

$$I \propto \rho(\vec{r}_0, E_F) \equiv \sum_s |\psi_s(\vec{r}_0)|^2 \delta(E_s - E_F) \tag{2.15}$$
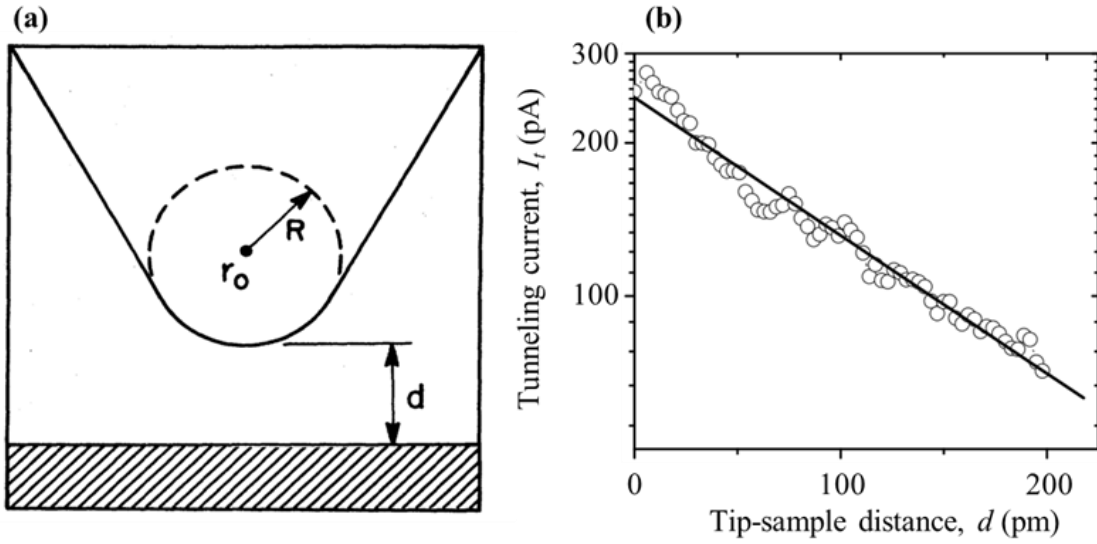
Figure 20: (a) Schematic illustration of tunneling geometry. The tip is considered as a locally spherical potential well with a radius of curvature R, where it is separated from the sample surface by a distance d. The center position of the curvature is labeled $\vec{r}_0$ [12]. **(b)** Dependence of the tunneling current (I_t) on the relative tip-sample distance (d) on a semilogarithmic scale measured by STM. Reproduced from reference [13].

Since the direction of the tunneling current is perpendicular to the sample surface, the wave function of the sample $\psi_s(\vec{r})$ can be written as follows:

$$\psi_s(\vec{r}) \propto exp(-k\vec{r}_\perp) \tag{2.16}$$

The square of the wave function $|\psi_s(\vec{r}_0)|^2$ is determined as [12]:

$$|\psi_s(\vec{r})|^2 \propto exp[-2k(R+d)] \tag{2.17}$$

Therefore, the tunneling current is given by:

$$I \propto exp(-2kd) \tag{2.18}$$

Equation (2.18) indicates that the tunneling current depends exponentially on the tip-sample distance. For a tip made from Tungsten (W), with a typical work function of 4.5 eV, the tunneling current decreases by three orders of magnitude when the tip-sample distance increases by 0.1 nm (Figure 20b). Most importantly, the tunneling current is closely related to the DOS, and the STM thus provides a direct measurement of the electronic properties of materials, also known as scanning tunneling spectroscopy.

2.2.4. The working principle of STM

Scanning tunneling microscopy (STM) is a branch of scanning probe microscopy (SPM) that forms topographic images by using a metallic probe to scan the material surface. Figure 21 shows the working scheme of an STM system. An atomic-sized probe is mounted on the piezo scanner and adjusted in vertical quarters (+x, -x, +y, -y) by an electrical circuit. Meanwhile, the height of the tip (z-axis) is adjusted by changing the applied bias voltage or the set-point current through the feedback controller. The STM works based on the tunneling phenomenon between the tip and the sample. Specifically, the tip is brought closest to the sample ($d < 1$ nm), if a positive bias (V_b) is applied to the sample, electrons can tunnel the potential barrier to the tip, resulting in the formation of the tunneling current $I_t(d, V_b)$. Depending on each STM system, the bias voltage can apply to either the tip or the sample.
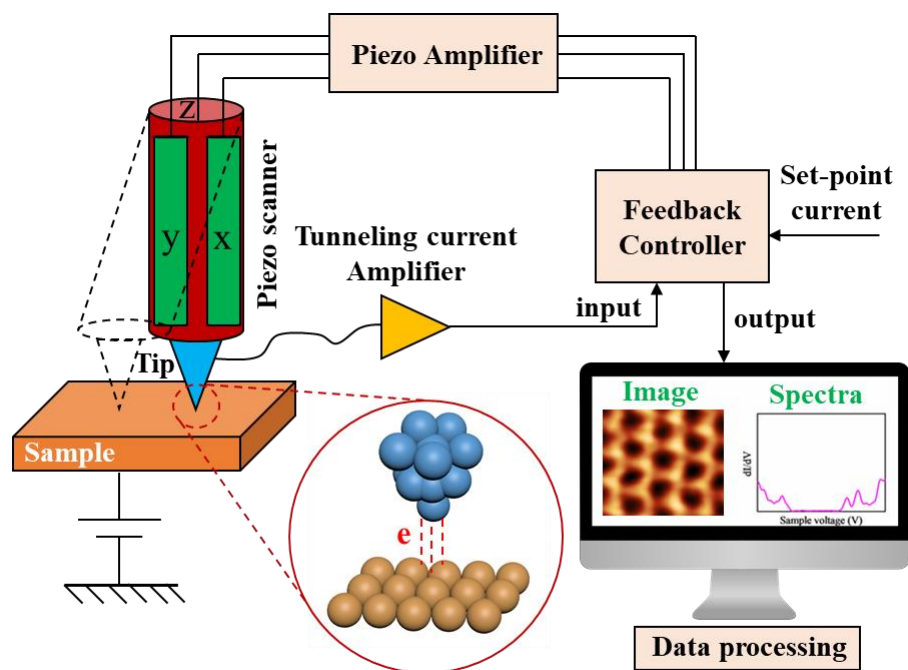
Scanning Tunneling Microscopy

Figure 21: The working scheme of an STM system. Materials are deposited on a conductive substrate which is connected to the ground. An STM tip with atomic size is connected to a piezo scanner and controlled by an electrical circuit. When applying a positive bias voltage to the tip, a tunneling current is created and amplified by a current amplifier before going to the feedback controller.

Technically, the STM operates in two distinct modes: constant height mode, and constant current mode. Figure 22 illustrates the two operation modes of STM.

In constant height mode (Figure 22a), the height of the tip (z) is kept fixed while the tip is moved over the sample surface at a constant bias voltage. By measuring the variation in the current intensity as a function of the tip position (x,y), one can map the density of states of the sample surface containing information about defects, surface traps, and electronic band structure. Therefore, this mode is mainly used to study the electronic properties of materials.

In constant current mode (Figure 22b), the feedback loop will keep the tunneling current as constant by adjusting the tip-sample distance. Specifically, when the tunneling current exceeds the expected value (set-point current), the feedback loop

will increase the tip-sample distance. On the opposite, when the current is less than the expected value, the feedback loop will bring the tip closer to the sample (decreasing the tip-sample distance). By scanning the tip over the sample surface, the exponential dependence of the tunneling current on the tip-sample distance is collected and used to map the topography of the sample. STM topographic images provide information about surface roughness, defects, shape, and size of the sample. This mode is commonly used to study the surface properties of materials. The resolution of STM images is affected by the tip and sample quality. For example, it is difficult to obtain high-resolution STM images of colloidal semiconductor NCs because they are unstable on a substrate and contain organic contaminations.
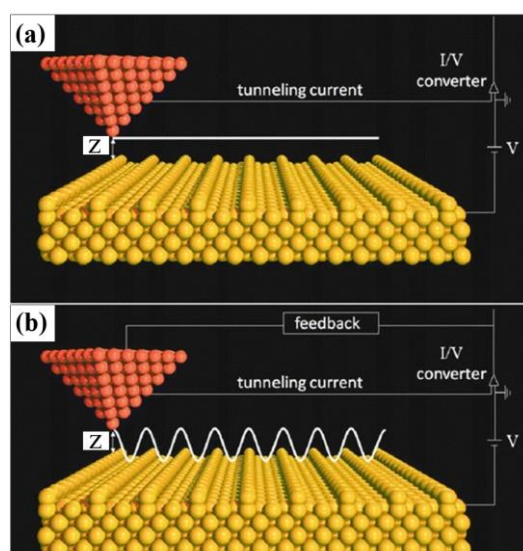
Figure 22: (a) Schematic representation of two operation modes in STM. (a) Constant height mode. **(b)** Constant current mode. Reproduced from reference [14].

2.2.5. Low-temperature scanning tunneling microscopy (LT-STM)

In this thesis, the apparatus used for investigating the structural and electronic properties of our NPL samples is low-temperature scanning tunneling microscopy (LT-STM), produced by Omicron company. The photo of the LT-STM system is displayed in Figure 23a. The system is designed to operate at cryogenic temperatures (T ~ 4 K) under ultrahigh vacuum (UVH ~ 10^{-11} Torr), it is thus a complex system composed of many different components. The LT-STM system can be divided into three main chambers: (1) the load lock, (2) the preparation chamber, and (3) the

analysis chamber (Figure 23a). The analysis and preparation chamber are always kept under UHV thanks to the combination of an ion ion-getter pump, a turbomolecular pump, and a titanium sublimation pump (TSP).
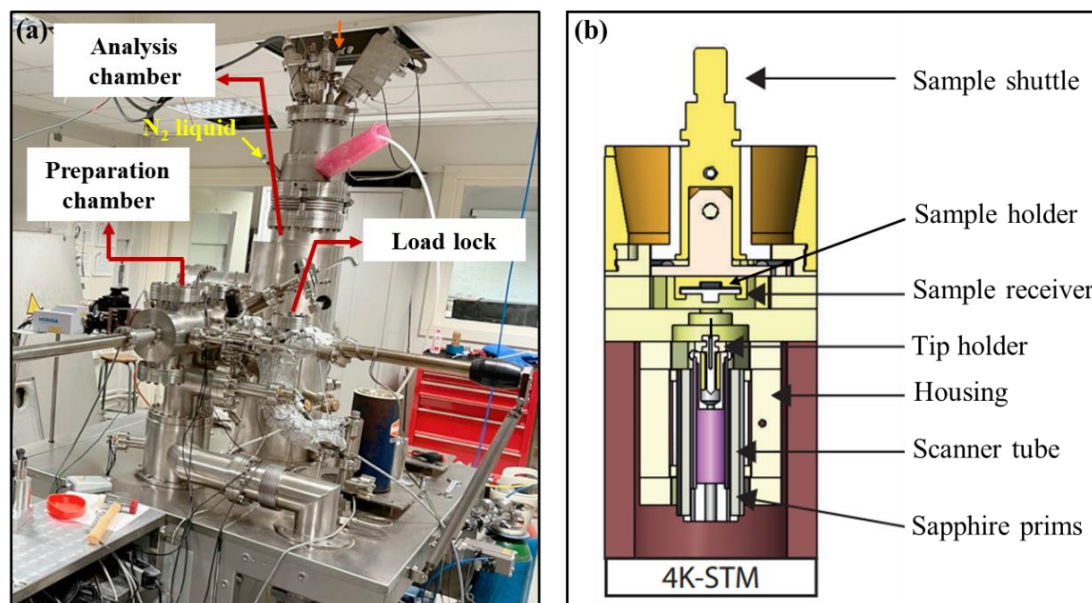
Figure 23: **(a)** The photography of the LT-STM system manufactured by Omicron company, including an analysis chamber (the longest and biggest part), a preparation chamber (at the center of the STM), and a load lock. **(b)** Simplified schematic of the analysis chamber, where the STM stage is located in the center of the chamber. Figure b was taken from the reference [15] with a slight modification.

The load lock: The component can be considered as a gate of the STM that allows us to load or withdraw samples/tips from the preparation chamber. The load lock is a small chamber connected to a turbo molecular pump coupled to a primary pump. This chamber is separated from the preparation chamber by a valve and can hold up to three samples. For the loading process, samples are first placed in corresponding holders inside the chamber, and then a metal lid with a copper gasket and screws are used to cover the chamber (must turn the screws tighten). The chamber is then pumped by the turbo and primary pump to reach a vacuum $\sim 10^{-7}$ Torr, while the samples are annealed at 120 °C for 9 hours. This annealing process will remove water molecules, and contaminations before loading the samples into another chamber. Note that the vacuum level inside the load lock must reach 10^{-7} torr before connecting to the

preparation chamber. This requirement also applies to withdrawing the samples (or tips) from the preparation chamber.

Preparation chamber: This chamber is placed in the middle of the STM system where samples (or tips) are prepared before inserting into the analysis chamber. The pressure inside the chamber is always maintained under UHV $\sim 10^{-10}$ Torr. The chamber is equipped with a manipulator integrated with a resistive heater where the samples can be heated to 150 ºC to remove contaminations. In addition, the manipulator is also used for the tip-sharpening process.

Analysis chamber: The most important part of the STS system is the analysis chamber, where the STM stage is positioned. The samples and tips are transferred from the preparation chamber and placed on a carousel with six available slots. To initiate the measurement, a wobble stick is used to transfer the sharpest tip from the carousel to the STM chamber. The tip is then mounted on the top of a piezo-ceramic tube where a magnet is placed to secure the tip. Afterward, a sample is introduced and mounted on a sample holder in the STM stage. With the assistance of an electrical controller, the tip can be moved in x, y, and z directions to approach the sample surface at a specific distance (Figure 23b). The tip is then brought to the sample surface thanks to the piezoelectric scanner before scanning across the surface. The entire system is suspended with metallic springs to reduce mechanical vibration from the outside. The STM stage is placed inside two cryostats to cool down the STM system. The outer cryostat is filled with liquid nitrogen (LN) to cool the system down to 77 K (Figure 23a, the yellow arrow). The inner cryostat is in contact with the STM stage and can be filled with liquid helium (or LN) to cool the tip and the sample down to 4 K (Figure 23a, the orange arrow). The analysis is always maintained under UHV ($\sim 10^{-11}$ Torr).

2.2.6. Scanning tunneling spectroscopy

One of the important functions of STM is spatially resolved scanning tunneling spectroscopy (STS), which is used to study the electronic properties of materials. Therefore, understanding the working principle and the resulting information from the

STS measurement is necessary for studying optoelectronic materials such as colloidal semiconductor nanocrystals.
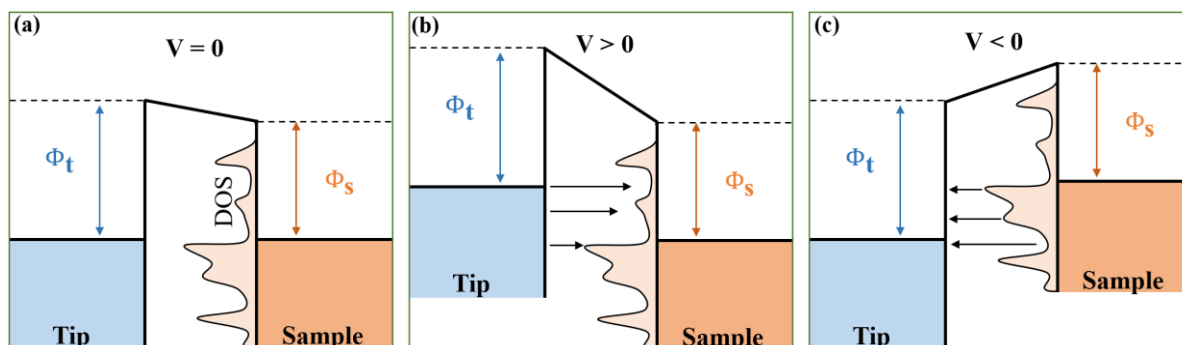
Figure 24: Energy band diagram of the tip and sample in STM at different bias voltages. **(a)** At zero voltage, there is no tunneling current. **(b)** At a positive voltage, electrons can tunnel from the tip to unoccupied states of the sample. **(c)** At a negative voltage, electrons from the occupied states of the sample tunnel through the barrier to the tip.

Figure 24 shows the energy band diagram of the tip and sample in the STM system at different voltages. The tip is made from good metals, and its density of state (DOS) is considered flat near the Fermi level, while the DOS of the sample is more complicated. At zero voltage, the Fermi level of the tip and the sample are aligned at the same energy, thus no tunneling current is formed in the system (Figure 24a). When a positive bias voltage is applied to the sample, electrons tunnel from the tip into unoccupied states above the Fermi level of the sample, as there are no empty states below the $E_{F,s}$ at low temperatures (Figure 24b). Therefore, the tunneling current of the system is proportional to the number of unoccupied states of the sample, as shown in equation (2.15). In contrast, at a negative bias voltage, electrons tunnel from occupied states of the sample to the tip, the tunneling current thus depends on the number of occupied electron states (Figure 24c). The tunneling current expression (equation 2.13) was established based on conditions, including (1) the DOS of the tip is uniform, (2) the only s-wave function of the tip is critical, (3) the STM operates at low temperatures and bias voltages (less than 10 mV) [12]. Under these conditions, the Tersoff–Hamann theory contributes to the understanding of STM. However, most STM experiments are carried out with high bias voltages (1 – 3 V), thus the low-

voltage approximation used in equation (2.15) is violated in practice. In this context, Hamers [16] has rewritten the tunneling current expression using the Wentzel–Kramers–Brillouin (WKB) approximation as follows:

$$I = \int_0^{eV} \rho_s(r,E)\rho_t(r,-eV+E)T(E,eV,r)dE \qquad (2.19)$$

The above formula is for the interpretation of STM experiments performed at high bias. $\rho_s(r,E)$ and $\rho_t(r,E)$ are the DOS of the sample and tip at the position r and energy E. $T(E,eV,r)$ is the transmission probability for electrons at energy E and applied bias voltage V_b. By differentiating the tunneling current (I) with respect to the applied voltage V, we obtain [16]:

$$\frac{dI}{dV} = \rho_s(r,eV)\rho_t(r,0)\,T(E,eV,r) + \int_0^{eV} \rho_s(r,E)\rho_t(r,E-eV)\frac{dT(E,eV,r)}{dV}dE$$

$$(2.20)$$

The transmission probability $T(E,eV,r)$ is still unknown in the above equation. However, at low bias voltages (lower than the work function of the tip and sample), the transmission probability is a smooth and monotonic function of the applied voltage V, which only contributes to a smooth background. Therefore, dT/dV can be neglected and we will obtain [17]:

$$\frac{dI}{dV} \propto \rho_s(r,eV)\rho_t(r,0) \qquad (2.21)$$

The density of states of the tip $\rho_t(r,0)$ is typically considered as a constant within the energy range of the measurement. The derivative dI/dV is thus reduced to.

$$\frac{dI}{dV} \propto \rho_s(r,eV) \qquad (2.22)$$

According to the above equation, scanning tunneling dI/dV spectroscopy (STS) provides a direct measure of the local density of states of the sample.

Lock-in amplifier for STS

Chapter II: Experimental Method

Although tunneling dI/dV spectroscopy (STS) is a powerful tool for investigating the electronic properties of materials, it is nonetheless very sensitive to variation in the tip-sample distance. In reality, the tip-sample distance is affected by noise from outside resources. Therefore, dI/dV signals also contain noise signals, leading to a deviation in STS results. To address this, we use a lock-in amplifier that effectively removes the mechanical noise.

Lock-in amplifiers provide the ability to measure the amplitude and phase of a signal in the presence of noise. When a disturbed signal passes through a lock-in amplifier, the amplifier will first multiply its input signal with a reference signal and then apply an adjustable low-pass filter to remove noisy signals from the input (Figure 25). This method is called phase-sensitive detection and isolates the signal from noisy components.
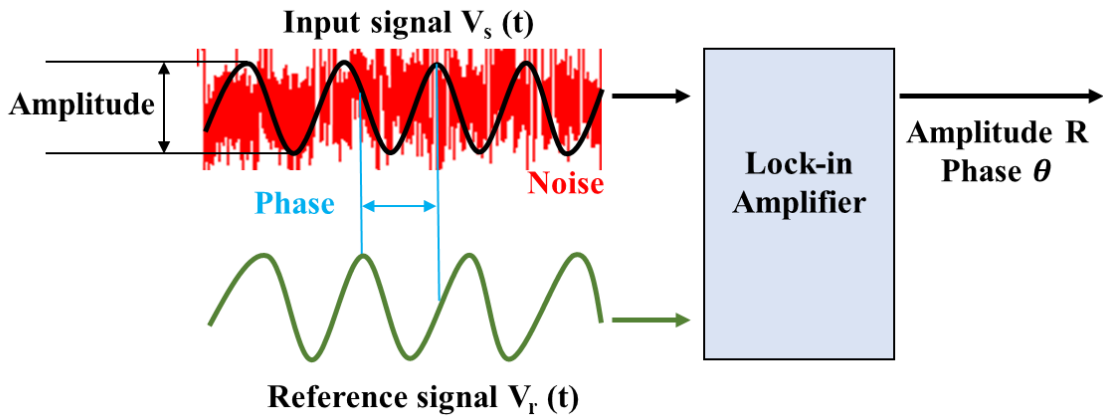
Figure 25: Schematic illustration of a lock-in amplifier capable of measuring the amplitude and phase of an input signal even when this input signal is seriously noisy.

In the STM system, the input signal is the tunneling current measured from the sample. This will be collected by a lock-in amplifier where the current signal is converted to a voltage signal labeled V_I, which can be written as:

$$V_I \propto V_{sig} \sin(\omega t + \theta) + V_{noisy} \tag{2.23}$$

The input signal V_I is then multiplied by the reference signal $V_{ref} \sin(\omega t)$. We obtain:

$$V_I = -\frac{1}{2}V_{sig}V_{ref}[cos(2\omega t + \theta) - \cos(\theta)] + V_{noisy} V_{ref} \sin(\omega t) \tag{2.24}$$

Noise can be minimized using a low-pass filter with a threshold lower than ω, the output signal comprises only the DC component proportional to the DOS of the sample.

$$V_I = -\frac{1}{2}V_{sig}V_{ref}cos(2\omega t + \theta) \approx \rho_s(eV)eV_{mod}cos(2\omega t + \pi + \theta) \qquad (2.25)$$

Considering the condition: $(2\omega t + \pi + \theta) = 0$, the output signal is maximized to:

$$V_I \approx \rho_s(eV)eV_{mod} \qquad (2.26)$$

The above equation represents the output signal obtained from STS measurements, providing insight into the electronic band structure of materials, such as band gap energy, band edges, and in-gap states. Detailed information on the STS results measured on CdSe NPLs is presented in Chapter III.

2.2.7. The role of tip and sample in STM

The tip and sample quality strongly influence the resolution of STM images and the stability of STS. Therefore, meticulous preparation of high-quality tips and samples is necessary to ensure the effectiveness of STM measurements.

2.2.7.1. STM tip quality

STM is an advanced microscopy that utilizes a physical probe to generate topographic images of materials. Therefore, it is accurate to assert that the tip is the heart of the STM system. Two factors significantly influence STM and STS results: the shape and chemical composition of the tip [18], [19]. The chemical composition of the tip is associated with two issues: the material from which the tip is made, and the contaminations present on the tip apex. Contaminations, such as organic materials, and metal oxides can lead to severe tip distortion. Moreover, metal oxides (e.g. WO_2) surrounding the tip apex create a double potential barrier, preventing the tunneling of electrons. Therefore, the STM resolution can seriously be reduced because it is more difficult to stabilize the tunneling current filament.

As shown in equation (2.13), the tunneling current depends not only on the DOS of the sample but also on the DOS of the tip. In practice, various materials have been

chosen for the tip fabrication depending on each particular STM measurement. For example, superconducting tips have been fabricated from Niobium (Nb) [20], Lead (Pb), and Aluminum (Al) [21] are used in STM measurements at very low temperatures (^{3}He cryostat). Spin-polarized STM experiments typically use tips made from Nickel (Ni) [22], and Chromium oxide (CrO_2) [23]. For normal STM experiments, tips are usually made from Tungsten (W), and Platinum Iridium (PtIr). Therefore, the selection of the tip material itself is also crucial in the STM.

Another factor influencing the STM resolution is the tip shape. The lateral resolution of STM depends on the tip radius through the equation: $\Delta x \sim 1.4\sqrt{R}$. With a tip made from Tungsten with a radius of R = 5 nm, the atomic resolution $\Delta x \approx 4$ Å is acquired. To achieve high-resolution STM images and stable dI/dV spectra, an atomically sharp tip without contaminations is required for STM/STS measurements.

2.2.7.2.   Sample quality

Sample quality is a critical factor that directly influences STM and STS results. In general, the STM experiment always requires a clean and stable sample surface. A target material is deposited on a conductive substrate such as gold (Au), copper (Cu), highly oriented pyrolytic graphite (HOPG), and graphene by simple methods, including spin-coating, dip-coating, and drop-casting. Here, we used a gold substrate for the sample deposition. The sample is annealed at 120 °C for 9 hours in the load lock (P ~ 10^{-7} Torr). After annealing, the sample is introduced into the preparation chamber and then the STM chamber. For our colloidal CdSe NPLs, the sample preparation is presented in Chapter III.

2.3.   Optical spectroscopy techniques

CdSe NPLs have attracted considerable attention due to their narrow emission linewidth and tunable emission wavelength [24], [25]. Despite these, exploiting the NPLs in optoelectronic devices is still challenging because of their low quantum efficiency and chemical stability [26]. In this context, CdSe NPL-based heterostructures have emerged as promising candidates which are expected to improve the disadvantages of CdSe NPLs. Among them, CdSe/CdS core/crown NPLs have

been demonstrated to enhance significantly the quantum efficiency compared to the bare CdSe NPLs [4], [27]. However, the optical properties of core/crown NPLs at low temperatures have not been fully investigated yet. Therefore, understanding the optical properties of NPLs at low temperatures or in an external magnetic field is necessary for optoelectronic research.

2.3.1. Steady-state optical spectroscopy

After the material synthesis, colloidal NPLs will be checked for their absorption and emission properties using UV-vis and photoluminescence (PL) spectra at room temperature. The results obtained help to determine the optical transitions and optical bandgap, contributing to the determination of the NPL thickness.

2.3.1.1.   Absorption spectroscopy

This spectroscopic technique operates based on the interaction between light and matter. When a semiconductor undergoes photoexcitation, electrons are excited to the conduction band, leaving corresponding holes in the valence band. This process is referred to as an optical transition, and each optical transition strongly absorbs a specific wavelength of light. By measuring the absorbance of light at different wavelengths, it is possible to identify the optical transitions in colloidal NPLs. The measured absorbance (A) is determined using the Beer-Lambert law, which is expressed as follows:

$$A = log\left(\frac{I_0}{I}\right) = \varepsilon l c \tag{2.27}$$

Where I_0 and I are the initial intensity of light and the intensity of the transmitted light, respectively. ε is the linear extinction coefficiency ($L.mol^{-1}.cm^{-1}$), l is the optical path length (cm), and c is the concentration of absorbers ($mol.L^{-1}$). As mentioned in Chapter I, absorption spectroscopy is a commonly used technique for probing the optical transition in colloidal NCs. In our case, this spectroscopy technique helps to confirm the formation of the CdS crown by comparing the absorption characteristics between bare CdSe and CdSe/CdS core/crown NPLs.

2.3.1.2. Photoluminescence spectroscopy

PL spectroscopy is a non-destructive and non-contact method used for probing the light emission from any matter. Here, we employ this spectroscopic technique to investigate the emission properties of colloidal nanoplatelets (NPLs). This spectroscopic technique provides optical band gaps that are useful in estimating the thickness of NPLs as well as understanding quantum confinement effects. The PL spectrum of NPLs is acquired by exciting the sample at a fixed energy level, typically higher than their band gap, and by scanning the emitted light in wavelength. In PL spectroscopy, the intensity of the emission peak can be measured as a function of wavelength using an optical spectrometer.

2.3.1.3. Optical spectrometer

Our absorption measurements were performed using a UV-vis Lambda 365 spectrophotometer (PerkinElmer, United States) with a wavelength range from 190 nm to 1100 nm for the transmission of liquid samples (Figure 26a). The system offers a spectral bandwidth varying from 0.5 nm to 20 nm, with a spectral resolution reaching 0.5 nm. The measurement is conducted in a 1 nm quartz cuvette containing 3 mL of a hexane solution. The instrument was calibrated at 0 % transmittance (auto zero) without any sample and at 100 % transmittance (baseline) using the hexane solvent (3 mL).
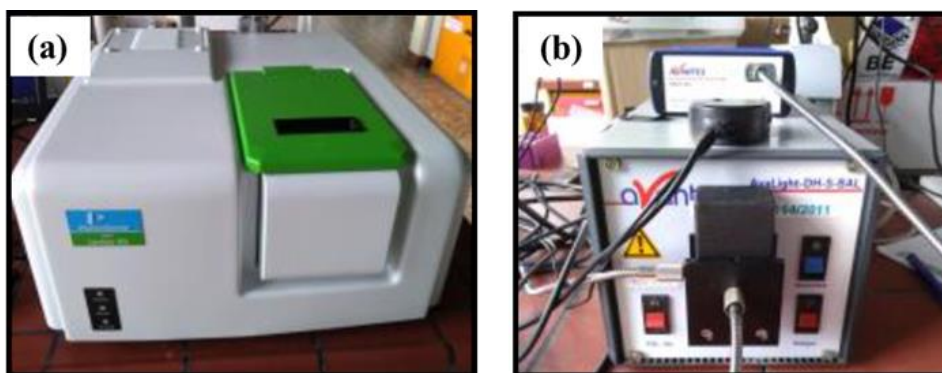

Figure 26: Photo of **(a)** UV-vis spectroscopy and **(b)** Photoluminescence (PL) spectroscopy at the physics and chemistry of nanostructures (PCN) group, Ghent University, Belgium.

To swiftly measure the photoluminescence of colloidal samples, we utilized the AvaLight-DH-S-BAL lamp (Avantes, the Netherlands), covering a wide spectrum range (215 – 2500 nm) combined with an optical spectrometer StarLine AvaSpec 2048L (Avantes, the Netherlands) (Figure 26b). The spectrometer has a wavelength range from 200 nm to 1100 nm and is equipped with a CCD linear array detector of 2048 pixels, offering an integration time between 1.11 ms and 10 minutes. The samples used for the absorption measurement were subsequently employed for measuring the PL spectroscopy. Note that the absorption and PL spectra were measured at room temperature.

2.3.2. Magnetic field- and temperature-dependent PL spectroscopy

2.3.2.1. Excitation source

The laser excitation source, a critical component in each PL spectroscopic system, generates laser light in the pulsed and continuous wave (CW) modes. Here, our spectroscopic system uses a PicoQuant semiconductor diode laser that generates a laser wavelength of 405 nm (photon energy of 3.06 eV). In the pulsed mode, the laser repetition rate is up to 80 MHz and can be adjusted down to 1 kHz using an external trigger, e.g., DG535 Digital Delay/Pulse generator [28].

2.3.2.2. Time-correlated single photon counter

Time-resolved PL spectroscopy is a powerful tool for analyzing the emission dynamics in materials, such as PL lifetime, decay rate, and recombination mechanism. Performing this measurement in the time domain required recording the time-dependent intensity of the emitted light upon the short-pulsed laser excitation. In this excitation mode, the pulsed repetition rate is much higher than the photon detection rate. Therefore, detecting several photons per signal period is very difficult. The solution for this issue is to use a time-correlated single photon counter (TCSPC). Here, we employed a PicoQuant TCSPC device (PicoHarp 300), thus the technical parameters presented in the below content were referred to the technical note of PicoQuant company [29].
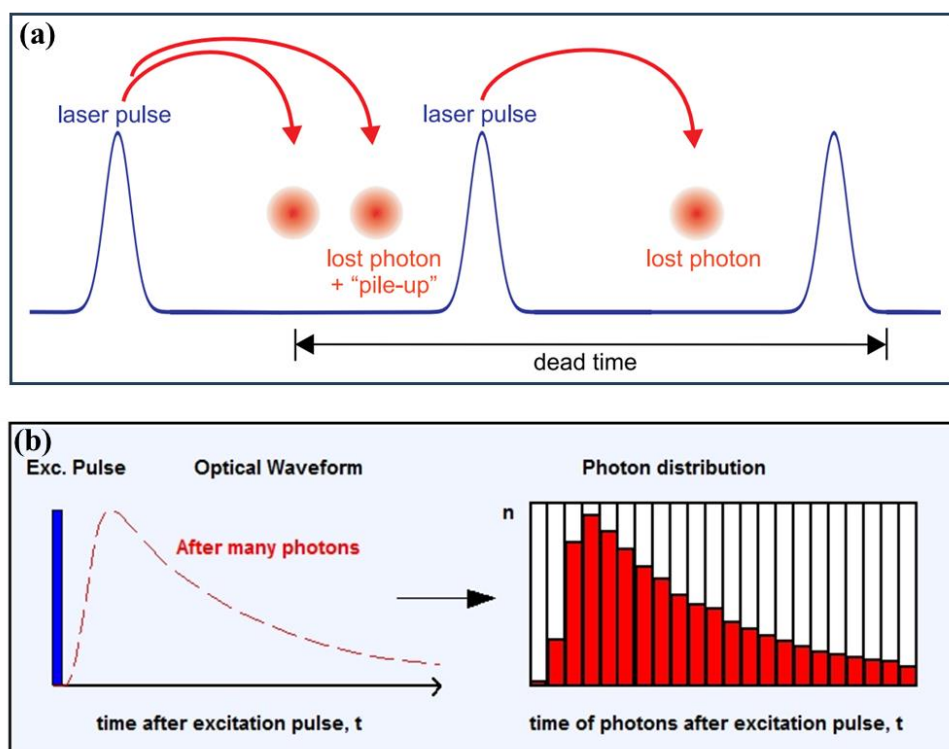
Figure 27: (a) Illustration of the "Dead" time in the detectors and the pile-up effect in a TCSPC device [29]. **(b)** A complete PL decay curve (left) and a histogram of the number of photons after many excitation pulses (right). Reproduced from reference [30].

The TCSPC device operates based on detecting single emitted photons from the sample and measuring the time of the photons after each pulsed laser excitation. Specifically, the sample is excited repetitively by short laser pulses, and emitted photons are detected by a single-photon-sensitive photomultiplier tube (PMT) or avalanche photodiode (APD). Meanwhile, the time difference between excitation and emission events is measured by electronics acting as a stopwatch. As a result, it is possible to obtain a histogram of the number of photons detected at various times, forming a PL decay curve. However, the measurement is not as simple as the above description. This is because the photodetectors and electronics have "dead" time for at least several nanoseconds after a photon event, which means these devices can not process the next photon event during the dead time. Therefore, the TCSPC device will miss photons if the number of photons exceeds 1 after each excitation cycle. This may lead to the "pile-up" effect, meaning an over-representation of early photons in a

histogram (Figure 27a) [29]. To address this issue, the count rate of the photodetector is set much lower than the excitation rate. Finally, to obtain a complete PL decay with high reliability, the experiment must be repeated many times to collect emitted photons with sufficient counting statistics (Figure 27b).

2.3.3. Setup of Magneto PL spectroscopy

Here, we use the magnetic-dependent PL spectroscopy technique to investigate the low-temperature emission properties of bare CdSe and CdSe/CdS core/crown NPLs. This technique is very powerful for obtaining information on the g-factor and spin relaxation of excitons and trions in the NPLs. The schematic of magneto PL spectroscopy is illustrated in Figure 28. This system is located in the Laboratory of Experimental Physics 2, Technical University of Dortmund, Germany. The samples are mounted on a titanium holder in Faraday geometry surrounded by magnetic coils. The sample tube is immersed in a liquid helium (LH) bath, and the thermal exchange between the samples and liquid helium is carried out via helium gas. At cryogenic temperatures, the magnetic coil can generate a strength of magnetic field (B) up to 17 Tesla (T), and its direction ($\vec{B}$) is perpendicular to the sample plate and parallel to the light wave vector. By heating the sample chamber with a thermistor, one can regulate the sample temperature for temperature-dependent measurements [28].
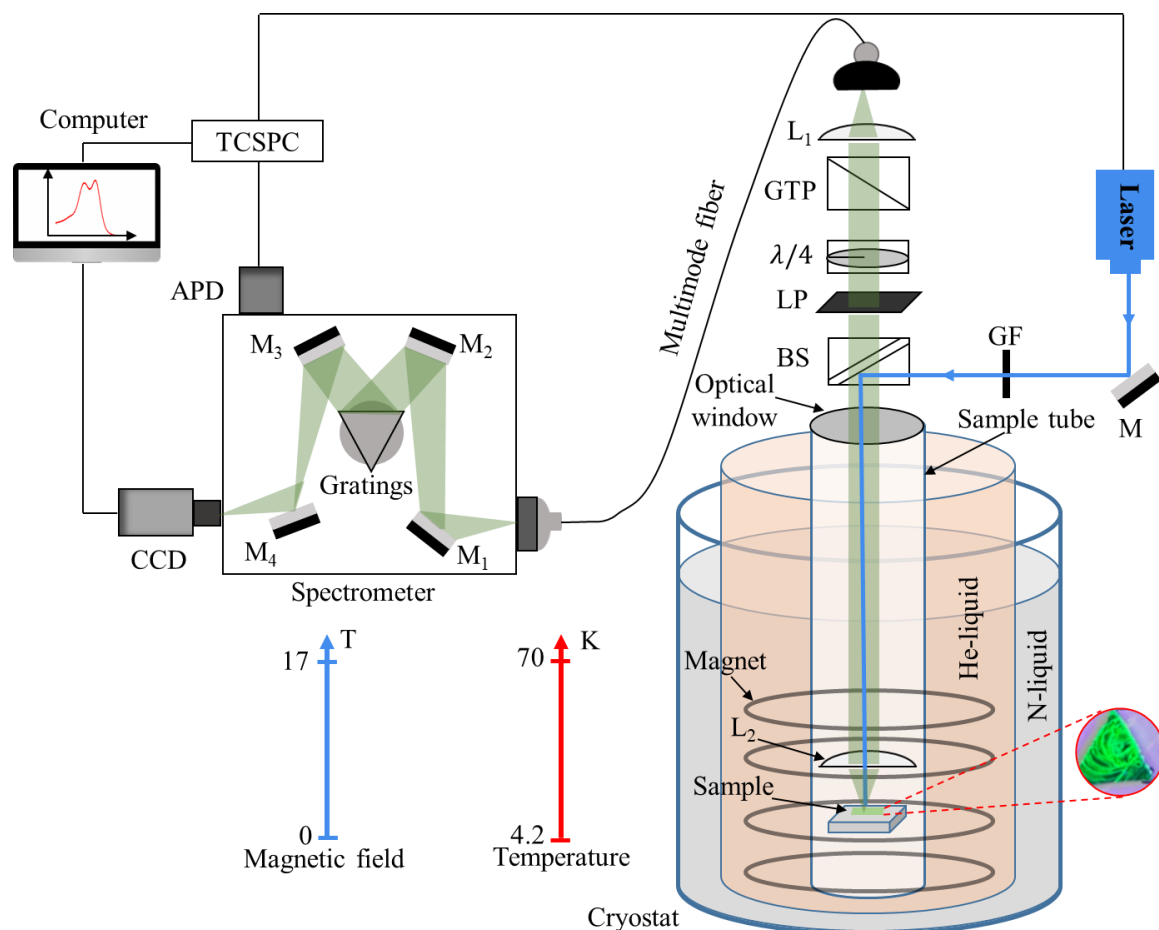
Figure 28: Schematic illustration of magnetic field-dependent PL and PL decay. GF refers to the grey filter used to adjust the laser excitation power. TCSPC is the time-correlated single photon counter. APD is the avalanche photodiode, L represents the lends (L_1, L_2), GTP is the Glan-Taylor prism, LP is the long pass filter, and BS is a beam splitter. M_1, M_2, and M_3 are the mirrors inside the spectrometer, and by flipping M_4. The PL signal can be sent either to CCD or to APD.

For magnetically dependent polarization PL spectroscopy, the sample is excited nonresonantly by laser light (CW mode, laser wavelength = 405 nm) at low excitation power density (< 0.02 W.cm^{-2}), which helps to exclude the effect of multi-excitation states. The PL signal obtained from the sample was filtered out of the scatter laser light by using a long-pass (LP) filter and detected in backscattering geometry through a multimode fiber. The PL signal is sent to a 0.55 nm spectrometer where the signal is dispersed by the mirrors (M_1, M_2, M_3), and then flipped by the mirror M_4 before being measured by a liquid nitrogen-cooled charge-coupled-device (CCD) camera. To

measure the degree of circular polarization, a Glan-Taylor (GTP) prism and a $\lambda/4$ plate were inserted in between the LP filter and the detection fiber (Figure 27), allowing us to separate the right-hand (σ^+) and left-hand (σ^-) circular polarization of PL components by adjusting the angle between the optical axis of $\lambda/4$ and GTP.

For magnetically dependent polarization PL decay, we use the same laser source, but the laser light is in the pulsed mode. The internal repetition rate of the laser is in the frequency range of 31.25 kHz – 80 MHz (the pulse width $\sim$ 100 ps). The laser source is connected to a time-correlated single photon counter (TCSPC, PicoHarp 300) manufactured by PicoHarp company. An avalanche photodiode (APD) is connected to the TCSPC device, which is after connected to a computer, which is connected to an avalanche photodiode (APD). The measurement process is similar to the previous measurement (magnetic-dependent polarization PL spectroscopy), however, the polarized PL signal here is detected by the ADP device, instead of the CCD (Figure 28).

By using the same setup described above, we can investigate the characteristic temperature and magnetic field dependence of PL spectra and PL decay in colloidal NPLs. In this thesis, we deposited the NPLs on silicon dioxide (SiO_2) substrates using the drop-cast method used for temperature and magnetic field-dependent PL decay and PL spectroscopy.

2.4. Conclusion

This chapter provided the synthetic protocol of 4.5 ML CdSe and CdSe/CdS core/crown NPLs used for low-temperature STM/STS and magneto-PL spectroscopy measurements. In this work, our STM measurements were performed on individual CdSe NPLs, providing detailed information on the topography and overall shape of NPLs at the nanoscale and in three dimensions. Meanwhile, STS measurements offer direct access to the electronic band structure, particularly the spatial distribution of surface traps in single NPLs. Knowing the trap distribution and surface characteristics of NPLs is very important for improving the optoelectronic properties. On the other hand, temperature and magnetic-dependent PL spectra provide insight into the optical properties of CdSe NPLs and CdSe/CdSe core/crown NPLs. In particular, understanding the radiative recombination process and spin dynamics in NPLs is necessary for studying and extending the application of NPLs in optoelectronic devices.

Bibliography

[1]   S. O. M. Hinterding *et al.*, "Single Trap States in Single CdSe Nanoplatelets," *ACS Nano*, vol. 15, no. 4, pp. 7216–7225, 2021, doi: 10.1021/acsnano.1c00481.

[2]   S. Pokrant and K. B. Whaley, "Tight-binding studies of surface effects on electronic structure of CdSe nanocrystals: the role of organic ligands, surface reconstruction, and inorganic capping shells," *Eur. Phys. J. D - At. Mol. Opt. Plasma Phys.*, vol. 6, no. 2, pp. 255–267, 1999, doi: 10.1007/s100530050307.

[3]   A. F. Vong, S. Irgen-Gioro, Y. Wu, and E. A. Weiss, "Origin of Low Temperature Trion Emission in CdSe Nanoplatelets," *Nano Lett.*, vol. 21, no. 23, pp. 10040–10046, 2021, doi: 10.1021/acs.nanolett.1c03726.

[4]   C. Rodà *et al.*, "Colloidal CdSe/CdS Core/Crown Nanoplatelets for Efficient Blue Light Emission and Optical Amplification," *Nano Lett.*, vol. 23, no. 8, pp. 3224–3230, 2023, doi: 10.1021/acs.nanolett.2c05061.

[5]   J. Yu and R. Chen, "Optical properties and applications of two-dimensional CdSe nanoplatelets," *InfoMat*, vol. 2, no. 5, pp. 905–927, Sep. 2020, doi: https://doi.org/10.1002/inf2.12106.

[6]   G. H. V Bertrand, A. Polovitsyn, S. Christodoulou, A. H. Khan, and I. Moreels, "Shape control of zincblende CdSe nanoplatelets," *Chem. Commun.*, vol. 52, no. 80, pp. 11975–11978, 2016, doi: 10.1039/C6CC05705E.

[7]   A. Di Giacomo, C. Rodà, A. H. Khan, and I. Moreels, "Colloidal Synthesis of Laterally Confined Blue-Emitting 3.5 Monolayer CdSe Nanoplatelets," *Chem. Mater.*, vol. 32, no. 21, pp. 9260–9267, Nov. 2020, doi: 10.1021/acs.chemmater.0c03066.

[8]   A. W. Achtstein, A. Antanovich, A. Prudnikau, R. Scott, U. Woggon, and M. Artemyev, "Linear Absorption in CdSe Nanoplates: Thickness and Lateral Size Dependency of the Intrinsic Absorption," *J. Phys. Chem. C*, vol. 119, no. 34, pp. 20156–20161, Aug. 2015, doi: 10.1021/acs.jpcc.5b06208.

[9]   G. Binnig and H. Rohrer, "Scanning tunneling microscopy," *Surf. Sci.*, vol. 126,

no. 1, pp. 236–244, 1983, doi: https://doi.org/10.1016/0039-6028(83)90716-1.

[10] M Szopa, E Zipper, M Szelag, and M Kurpas, "Coherent quantum dynamics of mesoscopic metallic ring with a barrier," *J. Phys. Conf. Ser.*, vol. 30, no. 1, p. 224, 2006, doi: 10.1088/1742-6596/30/1/027.

[11] J. Bardeen, "Tunnelling from a Many-Particle Point of View," *Phys. Rev. Lett.*, vol. 6, no. 2, pp. 57–59, Jan. 1961, doi: 10.1103/PhysRevLett.6.57.

[12] J. Tersoff and D. R. Hamann, "Theory of the scanning tunneling microscope," *Phys. Rev. B*, vol. 31, no. 2, pp. 805–813, Jan. 1985, doi: 10.1103/PhysRevB.31.805.

[13] S Rößler, J Jesudasan, K Bajaj, P Raychaudhuri, F Steglich, and S Wirth, "Influence of microstructure on local conductivities in La0.7Ce0.3MnO3 thin film," *J. Phys. Conf. Ser.*, vol. 150, no. 4, p. 42164, 2009, doi: 10.1088/1742-6596/150/4/042164.

[14] A. Della Pia and G. Costantini, "Scanning Tunneling Microscopy BT - Encyclopedia of Nanotechnology," B. Bhushan, Ed., Dordrecht: Springer Netherlands, 2016, pp. 3531–3543. doi: 10.1007/978-94-017-9780-1_45.

[15] C. Hanneken, "Observation of non-collinear magnetoresistance by scanning tunneling spectroscopy on skyrmions in PdFe/Ir (111)," University of Hamburg, 2015. [Online]. Available: https://ediss.sub.uni-hamburg.de/handle/ediss/6626

[16] R. Hamers, "Methods of Tunneling Spectroscopy With the STM," p. 32, Jun. 1993.

[17] L. . Ernst, S., Steglich, F., & Eng, "Optimisation of the preparation process for tips used in scanning tunneling microscopy."

[18] L. M. Ernst, S., Steglich, F., & Eng, "Optimisation of the preparation process for tips used in scanning tunneling microscopy." 2006. [Online]. Available: https://api.semanticscholar.org/CorpusID:53078325

[19] S. Watanabe, M. Aono, and M. Tsukada, "Effects of the tip shape on scanning

tunneling microscope images: First-principles calculations," *J. Vac. Sci. Technol. B Microelectron. Nanom. Struct. Process. Meas. Phenom.*, vol. 12, no. 3, pp. 2167–2170, May 1994, doi: 10.1116/1.587733.

[20] S. H. Pan, E. W. Hudson, and J. C. Davis, "Vacuum tunneling of superconducting quasiparticles from atomically sharp scanning tunneling microscope tips," *Appl. Phys. Lett.*, vol. 73, no. 20, pp. 2992–2994, Nov. 1998, doi: 10.1063/1.122654.

[21] J. G. Rodrigo, H. Suderow, and S. Vieira, "On the use of STM superconducting tips at very low temperatures," *Eur. Phys. J. B*, vol. 40, no. 4, pp. 483–488, Aug. 2004, [Online]. Available: https://doi.org/10.1140/epjb/e2004-00273-y

[22] S. F. Alvarado and P. Renaud, "Observation of spin-polarized-electron tunneling from a ferromagnet into GaAs," *Phys. Rev. Lett.*, vol. 68, no. 9, pp. 1387–1390, Mar. 1992, doi: 10.1103/PhysRevLett.68.1387.

[23] R. Wiesendanger *et al.*, "Vacuum tunneling of spin-polarized electrons detected by scanning tunneling microscopy," *J. Vac. Sci. Technol. B Microelectron. Nanom. Struct. Process. Meas. Phenom.*, vol. 9, no. 2, pp. 519–524, Mar. 1991, doi: 10.1116/1.585560.

[24] S. Christodoulou *et al.*, "Chloride-Induced Thickness Control in CdSe Nanoplatelets," *Nano Lett.*, vol. 18, no. 10, pp. 6248–6254, 2018, doi: 10.1021/acs.nanolett.8b02361.

[25] M. D. Tessier, C. Javaux, I. Maksimovic, V. Loriette, and B. Dubertret, "Spectroscopy of Single CdSe Nanoplatelets," *ACS Nano*, vol. 6, no. 8, pp. 6751–6758, 2012, doi: 10.1021/nn3014855.

[26] S. Yadav, A. Singh, L. Thulasidharan, and S. Sapra, "Surface Decides the Photoluminescence of Colloidal CdSe Nanoplatelets Based Core/Shell Heterostructures," *J. Phys. Chem. C*, vol. 122, no. 1, pp. 820–829, Jan. 2018, doi: 10.1021/acs.jpcc.7b09033.

[27] J. Leemans *et al.*, "Near-Edge Ligand Stripping and Robust Radiative Exciton

Recombination in CdSe/CdS Core/Crown Nanoplatelets," *J. Phys. Chem. Lett.*, vol. 11, no. 9, pp. 3339–3344, May 2020, doi: 10.1021/acs.jpclett.0c00870.

[28] G. Qiang, "Magneto-optical properties of semiconductor nanocrystals in glass." 2022. [Online]. Available: https://scholar.google.com/citations?view_op=view_citation&hl=en&user=Am1 jY2wAAAAJ&citation_for_view=Am1jY2wAAAAJ:LkGwnXOMwfcC

[29] "Time-Correlated Single Photon Counting," *Time-Correlated Single Photon Counting*. 1984. doi: 10.1016/b978-0-12-524140-3.x5001-1.

[30] W. Becker, "The bh TCSPC handbook." 2023. [Online]. Available: https://www.becker-hickl.com/

Chapter III: Atomic Structure & Trap States In Colloidal CdSe Nanoplatelets Revealed By Scanning Tunneling Microscopy

Abstract

Among anisotropic semiconductor nanocrystals, CdSe colloidal nanoplatelets (NPLs) stand out for their outstanding optoelectronic properties and distinctive shapes. The NPLs exhibit sharp emission linewidth [1] as well as a peculiar electronic density of states (DOS) [2] for which the electrons can "feel" in-plane and out-of-plane dimensions. However, the NPLs host many surface traps that significantly affect their optoelectronic properties. Despite this, the spatial and energetic distribution of surface traps on single NPLs remains unknown. Furthermore, the lack of information on the true shape of NPLs constrains the understanding of the physical mechanisms governing their optoelectronic properties, particularly quantum effect and charge transport in NPL-based heterostructures (HSs). In this work, we employed low-temperature scanning tunneling microscopy (LT-STM) and spectroscopy (LT-STS) to investigate the structural and electronic properties of 4.5 ML CdSe NPLs. By mapping the topography of individual NPLs, we found that their long edges are truncated and exhibit atomic terraces. The concomitant measurement of the tunnel current fluctuations evidence that most of the surface traps are concentrated on the side facets. The STS measurements revealed details about the electronic band structure, notably the random distribution of sparse electron traps on the top facet of individual NPLs. Surface traps caused the blinking effect in the tunneling current was detected by current-time (I(t)) measurements. The power spectral density (PSD) analysis of the blinking traces revealed that a single electron trap behaves as a stochastic two-level system (TLS) with a characteristic timescale of 17 – 69 ms.

Graphic abstract: Schematic illustration of STM/STS measurements on CdSe NPLs (the top panel, on the left). The three-dimensional (3D) STM topographic image of an individual NPL (the top panel, on the right). The dI/dV spectroscopy measured on an isolated NPL shows the electronic band structure (the bottom panel, on the right). The blinking traces in the tunneling current are caused by surface traps (the bottom panel, on the left).
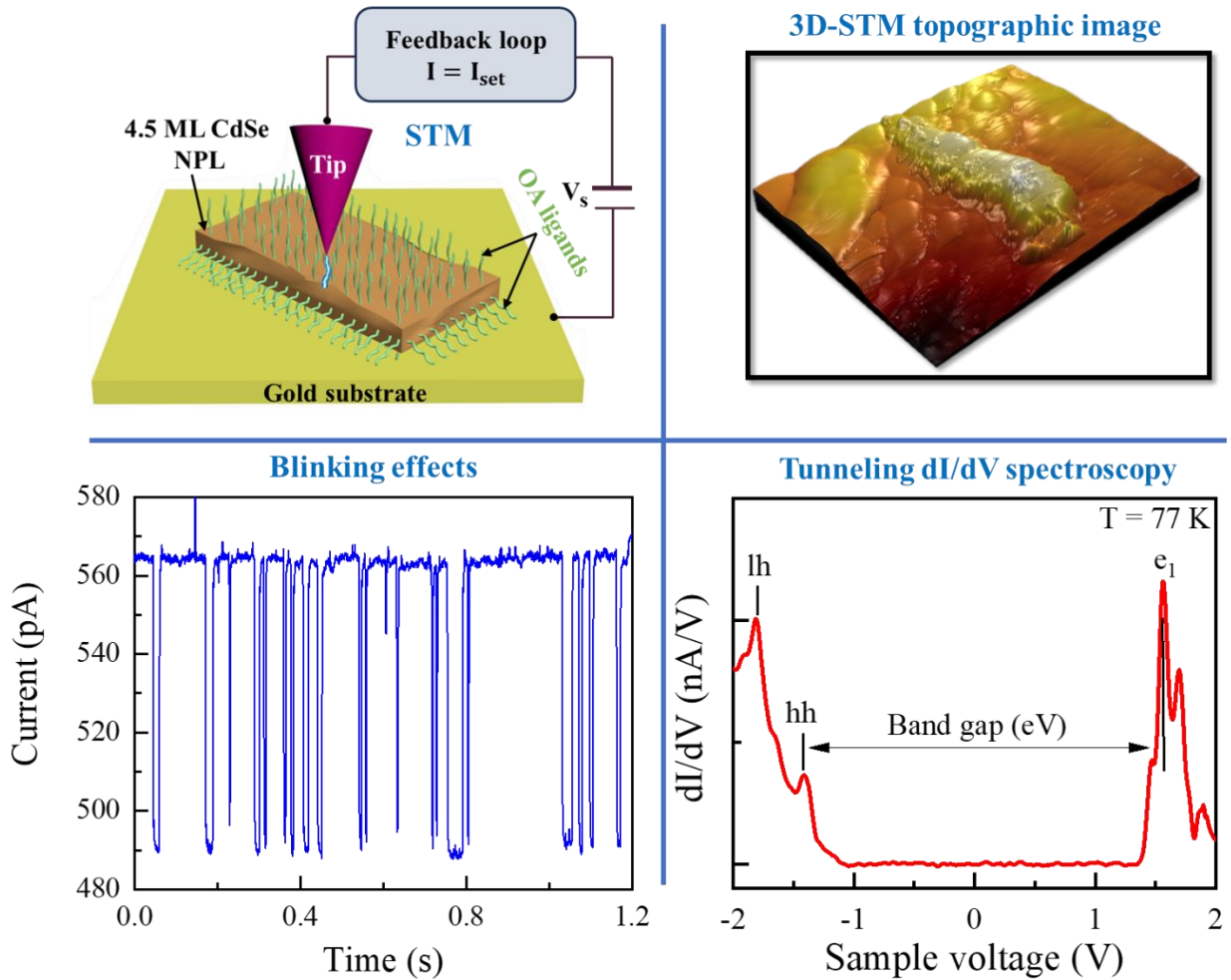
3.1. Introduction

Colloidal CdSe NPLs have emerged as a promising material for optoelectronic devices due to their outstanding optical properties, such as narrow emission bandwidth [3], fast photoluminescence decay time [1], high intrinsic absorption coefficient [4], and suppressed Auger recombination [3], [5]. Interestingly, these properties can be regulated by controlling their thickness, a phenomenon known as the one-dimensional (1D) quantum confinement [2], [6]. However, the NPLs host many surface traps which strongly reduce the overall quantum efficiency, thus affecting the performance of NPL-based optoelectronic devices [7]. Despite this, not all surface traps are harmful. For example, shallow traps favor the separation and transfer of the photogenerated carriers, contributing to enhanced photocatalytic efficiency [8].

In past years, optical spectroscopy techniques have been widely used to investigate surface traps in colloidal NCs [7], [9], [10]. For instance, Irgen Gioro and co-workers [9] reported the PL blinking phenomenon caused by surface traps in ensemble CdSe NPLs. They concluded that the nonradiative recombination of trapped excitons caused the PL blinking on a time scale (1 µs – ms), and the blinking on a longer time scale (≥ 3s) is attributed to switching between trapped excitons and trions. In another study, O. M. Hinterding et al [7] tracked both the delayed PL emission and PL blinking caused by surface traps in single CdSe NPLs. The authors pointed out that single traps caused a PL spectral diffusion while reversible trapping induced exponentially delayed PL and trap PL with a short lifetime range (40 – 1300 ns). In general, the optical spectroscopic techniques allowed the investigation of the trapping and de-trapping mechanisms in both single and ensemble NPLs. However, these methods do not directly provide information on the energetic level of traps as well as cannot approach single traps because the size of the laser beam is much larger than the size of a single trap.

In colloidal NCs, surface traps typically originate from structural defects and the bad coordination between surface atoms with ligands [7], [11]. CdSe NPLs are two-dimensional (2D) nanostructures with well-defined surfaces upon their orientation. Therefore, the nature of trap states differs in each specific surface. For example, the top and bottom facets contain electron traps while the side facets host both electron and hole

traps [12]. This requires a method that allows studying the surface and electronic characteristics with high precision. In the field of nanoscience, scanning tunneling microscopy (STM)/spectroscopy (STS) is a powerful technique widely used for investigating the structural and electronic properties of materials [2], [13]. Unlike optical spectra, the STS technique provides the ability to directly probe the electronic properties of materials at the nanoscale, including band structure, band edge, band gap, and trap states. For example, Peric and co-workers measured the density of states (DOS) on isolated and stacked CdSe NPLs using the STS and they found the presence of in-gap states at a negative bias (below the Fermi level, around -0.6 V) which is attributed to deep hole traps. However, the trapping mechanism has not been investigated with the STS technique until now [2]. Therefore, knowing the energetic level, trapping mechanism, and distribution of surface traps in single NPLs is critical for improving their optical properties as well as their potential applications, such as photocatalysis [8], and resistive random-access memory (RRAM) [14].

In addition, the 2D shape also has an impact on the optoelectronic properties of NPLs. For instance, NPLs with a large lateral size typically contain more surface traps than small-sized NPLs [15]. This raises the question about the true shape of NPLs. Some techniques such as scanning transmission electronic microscopy (STEM) and high-resolution TEM (HR-TEM) offer the ability to observe the NPL structure at high resolutions. Nonetheless, these techniques result in 2D images that do not provide in detail the topography and overall shape of NPLs. This restricts the understanding of the influence of the shape on the optoelectronic properties of NPLs.

To address these mentioned issues, we employed low-temperature scanning tunneling microscopy (LT-STM) and spectroscopy (LT-STS) to investigate the structural and electronic properties of CdSe NPLs. Additionally, high-angle annular dark field-scanning transmission electron microscopy (HAADF-STEM) was also used to analyze the morphological properties of NPLs, including the shape, size, and crystal structure. To perform these measurements, we synthesized CdSe NPLs with a thickness of 4.5 monolayers (ML). The detailed protocol has been presented in Chapter II. After the synthesis, the NPL solution (20 µL) and n-hexane (3 mL) were added to a Quartz cuvette

and then investigated with UV-vis and PL spectra at room temperature (RT). The absorption spectroscopy (red) exhibits two absorption lines corresponding to the heavy hole (hh) at 2.45 eV and the light hole (lh) at 2.59 eV (Figure 29a). Meanwhile, the PL spectroscopy (black) shows a maximum emission peak at 2.44 eV with a full width at half maximum (fwhm) of 60 meV (Figure 29a). Therefore, the optical bandgap is determined to be 2.44 eV which is the required energy to excite an electron from the valence band (VB) to the conduction band (CB). In addition, our NPL solution emitted a green emission when exposed to UV light (Figure 29b). These results are in good agreement with previous studies [6], [16].
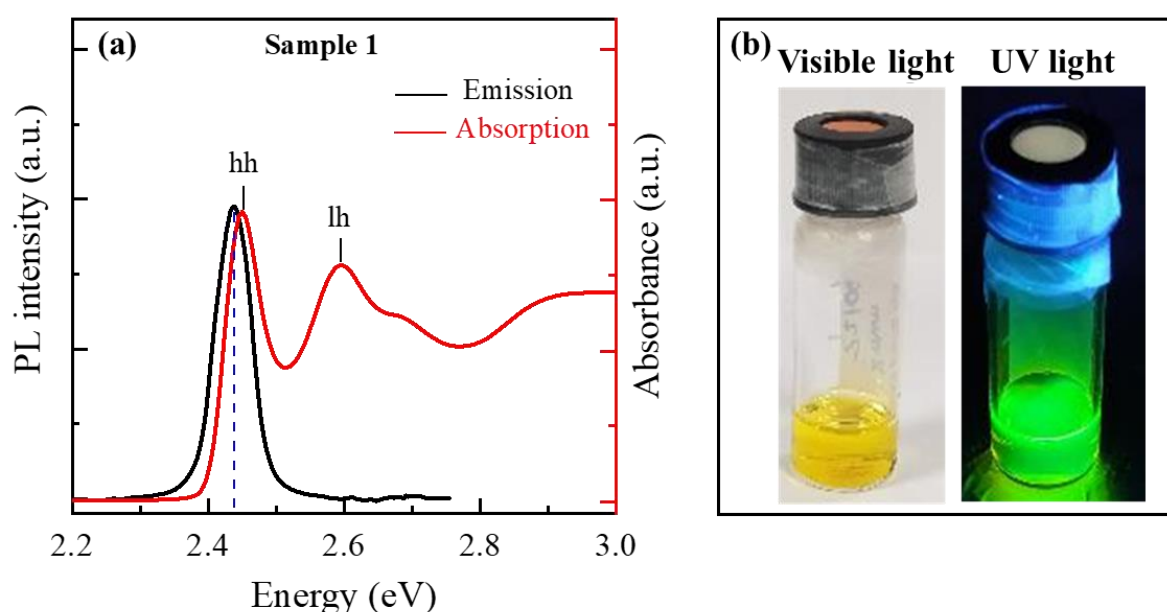
Figure 29: (a) Absorption (red) and PL (black) spectra of 4.5 ML CdSe NPLs (sample 1) at room temperature. **(b)** Bright photoluminescence (PL) from the NPL solution under visible (left) and UV (right) light.

3.2. Structural characterization of CdSe NPLs analyzed by high-angle annular dark field-scanning transmission electron microscopy.

CdSe NPLs are typically oriented in two different styles in solution, including stacked and flat-lying NPLs. Thanks to this characteristic, one can determine the thickness of NPLs using transmission electron microscopies (TEM). Here, we employed high-angle

annular dark field-scanning transmission electron microscopy (HAADF-STEM) to study the structural properties of NPLs, including thickness, shape, and crystal structures. To do that, the NPL solution (sample 1) was dropped cast on a TEM grid and then investigated with the HAADF-STEM technique. The HAADF-STEM images were acquired from a FEI Titan Themis 300 microscope equipped with a probe aberration corrector, operated at 300 kV. The microscopy system was located at the UMET laboratory – University of Lille.
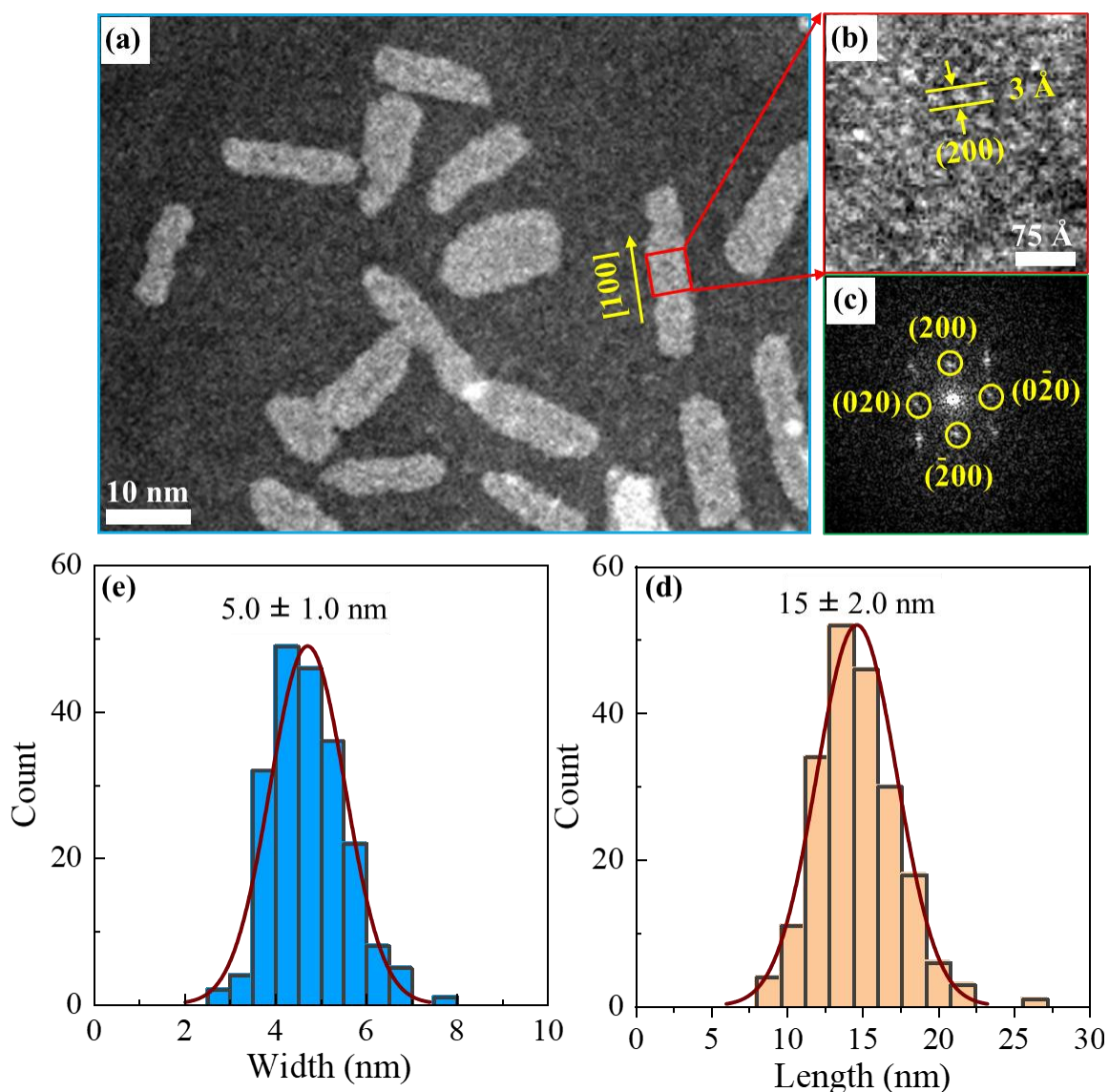
Figure 30: (a) HAADF-STEM image of 4.5 ML CdSe NPLs (sample 1). **(b)** Zoomed-in HAADF-STEM image of a small area on the top surface of a flat-lying NPL (the red rectangle). **(c)** FFT pattern extracted from Figure c. **(d-e)** Lateral size distribution acquired from 200 NPLs. **(d)** Length. **(e)** Width.

Figure 30a shows rectangular NPLs with various lateral sizes on a TEM grid. By analyzing 200 NPLs, the average lateral size was estimated to be 5.0 ± 1.0 nm in width and 15 ± 2.0 nm in length (Figures 30d and e). We now turn to analyze the morphology of NPLs. Figure 30b displays the HAADF-STEM image of a small area on the top surface of a flat-laying NPL. In this image, we can observe the arrangement of Cd atoms even though the resolution is slightly affected by OA ligands surrounding the NPL. The corresponding fast Fourier transform (FFT) pattern is presented in Figure 30c, showing a set of lattice fringes such as (200), (020), etc, indicating the zinc-blende (ZB) structure of NPLs [17]. The distance of the (200) lattice fringe was estimated to be 3 Å which coincides with the (200) lattice spacing (Figure 30b) [18]. The lateral growth direction of NPLs is [100] which coincides with their long edges (Figure 30a, the yellow arrow). These results are in good agreement with references [18], [19].
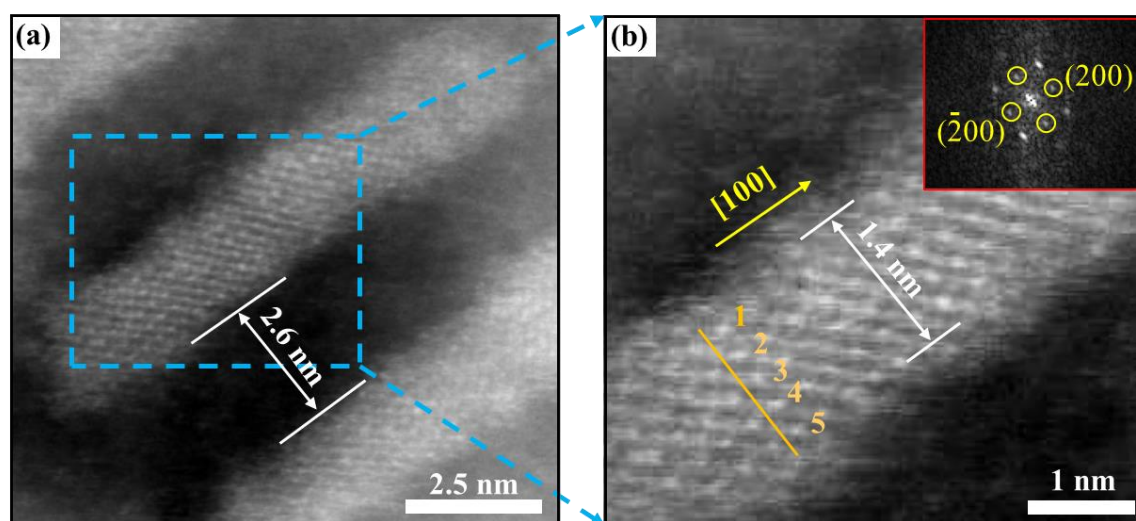
Figure 31: (a) HAADF-STEM image of stacked NPLs. **(b)** Zoomed-in HAADF-STEM image of an area (blue dashed rectangle) on the side facet of a stacked NPL. The corresponding FFT pattern was inserted in Figure b.

Thickness is an important parameter that governs the optoelectronic properties of CdSe NPLs [6]. To determine the NPL thickness, we performed HAADF-STEM measurements on stacked NPLs, as shown in Figure 31a. The spacing between two neighbor NPLs is estimated to be 2.6 nm which is smaller than the length of two OA ligands (4 nm). This is due to the interlace of OA ligands surrounding the NPLs, a phenomenon was also observed in other ligands such as stearic acid (SA), and hexadecyl

phosphonic acid (HDPA) [20]. Figure 31b presents a HAADF-STEM image measured on a small area on the stack NPL (the blue dashed rectangle). The side-view image (Figure 31b) shows the arrangement of atoms along the thickness direction [001], particularly we can see a roll of five Cd atoms corresponding to five monolayers of Cd elements. Theoretically, 4.5 ML CdSe NPLs are composed of four Se-atomic monolayers interspersed with five Cd-atomic monolayers in the [001] direction, forming the thickness of NPLs [18]. With this arrangement, the top and bottom facets of NPLs should be Cd atomic planes. This is very consistent with the experimental results obtained from the HAADF-STEM images. The corresponding FFT pattern is also presented in Figure 31b, confirming the ZB structure of CdSe NPL. The estimated NPL thickness is 1.4 nm, which is slightly larger than the 1.3 nm thickness (for 4.5 ML NPL) reported by C. van der Bok and co-workers [21]. These findings confirm the formation of standard NPLs through our synthetic protocol.

3.3. Topographic and electronic properties of CdSe NPLs analyzed by scanning tunneling microscopy and spectroscopy

The HAADF-STEM images provided insight into the structural properties of NPLs including lateral size, thickness, and crystal structures. Despite this, the three-dimensional (3D) shape of NPLs has not been explored in the previous part, which would limit the understanding of the correlation between the surface characteristics and electronic properties of NPLs. Therefore, CdSe NPLs have been investigated with the STM/STS technique, which allows us to probe the structural and electronic properties of individual NPLS at a sub-nanometer spatial resolution [22], [23], [24]. However, the use of the STM/STS technique on colloidal NPLs faces several difficulties because these NPLs are typically unstable on a solid substrate and surrounded by organic ligands. To solve this issue, we have applied a special solution for the deposition of NPLs on a gold substrate.

3.3.1. Deposition of CdSe NPLs on gold substrate

For STM/STS measurements, 4.5 ML CdSe NPLs were deposited on a gold substrate following a four-step process, as described in Figure 32. Firstly, the NPL solution is dropped cast on a PDMS substrate placed at an angle (α) (step 1). The NPL thin films

are dried under nitrogen gas for a few minutes to evaporate the solvent (step 2). The NPLs are then transferred to a clean gold substrate by slightly forcing the substrate onto the PDMS (step 3). After this manipulation, the NPLs will be kept on the gold substrate which is mounted on a sample holder (step 4). The sample is annealed at 120 ℃ for 9 hours in the load lock (pressure ~ 10^{-7} Torr) before loading to the preparation chamber (pressure ~ 10^{-10} Torr) where it is again annealed at 150 °C for an hour. Finally, the sample is loaded into the analysis chamber where a STM tip is scanned over the sample surface.
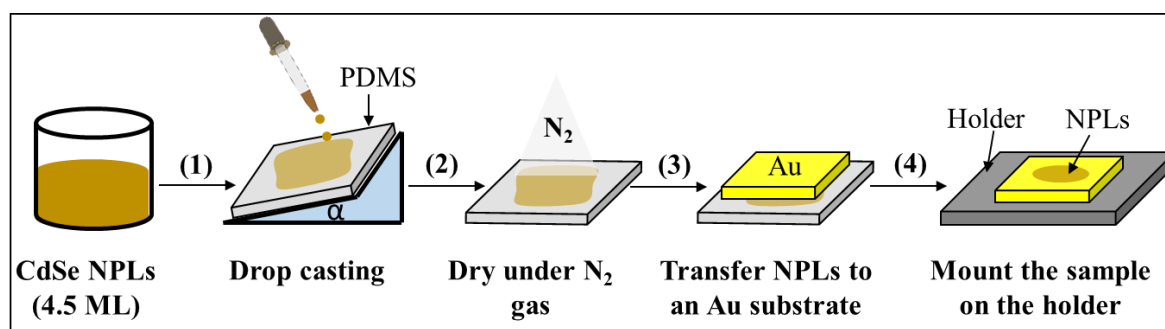
Figure 32: Schematic illustration of the deposition of CdSe NPLs on a gold (Au) substrate used for STM and STS measurements. To obtain uniform NPL films, we placed a PDMS substrate base at an angle (α).

3.3.2. Trap states in CdSe NPLs probed by scanning tunneling spectroscopy

Scanning tunneling spectroscopy (STS) was performed on individual NPLs to study their electronic band structure. These STS measurements were carried out under ultrahigh vacuum (UVH ~ 10^{-11} Torr) and at low temperatures (T = 77 K). Figure 33a describes the STM/STS measurement on a single NPL. Tunneling dI/dV spectra (STS) were acquired by positing the STM tip over an individual NPL, forming a double barrier tunnel junction (DBTJ), and disabling the feedback loop during the measurement. From the electrical point of view, the tip-NPL junction is considered a capacitor characterized by a resistance (R_1), and a capacitance (C_1) that can be determined based on the tunneling current (I_t) and bias voltage (V_s) (Figure 33b). Meanwhile, the NPL-substrate junction is characterized by a resistance (R_2), and a capacitance (C_2) that is fixed for a given NPL [13]. In this configuration, the so-called lever arm (η) is defined as

$$\eta = \frac{C_2}{C_1 + C_2} \qquad\qquad (3.1)$$

The capacitances are given by: $C_1 = \varepsilon A / d_1$ and $C_2 = \varepsilon A / d_2$, where ε is the dielectric constant, A is the area of the capacitor, and d_1 and d_2 are the widths of the tip-NPL and the NPL-substrate junctions, respectively [25]. In our STS experiment, the tunneling current and bias voltage were set as follows: $I_t = 200$ pA, $V_s = 1.6$ V (above the CB edge), so the width of the tip-NPL junction (d_1) is larger than that of the NPL-substrate junction (d_2). In this case, when an electron is injected into the NPL, it will leave the NPL before a second electron arrives, thus reducing the probability of the single electron charging effect and providing access to the quasi-particle band gap. To explain the STS data clearly, we first carried out STM measurements to find isolated NPLs and collect information on their shape, and size. The STM topographic image in Figure 33c shows an isolated and flat-lying NPL with a lateral size of 12 nm × 4 nm. To investigate its electronic band structure, the STS was measured at four different positions on the NPL (Figure 33c, empty circles). At position 1 (black circle), the STS shows a zero-conductance region (ZCR) surrounded by resonant peaks at different bias voltages. Specifically, the resonant peak at positive bias represents the first electron state (e_1) in the conduction band. The valence band consists of two resonant peaks at negative bias corresponding to the heavy hole (hh) and the light hole (lh). Assuming a lever arm of 1, the electronic band gap energy is estimated to be 2.77 eV (defined as the spacing between the first peaks in the CB and VB). At other positions, the density of states (DOS) slightly differs from the DOS measured at position 1. Particularly, the STS at positions 2 (purple circle) and 3 (red circle) exhibit in-gap states at a positive bias (around +1.0 V) attributed to electron trap states. In contrast, no in-gap states were detected in the STS at position 4. NPL. In general, all the tunneling dI/dV spectra show the expected features for the electronic band structure of 4.5 ML CdSe NPLs.
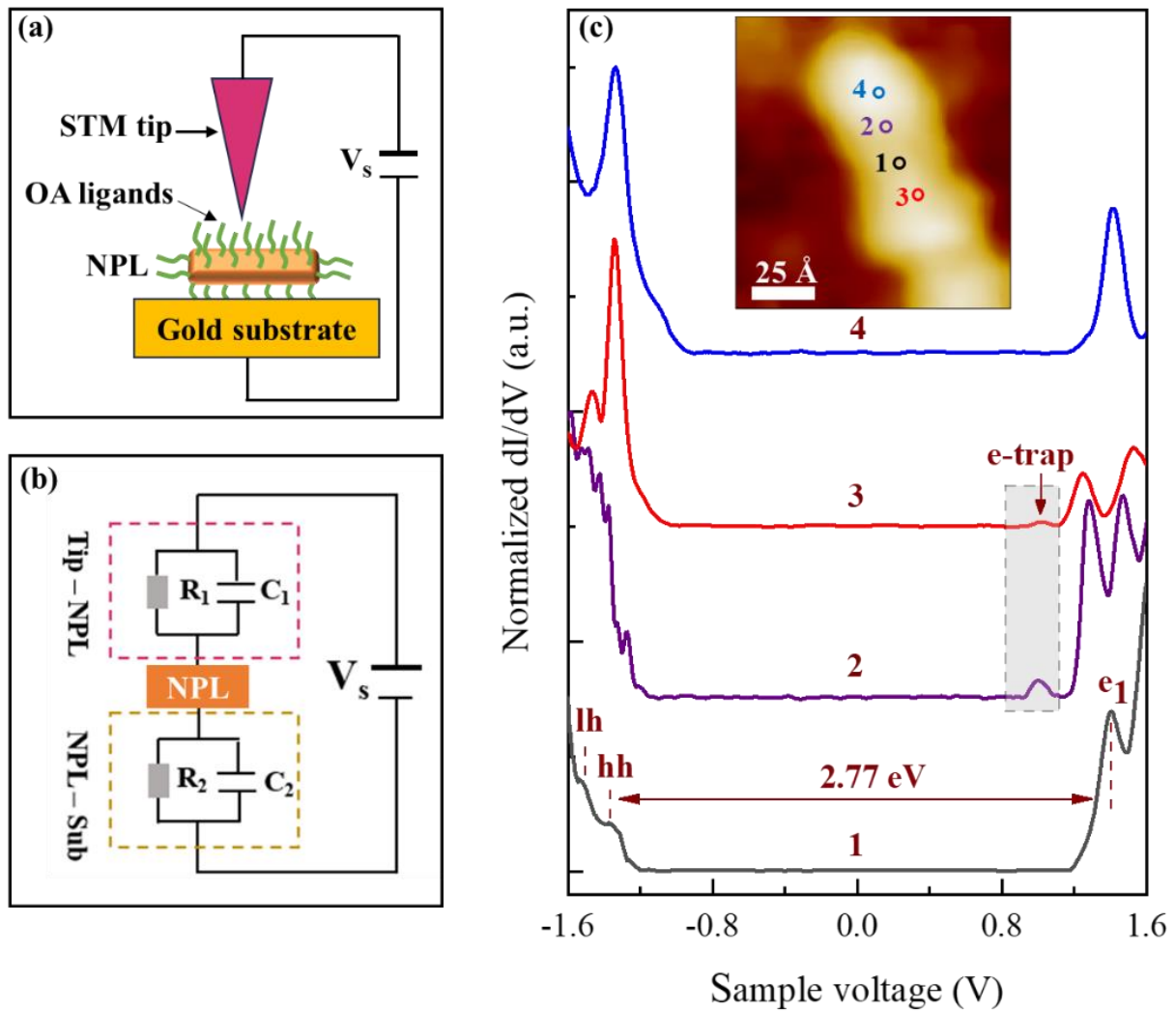
Figure 33: (a) Schematic illustration of STM/STS measurements on individual NPLs, where d_1 and d_2 are the tip-NPL and NPL-substrate distances, respectively. **(b)** Schematic illustration of an electrical model of a double barrier-tunnel junction (DBTJ). The DBTJ includes (1) the tip-NPL junction with capacitance C_1 and resistance R_1, and (2) the NPL-substrate junction with capacitance C_2 and resistance R_2. **(c)** Tunneling dI/dV spectra (STS) measured at four different positions on a flat-lying CdSe NPL with a lateral dimension of 12 nm × 4 nm (V_s = 1.6 V, I_t = 200 pA, T = 77 K). The STM topographic image of the NPL was inserted into Figure c (V_s = 5 V, I_t = 40 pA).

To better understand surface traps, we performed STS measurements on another flat-lying NPL (Figure 34, the STM image). Figure 34a shows the tunneling spectra measured at three different positions on the NPL (color circles). At position T_e, (the black circle), the dI/dV spectroscopy exhibits the typical band structure of NPLs with a band gap energy of 2.82 eV where the electron trap state is found at a positive bias (around +1.0 V). Meanwhile, no trap states were found in the band gap measured at positions N_1 and N_2 (green and blue circles). On the same NPL, we also probed the density of states (DOS) at four different positions near the NPL edges, as shown in Figure 34b. The estimated band gap energy is 2.73 eV which is quite consistent with the band gap measured at the center positions of the NPL. On the other hand, we observe the presence of electron trap states (around +1.0 V) at all the survey positions (Figure 34b). Remarkably, the STS at position T_{e-h} (the green star) shows an in-gap state at a negative bias (-0.78 V) which is attributed to the hole trap state [2]. In summary, these STS results indicate that the top facet of NPLs mainly hosts shallow electron traps, and their distribution is random. Indeed, the top and bottom facets of 4.5 ML CdSe NPLs are pure Cd (100) facets that host electron traps arising from Cd-dangling bond orbitals [12], [26]. Therefore, the observation of electron traps on the top facet is very consistent with the theoretical prediction [12] and the experimental study [13].
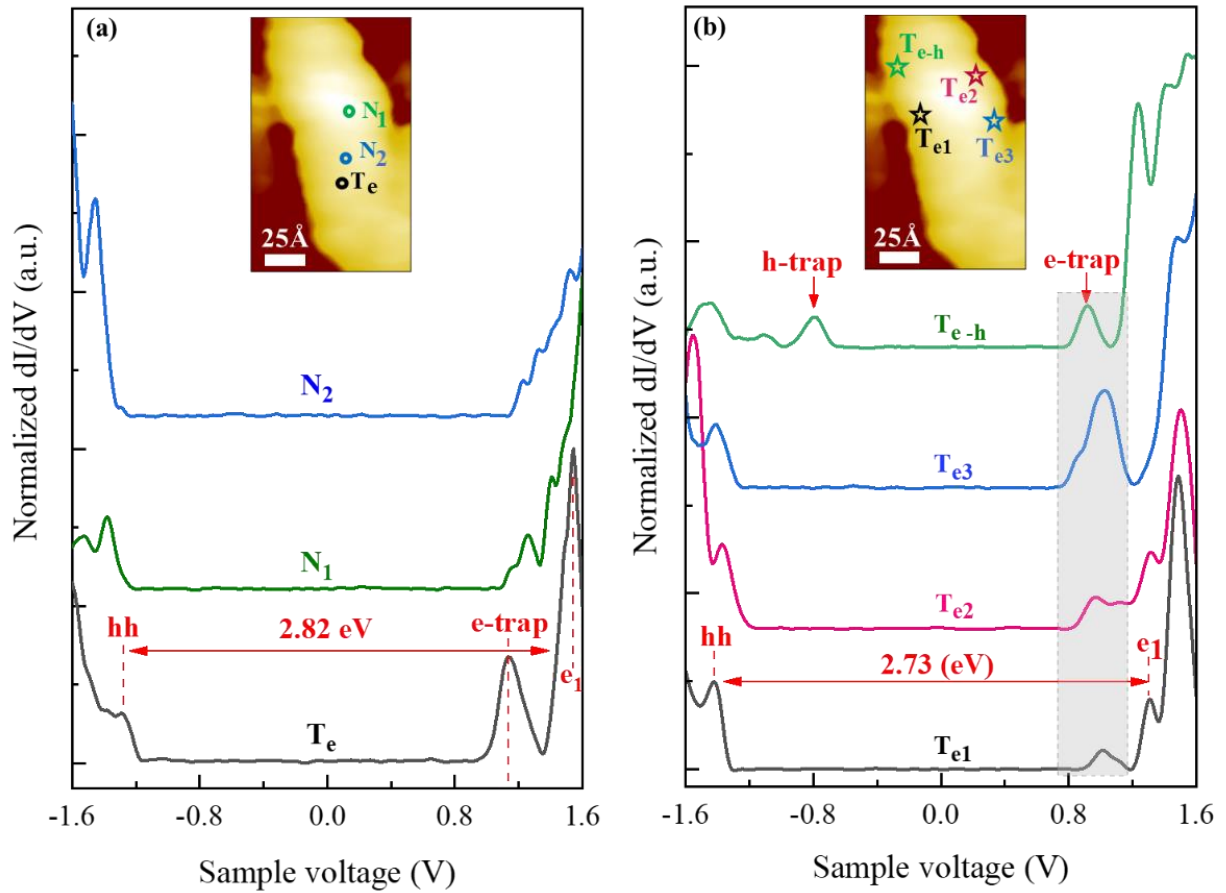
Figure 34: Tunneling dI/dV spectra were performed on an isolated and flat-lying CdSe NPL with a lateral size of 16 nm × 6 nm. **(a)** measured at three different positions (T_e, N_1, N_2). **(b)** measured at four different positions near the NPL edges (T_{e1}, T_{e2}, T_{e3}, and T_{e-h}). The STM topographic image was measured at $V_s = 5$ V, $I_t = 40$ pA. The STS measurements were carried out at $V_s = 1.6$ V, $I_t = 200$ pA, T = 77 K.

Comparison between the optical and electronic band gap.

In this study, the band gap energy of 4.5 ML CdSe NPLs was measured using both optical spectroscopy and STS techniques. The band gap energy was determined at 2.44 eV (measured by PL spectroscopy), and 2.73 – 2.82 eV (measured by STS). The difference in the band gap energy mainly comes from fundamental differences in the experiments. The STS technique directly probes the single energy level by adding one electron (or hole) from the tip to the NPL, thus providing direct access to the quasi-particle band gap. In contrast, PL spectroscopy is an indirect method for measuring the band gap energy of NPLs. In this method, the photon energy (ΔE_{opt}) required to excite an electron from the valence to conduction bands can be written as follows [27]:

$$\Delta E_{opt} = E_{e1} - E_{h1} + 2\Sigma - J_{e-h} \tag{3.2}$$

Where E_{e1} and E_{h1} are the energy levels of the electron (in CB) and hole (in VB), respectively. The polarization energy Σ is given by $\Sigma = \Sigma_e + \Sigma_h$, and J_{e-h} is the electron-hole Coulomb interaction. For our STS measurements, the tip-NPL distance is large enough to ensure that the probability of injecting an electron into the NPL is much smaller than that for an electron to tunnel to the substrate ($\Gamma_{in} \ll \Gamma_{out}$). Therefore, the STM band gap is written as follows:

$$\eta e \Delta V_{STM} = E_{e1} - E_{h1} + 2\Sigma \tag{3.3}$$

Combining equations (3.2) and (3.3), we obtain the equation that shows the relationship between the optical and STM band gap.

$$\Delta E_{opt} = \eta e \Delta V_{STM} - J_{e-h} \tag{3.4}$$

According to our STS results, the lever arm (η) is determined at 1 because of the condition $\Gamma_{in} \ll \Gamma_{out}$. Therefore, equation (3.4) is reduced to.

$$\Delta E_{opt} = e \Delta V_{STM} - J_{e-h} = \Delta E_{STM} - J_{e-h} \tag{3.5}$$

The above equation indicates the correct band gap energy of NPLs is always larger than the optical gap due to the electron-hole Coulomb interactions. For example, $\Delta E_{opt} =$ 2.44 eV and $\Delta E_{STM} =$ 2.73 eV, thus the Coulomb interaction energy (J_{e-h}) is estimated to be 290 meV (for 4.5 ML CdSe NPLs). In the literature [2], the Coulomb interaction energy is determined at 150 meV for 5.5 ML CdSe NPLs ($\Delta E_{opt} =$ 2.25 eV, $\Delta E_{STM} =$ 2.40 eV). Therefore, we conclude that our result is consistent with the literature.

3.3.3. Further analysis of the topography of CdSe NPLs by scanning tunneling microscopy

The detection of hole traps on the top facet near the NPL edges raises a question about the surface characteristics and overall shape of NPLs. This is due to two following reasons: (1) hole traps originating from dangling bonds of Se atoms [12], and (2) Only the side facets of NPLs can consist of rich-Se planes [18]. Experimentally, Peric and co-workers reported the electronic band structure measured at the side facets of NPLs by the LT-STS technique [2]. They found an in-gap state at a negative bias (near the Fermi level) within the band gap energy, which is attributed to deep hole traps in NPLs. To investigate the topography of NPLs, STM measurements were performed on two different CdSe NPL samples with the same thickness of 4.5 monolayers (ML). Investigating two different samples ensures that our conclusion or observation is general and not sample-specific. The synthetic protocol for each sample has been presented in Chapter II.

Figure 35 presents the STM and STS results measured on the NPL sample (sample 2) synthesized by our collaborators from Ghent University (Belgium). Figure 35a shows the STM topographic image of an isolated and flat-lying NPL on a gold substrate. The NPL has a rectangular shape with a lateral size of 20 nm × 5 nm. Additionally, we also observed the area marked by the dashed white circle on the NPL which is attributed to the tip-ligand interaction. To observe the NPL edge clearly, the STM tip was slowly scanned over the small area marked by the green rectangle on the NPL (see Figure 35a). The topography of the NPL edge is presented in Figure 35b, showing the complex and irregular edge (the red dashed rectangle). Figure 35c presents the three-dimensional (3D) STM image extracted from Figure 35b. To get more details on the NPL edge, the 3D-STM image was slightly rotated by an angle compared to the 2D-STM image and we used a color palette to map the topography of the NPL. The 3D-STM image exhibits the truncated edge which exposes atomic terraces on the NPL side facet. This finding raises a question about the formation mechanism of NPLs. According to our learning, the formation mechanisms of CdSe NPLs have been reported in previous studies, however, a general mechanism for forming NPLs has not been unified [28], [29], [30],

[31]. Among them, Riedinger et al have used experimental results, kinetic modeling, density functional theory (DFT), and Monte Carlo simulations to prove an intrinsic growth instability that can explain the formation of ZB-CdSe NPLs [28]. According to the authors, the mechanism can occur when the concentration of reactive monomers is sufficiently large so that the growth process becomes the reaction at the nanocrystals/solution interface. In this case, the 2D growth at the edges is energetically preferred over the growth on large planar surfaces. This mechanism is consistent with experimental studies of the ripening of thin NPLs into thicker ones as the reaction temperature is increased, or the stability of thick NPLs depending on the material type [32]. However, the surface characteristics of NPLs have not been experimentally investigated in this study. Instead, the authors assumed CdSe NPLs with atomically flat surfaces. Recently, Zhu et al demonstrated the irregular edges of 4.5 ML CdSe NPLs using the HR-TEM technique [17]. They concluded that the irregular edges are seldom parallel to either of the two [100] directions and suggested that the side facets consist of very small (110) and other types of facets. In another study, Yoon et al have used the HAADF-STEM technique, and DFT simulations to evidence the asymmetric lateral growth of 4.5 ML CdSe NPLs [18]. They suggested that the lateral growth of rectangular NPLs could proceed based on (101) facets at the locally wedge-shaped NPL side morphologies. Based on the studies by Zhu [17] and Yoon [18], we believe that the edges of NPLs (4.5 ML) are truncated and expose an atomic terrace as observed in our STM image (Figure 35c). To investigate the electronic properties of this NPL, we probed the DOS at the position marked by the blue cross on the NPL top surface (Figure 35d). The STS exhibits a typical electronic band structure of NPLs with a band gap energy of 2.63 eV, in which we observed the evidence for in-gap states (the red dashed circle) adjacent to the CB edge that is attributed to electron trap states [13]. This finding is consistent with the fact that the truncated edge hosts structural defects and dangling bonds which give rise to surface traps [7], [12].
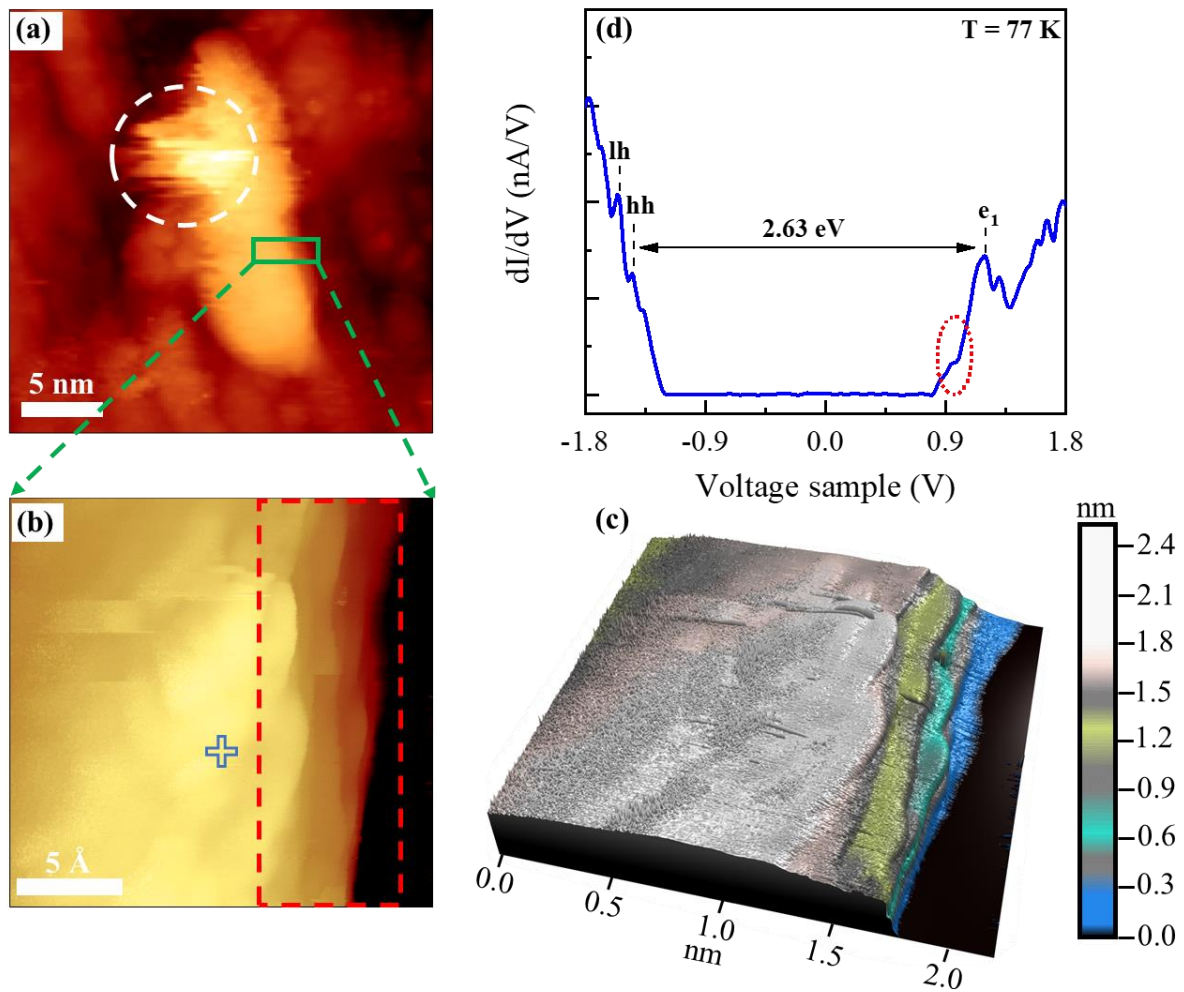
Figure 35: STM/STS measurements on 4.5 ML CdSe NPLs (sample 2). **(a)** STM image of an isolated and flat-lying NPL (V_s = 2 V, I_t = 100 pA). **(b)** Topographic STM image measured at a small area (the green rectangle) on the NPL (V_s = 2 V, I_t = 43 pA, the number of pixels = 512, T = 77 K). **(c)** 3D-STM topographic image extracted from Figure b. **(d)** Average dI/dV spectrum measured at the position marked by the blue cross on the NPL (V_s = 2 V, I_t = 80 pA, T = 77 K).

The striking thing about NPLs is that the STM can probe the NPL topography at high resolutions, so we comment on the 3D shape of NPLs. Based on Figure 35c, we suspect that the NPLs have a trapezoidal shape instead of a complete rectangle. To check this hypothesis, STM topographic measurements were performed on individual NPLs of the other sample (sample 1). Figure 36a shows an STM topographic image of an individual and flat-lying NPL with a lateral dimension of 14 nm × 5 nm. We scanned the tip over a large enough area marked by the green rectangle to study the topography of both long

edges of the NPLs (see Figure 36a). The corresponding 3D-STM image is presented in Figure 36b, indicating that both long edges of the NPL are truncated and localized defects concentrate near the NPL edges (the blue dashed circles). The truncated facet on the right exposes four monolayers overlapping each other in the [001] direction, forming the NPL thickness. The average height of each monolayer is estimated to be 0.3 nm which is very consistent with the (200) lattice spacing obtained from the HAADF-STEM images. Figure 36c shows the height profile extracted along the red curve in Figure 36b. Based on this height profile (Figure 36c), the NPL overall height is estimated to be 1.4 nm which is consistent with the NPL thickness measured by the HAADF-STEM technique. The truncated width was also estimated to be 1.0 nm. These findings confirm that the atomic terrace seen in the previous NPL sample is also observed in the other sample. The resulting STM topographic images on the two different samples demonstrate the NPLs have a trapezoidal shape. In this work, we did not investigate NPLs with various thicknesses, thus we will not discuss in detail the growth mechanism of NPLs because it is beyond the scope of the thesis. However, the truncated edges of NPLs can be attributed to several factors related to the colloidal synthesis conditions and the intrinsic properties of the material [28], [33]. For example, the balance between thermodynamic and kinetic factors decides the shape of NPLs. The formation of sharp edges is often energetically unfavorable while the truncated edges can minimize the overall surface energy of the NPLs. Under the thermodynamic aspect, the NPLs will prioritize growth in such a way that their surface energy is minimized, which results in truncated edges [34], [35]. Under the kinetic aspect, different growth rates in the lateral direction can also lead to truncated edges.
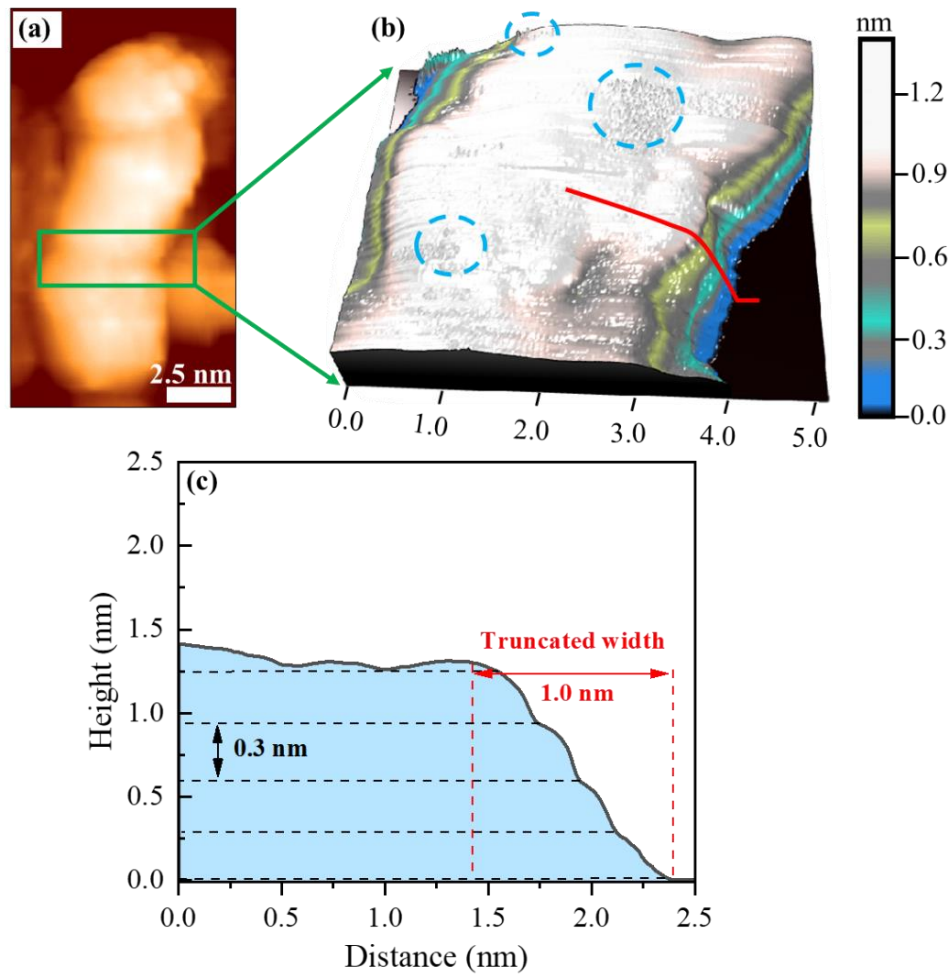
Figure 36: STM measurements on 4.5 ML CdSe NPLs (sample 1). **(a)** STM topographic image of an individual and flat-lying NPL. **(b)** 3D-STM topographic image of a small area on the NPL (Figure a, the green rectangle). **(c)** Height profile extracted along the red curve on the NPL (Figure b). The STM measurements were performed at $V_s = 5$ V, $I_t = 30$ pA, $T = 77$ K, and the number of pixels = 256.

3.3.4. Spatial distribution of surface traps in individual CdSe NPLs

In colloidal NPLs, surface traps typically arise from structural imperfections and unsuccessful ligand passivation [7], [36]. According to our understanding, ligand passivation smoothly occurs on polar (100) surfaces because these surfaces are flat and have the largest area in NPLs, leading to the high coverage of ligands on these surfaces [18], [37]. Additionally, the surface reconstructions also reduce the structural defect density in NPLs [36]. On the other hand, we did not explicitly add any ligands that can passivate Se atoms during the synthesis, thus any exposed Se atoms on the side facets

can lead to the formation of hole traps. Moreover, the irregular edges of NPLs also favor the formation of structural defects and dangling bonds, which contributes to forming more surface traps on the side facets. Therefore, the observation of the truncated edges raises a question about the distribution of surface traps on the side facets of NPLs. To know trap distribution, we used the STM to map the spatial distribution of the tunneling current fluctuations on the sample surface, which is generally acquired at the same time as STM topographic images.
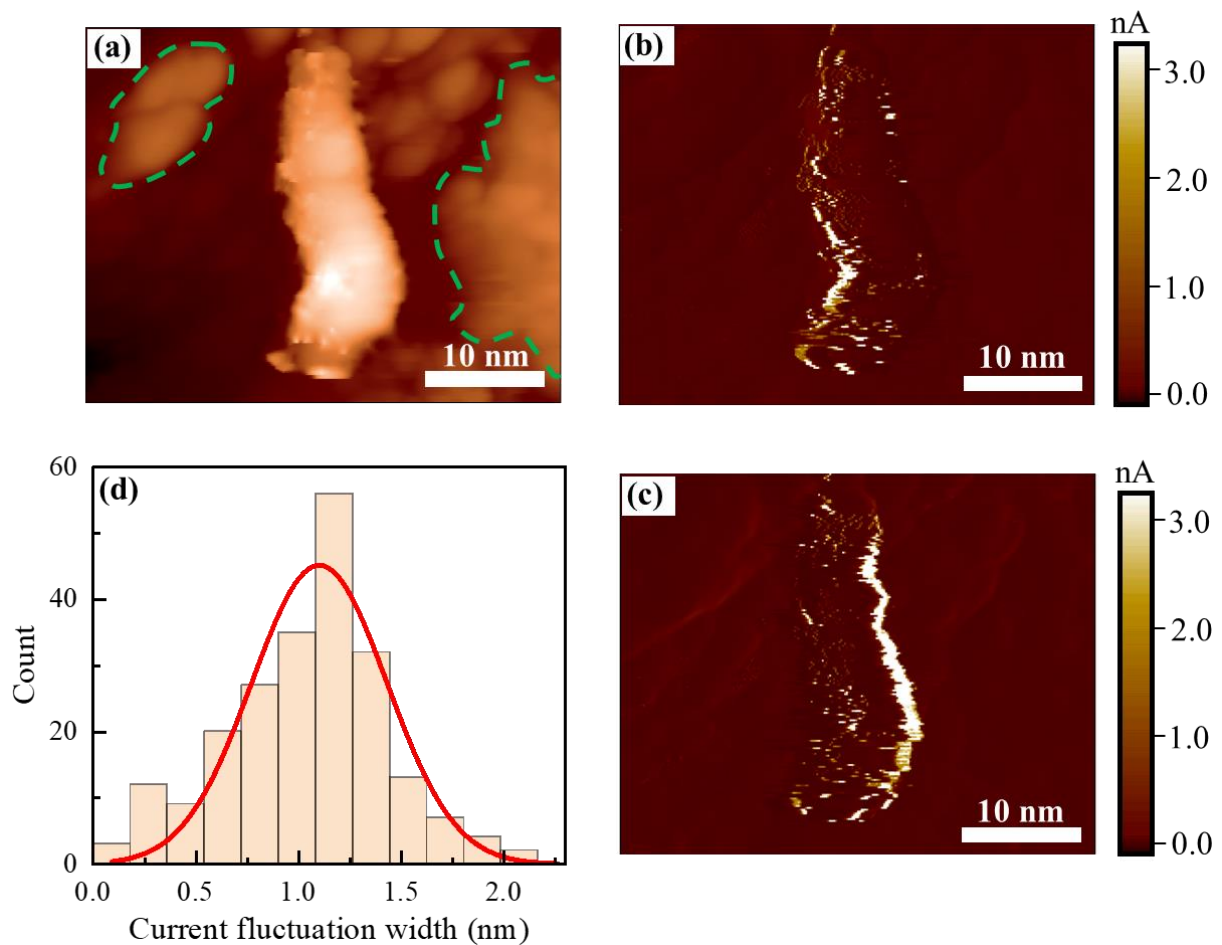
Figure 37: (a) STM topographic image of an isolated and flat-lying CdSe NPL (sample 1). **(b)** Forward and **(c)** Backward tunneling current map extracted from Figure a. **(d)** Statistic on current fluctuation width (W). The STM images were measured at $V_s = 6$ V, $I_t = 30$ pA, the number of pixels = 256, and T = 77 K.

Figure 37a shows an STM topographic image of an isolated and flat-lying NPL. The corresponding STM current-mapping images are presented in Figures 37b and c, which show a strong fluctuation of the tunneling current on the NPL edges, whereas the top

surface exhibits only current fluctuation on some very localized positions. The tunneling current fluctuations can be attributed to the effect of the feedback loop or surface traps in NPLs. Figure 37a shows an uneven gold substrate with very rough regions (dashed-green lines), however, no current fluctuations are observed at these regions in the current mapping images. This indicates that the current fluctuations at the NPL edges are not caused by the effect of the feedback loop. On the other hand, surface traps can capture and release electrons from the STM tip, affecting the tunneling probability of electrons, and thus causing the current fluctuations. Moreover, surface traps can modify the local DOS at the surface, thus when the tip scans over areas with different densities or states, the tunneling current can vary accordingly. To better understand this phenomenon, the width (W) of the current fluctuation at the NPL edges was calculated and presented in Figure 37d. The estimated average width (W) is 1.0 ± 0.3 nm which is consistent with the width of the truncated side facets. In summary, the STM topographic and current mapping images demonstrate the dense presence of surface traps (electron and hole traps) on the side facets and near the edges of NPLs. This is highly related to the truncated edges which expose atomic terraces on the side facets.

3.4. Trapping mechanisms in CdSe NPLs

In this section, I would like to remind why the STM approach is interesting regarding blinking effects caused by trap states compared to optics. In STM, we can find single NPLs and isolate individual traps regarding their spatial and energetic positions. This is very meaningful for studying trapping mechanisms in NPLs.

After having the information on the structural and electronic properties of NPLs, we now turn to the investigation of the trapping mechanism in NPLs. This 3D-STM topographic image in Figure 38a (the inset image) exhibits the truncated edges and localized defects near the edges of a flat-lying NPL. Figure 38a presents the STS measured at the position marked by the red star on the NPL top surface. As this STS was measured at a small bias voltage ($V_s = 1.0$ V), thus the band edges (typically above ± 1.2 V) are not displayed in the tunneling spectroscopy. Instead, an in-gap state is found at around +0.65 V which is attributed to an electron trap state. This electron trap state differs from our previous findings on shallow electron traps (around +1.0 V). This

difference mainly originates from the complex origin of surface traps in NPLs. Theoretically, one demonstrated that Cd (111) and Cd (100) facets give rise to electron traps with different energetic levels in CdSe NCs [38], [39].
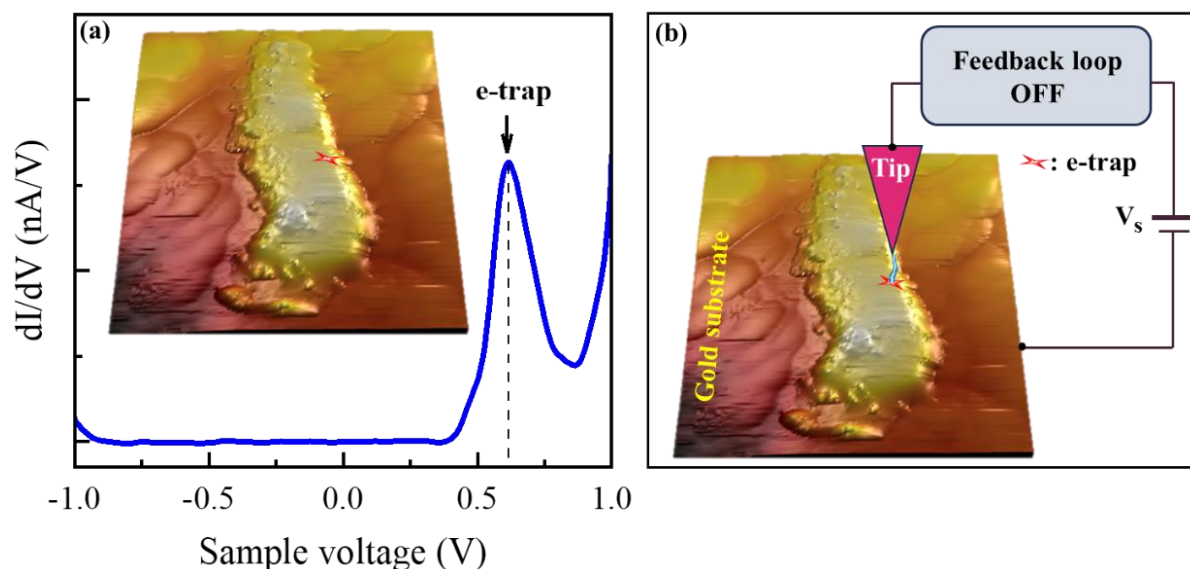
Figure 38: STM/STS measurements on an isolated and flat-lying CdSe NPL (4.5 ML). **(a)** Tunneling dI/dV spectroscopy was measured at the position (the red star) near the NPL edge. The inserted 3D-STM topographic image was extracted from Figure a. The spectroscopy was performed at $V_s = 1$ V, $I_t = 200$ pA, T = 77 K. **(b)** Schematic illustration of the current-time (I (t)) measurement on the NPL.

After knowing the energetic level of the electron trap, the STM tip was kept at the same position where we probed the tunneling spectroscopy (the red star) to investigate the trapping mechanism. The tip is vertically moved closer to the NPL by reducing the bias voltage and increasing the set-point current. Then, the feedback loop is switched off to record the traces of the tunneling current in real-time (Figure 38b). The setting parameters for the I(t) measurement are respectively $V_s = 0.65$ V, $I_t = 500$ pA. Figure 39a presents the traces of current recorded within 12 seconds, revealing a blinking effect similar to photoluminescence (PL) blinking observed in colloidal NCs [9], [10]. The image inset (outlined in green, Figure 39b) shows the blinking traces within a short period (0.7 s) extracted from Figure 39a (the green rectangle). This graph exhibits two different states of the tunneling current, including the ON state (defined as the switching

from the lowest to highest currents), and the OFF state (defined as the switching from the highest to lowest currents).

For PL blinking in colloidal NCs, surface traps cause the ON/OFF events within milliseconds to hours, and their trapping mechanisms are typically investigated by analyzing the probability statistic of ON/OFF events. However, this method may encounter some mistakes related to the parameters including power law exponent (β), and truncation time [40]. Specifically, the power law exponent (β) can vary in a wide range for ON/OFF times, e.g., the exponent varies from 0.85 to 1.4 for the ON time, and from 1.87 to 2.2 for the OFF time in CdSe/CdS core/shell NCs [41], [42]. This is typically due to the complexity of the trapping mechanisms in NCs. On the other hand, the ON/OFF time values strongly depend on the threshold and time binning, thus extracting the truncation time from the ON/OFF time distributions can be ambiguous [43], [44]. To avoid these disadvantages, some alternative methods have been applied to analyze the PL blinking in colloidal NCs, such as the autocorrelation function [45], [46], and power spectral density (PSD) [40], [47]. PSD is a method used in analyzing how the energy of a signal or a time series is distributed with frequency. This method has been demonstrated effective in studying the PL blinking in single QDs (e.g., CdSe, CdSe/CdS core/shell) [46], [47], [48]. Therefore, we believe that the PSD is a powerful method to rapidly characterize the blinking effect in the tunneling current, leading to a better understanding of the trapping mechanism in single NPLs. Figure 39b presents the PSD versus frequency extracted from the I(t) graph in Figure 39a. The PSD seems saturated in low frequencies (below 10 Hz) while it follows a straight line in high frequencies (above 10 Hz), implying a power law dependence. To characterize this complex behavior, the PSD curve is fitted by a stretched Lorentzian function which is written as follows [40]:

$$PSD = \frac{A}{1 + \left(\frac{f}{f_0}\right)^{\beta}} \qquad (3.6)$$

Where A is a constant, and β is the power law exponent. The characteristic frequency (f_0) is given by $f_0 = 1/(2\pi\tau)$, which represents the crossover point between the

saturation and power law. Here, τ is the characteristic time of the current fluctuation. Note that for $\beta = 2$, the above equation gives an ideal Lorentzian function to fit the PSD for a stochastic two-level system (TLS) with a total switching rate of $2\pi\tau = 1/f_0$ [40]. Based on the fitting curve (red) in Figure 39b, we determined an exponent (β) of 2 and a characteristic time (τ) of 17 ms.
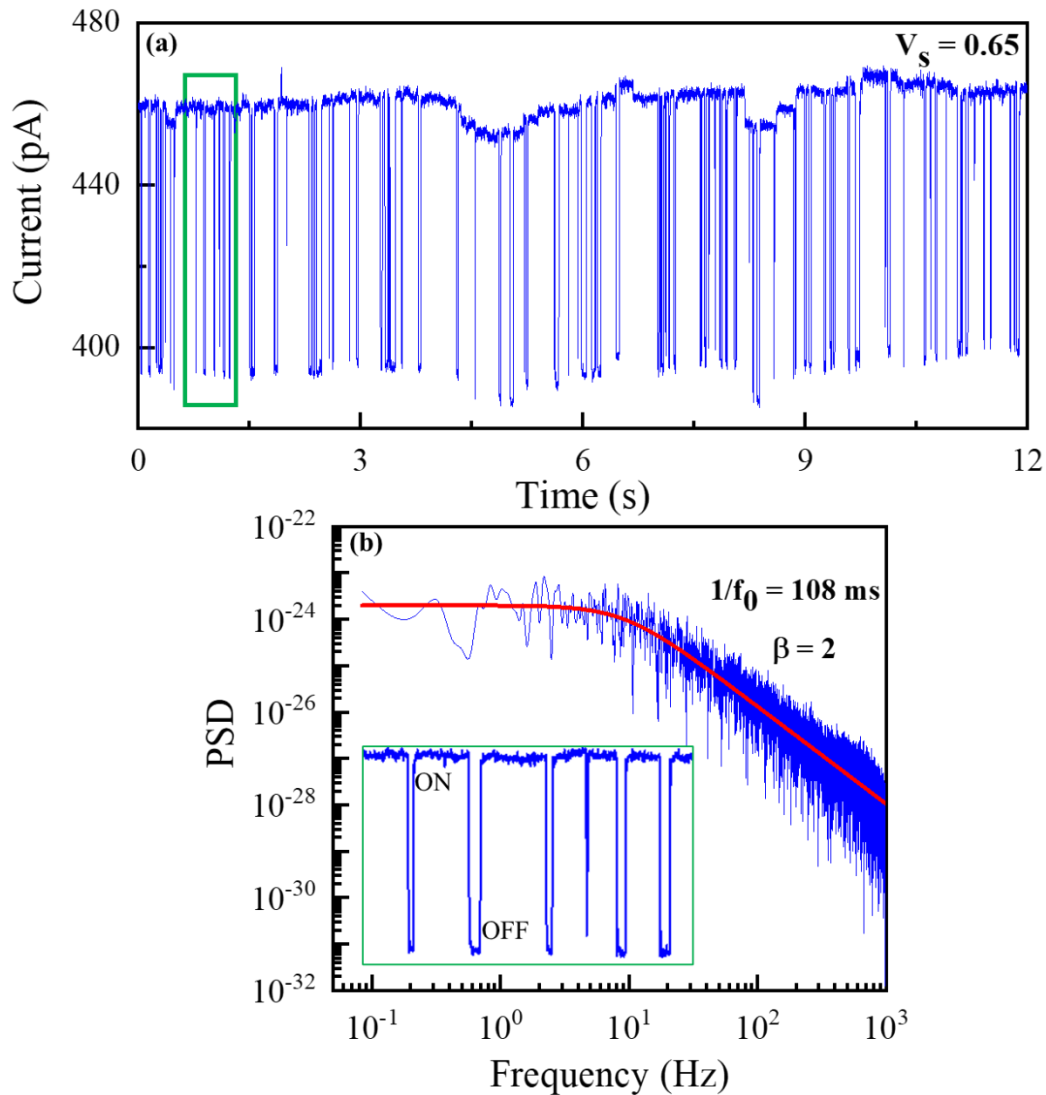
Figure 39: (a) Tunneling current was recorded within 12 seconds. This data was acquired at the setting parameters: $V_s = 0.65$, $I_t = 500$ pA, frequency = 2 KHz, and T = 77 K. Note that, this measurement was performed at the position marked by the red star in **Figure 38**. **(b)** The plot of power spectral density (PSD) versus frequency was extracted from **Figure (a)**. The fitting curve (red) was acquired by fitting the PSD curve with a stretched Lorentzian function. The zoomed-in image outlined in green was extracted from the short period marked by the green rectangle in **Figure (a)**.

To get more evidence of the blinking, the traces of the tunneling current were recorded within 25 seconds at a higher set-point current (I_t = 800 pA) on the same NPL (Figure 38, the red star). Once again, the blinking effect is observed in the tunneling current (see Figure 40a, the inset image extracted from the red rectangle). However, this effect includes the exceeded parts of the tunneling current (Figure 40a, the black arrows). According to our knowledge, these exceeded parts are mainly caused by the influence of noise and tip height [49]. Indeed, our STM measurements were performed at 77 K, thus it is impossible to completely remove the tip drift caused by thermal, resulting in the oscillation of the tunneling current. Figure 40b shows the PSD versus frequency calculated from the I(t) graph in Figure 40a. The PSD was fitted with the same Lorentzian function (Figure 40b, the red curve). As a result, the fitting curve shows an exponent of 2 and a characteristic time of 69 ms. Based on these experimental results, we conclude that a single electron trap behaves as a two-level system (TLS). The inset image in Figure 40b describes a stochastic TLS with the respective transition rates (k_1, k_2) between ON and OFF states. After knowing the trapping mechanism, we will now explain the blinking effect in the tunneling current by integrating the TLS into the STM system. In our I(t) measurements, the STM tip was applied with a bias voltage equal to the voltage of the electron trap state ($V_s = V_{e\text{-trap}}$ = +0.65 V). Under this condition, an electron from the tip is directly injected into the trap state, resulting in a drop in the tunneling current. This trapping process (1) corresponds to the OFF state in the TLS. When an electron de-traps out of the trap state, the electron can tunnel to the gold substrate, resulting in the formation of the tunneling current. In this case, the tunneling current is recovered towards the initial value, and the de-trapping process (2) thus corresponds to the ON state in the TLS (Figure 40c). The repetition of ON/OFF events within a certain time leads to the blinking effect in the tunneling current.
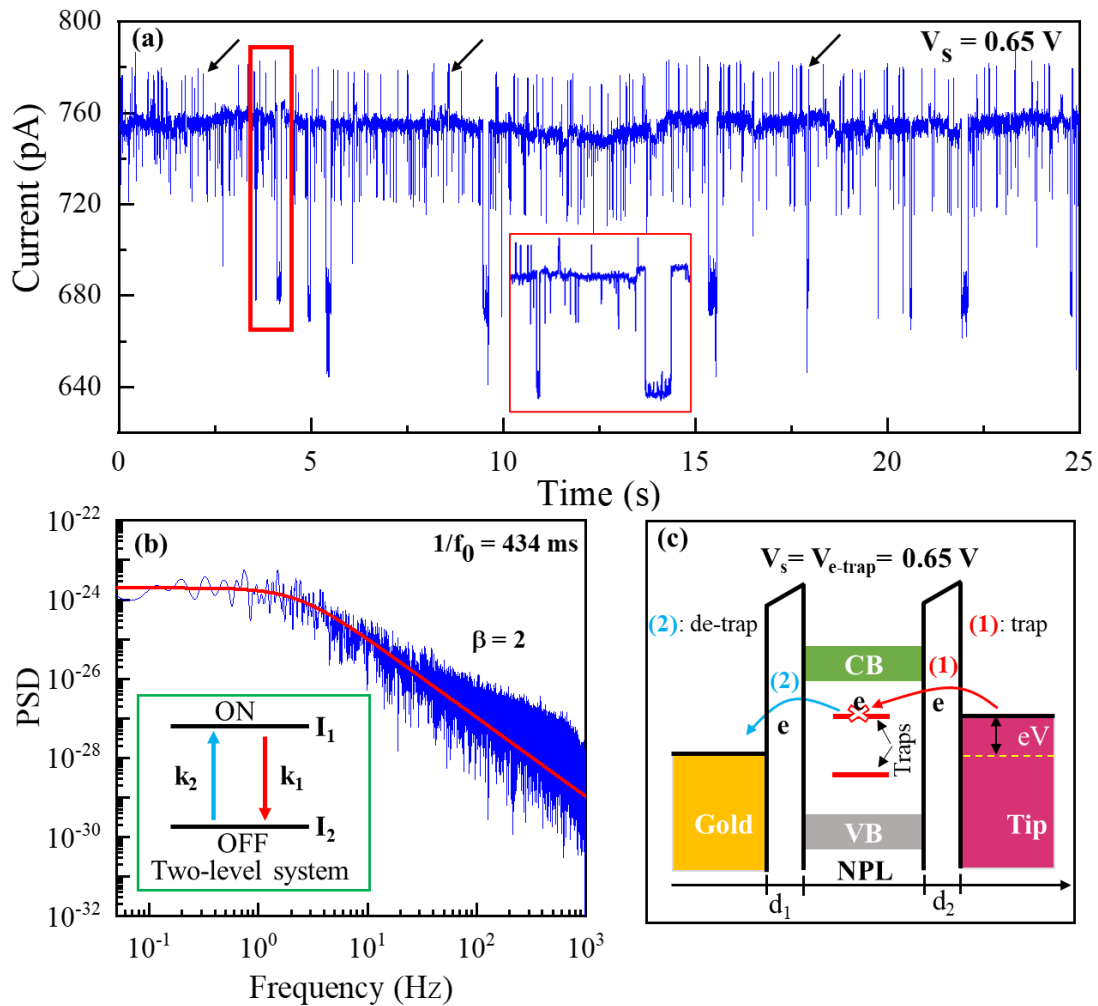
Figure 40: (a) Tunneling current-time (I(t)) graph was recorded within 25 seconds at $V_s = 0.65$, $I_t = 800$ pA, frequency = 2 KHz, and T = 77 K. Note that, this measurement was performed at the same survey position as the previous data. The zoomed-in image (outlined in red) of the I(t) data marked by the red rectangle was inserted into Figure a. **(b)** The corresponding plot of the PSD versus frequency. The inset image (outlined in green) describes a stochastic two-level system (TLS). k_1 and k_2 are the transition rate constants of the ON → OFF states, and vice versa. I_1 and I_2 are the tunneling currents at the ON and OFF states. **(c)** Schematic representation of the tunneling process in STM. The pink and yellow areas represent the occupied states of the tip and gold substrate, respectively. The green and grey areas are the conduction (CB) and valence (VB) bands of the NPL. d_1 and d_2 are the tip-NPL and NPL-substrate distances, respectively. When a positive bias ($V_s = 0.65$ V) is applied to the system, the Fermi level of the tip is shifted by energy (eV) compared to the Fermi level of gold. In this configuration, a symmetric DBTJ is formed between the tip and substrate ($d_1 \approx d_2$).

3.5. Conclusion

In summary, the structural and electronic properties of CdSe NPLs have been investigated by HAADF-STEM and STM/STS techniques. The HAADF-STEM images showed the arrangement of atoms on the top and side facets of NPLs, which provided information on the crystal structure, lattice spacing, and lateral growth direction. Based on the FFT patterns, we confirmed the formation of zinc-blende CdSe NPL with a thickness of 1.4 nm (4.5 ML). The lateral growth direction of NPLs is determined to be the [100] direction coinciding with their length. In addition, the irregular edges of NPLs were also observed in the high-resolution HAADF-STEM images.

STM measurements were performed on individual NPLs to further analyze their morphological properties. The 3D-STM topographic images showed the truncated edges which expose the atomic terraces corresponding to four monolayers forming the NPL thickness. The thickness of each monolayer is estimated to be 3 Å which is very consistent with the (200) lattice spacing determined by the HAADF-STEM technique. Moreover, the STM images also indicated the presence of localized defects near the NPL edges.

Tunneling dI/dV spectra (STS) provided insight into the electronic band structure of CdSe NPLs (4.5 ML), including the band edges, band gap energy (2.7 – 2.8 eV), and in-gap states. Particularly, the STS performed on isolated and flat-lying NPLs revealed that the top surfaces mainly host shallow electron traps likely originating from Cd-dangling bond orbitals and their distribution is random on these facets. Remarkably, the STM current-mapping images showed strong fluctuations of the tunneling current on the NPL edges, implying that most surface traps concentrate on the side facets. Based on the STM topographic and current mapping images, we conclude that the truncated edges cause structural defects and dangling bonds, which favor the formation of surface traps on the side facets of NPLs.

After knowing the energetic level of single electron traps, we performed tunneling current-time (I(t)) measurements to investigate the trapping mechanism in single NPLs. Power spectral density (PSD) was used to characterize such complex blinking effects. As a result, all the PSD curves show a power–law dependence in high frequencies with

an exponent of 2. This result indicated that a single electron trap behaves as a stochastic two-level system (TLS) in single NPLs. Moreover, the PSD analyses also revealed the presence of characteristic times in the range of 17 – 69 ms.

The findings on the trap distribution and the trapezoidal shape of NPLs provided valuable information for improving their optoelectronic properties. Specifically, the truncated edges reflect the important role of optimizing the material synthesis because the truncated edges will create complex interfaces containing surface traps which strongly affect the optical properties of NPL-based heterostructures such as core/crown, and core/shell NPLs. To achieve a high quantum efficiency, it is necessary to remove surface traps on the side facets of CdSe NPLs. The dense presence of trap states on the side facets, including deep hole traps, strengthens the understanding of physical mechanisms governing the optical properties of NPLs, e.g., the formation mechanism of the negatively charged exciton [50], and the PL blinking effect in self-assembly stacked CdSe NPLs [10], which are related to surface traps. Importantly, our all tunneling spectra measured on flat-lying NPL exhibited the electronic band structure with extreme peaks instead of the typical steplike function of the quantum wells. This finding is in good agreement with the study by Peric et al [2], reflecting the complexity of the true nature of NPLs.

Bibliography

[1]   M. D. Tessier, C. Javaux, I. Maksimovic, V. Loriette, and B. Dubertret, "Spectroscopy of Single CdSe Nanoplatelets," *ACS Nano*, vol. 6, no. 8, pp. 6751–6758, 2012, doi: 10.1021/nn3014855.

[2]   N. Peric *et al.*, "Van Hove Singularities and Trap States in Two-Dimensional CdSe Nanoplatelets," *Nano Lett.*, vol. 21, no. 4, pp. 1702–1708, Feb. 2021, doi: 10.1021/acs.nanolett.0c04509.

[3]   A. Di Giacomo, C. Rodà, A. H. Khan, and I. Moreels, "Colloidal Synthesis of Laterally Confined Blue-Emitting 3.5 Monolayer CdSe Nanoplatelets," *Chem. Mater.*, vol. 32, no. 21, pp. 9260–9267, Nov. 2020, doi: 10.1021/acs.chemmater.0c03066.

[4]   A. W. Achtstein, A. Antanovich, A. Prudnikau, R. Scott, U. Woggon, and M. Artemyev, "Linear Absorption in CdSe Nanoplates: Thickness and Lateral Size Dependency of the Intrinsic Absorption," *J. Phys. Chem. C*, vol. 119, no. 34, pp. 20156–20161, Aug. 2015, doi: 10.1021/acs.jpcc.5b06208.

[5]   C. She *et al.*, "Low-Threshold Stimulated Emission Using Colloidal Quantum Wells," *Nano Lett.*, vol. 14, no. 5, pp. 2772–2777, May 2014, doi: 10.1021/nl500775p.

[6]   S. Christodoulou *et al.*, "Chloride-Induced Thickness Control in CdSe Nanoplatelets," *Nano Lett.*, vol. 18, no. 10, pp. 6248–6254, 2018, doi: 10.1021/acs.nanolett.8b02361.

[7]   S. O. M. Hinterding *et al.*, "Single Trap States in Single CdSe Nanoplatelets," *ACS Nano*, vol. 15, no. 4, pp. 7216–7225, 2021, doi: 10.1021/acsnano.1c00481.

[8]   W. D. Kim *et al.*, "Role of Surface States in Photocatalysis: Study of Chlorine-Passivated CdSe Nanocrystals for Photocatalytic Hydrogen Generation," *Chem. Mater.*, vol. 28, no. 3, pp. 962–968, Feb. 2016, doi: 10.1021/acs.chemmater.5b04790.

[9]   S. Irgen-Gioro, Y. Wu, R. López-Arteaga, S. Padgaonkar, J. N. Olding, and E. A.

Weiss, "Evidence for Two Time Scale-Specific Blinking Mechanisms in Room-Temperature Single Nanoplatelets," *J. Phys. Chem. C*, vol. 125, no. 24, pp. 13485–13492, Jun. 2021, doi: 10.1021/acs.jpcc.1c03784.

[10] Z. Ouzit *et al.*, "FRET-Mediated Collective Blinking of Self-Assembled Stacks of CdSe Semiconducting Nanoplatelets," *ACS Photonics*, vol. 10, no. 2, pp. 421–429, Feb. 2023, doi: 10.1021/acsphotonics.2c01441.

[11] I. du Fossé, S. ten Brinck, I. Infante, and A. J. Houtepen, "Role of Surface Reduction in the Formation of Traps in n-Doped II–VI Semiconductor Nanocrystals: How to Charge without Reducing the Surface," *Chem. Mater.*, vol. 31, no. 12, pp. 4575–4583, Jun. 2019, doi: 10.1021/acs.chemmater.9b01395.

[12] S. Pokrant and K. B. Whaley, "Tight-binding studies of surface effects on electronic structure of CdSe nanocrystals: the role of organic ligands, surface reconstruction, and inorganic capping shells," *Eur. Phys. J. D - At. Mol. Opt. Plasma Phys.*, vol. 6, no. 2, pp. 255–267, 1999, doi: 10.1007/s100530050307.

[13] B. Ji *et al.*, "Dielectric Confinement and Excitonic Effects in Two-Dimensional Nanoplatelets," *ACS Nano*, vol. 14, no. 7, pp. 8257–8265, Jul. 2020, doi: 10.1021/acsnano.0c01950.

[14] W. Banerjee, Q. Liu, and H. Hwang, "Engineering of defects in resistive random access memory devices," *J. Appl. Phys.*, vol. 127, no. 5, p. 51101, Feb. 2020, doi: 10.1063/1.5136264.

[15] M. Olutas, B. Guzelturk, Y. Kelestemur, A. Yeltik, S. Delikanli, and H. V. Demir, "Lateral Size-Dependent Spontaneous and Stimulated Emission Properties in Colloidal CdSe Nanoplatelets," *ACS Nano*, vol. 9, no. 5, pp. 5041–5050, May 2015, doi: 10.1021/acsnano.5b01927.

[16] G. H. V Bertrand, A. Polovitsyn, S. Christodoulou, A. H. Khan, and I. Moreels, "Shape control of zincblende CdSe nanoplatelets," *Chem. Commun.*, vol. 52, no. 80, pp. 11975–11978, 2016, doi: 10.1039/C6CC05705E.

[17] C. Zhu *et al.*, "Facet-Dependent On-Surface Reactions in the Growth of CdSe

Nanoplatelets," *Angew. Chemie Int. Ed.*, vol. 58, no. 49, pp. 17764–17770, Dec. 2019, doi: https://doi.org/10.1002/anie.201909576.

[18] D.-E. Yoon *et al.*, "Atomistics of Asymmetric Lateral Growth of Colloidal Zincblende CdSe Nanoplatelets," *Chem. Mater.*, vol. 33, no. 12, pp. 4813–4820, 2021, doi: 10.1021/acs.chemmater.1c00563.

[19] Y. Deng, X. Chen, J. Liang, and Y. Wang, "Triethyl-Borates as Surfactants to Stabilize Semiconductor Nanoplatelets in Polar Solvents and to Tune Their Optical Properties ," *Frontiers in Chemistry* , vol. 10. 2022. [Online]. Available: https://www.frontiersin.org/articles/10.3389/fchem.2022.860781

[20] A. Antanovich, A. Prudnikau, A. Matsukovich, A. Achtstein, and M. Artemyev, "Self-Assembly of CdSe Nanoplatelets into Stacks of Controlled Size Induced by Ligand Exchange," *J. Phys. Chem. C*, vol. 120, no. 10, pp. 5764–5775, 2016, doi: 10.1021/acs.jpcc.5b12139.

[21] J. C. van der Bok *et al.*, "In Situ Optical and X-ray Spectroscopy Reveals Evolution toward Mature CdSe Nanoplatelets by Synergetic Action of Myristate and Acetate Ligands," *J. Am. Chem. Soc.*, vol. 144, no. 18, pp. 8096–8105, May 2022, doi: 10.1021/jacs.2c00423.

[22] L. Jdira, P. Liljeroth, E. Stoffels, D. Vanmaekelbergh, and S. Speller, "Size-dependent single-particle energy levels and interparticle Coulomb interactions in CdSe quantum dots measured by scanning tunneling spectroscopy," *Phys. Rev. B*, vol. 73, no. 11, p. 115305, Mar. 2006, doi: 10.1103/PhysRevB.73.115305.

[23] B. Alperson, I. Rubinstein, G. Hodes, D. Porath, and O. Millo, "Energy level tunneling spectroscopy and single electron charging in individual CdSe quantum dots," *Appl. Phys. Lett.*, vol. 75, no. 12, pp. 1751–1753, Sep. 1999, doi: 10.1063/1.124808.

[24] T. H. Nguyen *et al.*, "Charge carrier identification in tunneling spectroscopy of core-shell nanocrystals," *Phys. Rev. B*, vol. 84, no. 19, p. 195133, Nov. 2011, doi: 10.1103/PhysRevB.84.195133.

[25] I. Swart, P. Liljeroth, and D. Vanmaekelbergh, "Scanning probe microscopy and spectroscopy of colloidal semiconductor nanocrystals and assembled structures," *Chem. Rev.*, vol. 116, no. 18, pp. 11181–11219, Sep. 2016, doi: 10.1021/acs.chemrev.5b00678.

[26] A. J. Houtepen, Z. Hens, J. S. Owen, and I. Infante, "On the Origin of Surface Traps in Colloidal II–VI Semiconductor Nanocrystals," *Chem. Mater.*, vol. 29, no. 2, pp. 752–761, Jan. 2017, doi: 10.1021/acs.chemmater.6b04648.

[27] P. Liljeroth, B. Grandidier, C. Delerue, and D. Vanmaekelbergh, "Scanning Probe Microscopy and Spectroscopy BT - Nanoparticles: Workhorses of Nanoscience," C. de Mello Donegá, Ed., Berlin, Heidelberg: Springer Berlin Heidelberg, 2014, pp. 223–255. doi: 10.1007/978-3-662-44823-6_8.

[28] A. Riedinger *et al.*, "An intrinsic growth instability in isotropic materials leads to quasi-two-dimensional nanoplatelets," *Nat. Mater.*, vol. 16, no. 7, pp. 743–748, 2017, doi: 10.1038/nmat4889.

[29] S. Ithurria, G. Bousquet, and B. Dubertret, "Continuous Transition from 3D to 1D Confinement Observed during the Formation of CdSe Nanoplatelets," *J. Am. Chem. Soc.*, vol. 133, no. 9, pp. 3070–3077, Mar. 2011, doi: 10.1021/ja110046d.

[30] F. D. Ott *et al.*, "Ripening of Semiconductor Nanoplatelets," *Nano Lett.*, vol. 17, no. 11, pp. 6870–6877, Nov. 2017, doi: 10.1021/acs.nanolett.7b03191.

[31] Y. Chen, D. Chen, Z. Li, and X. Peng, "Symmetry-Breaking for Formation of Rectangular CdSe Two-Dimensional Nanocrystals in Zinc-Blende Structure," *J. Am. Chem. Soc.*, vol. 139, no. 29, pp. 10009–10019, Jul. 2017, doi: 10.1021/jacs.7b04855.

[32] N. Castro *et al.*, "Insights into the Formation Mechanism of CdSe Nanoplatelets Using in Situ X-ray Scattering," *Nano Lett.*, vol. 19, no. 9, pp. 6466–6474, Sep. 2019, doi: 10.1021/acs.nanolett.9b02687.

[33] N. T. K. Thanh, N. Maclean, and S. Mahiddine, "Mechanisms of Nucleation and Growth of Nanoparticles in Solution," *Chem. Rev.*, vol. 114, no. 15, pp. 7610–

7630, Aug. 2014, doi: 10.1021/cr400544s.

[34] M. A. Lovette, A. R. Browning, D. W. Griffin, J. P. Sizemore, R. C. Snyder, and M. F. Doherty, "Crystal Shape Engineering," *Ind. Eng. Chem. Res.*, vol. 47, no. 24, pp. 9812–9833, Dec. 2008, doi: 10.1021/ie800900f.

[35] R. C. R. Makoto Ohara, *Modeling crystal growth rates from solution*. [Online]. Available: https://cir.nii.ac.jp/crid/1572261549706559104

[36] S. Singh *et al.*, "Colloidal CdSe Nanoplatelets, A Model for Surface Chemistry/Optoelectronic Property Relations in Semiconductor Nanocrystals," *J. Am. Chem. Soc.*, vol. 140, no. 41, pp. 13292–13300, Oct. 2018, doi: 10.1021/jacs.8b07566.

[37] J. Zhang *et al.*, "Identification of Facet-Dependent Coordination Structures of Carboxylate Ligands on CdSe Nanocrystals," *J. Am. Chem. Soc.*, vol. 141, no. 39, pp. 15675–15683, Oct. 2019, doi: 10.1021/jacs.9b07836.

[38] O. Voznyy and E. H. Sargent, "Atomistic Model of Fluorescence Intermittency of Colloidal Quantum Dots," *Phys. Rev. Lett.*, vol. 112, no. 15, p. 157401, Apr. 2014, doi: 10.1103/PhysRevLett.112.157401.

[39] I. du Fossé, S. C. Boehme, I. Infante, and A. J. Houtepen, "Dynamic Formation of Metal-Based Traps in Photoexcited Colloidal Quantum Dots and Their Relevance for Photoluminescence," *Chem. Mater.*, vol. 33, no. 9, pp. 3349–3358, May 2021, doi: 10.1021/acs.chemmater.1c00561.

[40] S. Seth *et al.*, "Presence of Maximal Characteristic Time in Photoluminescence Blinking of MAPbI$_3$ Perovskite," *Adv. Energy Mater.*, vol. 11, no. 44, p. 2102449, Nov. 2021, doi: https://doi.org/10.1002/aenm.202102449.

[41] H. Chung, K.-S. Cho, W.-K. Koh, D. Kim, and J. Kim, "Composition-dependent trap distributions in CdSe and InP quantum dots probed using photoluminescence blinking dynamics," *Nanoscale*, vol. 8, no. 29, pp. 14109–14116, 2016, doi: 10.1039/C5NR09291D.

[42] O. Chen *et al.*, "Compact high-quality CdSe–CdS core–shell nanocrystals with

narrow emission linewidths and suppressed blinking," *Nat. Mater.*, vol. 12, no. 5, pp. 445–451, 2013, doi: 10.1038/nmat3539.

[43] N. Amecke, A. Heber, and F. Cichos, "Distortion of power law blinking with binning and thresholding," *J. Chem. Phys.*, vol. 140, no. 11, p. 114306, Mar. 2014, doi: 10.1063/1.4868252.

[44] J. Geordy, L. J. Rogers, C. M. Rogers, T. Volz, and A. Gilchrist, "Bayesian estimation of switching rates for blinking emitters," *New J. Phys.*, vol. 21, no. 6, p. 63001, 2019, doi: 10.1088/1367-2630/ab1dfd.

[45] J. J. Glennon, R. Tang, W. E. Buhro, and R. A. Loomis, "Synchronous Photoluminescence Intermittency (Blinking) along Whole Semiconductor Quantum Wires," *Nano Lett.*, vol. 7, no. 11, pp. 3290–3295, Nov. 2007, doi: 10.1021/nl0714583.

[46] M. Pelton, G. Smith, N. F. Scherer, and R. A. Marcus, "Evidence for a diffusion-controlled mechanism for fluorescence blinking of colloidal quantum dots," *Proc. Natl. Acad. Sci.*, vol. 104, no. 36, pp. 14249–14254, Sep. 2007, doi: 10.1073/pnas.0706164104.

[47] P. A. Frantsuzov, S. Volkán-Kacsó, and B. Jankó, "Universality of the Fluorescence Intermittency in Nanoscale Systems: Experiment and Theory," *Nano Lett.*, vol. 13, no. 2, pp. 402–408, Feb. 2013, doi: 10.1021/nl3035674.

[48] M. Pelton, D. G. Grier, and P. Guyot-Sionnest, "Characterizing quantum-dot blinking using noise power spectra," *Appl. Phys. Lett.*, vol. 85, no. 5, pp. 819–821, Aug. 2004, doi: 10.1063/1.1779356.

[49] S. Zhang, D. Huang, and S. Wu, "A cryogen-free low temperature scanning tunneling microscope capable of inelastic electron tunneling spectroscopy," *Rev. Sci. Instrum.*, vol. 87, no. 6, p. 63701, Jun. 2016, doi: 10.1063/1.4952577.

[50] A. F. Vong, S. Irgen-Gioro, Y. Wu, and E. A. Weiss, "Origin of Low Temperature Trion Emission in CdSe Nanoplatelets," *Nano Lett.*, vol. 21, no. 23, pp. 10040–10046, 2021, doi: 10.1021/acs.nanolett.1c03726.

Chapter IV: Effect Of Surface Dangling Bond Spins On Polarized Emission In CdSe And CdSe/CdS Core/Crown Nanoplatelets

Abstract

Magneto-optical effects in colloidal semiconductor nanocrystals, such as cadmium selenide (CdSe) nanoplatelets (NPLs), are critical for optoelectronic [1], [2], and magnetic [3], [4] applications due to their ability to respond to both magnetic fields and light. In NPLs, the interplay between the electronic and magnetic properties gives rise to the phenomenon, where the polarization state or intensity of light is altered in the presence of magnetic fields [5], [6], [7]. Most interestingly, CdSe NPLs exhibit surface magnetism caused by surface dangling bonds (DBs). The spins of surface DBs have been demonstrated to affect the polarized emission in NPLs at cryogenic temperatures via their interaction with the dark excitons [5], [8]. However, a critical question has not been clarified, which is how surface DBs on different surfaces of NPLs influence their emission properties. Therefore, knowing the distribution of surface DBs in NPLs will clarify two key issues: (1) the interactions between the electron wavefunctions and the surface DB spins, and (2) which surface DBs mainly affect the emission properties of NPLs. In this work, we employed magneto-PL spectroscopy to probe the polarized emission in CdSe and CdSe/CdS core/crown NPLs at cryogenic temperatures. The role of surface DB spins is evaluated by analyzing the degree of circular polarization (DCP) of exciton and trion emission. We demonstrated that the DB-dark exciton spin interaction is responsible for the nonlinear magnetic field dependency of the exciton DCP in CdSe NPLs. On the other hand, growing the CdS crown around the CdSe core NPLs significantly changes the DB-dark exciton spin interactions, leading to a change in the DCP behavior. Particularly, CdSe/CdS core/smallest crown NPLs exhibit an exciton DCP behavior similar to the bare CdSe NPLs, but the magnitude of the polarization is significantly increased. On the contrary, when the crown size becomes large, the exciton DCP decreases linearly on increasing magnetic fields. This indicates that dangling bond spins on the side facets of NPLs play a major role in shaping magneto-optical effects in CdSe NPLs, particularly in the dangling bond spin-assisted recombination of dark excitons. Meanwhile, all the NPL sample exhibits the negative

DCP values of trion emission depending on external magnetic fields, indicating the formation of negatively charged excitons (negative trions) in NPLs. In addition, we also observed the linear dependency of the spin-relaxation time on magnetic fields in CdSe/CdS core/giant crown NPLs.

Graphic abstract: Schematic illustration of the DB spin-assisted recombination of dark excitons in CdSe NPLs at cryogenic temperatures. The DB-electron spin interactions are responsible for the non-monotonous DCP of the dark exciton in NPLs.
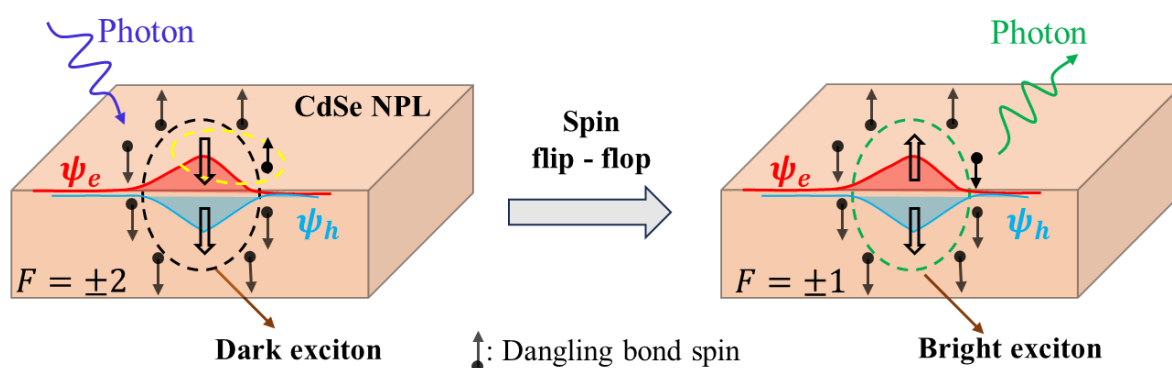
4.1. Introduction

In addition to size, the surface of CdSe NCs is also an important characteristic that strongly affects their optoelectronic properties. Indeed, the NC surface typically contains dangling bonds (DBs) of under-coordinated atoms responsible for forming surface traps [9], [10], [11]. In colloidal synthesis, organic ligands are added to the reaction bath to passivate the surface of NCs and quench the reaction. However, not all dangling bonds (DBs) are passivated during the synthesis due to a lattice mismatch and weak interaction between bulky ligands with the atomic planes of NCs. Surface magnetism in CdSe NCs can be induced via the effective transfer of electrons from Cd-4d orbitals to surface ligands, to which the unpassivated DB spins can also contribute [4].

Surface magnetism is interesting because it relates to magneto-optical effects observed in CdSe NCs. The exciton band edge of CdSe is split into five sub-energy levels due to the shape asymmetry, intrinsic field, and electron-hole interaction [12]. This splitting is significantly enhanced by the quantum confinement effect in NCs. As a consequence, the two lowest levels correspond to the bright ($F_z = \pm 1$) and dark ($F_z = \pm 2$) excitons. Theoretically, the dark excitons are optically forbidden states within the electric dipole approximation [13]. However, increasing theoretical and experimental studies suggest that the dark excitons can contribute to the radiative recombination at low temperatures in CdSe NCs by mixing with the bright exciton states, for example, via phonons [13], external magnetic field, and dangling bond spins [8], [14], [15], [16]. Among these processes, the radiative recombination of dark excitons via dangling bond spins has raised curiosity about how surface DB spins interact with excitons in NCs. In 2015, Rodina and co-workers theoretically predicted that surface DB spins can interact with an electron spin localized in the NC, resulting in the radiative recombination of dark excitons [8]. This mechanism was also demonstrated in the recent study by Shornikova et al when they investigated the polarized emission in CdSe NPLs at cryogenic temperatures by magneto-PL spectroscopy [5]. This finding confirmed the surface magnetism in CdSe NPLs. However, the authors did not mention the spatial distribution of unpassivated dangling bonds in NPLs. This is very important because the NPLs have

a large surface area and well-defined surfaces upon their orientation. Therefore, the nature and number of dangling bonds differ on each surface. Knowing the distribution and contribution of dangling bonds on each specific surface will provide valuable information about the magnetic and optical properties of CdSe NPLs.

Here, we study the magneto-optical properties of 4.5 ML CdSe NPLs (sample 1), which stem from the spin interaction between surface DBs and excitons. To further investigate the dangling bond distribution, 4.5 ML CdSe/CdS core/crown NPLs with various crown sizes were synthesized based on the same CdSe NPLs. This manipulation is to passivate dangling bonds on the side facets of CdSe NPLs. The magneto-optical properties of these core/crown NPL samples are compared to the bare NPL sample. For the above targets, we performed PL spectroscopy in an external magnetic field (up to 15 Tesla) at cryogenic temperatures (down to 4.2 K).

4.2. Recombination mechanisms of dark excitons in CdSe nanocrystals, followed by CdSe nanoplatelets.

4.2.1. Bright & Dark excitons in CdSe nanocrystals

As mentioned previously, CdSe NCs have a fine exciton structure where the exciton energy is split into five sub-energy levels. The two lowest levels correspond to the bright and dark excitons. The bright exciton with a total angular momentum of 1 (projection: $F_z = \pm 1$, 1^L) is denoted as $|A\rangle$ while the dark exciton is denoted as $|F\rangle$ having a total angular momentum of 2 (projection: $F_z = \pm 2$). Figure 41 shows the exciton energy level in CdSe NCs. In bulk CdSe, the bright-dark exciton splitting is very small ($\Delta E_{AF} = 0.13$ meV), thus inhibiting the observation of dark exciton due to Boltzmann factors [13], [17]. In contrast, the exciton splitting energy is a few meV in CdSe NCs such as ΔE_{AF} = 19 meV (CdSe QDs) [13], ΔE_{AF} = 6 meV (3ML CdSe NPLs) [18], which is larger than thermal energy $k_B T$ at cryogenic temperature. Therefore, excited electrons at the bright excitonic state will relax to the dark exciton state before returning to the ground state with a recombination rate Γ_F and emitting photons (Figure 41). This implies that it is possible to observe the dark excitons in CdSe NCs. Indeed, previous experimental studies demonstrated that the dark exciton recombination in CdSe NCs occurs through two main mechanisms: (1) phonon-assisted recombination [13], and (2) dangling bond

spin-assisted recombination [16]. These recombination mechanisms were also found in CdSe NPLs [5], [18]. In the scope of the thesis, we will present the general content of the recombination mechanisms of dark excitons in CdSe NCs before discussing the case of CdSe NPLs.
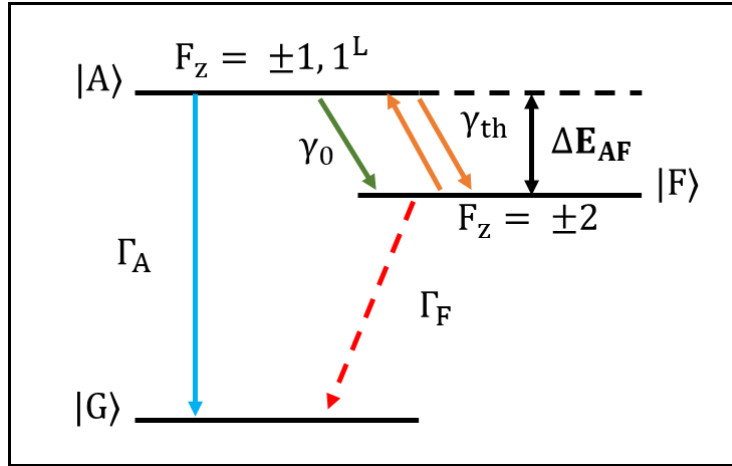
Figure 41: Schematic illustration of the exciton fine structure in CdSe NCs. Note that only the two lowest energy levels of excitons are considered in this schematic. $|A\rangle$ and $|F\rangle$ are the bright and dark excitons. $|G\rangle$ is the ground state. Γ_A, Γ_F are the bright and dark exciton recombination rates, γ_0 is the relaxation rate from the bright exciton to the dark exciton, $\gamma_{th} = \gamma_0 N_B$ is the thermal activation rate of the reverse process. N_B is the Bose-Einstein phonon occupation.

4.2.2. Phonon-assisted recombination of dark excitons in CdSe nanocrystals

In the electric dipole approximation, the dark excitons are optically forbidden states because their total angle momentum projection is ±2 while a photon can only carry a momentum projection of ±1. To address this issue, particles and quasi-particles are considered to add to the dark exciton states. Among them, quasi-particle phonons, known as the quanta of atomic vibrations around their equilibrium positions in a crystal lattice, are the best candidates to address the conservation law of angular momentum. Since phonons are easily populated or depopulated by increasing or decreasing temperatures, the NCs exhibit the characteristic dependency of the PL decay on temperatures [18], [19].

Chapter IV: Surface Dangling Bond Spins

Experimentally, the radiative recombination process has been studied using optical spectroscopy techniques such as temperature-dependent PL spectroscopy, time-resolved PL decay, and spectrally-resolved PL decay [18], [20]. The PL intensity can be written as follows:

$$I(t) = \eta_A \Gamma_A \rho_A + \eta_F \Gamma_F \rho_F \tag{4.1}$$

Where η_A and η_F are the corresponding quantum efficiencies. ρ_A and ρ_F are the occupation numbers of the bright and dark exciton states. γ_0 is the relaxation rate from the $|A\rangle$ to $|F\rangle$ states at zero temperature, and $\gamma_0 = \gamma_{th} N_B$ is the thermal activation rate of the reverse process (Figure 41). The Bose-Einstein phonon occupation is given by: $N_B = [\exp(\Delta E_{AF}/k_B T) - 1]^{-1}$, where k_B is the Boltzmann constant, and T is the temperature. If γ_0, Γ_A, and Γ_F are the temperature-independent parameters, we can use rate equations to derive the populations of the bright and dark excitons [18].

$$\frac{d\rho_A}{dt} = -[\Gamma_A + \gamma_0(N_B + 1)]\rho_A + \gamma_0 N_B \rho_F \tag{4.2}$$

$$\frac{d\rho_F}{dt} = -[\Gamma_F + \gamma_0 N_B]\rho_F + \gamma_0(N_B + 1)\rho_A \tag{4.3}$$

The solutions of the above equation are [19]

$$\rho_A = C_1 e^{-t\Gamma_{sh}} + C_2 e^{-t\Gamma_L} \tag{4.4}$$

$$\rho_F = C_3 e^{-t\Gamma_{sh}} + C_4 e^{-t\Gamma_L} \tag{4.5}$$

Here, Γ_L and Γ_{Sh} are the decay rates of the long and short components. After absorption a non-resonant laser pulse and exciton energy relaxation, $|A\rangle$ and $|F\rangle$ states are populated equally at $t = 0$ which leads to the condition: $\rho_A(t = 0) = \rho_F(t = 0) = 0.5$ [20]. Therefore, the temperature-dependent decay rates (Γ_L, Γ_{sh}) can be induced from the above solutions [20].

$$\Gamma_{sh,L} = \frac{1}{2}[\Gamma_A + \Gamma_F + \gamma_0 \coth(\frac{\Delta E_{AF}}{2k_B T}) \pm \sqrt{(\Gamma_A - \Gamma_F + \gamma_0)^2 + \gamma_0^2 \sinh^{-2}(\frac{\Delta E_{AF}}{2k_B T})}] \tag{4.6}$$

The "+" sign before the square root in the above formula corresponds to $\Gamma_{sh} = (\tau_{sh})^{-1}$, and the "−" sign is for $\Gamma_L = (\tau_L)^{-1}$. The condition: $\rho_A(t = 0) = \rho_F(t = 0) = 0.5$ also leads to the temperature-dependent parameters C_1, C_3 as follows:

$$C_1 = \frac{\gamma_0 + \Gamma_A - \Gamma_L}{2(\Gamma_{Sh} - \Gamma_L)} \tag{4.7}$$

$$C_3 = \frac{-\gamma_0 + \Gamma_F - \Gamma_L}{2(\Gamma_{Sh} - \Gamma_L)} \tag{4.8}$$

Inserting C_1 and C_3 into equation (4.1), we will obtain:

$$I(t) = [\eta_A \Gamma_A C_1 + \eta_F \Gamma_F C_3] e^{-t\Gamma_{sh}} + [\eta_A \Gamma_A (0.5 - C_1) + \eta_F \Gamma_F (0.5 - C_3)] e^{-t\Gamma_L} \tag{4.9}$$

The above formula represents a biexponential dependency of PL intensity at cryogenic temperatures in colloidal NCs. Immediately, after a nonresonant photoexcitation and exciton energy relaxation [21], only the bright exciton contributes to the photoluminescence (PL) due to its fast recombination rate ($\Gamma_A \gg \Gamma_F$). Therefore, the short component of the PL decay is determined by the recombination of bright excitons and the exciton relaxation from the upper bright exciton state to the dark exciton state, occurring at a rate of $\gamma_0(1 + N_B)$. To better understand the phonon-assisted recombination of dark excitons in CdSe NPLs, we referred to the study by Shornikova et al [18] in which they measured the time-resolved PL decay at various temperatures, (Figure 42a). At temperatures below 7 K, such that $\Delta E_{AF} \gg k_B T$ (k_B: the Boltzmann constant) the PL decay shows a bi-exponential behavior with a short component decay occurring within less than ns compared to a long component decay. The rates of the short (Γ_{sh}) and long (Γ_L) component decay is defined as shown in equation (4.6). When the temperature is increased (T > 10 K), the short component decay decreases in amplitude and vanishes when the temperature exceeds 30 K. When $\Delta E_{AF} \ll k_B T$ (at elevated temperatures), the PL decay is mono-exponential with $\Gamma_L = (\Gamma_A + \Gamma_F)/2$. At longer delays, the emission only comes from the dark exciton with the long component decay rate $\Gamma_L = \Gamma_F$ and $\Gamma_{sh} = \Gamma_A + \gamma_0$. Inserting $\gamma_0 = \Gamma_{sh}$ (2 K) $- \Gamma_A$ into equation (4.6), the temperature-dependent Γ_L curve can be fitted as shown in Figure 42b, according to Shornikova et al [18]. The recombination rate of the bright exciton (Γ_A) and the bright-dark exciton splitting energy (ΔE_{AF}) can be extracted from the fitting curves. In

summary, the time-resolved PL decay is a method for studying the exciton recombination dynamics in NPLs at low temperatures. Specifically, the fast component decay is attributed to the bright exciton recombination with a rate Γ_A and the rapid thermal relaxation of excitons ($|A\rangle \rightarrow |F\rangle$ states). The long-component decay originates from the radiative recombination of dark excitons assisted by phonons [13], [19], [20].
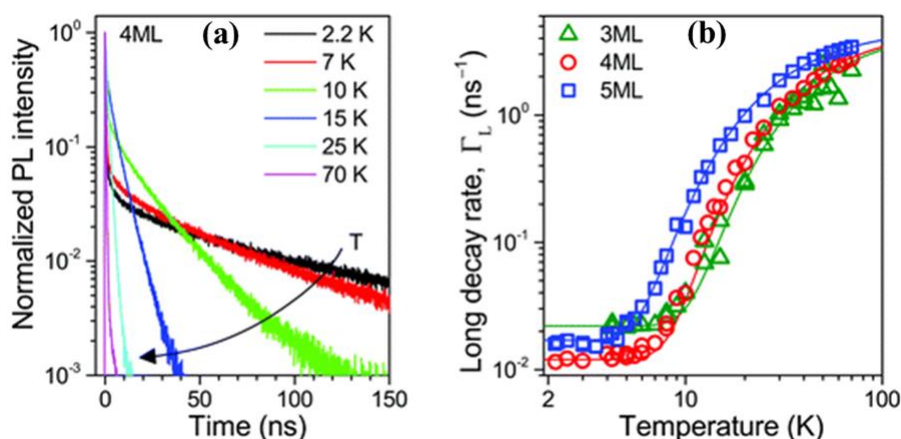

Figure 42: (a) Time-resolved PL decays (at the exciton energy) of 4 ML CdSe NPLs measured at various temperatures. **(b)** Long decay components as a function of temperatures in three different NPL samples: 3 ML, 4 ML, and 5 ML in thicknesses. Lines are fitted with equation (**4.6**). Reproduced from reference [18].

4.2.3. Dangling bond spins-assisted recombination of dark exciton in CdSe nanocrystals

Normally, organic ligands are utilized to passivate dangling bonds during the synthesis of colloidal NCs. However, it is impossible to passivate all dangling bonds on the surface of NCs. In CdSe NCs, surface dangling bonds can receive electrons through effective charge transfers from Cd-4d orbitals, leading to the intrinsic magnetic properties of NCs such as CdSe QDs capped with thiol [22] or TOPO (tri-n-octylphosphineoxide) [3], [4]. Not all colloidal CdSe NCs have surface magnetism because the magnetic behavior depends on the number of dangling bonds and the interactions between the NCs with ligands [4]. Most importantly, the spin of surface dangling bonds has been demonstrated to affect the exciton recombination process in CdSe NCs [8], [16].

Chapter IV: Surface Dangling Bond Spins

In CdSe NCs, the bright-dark exciton splitting energy (ΔE_{AF}) strongly depends on the shape and size of NCs [14], [23]. The splitting energy increases with decreasing the NC radius as $\Delta E_{AF} \approx 3\eta a \propto a^{-3}$, and will be saturated in very small NCs as $\Delta E_{AF} \approx 3\Delta/4$, where η is the electron-hole exchange constant and Δ is the splitting between the heavy and light holes in NCs. As a result, the PL in NCs is completely controlled by the dark exciton states ($F_z = \pm 2$) at cryogenic temperatures [8], [14]. In the presence of surface dangling bonds (SDBs), dark excitons can be admixed with bright excitons via their interactions with surface DB spins (SDBSs), leading to the recombination of dark excitons. This recombination process has been investigated both experimentally [16] and theoretically [8]. Figure 43 presents the DB spin-assisted recombination mechanism of dark excitons in CdSe NCs.

At high temperatures such that $kT \geq \Delta E_{AF}$, the bright and dark excitons are populated about equally. However, the PL is dominated by the bright exciton state ($F_z = \pm 1$, 1^L) due to $\Gamma_A \gg \Gamma_F$, in contrast, the dark exciton insignificantly contributes to the emission (Figure 43a). This process was discussed in the previous part (the phonon-assisted recombination mechanism). When the temperature exceeds the critical temperature (T_c) of polaron formation ($T > T_c$) but is low enough not to populate the bright excitons (± 1, 1^L), the surface magnetic momentums are randomly orientated, which favors the spin interactions between the surface DBs and dark excitons. As a result, the dark excitons are completely transformed into the bright excitons which contribute to the emission of NCs. In this case, the PL spectrum exhibits two emission lines corresponding to the dark exciton line shifted by ΔE_{AF} and the phonon replica (I_{1PL}) (Figure 43b). At low temperatures such that $T < T_c$, when the optical pumping rate is faster than the DB spin relaxation rate, the dark-exciton line and its phonon replica are additionally shifted by an energy of $E_\rho \rho_{db}$ as shown in the PL spectrum (Figure 43c). Here, $\rho_{db} = (N_{db}^- - N_{db}^+)/N_{db}$ is the DB spin polarization degree, $N_{db} = N_{db}^- + N_{db}^+$ is the total number of surface DB spins, $E_\rho = \alpha N_{db}$ is the DBMP binding energy for complete DB polarization ($\rho_{db} = 1$) and α is the dangling bond and electron spin constant [16]. If $\rho_{db} = 0$, the DB spins are unpolarized and the electron-DB spin interactions are antiferromagnetic exchanges described by $\alpha < 0$. On the opposite, the positive constant ($\alpha > 0$) describes the ferromagnetic exchange interaction between electron and dangling

bond spins. In summary, the surface DB spins are responsible for the radiative recombination of dark excitons at low temperatures (6 – 10 K) in CdSe QDs [8]. Recently, Shornikova et al reported the DB-dark exciton spin interactions in CdSe NPLs, which indicates the vital role of surface DBs in magneto-optical effects. How do surface DB spins interact with dark exciton in NPLs? and how to probe this spin interaction in NPLs? These questions will be clarified in this chapter.
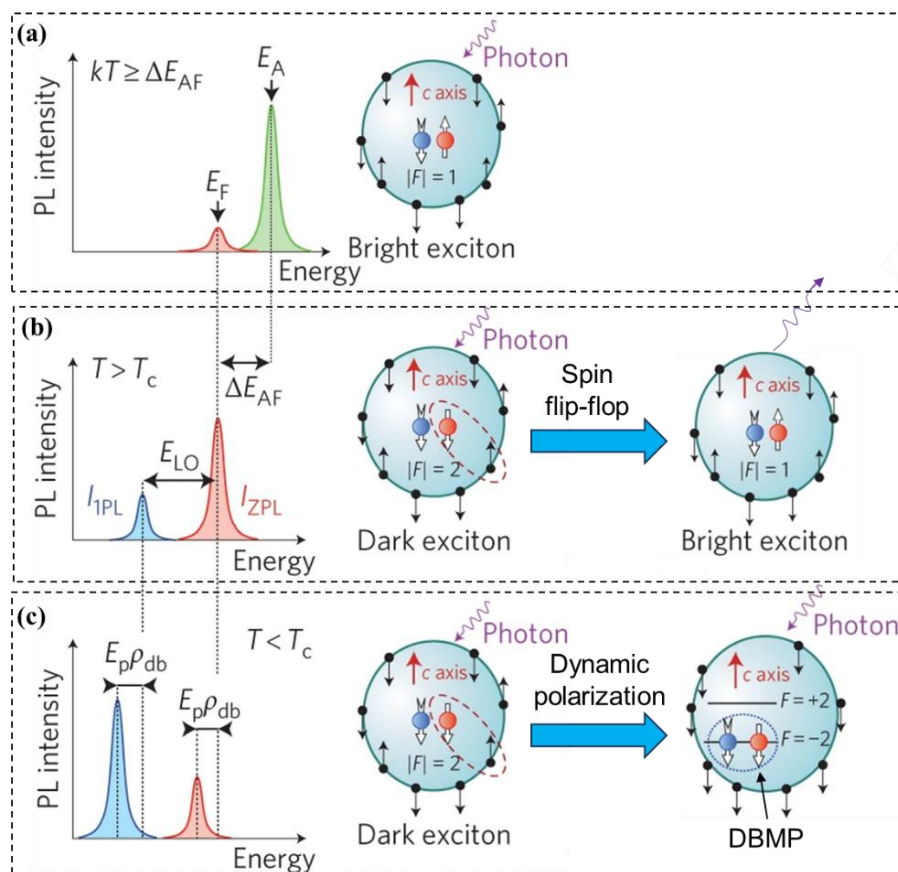
Figure 43: Scheme of the various lines in the PL spectra measured at different temperatures (on the left side). The laser is resonant with the bright exciton that has a photon energy E_A. Schematic illustration of the bright and dark exciton decays via the surface dangling bond spin (DBS) flip-flop-assisted recombination. **(a)** At $kT \geq \Delta E_{AF}$, the green spectrum stems from the bright exciton recombination. The surface DB spins are randomly orientated. **(b)** At $T > T_c$, the dark excitons are transformed into the bright exciton via the surface DB spin flip-flop mechanism. As a result, the PL spectrum shows a zero-phonon line (ZPL) originating from the radiative recombination of dark excitons, and its phonon replica (1PL). **(c)** At $T < T_c$, all surface DB spins are polarized, leading to the spitting of the ground dark exciton into two sub-levels and the formation of

DBMP. As a result, the PL intensity of the ZPL is dropped and the overall spectra are shifted towards lower energy by $E_\rho \rho_{db}$. Reproduced from reference [16].

4.3. Materials characterization

4.3.1. Optical properties of 4.5 ML CdSe and CdSe/CdS core/crown nanoplatelets

To investigate the effect of dangling bonds on the optical properties of NPLs, we used 4.5 ML CdSe NPLs (sample 1) to synthesize 4.5 ML CdSe/CdS core/crown NPLs with various crown sizes via a hot injection process. The synthetic protocol has been presented in Chapter II. After the material synthesis, absorption and PL spectra were employed to study the optical properties of NPLs at room temperature. Figure 44a presents the absorption (black) spectroscopy of CdSe NPLs, showing two distinct peaks: the light-hole (LH) at 478 nm (2.59 eV), and the heavy-hole (HH) at 506 nm (2.45 eV). The PL spectroscopy of the bare NPLs exhibits an emission at 508 nm (E_g = 2.44 eV) (Figure 44a, red). The core/crown NPLs were acquired by injecting the CdS crown solution into the mixture of CdSe NPLs, ODE, oleic acid, and Cd(OAc)$_2$.2H$_2$O at 150 ºC. The crown lateral size is adjusted by controlling the quantity of the CdS precursor injected into the reaction bath. In the core/crown synthesis, the injection rate of the CdS solution is 0.2 mL/min, and the crown growth is monitored by taking aliquots from the reaction bath to check absorption and PL spectra, as shown in Figure 44b. When the crown lateral size is increased, the absorption line of the CdS crown (at 405 nm) becomes more and more dominant. However, we observed another absorption peak at around 375 nm when the lateral size of the CdS crown became larger (Figure 44b, the black dashed rectangle). This peak is attributed to another CdS NPL population with an even thinner thickness than the CdS crown [24]. Indeed, when the crown becomes too large, some cracks appear on the core/crown NPLs, leading to the independent existence of CdS NPLs in the core/crown NPL solution [25]. On the other hand, the absorption spectra exhibit the heavy (HH) and light (LH) holes of the CdSe core, in which the HH peak tends to shift towards large wavelengths when the crown lateral size is increased (Figure 44c). To clarify this, the emission characteristic of the core/crown NPLs was checked with PL spectroscopy at room temperature. As expected in these

core/crown NPLs, the PL spectra show only an emission peak originating from the electron-heavy hole transition in the core NPL (Figure 44c). This confirms the formation of the type I band offset in the core/crown NPLs [25]. In the type I band structure (Figure 44d), as the band edges of CdSe NPLs are lower than those of CdS NPLs, thus the excitons in the CdS crown are entirely transferred to the CdSe core which emits photons. To ensure no additional contribution of other NPL populations to the emission of the core/crown NPLs, the PL spectroscopy of the core/crown NPL (30 min) was measured at a wide range of wavelengths. Figure 44d shows no emission peak of CdS NPLs at around 400 nm, implying that the secondary population of CdS NPLs does not affect the emission properties of the core/crown NPLs. However, we observed a shift of the emission peak toward larger wavelengths as the crown size increased. Specifically, the core/crown NPLs (5 mins, smallest crown size) have an emission at 508 nm (2.44 eV) similar to the core NPLs, whereas the emission peak is observed at 514 nm (2.41 eV) for the core/crown NPLs (30 min, giant crown size) (see Table 1). The difference in the emission peak position is 30 meV which is larger than the redshift reported in previous studies [25], [26]. Despite this, this peak shift is negligible compared to a change in the NPL thickness and can be attributed to the change in the dielectric environment or the weak lateral quantum confinement after the crown growth [27], [28]. The absorption and PL spectra confirmed the formation of CdSe/CdS core/crown NPLs with an unchanged core thickness.

Table 1: Absorption maxima of optical transition, and exciton in CdSe NPLs, and CdSe/CdS core/crown NPLs with various crown sizes.

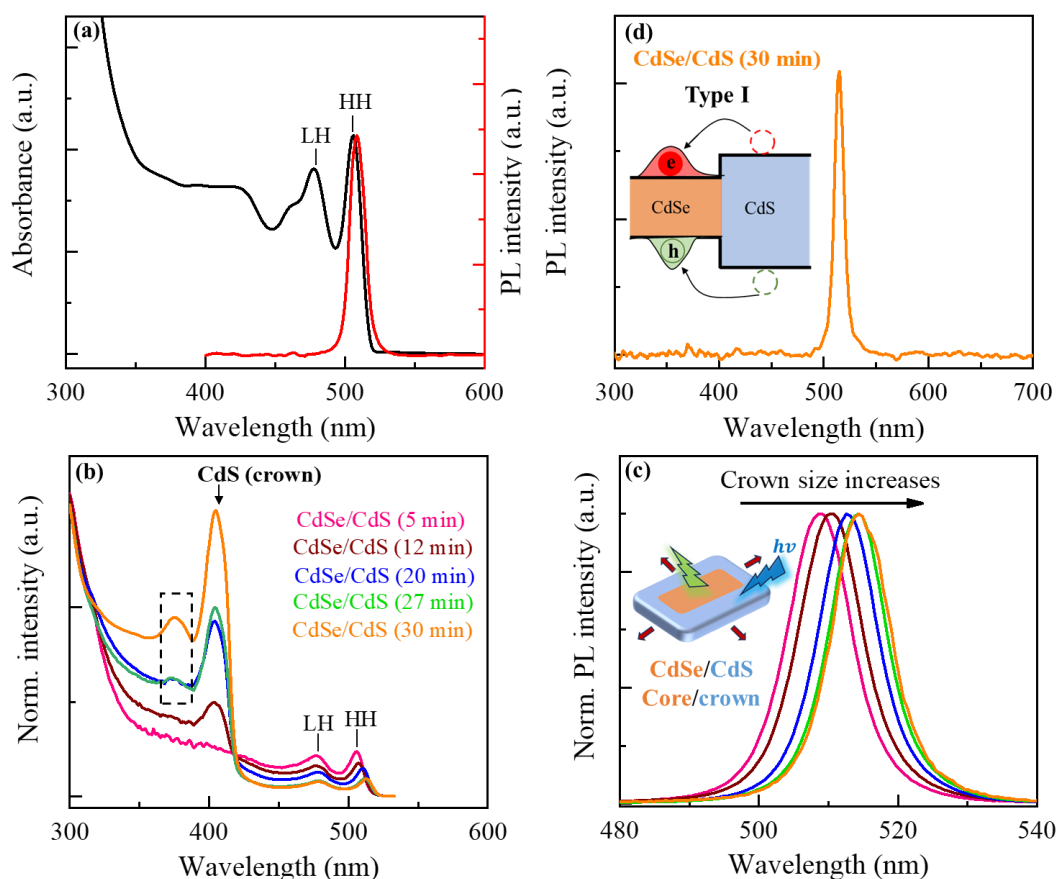| Sample	Light hole (LH) (nm)	Heavy hole (HH) (nm)	CdSe exciton (nm)
CdSe (core)	478	506	508
CdSe/CdS (5 min)	477	506	508
CdSe/CdS (12 min)	476	507	510
CdSe/CdS (20 min)	478	510	512
CdSe/CdS (27 min)	478	512	514
CdSe/CdS (30 min)	478	513	514

Figure 44: (a) Absorption (black) and emission (red) spectra of 4.5 ML CdSe NPLs. **(b)** Absorption and **(c)** Emission spectra of 4.5 ML CdSe/CdS core/crown NPLs with various crown sizes. **(d)** Emission spectroscopy of the core/crown NPLs (30 mins) measured at a wide range of wavelengths. Note that all the spectra were acquired at room temperature.

4.3.2. Structural properties of 4.5 ML CdSe and CdSe/CdS core/crown nanoplatelets analyzed by scanning transmission electron microscopy

In the previous part, we observed the absorption line of the secondary population of CdS NPLs in the absorption spectra of the core/large crown NPLs. This reflected the complexity of the morphology of core/crown NPLs. Here, scanning transmission electron microscopy (STEM) was employed to investigate the morphological properties of NPLs. Figure 45a presents a STEM image of 4.5 ML CdSe NPLs, showing flat-lying NPLs in a rectangular shape with irregular edges. We extracted an FFT pattern of a flat-lying NPL (the red dashed rectangle) to identify its crystal structure. As expected for the CdSe NPLs, the FFT pattern exhibits a series of typical lattice fringes such as (020),

(200), (0-20), and (-200) representing the zinc-blende (ZB) structure of NPLs. Figure 45b shows a STEM image of 4.5 ML CdSe/CdS core/crown NPLs after 5 min of the injection of the crown solution. The core/crown NPLs have a more rectangular shape with straight edges compared to the CdSe (core) NPLs. By analyzing 200 NPLs (Figures 45d, e), the estimated average lateral size of the core/crown NPLs is 15 nm × 5.0 nm, equal to the lateral size of the core NPLs (as reported in Chapter III). After 30 min of the CdS injection, we observed the appearance of the core/crown NPLs in twisted (red arrow) and tree branch (blue dashed circle) shapes (Figure 45c). In this sample, it is impossible to define the width of NPLs while the average length is estimated to be 27 nm (Figure 45f). Based on Figure 45c, we can conclude that the crown lateral extension becomes non-oriented with increasing the amount of CdS precursors injected into the reaction solution. Therefore, these core/crown NPLs will expose the branches of the CdS NPLs which causes the additional absorption peak (around 375 nm) as observed in the absorption spectroscopy. In addition, the injection rate of the CdS solution also affects the shape of core/crown NPLs [24].
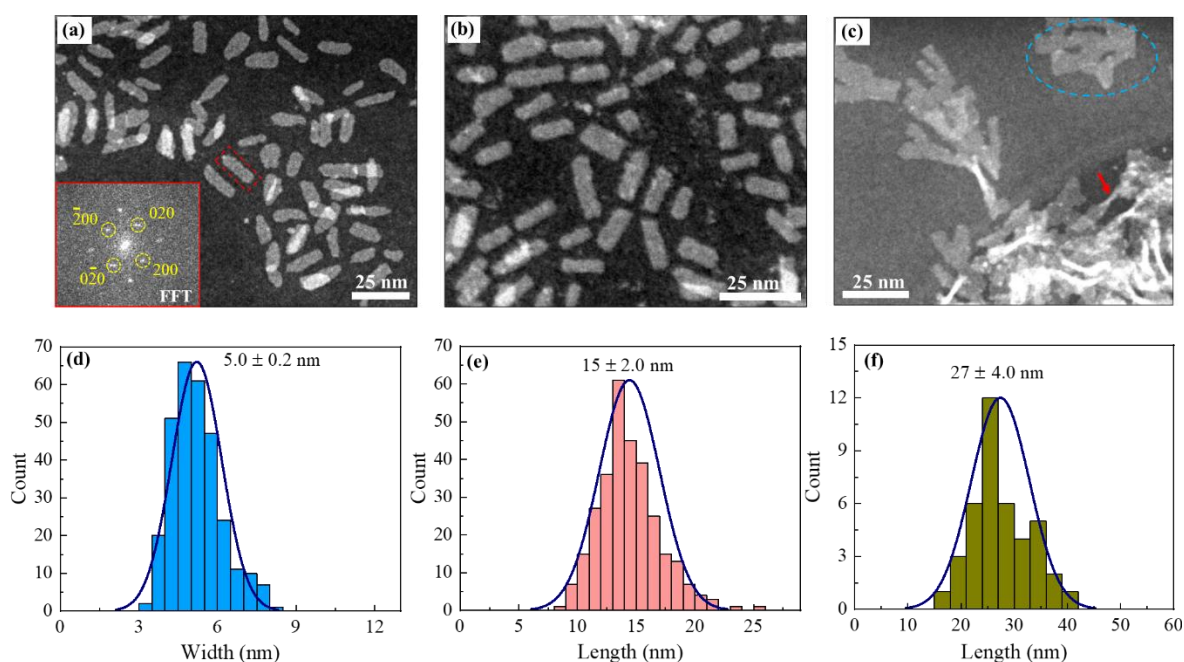

Figure 45: STEM images of **(a)** 4.5 ML CdSe NPLs. The corresponding FFT is inserted in Figure a. **(b)** 4.5 ML CdSe/CdS core/crown NPLs (5 min). **(c)** 4.5 ML CdSe/CdS core/crown NPLs (30 min). **(d – e)** Statistic on the lateral size of the core/crown NPLs (5 min). **(f)** Statistic on the length of the core/crown NPLs (30 min).

The CdSe/CdS core/crown NPLs (5 min) do not show significant differences in the lateral dimension compared to the CdSe (core) NPLs, thus it is difficult to confirm the presence of the CdS crown through STEM images. Hence, the energy-dispersive X-ray (EDX) technique was employed to analyze the chemical composition of core/crown NPLs. Figure 46a shows a STEM image of stacked CdSe/CdS core/crown NPLs (5 min). The corresponding EDX element map is presented in Figure 46b, showing the dense presence of Cd and Se elements. In contrast, only a small quantity of S elements are found on the side facet of the NPLs (the blue dashed rectangle). The EDX mapping image indicates that a small amount of the CdS precursor grew on the side facets of the core NPL. This finding is consistent with the absorption spectroscopy of the core/crown NPLs (5 min) where no specific absorption peak is found at around 405 nm because the CdS volume is insufficient to create a complete crown.
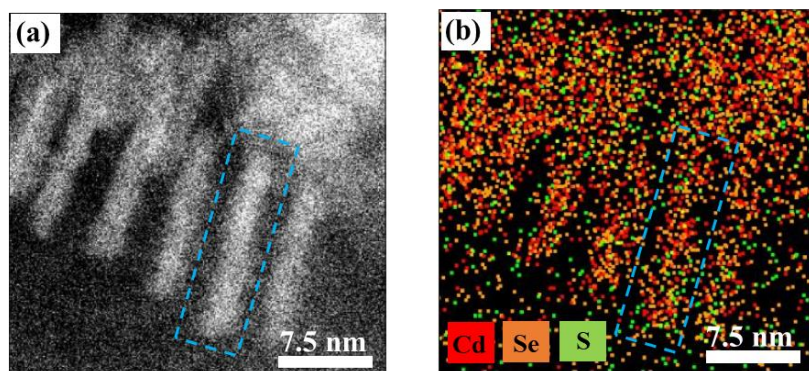
Figure 46: (a) STEM image of stacked CdSe/CdS core/crown NPLs (5 mins). **(b)** Corresponding EDX element mapping image.

4.4. Low-temperature emission properties of 4.5 ML CdSe NPLs

The emission properties of CdSe NPLs have already been studied at ensemble and single-scale at room temperature. It has been shown that single NPLs exhibit narrow emission bandwidth and spectrally stable emission spectra at room temperature [29], [30], [31], [32]. However, single NPLs show emission behaviors depending on temperature and environment. Specifically, NPLs displaying bright emissions at room temperature under an ambient atmosphere are quenched under a vacuum, after which the emission becomes brighter under an ambient atmosphere at cryogenic temperatures [29]. Moreover, the emission properties of NPLs at low temperatures are complicated

due to the splitting of the exciton band edge into five sub-energy levels. This splitting leads to the characteristic dependence of the PL decay on temperatures in CdSe NPLs, as discussed in part (4.2.2). Therefore, understanding the emission characteristics at low temperatures is the primary step for understanding the recombination mechanisms in NPLs. The PL spectroscopy of 4.5 ML CdSe NPLs (ensemble) at 4.2 K is presented in Figure 47a, which shows two emission lines including the exciton (X) at 2.52 eV, and a low-energy line at 2.50 eV attributed to the trion (T). Theoretically, the exciton is neutral particles composed of electrons and holes. However, the excitons can add one charge carrier to form three charged particles including negatively charged exciton (two electrons and one hole), and positively charged exciton (one electron and two holes) (Figure 47b). The trion can be distinguished from the exciton based on the difference in their fine structure. The exciton fine structure consists of the bright and dark excitonic states, thus the recombination dynamics of exciton depends on temperatures and external magnetic fields. In contrast, the trion ground state has no fine structure because of two identical particles, e.g., two opposite-spin electrons in a negatively charged trion form a singlet state with a total spin $S = 0$ (Figure 47b) [33]. In this spin configuration, the radiative recombination of trions is allowed, thus trions are always bright. As a result, the trion recombination process is insensitive to temperature and external magnetic fields [34]. Figure 47c shows the temperature-dependent PL decay measured at the exciton energy (2.52 eV) in the CdSe NPLs. As discussed previously, the PL emission in NPLs at low temperatures is dominated by the phonon-assisted recombination of dark excitons, resulting in a bi-exponential decay. At high temperatures (above 10 K), the population of the bright exciton becomes more dominant, resulting in a mono-exponential decay with the overall rate $(\Gamma_A + \Gamma_F)/2 \approx \Gamma_A/2$, where $\Gamma_A = 10$ ns^{-1} is the radiative recombination of bright excitons in CdSe NPLs [18]. The PL decay shows that the long component decays fast as the temperature is increased (Figure 47c). These findings are in good agreement with references [18], [34].

On the other hand, the PL emission in CdSe/CdS core/crown NPLs mainly originates from the CdSe core part due to the type-I band alignment, where both electrons and holes are confined in the core part, as proven in part (4.3.1.). Growing the CdS crown will help to passivate surface traps on the side facets of the core NPL, contributing to

enhanced quantum efficiency in core/crown NPLs [25], [26]. The emission properties of CdSe/CdS core/crown NPLs at 4.2 K are presented in Figure 50a (part 4.6.). In the scope of the thesis, we mainly focus on analyzing the impact of the CdS crown on the spin interaction between surface DBs and dark excitons in core/crown NPLs. Detailed discussion on the low-temperature emission of core/crown NPLs will be presented in part (4.5.3).
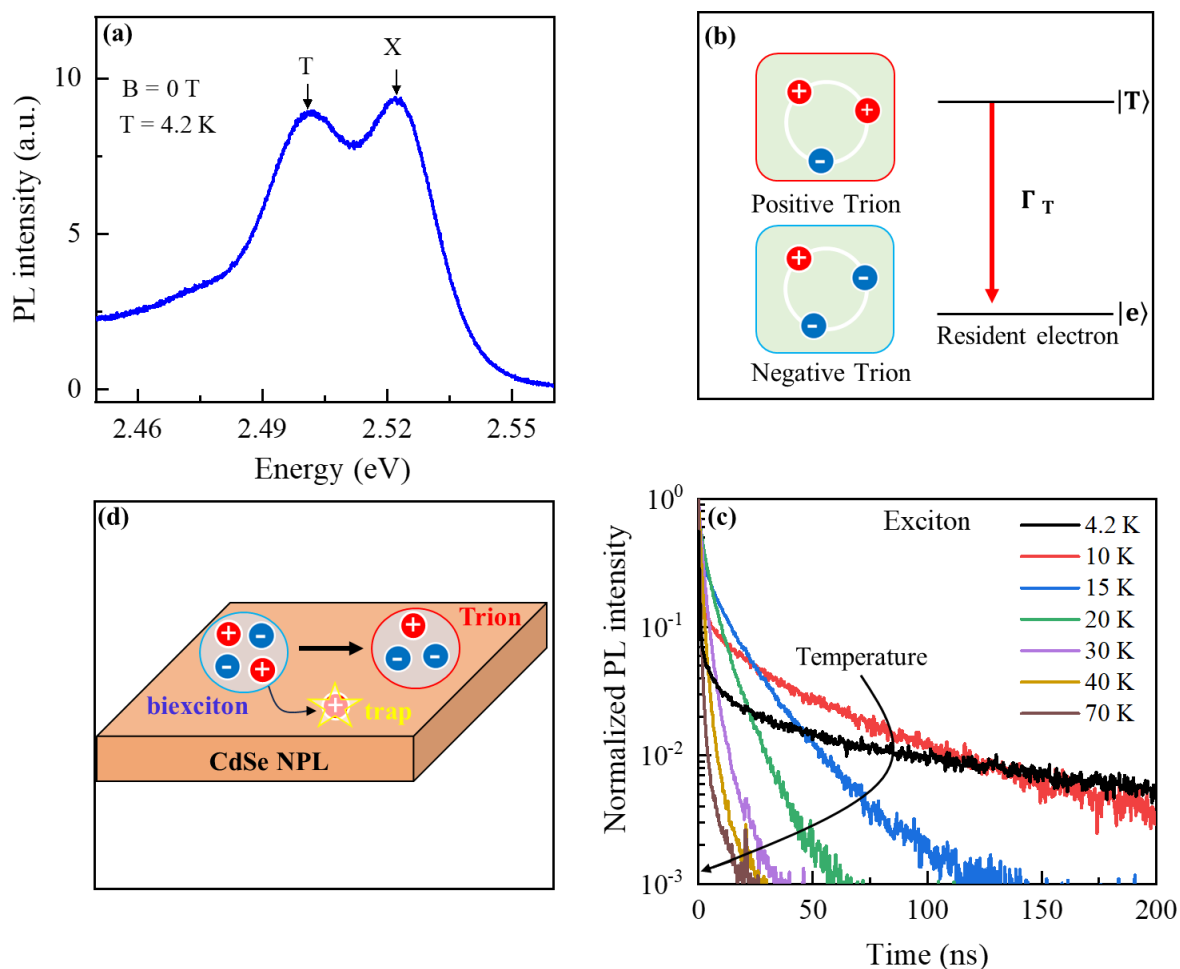

Figure 47: PL spectroscopy and decay of 4.5 CdSe NPLs. **(a)** PL spectroscopy measured at 4.2 K in a zero-magnetic field. **(b)** Schematic illustration of trion energy level structure and configuration. **(c)** Temperature-dependent PL decays from 4.2 K to 70 K measured at the exciton energy. **(d)** Formation of Trions in CdSe NPLs.

4.5. Effect of dangling bond spins on polarized emission in CdSe and CdSe/CdS core/crown nanoplatelets

The effective charged transfer from the Cd-4d orbitals to the empty orbital of surface DBs leads to the formation of surface magnetism in CdSe NPLs [4], [22]. As a result, surface DB spins can change the optical and magnetic properties of NPLs [5]. The effect of surface DB spins on the optical properties of NPLs is investigated here by magneto-photoluminescence (PL) spectroscopy at low temperatures (T = 4.2 K) and in an external magnetic field (up to 15 Tesla).

4.5.1. Polarized emissions in 4.5 ML CdSe NPL

In CdSe NPLs, the PL emission is dominated by the dark excitons ($F_z = \pm 2$) at cryogenic temperatures due to the bright-dark exciton splitting. In the presence of an external magnetic field, the dark exciton is split into two sub-levels with corresponding spin projections: $|+2\rangle$ and $|-2\rangle$ (lowest state). This phenomenon is called Zeeman splitting (Figure 48b). The splitting energy (ΔE_F) is given by

$$\Delta E_F(B) = g_F \mu_F B cos\theta \qquad (4.10)$$

Where μ_F is the Bohr magnetron, B is the strength of the external magnetic field, θ is the angle between the NPL surface and the direction of the magnetic field, and g_F is the dark exciton g factor which is defined as the response of electrons and holes to the magnetic field. At a temperature of a few Kelvins such that $\Delta E_F \gg k_B T$, the emission from NPLs is dominated by the lowest state ($F_z = -2$), and polarized circularly. In this configuration, the right-handed circular polarization (σ^+) represents the optical transition from the $|+2\rangle$ state to the ground state $|G\rangle$ while the left-handed circular polarization (σ^-) is for the optical transition from the $|-2\rangle$ to $|G\rangle$ states. The degree of circular polarization (DCP) of the PL emission is defined as follows:

$$P_c^{int}(t) = \frac{I^+(t) - I^-(t)}{I^+(t) + I^-(t)} \qquad (4.11)$$

Where $I^+(t)$ and $I^-(t)$ are the time-integrated intensities of the σ^+ and σ^- polarized emission. P_c^{int} is the time-integrated DCP which is determined based on magnetic-dependent PL spectroscopy. Figure 48a shows the polarized PL spectroscopy of CdSe

NPLs at B = 15 T. The experimental DCP (P_c^{int}) of excitons is determined as shown in Figure 48a. The exciton DCP (red circles) is plotted as a function of magnetic fields in Figure 48d. The DCP first increases to +2.0 % in low magnetic fields (0 – 2 T), and it then decreases and crosses the zero polarization at a critical magnetic field (B_c = 4.5 T). When the magnetic field exceeds 4.5 T, the DCP has a negative sign and reaches -5.0 % at B = 15 T. As shown in equation (**4.10**), the splitting energy varies with the strength of magnetic fields, and the population of the Zeeman sublevels is expected to change according to the Boltzmann distribution. In colloidal CdSe NCs and their heterostructures, the exciton DCP varies linearly on magnetic fields and reaches a saturated DCP level (P_c^{sat}) in high magnetic fields, which depends on the NC orientation [35], [36], [37], [38]. Our CdSe NPLs exhibit a non-monotonous DCP behavior with an increasing external magnetic field, in good agreement with the study by Shornikova et al [5], but differ from the literature [35], [36], [37], [38]. Similar to the exciton, the trion emission is also polarized under an external magnetic field that lifts the spin degeneracy of an unpaired electron or hole in the positive and negative trions. The spin structure of positive and negative trions is presented in Figure 48c. The positive trion has two holes and an electron, and its ground state thus has a spin projection S_z = ±1/2 on the magnetic field direction. The sign of the electron g-factor (g_e) will determine which level is the lowest in energy. In CdSe NCs, the electron g-factor is positive [39], [40], thus the lowest electron spin level is $S_z = -1/2$ and its energy is given by $E_e = S_z g_e \mu_B B$ [37]. Meanwhile, two electrons and a hole with momentum projection M = ±3/2 (onto the quantization axis) form the ground state of the negative trion. Thus, the Zeeman splitting in this trion is determined by the hole g-factor (g_h) which is negative, e.g., g_h= -0.73 for CdSe NCs [39]. In this case, the lowest hole spin level has a momentum projection -3/2 and its energy is strongly anisotropic and depends on the angle (θ) between the NPL surface and the magnetic field direction, as the hole energy is $E_{hh} = -M g_h \mu_B B cos\theta$. The σ^+ polarized emission is connected to the optical transitions which change the spin projection by +1 (Figure 48c, the red arrows), and the σ^- polarized emission corresponds to the transitions which change the spin projection by -1 (Figure 48c, the blue arrows). When $k_B T$ is smaller than the trion Zeeman splitting energy, the lowest spin levels are more populated and thus dominate the trion emission.

Figure 48d (green triangles) shows the time-integrated DCP of the trion emission as a function of magnetic fields, showing that the trion DCP has a negative sign. This confirms the trion in CdSe NPLs is negatively charged, which is consistent with references [5], [34]. On the other hand, the trion DCP does not exhibit strong interactions between trion emission and surface DB spins, thus the DCP monotonously increases with magnetic fields. According to F. Vong et al [41], the formation of the low-temperature trion emission in pristine CdSe NPLs stems from the hole trapping within a biexciton. At low temperatures, NPLs can absorb two photons (or multiphoton) to form a biexciton (or a multiexciton) [42]. As the NPL surface contains many traps, a hole within a biexciton is trapped in a hole surface trap to form a negatively charged exciton (negative trion) in NPLs (Figure 47d). This formation mechanism is very consistent with the observation of the negative trion probed by polarized PL emission in external magnetic fields [34]. However, the authors did not mention which surface of NPLs favors the formation of hole traps. In 4.5 ML CdSe NPLs, we demonstrated that (1) the bottom and top surfaces contain shallow electron traps and they randomly distribute on these surfaces, and (2) the edges of NPLs host many surface traps, particularly deep hole traps originating from rich-Se planes present on the side facets (see Chapter III). With this evidence, we believe that the negative trion is mainly formed due to the hole trapping on the side facets of NPLs.
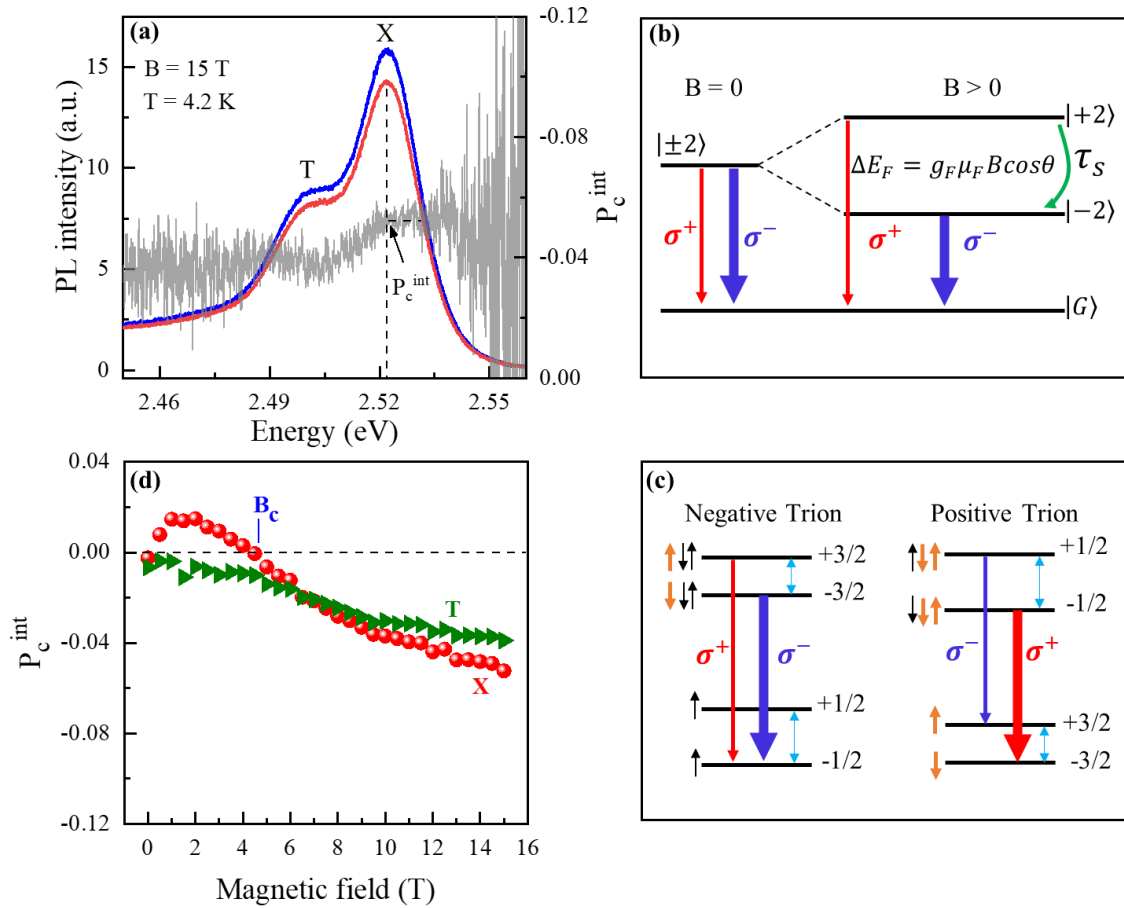
Figure 48: (a) Polarized PL spectra of 4.5 ML CdSe NPLs at B = 15 T and T = 4.2 K. **(b)** Scheme of the allowed optical transitions between dark exciton states ($F_z = \pm 2$) in magnetic fields. Note that τ_s is the spin relaxation time between the two spin levels of the dark exciton. **(c)** Schematic representation of the spin structure and optical transitions for positive and negative trions in magnetic fields. **(d)** Exciton and Trion DCP (P_c^{int}) as a function of the magnetic field.

4.5.2. Explanation of the non-monotonous DCP behavior in CdSe NPLs

Recently, Shornikova and co-workers reported the non-monotonous DCP behavior in CdSe NPLs synthesized in ambient conditions [5]. They concluded that such DCP behavior represents the antiferromagnetic properties caused by surface DB spins in NPLs. As mentioned previously, the dark excitons can admixture with the bright excitons via phonons, external magnetic field, and dangling bond spins. The NPL surface always hosts dangling bonds caused by unsuccessful ligand passivations during colloidal synthesis. Surface DB spins can interact with an electron localized in the dark

exciton, and thus the dark exciton is converted into the bright exciton (Figure 49a). As a result, the PL emission in NPLs is dominated by the radiative recombination of dark excitons at cryogenic temperature. In the presence of an external magnetic field, the DB-electron spin interaction changes the population of the lowest and highest spin sublevels of the dark exciton, leading to the non-monotonous exciton DCP as observed in Figure 48d. Specifically, in low magnetic fields, the optical transition from the state $|+2\rangle$ becomes more dominant, thus the intensity of the σ^+ polarized emission is higher than the other one. In this case, the DCP will have a positive sign and increase to a maximum value. After that, increasing the magnetic field gradually reduces the intensity of the σ^+ polarized emission, and thus the DCP gradually also decreases. The intensities of the σ^+ and σ^- polarized emissions will be equal at a critical magnetic field (B_c), resulting in zero polarization. If still increasing the magnetic field, the emission in the NPL is dominant by the state $|-2\rangle$, the DCP has thus a negative sign and monotonously increases with increasing magnetic fields. The above mechanism explains the non-monotonous DCP behavior of dark excitons caused by surface DB spins in NPLs.
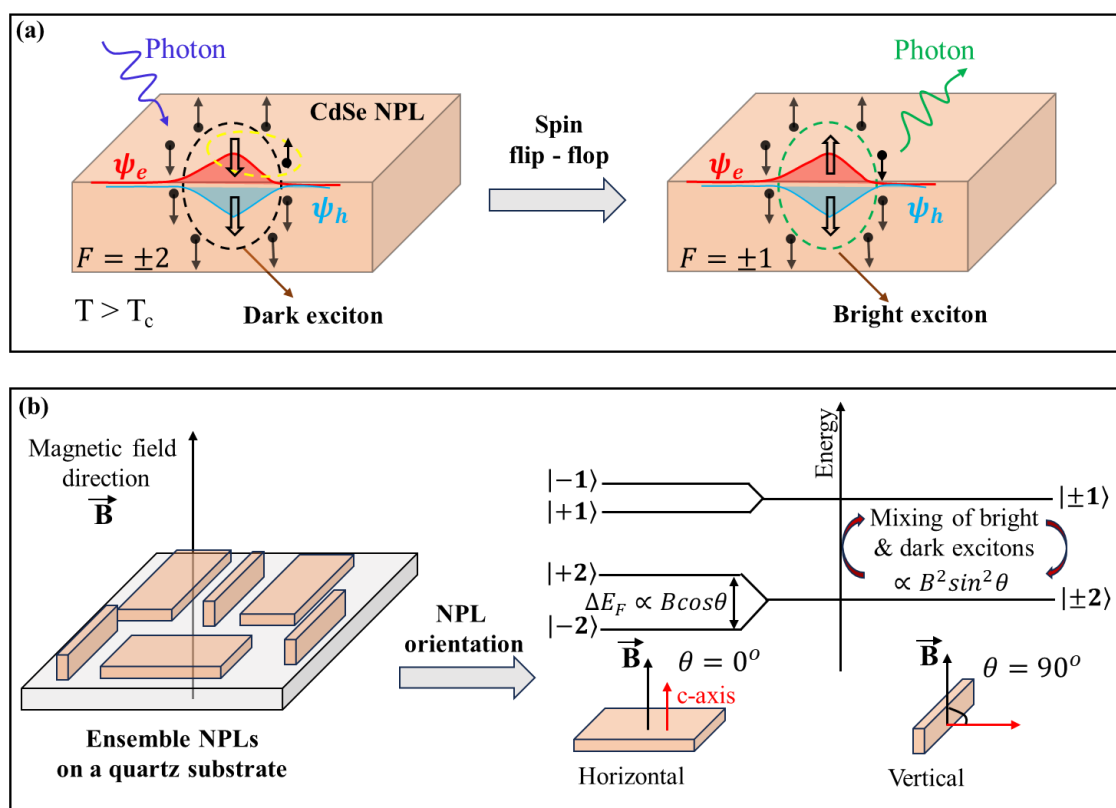

Figure 49: (a) Schematic illustration of surface DB spin-assisted recombination of dark exciton. **(b)** Schematic of exciton Zeeman sublevels in an external magnetic field.

In addition to the magnetic field, the Zeeman splitting also depends on the angle between the quantization c-axis of NPLs (typically the NPL surface) and the magnetic field direction. In horizontal NPLs, the Zeeman splitting is maximal because the NPL c-axis is parallel to the magnetic field vector (cos 0º = 1). In contrast, there is no Zeeman splitting between the two spin sub-levels in the case of vertical NPLs because the NPL c-axis is perpendicular to the magnetic field vector (cos 90º = 0). Instead, the emission in vertical NPLs is accelerated in external magnetic fields due to the mixing between the dark and bright excitonic states (Figure 49b, the panel on the left). In ensemble NPLs, the orientation of NPLs is random, which typically makes the exciton DCP reach a saturated level in high magnetic fields [5], [34], [43]. For our NPLs, the exciton DCP seems saturated in a magnetic field range of 12 – 14.5 Tesla (Figure 48d, the red circles).

4.5.3. Polarized emission in CdSe/CdS core/crown NPLs

The above experiment shows that surface DB spins changed the low-temperature emission properties of NPLs in external magnetic fields. However, the distribution of dangling bonds remains unknown. To clarify this, we propose growing the CdS crown around the CdSe NPLs (using the same NPL sample batch) to create CdSe/CdS core/crown NPLs. In these core/crown NPLs, surface traps on the side facets of the core NPLs will be passivated by the crown material, thus we will know how DB spins on the top surface affect the optical properties of NPLs.

To do that, CdSe/CdS core/crown NPLs were investigated with magneto-PL spectroscopy. Figure 50a shows the PL spectra of 4.5 ML CdSe and CdSe/CdS core/crown NPLs with various crown lateral sizes measured at B = 0 T and T = 4.2 K. The core/crown NPLs (5 min) exhibit two emission lines corresponding to the exciton at 2.52 eV and the trion at 2.49 eV. When the crown size is increased, all the core/crown NPL samples show a shift of the main emission peaks toward lower energies because the dielectric environment is changed or the weak lateral quantum confinement after the crown growth [27], [28] (see Table 2). This peak shift is consistent with the room-temperature PL spectra. The trion emission appears in all the core/crown NPL samples. To study the effect of surface DB spins, the exciton and trion DCP of all the samples were extracted from the polarized PL spectra. Figure 50b shows the magnetic-dependent

DCP of the exciton. For the core/crown NPLs (5 min), its exciton DCP increases to +11 % in a magnetic field range (0 – 3 T), then vanishes the zero polarization at B_c = 7.5 T. The exciton DCP changes from a positive sign to a negative sign, and it decreases to - 12 % at B = 15 T. This non-monotonous DCP behavior is the same as the exciton DCP of CdSe NPLs but its magnitude is larger than 5 – 6 times. When the crown size is increased, the non-monotonous DCP behavior disappears, instead, the exciton DCP monotonously increases with an increasing magnetic field. In the core/crown NPLs (27 and 30 min), the DCP is saturated in high magnetic fields due to the dependence of the Zeeman splitting on the orientation of NPLs. Similarly, the trion DCP of the core/crown NPLs is plotted as a function of magnetic fields (Figure 50c). In all the core/crown NPL samples, the trion DCP has a negative sign and increases linearly on magnetic fields (Figure 50c). These negative DCP values represent the negative trion in the core/crown NPLs.

Table 2: Exciton and Trion energy extracted from PL spectra of CdSe NPLs and CdSe/CdS core/crown NPLs with various crown sizes (T = 4.2 K, and B = 0 T).

Sample	Exciton (eV)	Trion (eV)
CdSe	2.52	2.50
CdSe/CdS (5 min)	2.52	2.49
CdSe/CdS (12 min)		2.49
CdSe/CdS (20 min)	2.50	2.47
CdSe/CdS (27 min)	2.50	2.47
CdSe/CdS (30 min)	2.49	2.46

4.6. Theoretical model for exciton Zeeman splitting

According to equation (4.10), the dark exciton DCP reflects the exciton spin polarization caused by its intrinsic Zeeman splitting. However, the exciton DCP in CdSe NPLs and CdSe/CdS core/crown NPLs (5 min) reflects an additional spin-polarized mechanism contributing to the Zeeman splitting under an external magnetic field. In this case, the Zeeman splitting energy can be written as follows [44]:

$$\Delta E_F(B, \theta) = \left[g_F \mu_F B + 2E_\rho \rho_{db}(B)\right] \cos\theta \qquad (4.12)$$

Here E_ρ is the exciton-DB spin exchange interaction energy. The DB spin polarization (ρ_{db}) is given by $\rho_{db} = (n_{db}^- - n_{db}^+)/(n_{db}^- + n_{db}^+)$, where n_{db}^+ (n_{db}^-) is the density of surface DBs with spins parallel (antiparallel) to the magnetic field direction. $n_{db} = n_{db}^- + n_{db}^+$ is the surface density of dangling bonds [5]. In NPLs, as the electron probability at the surface is much larger than that of the hole, the exciton-DB spin exchange interaction is mainly provided by the electron-DB spin interaction, $E_p = \alpha N_{db}$. α is the average electron-DB spin exchange constant and N_{db} is the number of dangling bonds interacting with the electron localized in the NPL. According to Shornikova et al [5], the ρ_{db} is characterized by the equilibrium polarization of the surface spins caused by their Zeeman splitting in an external magnetic field: $\rho_{db} = \tanh(g_{db}\mu_B B/2kT)$, where the dangling bond g-factor $g_{db} = 2$ [45]. In low magnetic fields, such that $g_{db}\mu_B B < 2kT$, the Zeeman splitting is given by

$$\Delta E_F(B) \approx (g_F + g_{db}E_\rho/kT)\mu_B B \qquad (4.13)$$

The above equation indicates two possible cases: if g_F and $g_{db}E_\rho$ have the same sign, the electron-DB spin interaction increases the exciton Zeeman splitting. In the opposite case, the electron-DB spin interaction decreases the exciton Zeeman splitting and can change its sign if $|g_F|$ is smaller than $|g_{db}E_\rho/kT|$ [5]. However, due to the saturation of the spin polarization of the dangling bonds (ρ_{db}) with increasing field, the Zeeman splitting ΔE_F scales non-monotonically with the magnetic field (B), crossing zero at $B_c = 2|\rho_{db}E_\rho|/|g_F|\mu_B$ and changing sign [5]. This explains why the exciton DCP changed from a positive sign to a negative sign in CdSe NPLs and CdSe/CdS core/crown NPLs (5 min).

The difference in the exciton DCP behavior between the bare NPLs and core/crown NPLs can originate from two following factors: (1) the surface density of dangling bonds in each sample, and (2) the number of surface DB spins oriented opposite to the electron spin. Compared to CdSe NPLs, the exciton DCP in the core/crown NPLs (5 min) has a larger magnitude than the exciton DCP of the bare NPLs. This can be explained because the core/crown NPLs (5 min) have many DB spins oriented opposite

to electron spins, and the electron-DB spin interaction thus becomes stronger. The strong spin interaction significantly enhances the intensity of the polarized emission, leading to positive DCP values larger than 5-6 times the exciton DCP in CdSe NPLs. In contrast, when the crown lateral size becomes larger, it is difficult for the electron wavefunction inside the NPL to feel dangling bonds on the edges, leading to a graduate suppression of the electron-DB spin interactions. Therefore, the exciton DCP becomes monotonous in the core/crown NPLs with large crown sizes, as observed in Figure 50b. Additionally, the exciton DCP of the bare NPLs and the core/smallest crown NPLs (5 min) also differ from each other at the critical magnetic field (B_c) for which the DCP changes its sign from positive to negative. Specifically, the B_c value is respectively 4.5 T (CdSe NPLs), and 7.5 T (CdSe/CdS core/smallest crown). This difference can be attributed to the spin polarization of surface DBs to external magnetic fields.
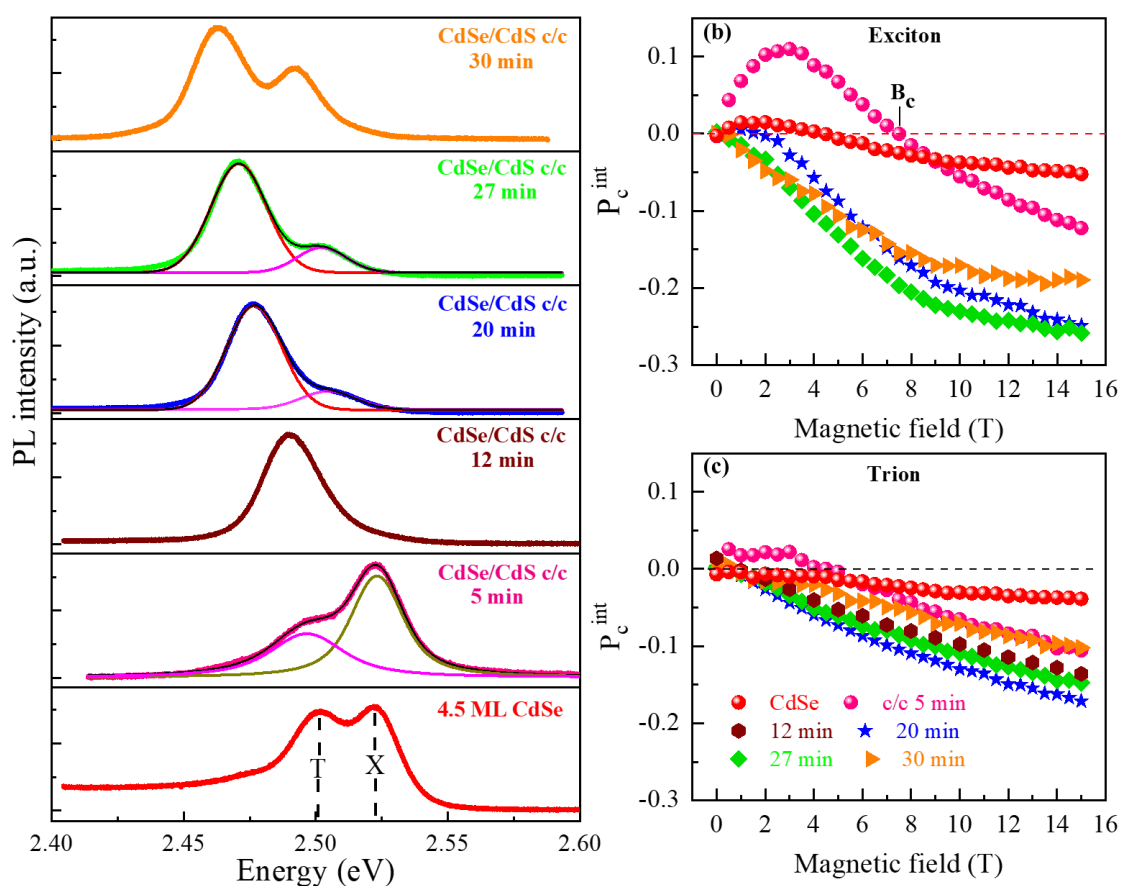

Figure 50: (a) PL spectra of 4.5 ML CdSe and CdSe/CdS core/crown NPLs with various crown sizes measured at T = 4.2 K and B = 0 T. **(b)** Exciton DCP and **(c)** Trion DCP as a function of magnetic fields. All the PL spectra were fit with a Gaussian function.

In addition to exciton DCP, analyzing the trion DCP is also important for studying the polarized emission in NPLs. As demonstrated previously, our bare and core/crown NPLs display the negatively charged exciton (negative trion) which is characterized by the hole g-factor. Theoretically, the hole g-factor ($g_h < 0$) is defined as the dimensionless quantity that characterizes the response of the magnetic momentum of a hole in semiconductors to an external magnetic field [46]. In our experiments, the hole g-factor can be extracted from the trion DCP by fitting it with $P_c^{int} = P_c^{eq}\tanh(-3g_h\mu_B B/2k_B T)$, where P_c^{eq} is the saturated DCP value in high magnetic fields [43]. However, we did not find clear DCP saturated values in all the NPL samples. In this case, the saturated DCP values were extracted from the experimental data. For 4.5 ML CdSe NPLs, the hole g-factor is determined at -0.21, in good agreement with the value measured by Shornikova et al (g_h = -0.2 for 5 ML CdSe NPLs) [34]. For CdSe/CdS core/crown NPLs, the hole g-factor is estimated to be -0.22 (core/crown-12 min), -0.24 (core/crown-20 min), -0.23 (core/crown-27 min), and -0.22 (core/crown-30 min). These g_h values are similar to those of the bare NPLs, but differ from the CdSe/CdS core/thick shell NPLs (g_h = -0.5) [43]. This finding indicates that the hole g-factor is not affected by the CdS crown. Indeed, the hole g-factor strongly depends on the mixing of the light-hole and heavy-hole and the spatial distribution of hole wavefunction in NPLs [43]. In CdSe/CdS core/crown NPLs, their electronic band structure is characterized by the type-I band alignment where both electron and hole wave functions are confined in the core NPL (CdSe). Therefore, growing the CdS crown does not change the confining potential type of the hole in the core NPL. This explains why the core/crown NPLs exhibit the hole g-factor similar to the bare NPLs.

4.7. Spin dynamics of the dark exciton in nanoplatelets

In the previous section, we have highlighted the effect of the surface DB spins on the magnetic-field-induced DCP in NPLs. To probe this effect, we performed magnetic-dependent PL spectroscopy at 4.2 K. Another possible approach to study is to measure the temporal dependence of the DCP. The idea of the measurement is presented in Figures 51a and c. Here, we compare the polarized PL decay in CdSe NPLs and CdSe/CdS core/giant crown (30 min). The spin dynamics can be studied by analyzing

the time-resolved DCP (P_c^{int}), as shown in Figures 51b and d. After pulsed laser excitation, the σ^+ and σ^- polarized components of the PL decays are traced as a function of time. The time-resolve DCP is calculated from the experimental data according to equation (4.13). The PL is unpolarized right after the excitation due to the off-resonant photo-excitations. The excitons then relax into the spin states with lower energy until they achieve thermal equilibrium [37], [47]. Therefore, the time-resolved DCP tends to be saturated at longer time as shown in Figures 51a and c (grey curves). To analyze the dependency of the characteristic time and saturated DCP on magnetic fields, the time-resolved DCP curves were fit with equation (4.13).

$$P_c^{int}(t) = P_c^{sat}[1 - \exp(-t/\tau_s)] \qquad (4.13)$$

Where P_c^{eq} is the DCP in thermal equilibrium, and τ_s is the spin-relaxation time of the dark exciton. The fit curves are shown in Figures 51a and c, which allow us to extract the value of the spin-relaxation time and the saturated DCP. The saturated value of the time-resolved DCP was plotted as a function of external magnetic fields (Figures 51b, d). For CdSe NPLs, the saturated DCP (P_c^{sat}) first increases to +1.5 % in low magnetic fields (0 – 3 T) and then decreases crossing the zero polarization at B_c = 6 T. Such non-monotonous DCP behavior is due to the DB-dark exciton spin interactions, in good agreement with the exciton DCP calculated from polarized-PL spectra. For CdSe/CdS core/largest crown (30 min), the saturated DCP gradually decreases with increasing magnetic fields and tends to be saturated in high magnetic fields due to the dependency on the NPL orientation (Figure 51d, black circles). This finding is consistent with the trend of the exciton DCP calculated from the polarized PL spectroscopy (Figure 50b, orange triangles). With this evidence, we conclude that the core/largest crown NPLs (30 min) do not exhibit the impact of surface DB spins on the Zeeman splitting of the dark excitons. This also confirms the important role of the complete CdS crown in passivating surface traps on the side facets of CdSe NPLs.
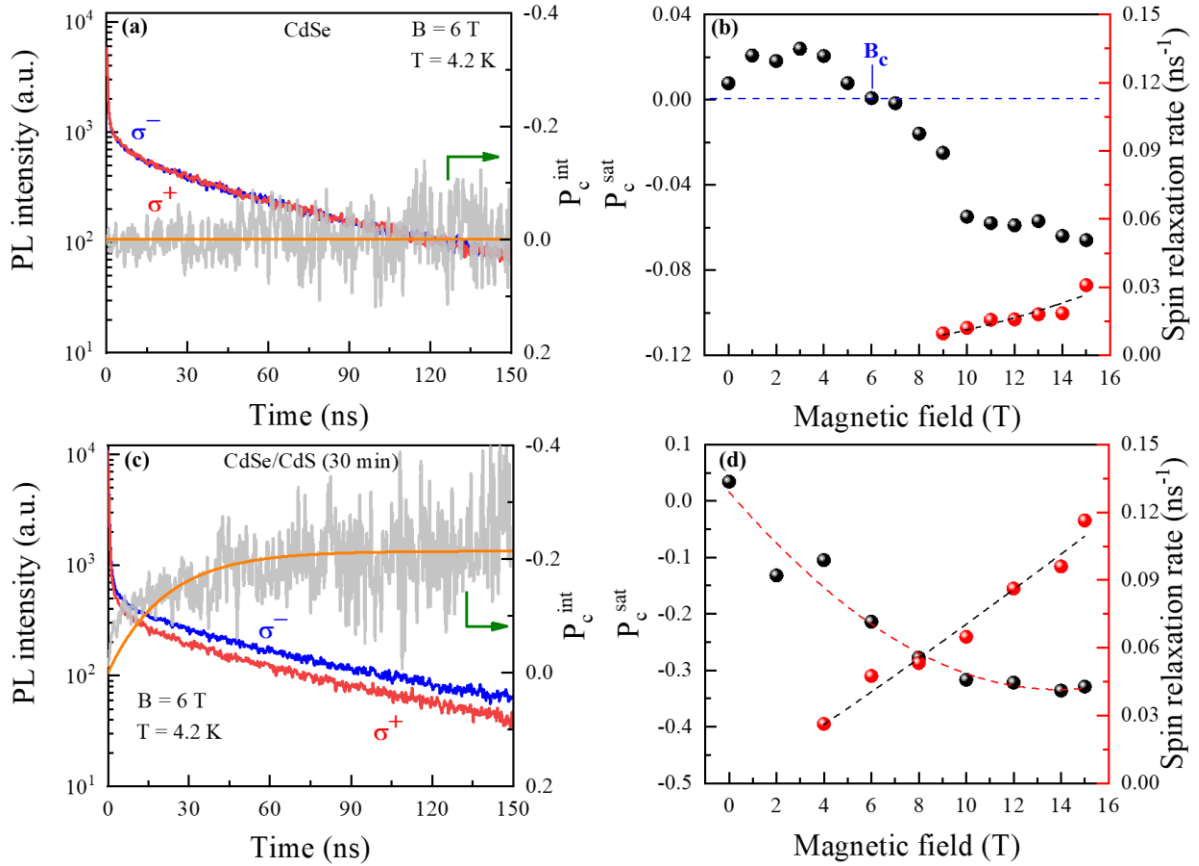
Figure 51: Polarization-resolved PL decays at T = 4.2 K for the exciton in (**a**) 4.5 ML CdSe NPLs, and (**c**) 4.5 ML CdSe/CdS core/crown NPLs (30 min). The time-resolved DCP curves were calculated according to equation (**4.11**), and fit (orange curves) to equation (**4.13**). The saturated DCP ($P_c^{sat} = P_c^{eq}$) and spin relaxation rate ($1/\tau_s$) were plotted as a function of external magnetic fields in (**b**) CdSe NPLs, and (**d**) CdSe/CdS core/crown NPLs (30 min).

It has been shown that a wide variety of spin interactions could take place in semiconductors such as spin-orbit interaction, electron-electron or electron-hole exchange interactions with magnetic impurities or phonons, and so on [48]. Each interaction type could provide a relaxation channel for the spin with a characteristic time referred to as the spin relaxation time (τ_s). In colloidal CdSe NPLs, the spin relaxation time relates to how long the dark exciton maintains its spin alignment before interacting with its environment (e.g., phonon, lattice vibrations, dangling bonds, etc) [49]. Such interactions randomize or flip the spin states of the dark exciton, as described in Figure 48b (the green arrow). As stated previously, the surface DB-electron spin interaction changed the polarized emission of the dark exciton in CdSe NPLs.

Therefore, studying the spin relaxation time (or rate) is necessary to understand the spin dynamics in NPLs. The spin relaxation rate ($1/\tau_s$) was plotted as a function of external magnetic fields (Figures 51b and d, red circles). The dynamics of the time-resolve DCP observed in the NPLs originate from relaxation between the dark exciton states $F = \pm 2$ [47]. For CdSe NPLs, the spin relaxation occurred ultrafast in low magnetic fields ($0 - 6$ T), thus our experiment can not probe the spin dynamics on such a very short time scale due to the limited resolution of 250 ps (see Figure 52). The ultrafast spin relaxation can be attributed to the surface DB-electron spin interactions. When the magnetic field exceeds 8 T, the spin relaxation rate increases linearly on the strength of magnetic fields (Figure 51b). For the core/largest crown NPLs, the spin relaxation rate increases linearly as the magnetic field increases from 4 T to 15 T (Figure 51d). Based on previous studies [47], [50], [51], we infer that acoustic phonons highly support the spin relaxation process in our core/crown NPLs. In contrast, the bare NPLs show the spin relaxation related to surface DB spins in the low-magnetic regime and phonons in the high-magnetic regime. In addition, the spin relaxation rate in the core/crown NPLs is larger by about two or three orders of magnitude compared to the bare NPLs. We suspect that the CdS crown part increased the number of acoustic phonons interacting with dark excitons in the core/crown NPLs (30 min).
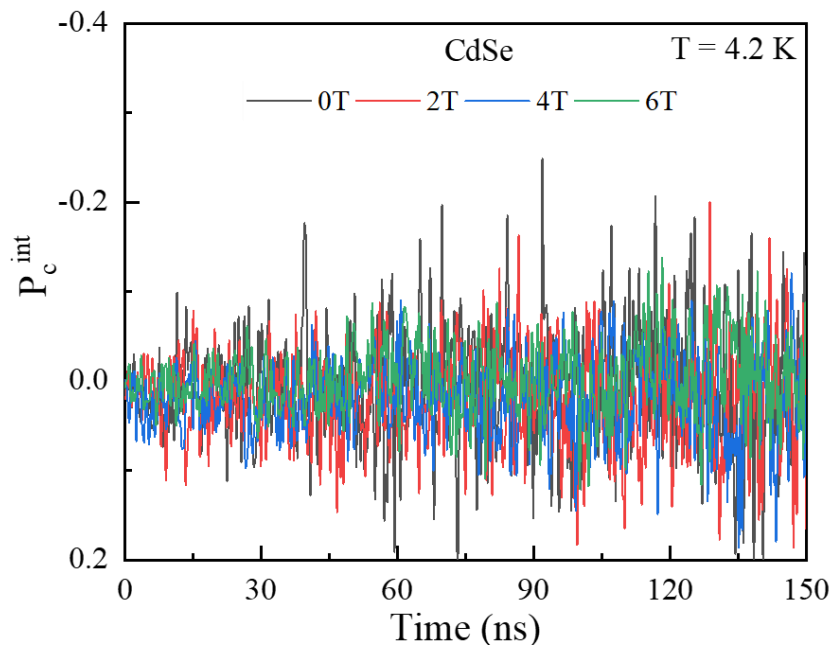

Figure 52: Magnetic field dependence of the time-resolved DCP (P_c^{int}) in 4.5 ML CdSe NPLs. The DCP curves were calculated according to equation (**4.11**).

4.8. Open discussion

Through analyzing the time-integrated and time-resolved DCP, we determined the effect of dangling bond spins on the polarized emission in 4.5 ML CdSe and CdSe/CdSe core/crown NPLs (5 min). The DB-dark exciton spin interaction caused the non-monotonous DCP depending on magnetic fields, in good agreement with the study by Shornikova et al [5]. However, what DB spins are the main responsibility causing the non-monotonous exciton DCP on the bare and core/crown NPLs (5 min) remains unknown. This originates from the fact that the side facets of CdSe NPLs consist of both Cd and rich-Se planes which give rise to the different nature of surface dangling bonds. Thus, knowing the contribution of each type of dangling bond will allow us to control or enhance the surface magnetism of NPLs with high precision. Another important question relates to the interface quality between CdS and CdSe NPLs in a heterostructure. An interface with fewer defects will favor good conditions for exciton transport from the crown to the core NPLs.

On the other hand, studying the spin relaxation time (or rate) emphasizes the important role of confined acoustic phonons in the relaxation and recombination processes of dark excitons in NPLs. To determine the role of acoustic phonons exactly, it is necessary to investigate the temperature-dependent spin relaxation rate in both the bare and core/crown NPLs. In addition, it is also necessary to investigate the effect of the CdS crown lateral size on the spin relaxation rate in core/crown NPLs. The obtained information may help to develop spintronic devices based on colloidal NPLs, e.g., spin storage.

4.9. Conclusion

In summary, we synthesized 4.5 ML CdSe/CdS core/crown NPLs with various crown lateral sizes by controlling the injection volume of the CdS precursors during a hot injection process. The formation of the CdS crown around the core NPLs was confirmed through STEM images and EDX element mapping. After that, we investigated the effect of surface dangling bond spins on the polarized emission in 4.5 ML CdSe NPLs and CdSe/CdS core/crown NPLs with various crown sizes using magneto-PL spectroscopy.

In external magnetic fields, the dark exciton spin structure is split into two spin sublevels, known as the exciton Zeeman splitting. As a result, the lowest level $|-2\rangle$ is circularly polarized and dominates the emission in the NPLs. Because of the spin interaction between surface dangling bonds and dark excitons, the exciton DCP shows a non-monotonous behavior with increasing magnetic fields. This finding indicates that surface dangling bonds can act similarly to diluted magnetic semiconductors, changing the magnetic and optical properties of NPLs at low temperatures. Based on the non-monotonous DCP behavior, we can conclude that surface DB spins induce antiferromagnetism behavior on the surface of CdSe NPLs.

To know the distribution of dangling bonds in NPLs, we calculated the exciton DCP in the CdSe/CdS core/crown NPLs with various crown sizes. We found that the CdSe/CdS core/smallest crown NPLs (5 min) also exhibit the non-monotonous DCP of the dark exciton similar to the CdSe NPLs. However, the DB-exciton spin interaction in the core/crown NPLs (5 min) is stronger than that in the bare NPLs, resulting in an enhancing exciton DCP (positive DCP values) in the core/crown NPLs.

When the crown lateral size becomes large, the CdS crown passivates surface dangling bonds on the side facets of the bare NPLs. As a result, the DB-dark exciton spin interaction is gradually suppressed, resulting in the disappearance of the non-monotonous DCP behavior in the core/crown NPLs (12 min – 30 min). This finding demonstrated that surface DB spins on the side facets strongly interact with electron spins localized in the CdSe NPLs, leading to the non-monotonous DCP of the dark exciton. This conclusion is very consistent with the STM/STS results in Chapter III, where the STM current mapping image showed that most surface traps (electron and

hole traps) concentrate on the side facets of NPLs. Indeed, surface traps mainly originate from structural defects and dangling bonds of under-coordinated atoms in NPLs. Therefore, trap states always accompany the presence of surface dangling bonds. On the other hand, the finding on the surface magnetism of NPLs indicates a potential for the use of colloidal NPLs as nanomagnetic markers.

Not only that, we also performed polarization-resolved PL decays in the bare NPLs and the core/largest crown NPLs (30 min). By analyzing the saturated DCP values of the time-resolved DCP (for exciton), we found that the saturated DCP (P_c^{sat}) non-monotonously varies with increasing magnetic fields, similar to the time-integrated DCP of the dark exciton measured by polarized-PL spectroscopy. This result confirms the impact of the surface DB-dark exciton spin interactions on the polarized emission in NPLs. Moreover, we observed the ultrafast spin relaxation in low magnetic fields caused by surface DBs in the bare NPLs. Meanwhile, CdSe/CdS core/crown NPLs (30 min) show the linear dependency of the spin relaxation rate on external magnetic fields.

Bibliography

[1]   A. Dutta *et al.*, "Hybrid Nanostructures of 2D CdSe Nanoplatelets for High-Performance Photodetector Using Charge Transfer Process," *ACS Appl. Nano Mater.*, vol. 3, no. 5, pp. 4717–4727, May 2020, doi: 10.1021/acsanm.0c00728.

[2]   B. Liu *et al.*, "Management of electroluminescence from silver-doped colloidal quantum well light-emitting diodes," *Cell Reports Phys. Sci.*, vol. 3, no. 5, p. 100860, 2022, doi: https://doi.org/10.1016/j.xcrp.2022.100860.

[3]   M. S. Seehra *et al.*, "Size-Controlled Ex-nihilo Ferromagnetism in Capped CdSe Quantum Dots," *Adv. Mater.*, vol. 20, no. 9, pp. 1656–1660, May 2008, doi: https://doi.org/10.1002/adma.200702382.

[4]   R. W. Meulenberg *et al.*, "Evidence for Ligand-Induced Paramagnetism in CdSe Quantum Dots," *J. Am. Chem. Soc.*, vol. 131, no. 20, pp. 6888–6889, May 2009, doi: 10.1021/ja8098454.

[5]   E. V Shornikova *et al.*, "Surface spin magnetism controls the polarized exciton emission from CdSe nanoplatelets," *Nat. Nanotechnol.*, vol. 15, no. 4, pp. 277–282, 2020, doi: 10.1038/s41565-019-0631-7.

[6]   M. A. Semina, A. A. Golovatenko, and A. V Rodina, "Electron, hole and exciton effective g-factors in semiconductor nanocrystals," *arXiv Prepr. arXiv2011.11041*, 2020.

[7]   D. Xiang, Y. Li, L. Wang, T. Ding, J. Wang, and K. Wu, "Electron and Hole Spin Relaxation in CdSe Colloidal Nanoplatelets," *J. Phys. Chem. Lett.*, vol. 12, no. 1, pp. 86–93, Jan. 2021, doi: 10.1021/acs.jpclett.0c03257.

[8]   A. Rodina and A. L. Efros, "Magnetic Properties of Nonmagnetic Nanostructures: Dangling Bond Magnetic Polaron in CdSe Nanocrystals," *Nano Lett.*, vol. 15, no. 6, pp. 4214–4222, Jun. 2015, doi: 10.1021/acs.nanolett.5b01566.

[9]   A. J. Houtepen, Z. Hens, J. S. Owen, and I. Infante, "On the Origin of Surface Traps in Colloidal II–VI Semiconductor Nanocrystals," *Chem. Mater.*, vol. 29,

no. 2, pp. 752–761, Jan. 2017, doi: 10.1021/acs.chemmater.6b04648.

[10] S. O. M. Hinterding *et al.*, "Single Trap States in Single CdSe Nanoplatelets," *ACS Nano*, vol. 15, no. 4, pp. 7216–7225, 2021, doi: 10.1021/acsnano.1c00481.

[11] S. Pokrant and K. B. Whaley, "Tight-binding studies of surface effects on electronic structure of CdSe nanocrystals: the role of organic ligands, surface reconstruction, and inorganic capping shells," *Eur. Phys. J. D - At. Mol. Opt. Plasma Phys.*, vol. 6, no. 2, pp. 255–267, 1999, doi: 10.1007/s100530050307.

[12] M. Nirmal and L. Brus, "Luminescence Photophysics in Semiconductor Nanocrystals," *Acc. Chem. Res.*, vol. 32, no. 5, pp. 407–414, May 1999, doi: 10.1021/ar9700320.

[13] M. Nirmal, D. J. Norris, M. Kuno, M. G. Bawendi, A. L. Efros, and M. Rosen, "Observation of the 'Dark Exciton' in CdSe Quantum Dots," *Phys. Rev. Lett.*, vol. 75, no. 20, pp. 3728–3731, Nov. 1995, doi: 10.1103/PhysRevLett.75.3728.

[14] A. L. Efros, M. Rosen, M. Kuno, M. Nirmal, D. J. Norris, and M. Bawendi, "Band-edge exciton in quantum dots of semiconductors with a degenerate valence band: Dark and bright exciton states," *Phys. Rev. B*, vol. 54, no. 7, pp. 4843–4856, Aug. 1996, doi: 10.1103/PhysRevB.54.4843.

[15] A. L. Efros, "Luminescence polarization of CdSe microcrystals," *Phys. Rev. B*, vol. 46, no. 12, pp. 7448–7458, Sep. 1992, doi: 10.1103/PhysRevB.46.7448.

[16] L. Biadala *et al.*, "Magnetic polaron on dangling-bond spins in CdSe colloidal nanocrystals," *Nat. Nanotechnol.*, vol. 12, no. 6, pp. 569–574, 2017, doi: 10.1038/nnano.2017.22.

[17] V. A. Kiselev, B. S. Razbirin, and I. N. Uraltsev, "Additional waves and Fabry-Perot interference of photoexcitons (polaritons) in thin II–VI crystals," *Phys. status solidi*, vol. 72, no. 1, pp. 161–172, Nov. 1975, doi: https://doi.org/10.1002/pssb.2220720117.

[18] E. V Shornikova *et al.*, "Addressing the exciton fine structure in colloidal nanocrystals: the case of CdSe nanoplatelets," *Nanoscale*, vol. 10, no. 2, pp. 646–

656, 2018, doi: 10.1039/C7NR07206F.

[19] G. Qiang, "Magneto-optical properties of semiconductor nanocrystals in glass." 2022. [Online]. Available: https://scholar.google.com/citations?view_op=view_citation&hl=en&user=Am1 jY2wAAAAJ&citation_for_view=Am1jY2wAAAAJ:LkGwnXOMwfcC

[20] L. Biadala, Y. Louyer, P. Tamarat, and B. Lounis, "Direct Observation of the Two Lowest Exciton Zero-Phonon Lines in Single CdSe/ZnS Nanocrystals," *Phys. Rev. Lett.*, vol. 103, no. 3, p. 37404, Jul. 2009, doi: 10.1103/PhysRevLett.103.037404.

[21] O. Labeau, P. Tamarat, and B. Lounis, "Temperature Dependence of the Luminescence Lifetime of Single CdSSe/ZnS Quantum Dots," *Phys. Rev. Lett.*, vol. 90, no. 25, p. 257404, Jun. 2003, doi: 10.1103/PhysRevLett.90.257404.

[22] S. B. Singh, M. V Limaye, S. K. Date, and S. K. Kulkarni, "Room temperature ferromagnetism in thiol-capped CdSe and CdSe:Cu nanoparticles," *Chem. Phys. Lett.*, vol. 464, no. 4, pp. 208–210, 2008, doi: https://doi.org/10.1016/j.cplett.2008.09.020.

[23] K. Leung, S. Pokrant, and K. B. Whaley, "Exciton fine structure in CdSe nanoclusters," *Phys. Rev. B*, vol. 57, no. 19, pp. 12291–12301, May 1998, doi: 10.1103/PhysRevB.57.12291.

[24] A. Schlosser, R. T. Graf, and N. C. Bigall, "CdS crown growth on CdSe nanoplatelets: core shape matters," *Nanoscale Adv.*, vol. 2, no. 10, pp. 4604–4614, 2020, doi: 10.1039/D0NA00619J.

[25] M. D. Tessier, P. Spinicelli, D. Dupont, G. Patriarche, S. Ithurria, and B. Dubertret, "Efficient Exciton Concentrators Built from Colloidal Core/Crown CdSe/CdS Semiconductor Nanoplatelets," *Nano Lett.*, vol. 14, no. 1, pp. 207–213, Jan. 2014, doi: 10.1021/nl403746p.

[26] C. Rodà *et al.*, "Colloidal CdSe/CdS Core/Crown Nanoplatelets for Efficient Blue Light Emission and Optical Amplification," *Nano Lett.*, vol. 23, no. 8, pp. 3224–

3230, 2023, doi: 10.1021/acs.nanolett.2c05061.

[27] Q. Li, K. Wu, J. Chen, Z. Chen, J. R. McBride, and T. Lian, "Size-Independent Exciton Localization Efficiency in Colloidal CdSe/CdS Core/Crown Nanosheet Type-I Heterostructures," *ACS Nano*, vol. 10, no. 3, pp. 3843–3851, Mar. 2016, doi: 10.1021/acsnano.6b00787.

[28] A. Prudnikau, A. Chuvilin, and M. Artemyev, "CdSe–CdS Nanoheteroplatelets with Efficient Photoexcitation of Central CdSe Region through Epitaxially Grown CdS Wings," *J. Am. Chem. Soc.*, vol. 135, no. 39, pp. 14476–14479, Oct. 2013, doi: 10.1021/ja401737z.

[29] M. D. Tessier, C. Javaux, I. Maksimovic, V. Loriette, and B. Dubertret, "Spectroscopy of Single CdSe Nanoplatelets," *ACS Nano*, vol. 6, no. 8, pp. 6751–6758, 2012, doi: 10.1021/nn3014855.

[30] F. V Antolinez *et al.*, "Trion Emission Dominates the Low-Temperature Photoluminescence of CdSe Nanoplatelets," *Nano Lett.*, vol. 20, no. 8, pp. 5814–5820, Aug. 2020, doi: 10.1021/acs.nanolett.0c01707.

[31] J. C. van der Bok, D. M. Dekker, M. L. J. Peerlings, B. B. V Salzmann, and A. Meijerink, "Luminescence Line Broadening of CdSe Nanoplatelets and Quantum Dots for Application in w-LEDs," *J. Phys. Chem. C*, vol. 124, no. 22, pp. 12153–12160, Jun. 2020, doi: 10.1021/acs.jpcc.0c03048.

[32] S. Christodoulou *et al.*, "Chloride-Induced Thickness Control in CdSe Nanoplatelets," *Nano Lett.*, vol. 18, no. 10, pp. 6248–6254, 2018, doi: 10.1021/acs.nanolett.8b02361.

[33] S. Ayari *et al.*, "Tuning trion binding energy and oscillator strength in a laterally finite 2D system: CdSe nanoplatelets as a model system for trion properties," *Nanoscale*, vol. 12, no. 27, pp. 14448–14458, 2020, doi: 10.1039/D0NR03170D.

[34] E. V Shornikova *et al.*, "Negatively Charged Excitons in CdSe Nanoplatelets," *Nano Lett.*, vol. 20, no. 2, pp. 1370–1377, 2020, doi: 10.1021/acs.nanolett.9b04907.

[35] M. Furis, J. A. Hollingsworth, V. I. Klimov, and S. A. Crooker, "Time- and Polarization-Resolved Optical Spectroscopy of Colloidal CdSe Nanocrystal Quantum Dots in High Magnetic Fields," *J. Phys. Chem. B*, vol. 109, no. 32, pp. 15332–15338, Aug. 2005, doi: 10.1021/jp051738b.

[36] E. Johnston-Halperin *et al.*, "Spin spectroscopy of dark excitons in CdSe quantum dots to 60 T," *Phys. Rev. B*, vol. 63, no. 20, p. 205309, Apr. 2001, doi: 10.1103/PhysRevB.63.205309.

[37] F. Liu *et al.*, "Spin dynamics of negatively charged excitons in CdSe/CdS colloidal nanocrystals," *Phys. Rev. B*, vol. 88, no. 3, p. 35302, Jul. 2013, doi: 10.1103/PhysRevB.88.035302.

[38] G. Qiang *et al.*, "Polarized emission of CdSe nanocrystals in magnetic field: the role of phonon-assisted recombination of the dark exciton," *Nanoscale*, vol. 13, no. 2, pp. 790–800, 2021, doi: 10.1039/D0NR07117J.

[39] J. A. Gupta, D. D. Awschalom, A. L. Efros, and A. V Rodina, "Spin dynamics in semiconductor nanocrystals," *Phys. Rev. B*, vol. 66, no. 12, p. 125307, Sep. 2002, doi: 10.1103/PhysRevB.66.125307.

[40] O. Z. Karimov *et al.*, "Electron g-factor for cubic Zn1-xCdSxSe determined by spin-flip Raman scattering," *Phys. Rev. B*, vol. 62, no. 24, pp. 16582–16586, Dec. 2000, doi: 10.1103/PhysRevB.62.16582.

[41] A. F. Vong, S. Irgen-Gioro, Y. Wu, and E. A. Weiss, "Origin of Low Temperature Trion Emission in CdSe Nanoplatelets," *Nano Lett.*, vol. 21, no. 23, pp. 10040–10046, 2021, doi: 10.1021/acs.nanolett.1c03726.

[42] Q. Li, Q. Liu, R. D. Schaller, and T. Lian, "Reducing the Optical Gain Threshold in Two-Dimensional CdSe Nanoplatelets by the Giant Oscillator Strength Transition Effect," *J. Phys. Chem. Lett.*, vol. 10, no. 7, pp. 1624–1632, Apr. 2019, doi: 10.1021/acs.jpclett.9b00759.

[43] E. V Shornikova *et al.*, "Electron and Hole g-Factors and Spin Dynamics of Negatively Charged Excitons in CdSe/CdS Colloidal Nanoplatelets with Thick

Shells," *Nano Lett.*, vol. 18, no. 1, pp. 373–380, Jan. 2018, doi: 10.1021/acs.nanolett.7b04203.

[44]   A. V Rodina, A. A. Golovatenko, E. V Shornikova, D. R. Yakovlev, and A. L. Efros, "Effect of Dangling Bond Spins on the Dark Exciton Recombination and Spin Polarization in CdSe Colloidal Nanostructures," *J. Electron. Mater.*, vol. 47, no. 8, pp. 4338–4344, 2018, doi: 10.1007/s11664-018-6269-7.

[45]   L. S. ZZ Ditina, "Investigation of the surface of cadmium selenide by the EPR method." SOV PHYS SOLID STATE, 1968.

[46]   M. A. Semina, A. A. Golovatenko, and A. V Rodina, "Influence of the spin-orbit split-off valence band on the hole g factor in semiconductor nanocrystals," *Phys. Rev. B*, vol. 104, no. 20, p. 205423, Nov. 2021, doi: 10.1103/PhysRevB.104.205423.

[47]   B. Siebers *et al.*, "Exciton spin dynamics and photoluminescence polarization of CdSe/CdS dot-in-rod nanocrystals in high magnetic fields," *Phys. Rev. B*, vol. 91, no. 15, p. 155304, Apr. 2015, doi: 10.1103/PhysRevB.91.155304.

[48]   M. Dyakonov, *Spin Physics in Semiconductors*, vol. 1. 2008. doi: 10.1007/978-3-540-78820-1.

[49]   D. Pines and C. P. Slichter, "Relaxation Times in Magnetic Resonance," *Phys. Rev.*, vol. 100, no. 4, pp. 1014–1020, Nov. 1955, doi: 10.1103/PhysRev.100.1014.

[50]   A. Granados del Águila *et al.*, "Observation of the Full Exciton and Phonon Fine Structure in CdSe/CdS Dot-in-Rod Heteronanocrystals," *ACS Nano*, vol. 8, no. 6, pp. 5921–5931, Jun. 2014, doi: 10.1021/nn501026t.

[51]   D. Oron, A. Aharoni, C. de Mello Donega, J. van Rijssel, A. Meijerink, and U. Banin, "Universal Role of Discrete Acoustic Phonons in the Low-Temperature Optical Emission of Colloidal Quantum Dots," *Phys. Rev. Lett.*, vol. 102, no. 17, p. 177402, Apr. 2009, doi: 10.1103/PhysRevLett.102.177402.

Dissertation Conclusion

The thesis explored the structural, and optoelectronic properties of 4.5 ML CdSe and CdSe/CdS core/crown NPLs through the LT-STM/STS and magneto-PL spectroscopy techniques. For CdSe NPLs, the STM topographic images revealed the truncated edges of NPLs and their side facets are atomic terraces. Consequently, most surface traps including electron and deep hole traps mainly concentrate on the side facets, leading to a strong fluctuation of the tunneling current as observed in the STM current mapping image. On the other hand, tunneling dI/dV spectra (STS) measured on isolated and flat-lying NPLs indicated that the top surface of NPLs mainly hosts shallow electron traps and their distribution is random. These results provided insight into the electronic band structure such as band edges, band gaps, and trap states in individual NPLs. In particular, the observation of truncated edges implied the complexity of the growth mechanism at the NPL edges, which provides critical information for optimizing the growth process of NPLs. On the other hand, after knowing the energetic level of an electron trap ($V_{e\text{-trap}} = +0.65$ V), we investigated the trapping mechanisms by recording the tunneling current in real-time. Interestingly, we observed the blinking behavior in the tunneling current caused by the electron trap. Power spectral density (PSD) was used to characterize the blinking behavior in the tunneling current. As a result, the PSD curves show a power law dependence in high frequencies (above 10 Hz) with an exponent of 2 and a characteristic timescale of $17 - 69$ ms. This result indicated that a single electron trap behaves as a stochastic two-level system. These findings are meaningful for developing strategies aimed at engineering the trap states with the desired properties.

Through a comprehensive investigation utilizing magneto-PL spectroscopy at 4.2 K, we demonstrated that the surface DB-electron spin interactions play a vital role in determining magneto-optical effects in NPLs. In low magnetic fields, surface DB spins can interact with the electron spin localized in the dark exciton, resulting in the reversed order of the exciton spin sublevels. As a result, the exciton DCP depends non-linearly on the strength of magnetic fields in CdSe NPLs (non-monotonous DCP behavior). Such exciton DCP behavior represents the antiferromagnetic properties on the surface

of CdSe NPLs. A similar DCP behavior of the exciton was also observed in CdSe/CdS core/smallest crown NPLs (5 min), but its DCP magnitude is larger than that of the bare NPLs. When the lateral size of the CdS crown becomes larger, the exciton DCP increases linearly on magnetic fields because the electron-DB spin interaction is gradually disabled. This indicated that dangling bonds on the side facets of CdSe NPLs play an important role in forming the magneto-optical effects in NPLs. This conclusion is consistent with the evidence of the dense presence of surface traps on the side facets of CdSe NPLs revealed by the STM technique. On the other hand, we also demonstrated the support of acoustic phonons in the relaxation and recombination of dark excitons in NPLs, contributing to the understanding of the spin dynamics in NPLs. These findings open promising avenues for adjusting magneto-optical functionalities for potential applications such as magnetic markers [1], spintronics [2], and quantum information processing [3].

In summary, our work emphasizes the importance of understanding and controlling the surface characteristics of colloidal nanoplatelets for improving or exploiting their full potential in applications. Future research directions will focus on optimizing the colloidal synthesis of NPLs to reduce or enhance surface dangling bonds for specific applications. Additionally, our study provided insight into the structural and optoelectronic properties of NPLs which will help to understand physical mechanisms governing their optoelectronic properties. The use of the STM/STS technique offers a chance to understand the electronic properties of colloidal semiconductor NCs at the nanoscale.

Bibliography

[1]   E. V Shornikova *et al.*, "Surface spin magnetism controls the polarized exciton emission from CdSe nanoplatelets," *Nat. Nanotechnol.*, vol. 15, no. 4, pp. 277–282, 2020, doi: 10.1038/s41565-019-0631-7.

[2]   S.-H. Yang, R. Naaman, Y. Paltiel, and S. S. P. Parkin, "Chiral spintronics," *Nat. Rev. Phys.*, vol. 3, no. 5, pp. 328–343, 2021, doi: 10.1038/s42254-021-00302-9.

[3]   J. Almutlaq *et al.*, "Engineering colloidal semiconductor nanocrystals for quantum information processing," *Nat. Nanotechnol.*, 2024, doi: 10.1038/s41565-024-01606-4.

Perspective Section: Quantum Confinement Effects In PbSe Nanoplatelets Probed By Scanning Tunneling Microscopy

Our studies have shed light on the pivotal role of measuring the DOS in correlation with the structural properties of colloidal nanomaterials. It is crucial to extend our understanding of promising materials in nanotechnology beyond CdSe.

In this regard, we will present recent results we obtained on the electronic properties of colloidal lead chalcogenide NPLs, which are highly interesting regarding their bandgap energy that lay in the infrared range. Utilizing low-temperature scanning tunneling microscopy (LT-STM), we aim to probe the electronic band structure of PbSe NPLs at the atomic level, particularly exploring quantum confinement effects occurring in NPLs.

Abstract

The growing attention paid to colloidal lead chalcogenide NPLs due to their outstanding optoelectronic properties, where lead selenide (PbSe) NPLs with emission wavelengths of 800 – 1000 nm and narrow photoluminescence are highly interesting materials for potential applications in the field of telecoms and optoelectronics [1], [2]. However, the electronic properties of PbSe NPLs have not been fully investigated at the atomic scale yet. This will restrict the understanding of quantum confinement effects occurring in NPLs. In this work, we employed low-temperature scanning tunneling microscopy (LT-STM) and spectroscopy (LT-STS) to investigate the structural and electronic properties of ultrathin PbSe NPLs (less Se). Analyzing STM topographic images of individual NPLs, we detected various thicknesses of NPLs in the same sample batch. STS measurements on isolated NPLs indicate distinct variations in the density of states (DOS) as the NPL thickness increases. Thicker NPLs exhibit a smaller band gap energy due to the strong quantum confinement effect along the thickness. We found that 1.6 nm thick NPLs have an electronic band gap of 1.0 eV which dominates the emission properties of the whole NPL sample. Based on experimental STS results, the band structure of NPLs was simulated by tight-binding calculations at different thicknesses and lateral sizes. As a result, we observed that the electronic properties of NPLs do not

only depend on the thickness but also on their lateral size. These findings provide critical insights into the tunability of the electronic properties of NPLs for nanoscale electronic, optoelectronic, and telecom applications.

Graphic abstract: (a) STEM and EDX element mapping image of PbSe NPLs. (b) Schematic illustration of LT-STM/STS measurements on an isolated NPL. (c) Tunneling dI/dV spectra were measured on 1.6 nm, 0.8 nm, and 0.45 nm thick-NPLs, showing the 1D quantum confinement effect occurring along the thickness of NPLs (d).
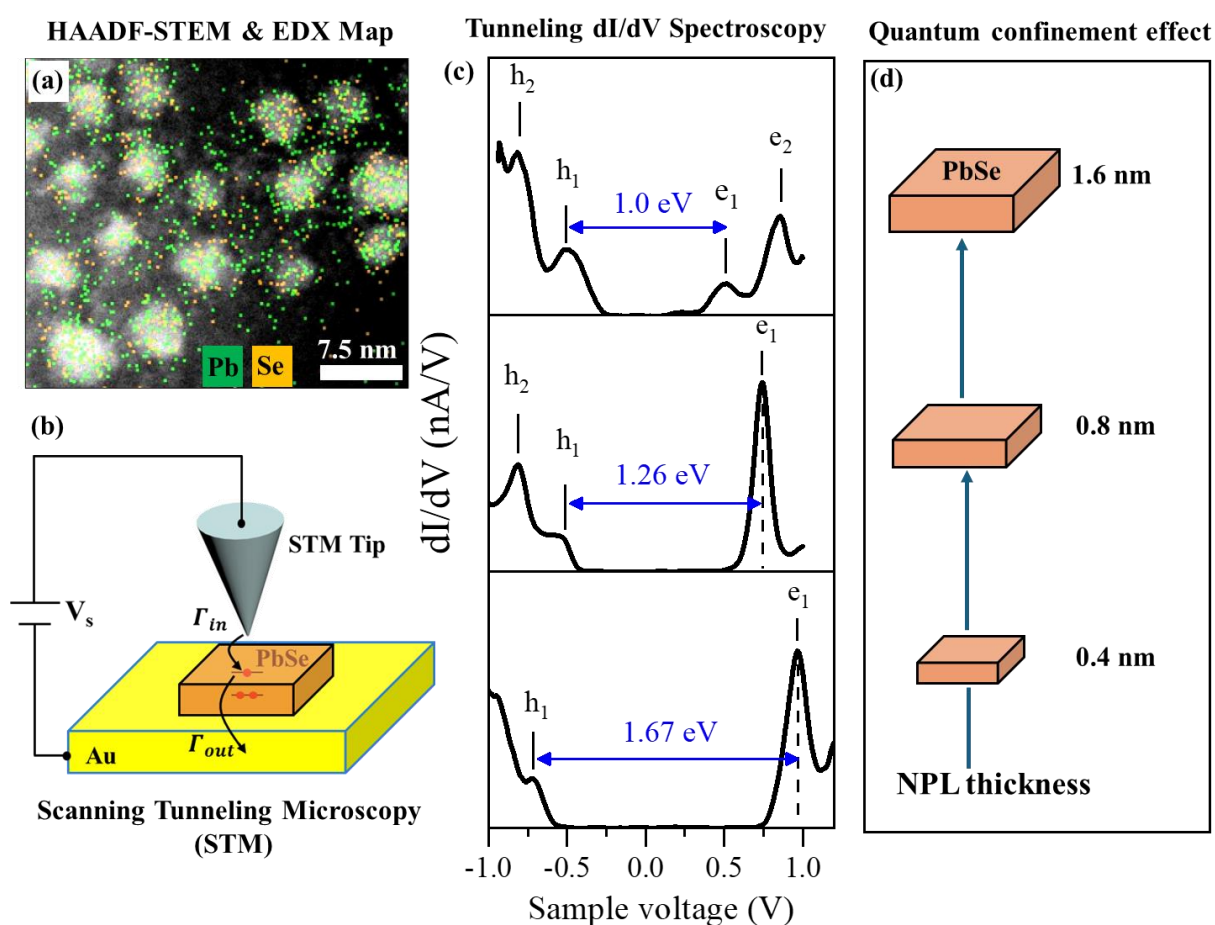
5.1. Introduction

The commonality of all colloidal semiconductor nanoplatelets (NPLs) is the possibility of adjusting the optoelectronic properties by controlling their shape and size during synthesis. The current synthesis of colloidal NPLs mainly concentrates on the II-VI semiconductor group with the CdX (X = S, Se, Te) being the most common. Recent advances in colloidal chemistry have enabled the synthesis of IV-VI semiconductors, specifically, lead selenium (PbSe) nanoplatelets with well-controlled thicknesses [3]. Colloidal PbSe NPLs have become a promising nanomaterial with tunable absorption and emission properties covering the near-infrared wavelength range (NIR) of the electromagnetic spectrum [1], [2], [3]. This optical property is suitable for applications in biological imaging [4], and fiber optics [5], [6]. In addition, the telecom wavelength of PbSe NPLs is highly interesting for developing single photon sources which are key components for quantum technologies such as quantum key distribution [7], quantum communication and computing [8].

Colloidal PbSe NPLs can be prepared via direct and indirect synthetic processes, for example, one can synthesize PbSe NPLs via the Cd^{2+} cation exchange in CdSe NPLs [3], [9], [10]. Recently, F. Klepzig and co-workers reported a direct synthesis of PbSe NPLs by injecting the Se-precursor solution into the mixture of $Pb(OA)_2$, octylamine, oleic acid, and hexane at 0 ºC [1]. The emission wavelength of NPLs is controlled by adjusting the amount of octylamine and the reaction temperature. The difference in the synthetic methods (direct and indirect) of PbSe NPLs results in exciting optical properties depending on the size of NPLs. Specifically, PbSe NPLs prepared via a Cd^{2+} cation exchange process exhibit thickness-dependent emission wavelengths that are the same as CdSe NPLs, known as the 1D-quantum confinement effect [3], [10]. In contrast, PbSe NPLs prepared via a direct synthesis show the dependency of the emission wavelengths on lateral sizes, like the quantum confinement effect occurring in 2D semiconductors [1]. The precise control over the lateral size and thickness offers opportunities for adjusting the absorption and emission properties of PbSe NPLs for various applications. Despite this, the electronic properties of NPLs have not been fully

investigated at the nanoscale until now. This can limit the understanding of physical mechanisms governing the optoelectronic properties of NPLs.

Here, the structural and electronic properties of PbSe NPLs were investigated with high-angle annular dark-field scanning transmission electron microscopy (HAADF-STEM), low-temperature scanning tunneling microscopy (LT-STM), and spectroscopy (LT-STS). The STM/STS technique was performed on individual NPLs at 77 K under an ultrahigh vacuum. The obtained results will clarify three main themes as follows: (1) the shape and thickness of NPLs, (2) the electronic band structure of NPLs (e.g. band edges, band gap, etc), and (3) quantum confinement effects in NPLs. For these targets, ultrathin PbSe NPLs (less Se) were synthesized based on the reported protocol of Biesterfeld et al [11] with a minor modification related to the amount of octylamine and hexane. Specifically, we used octylamine (18.0 mL, 108 mmol), and hexane (2.0 mL, 15.2 mmol). The detailed protocol and purification of NPLs were described in the reference [11]. The resulting PbSe NPLs were redispersed in hexane and stored at -25 ºC inside a nitrogen-filled glovebox for further use.
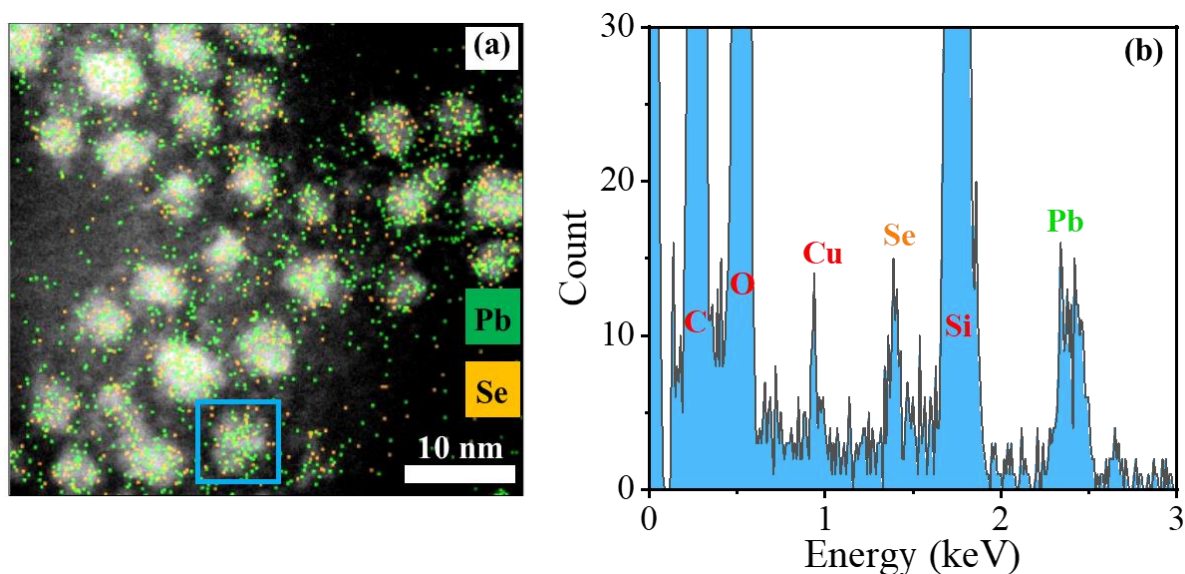

Figure 53: (a) STEM image and EDX element map of PbSe NPLs. **(b)** EDX spectrum of a single NPL marked by the blue rectangle in Figure b.

After the material synthesis, the chemical composition of NPLs was analyzed by energy-dispersive X-ray spectroscopy (EDX). Figure 53a shows a scanning transmission electron microscopy (STEM) image and an EDX element map of NPLs,

with Se and Cd atoms being found on the TEM grid. As expected for PbSe NPLs (less Se), the EDX map displays the dense presence of Pb atoms rather than Se atoms. Figure 53b presents the EDS spectrum of a single NPL (Figure 53a, the blue rectangle). The PbSe structure exhibits the lead peak (Mα = 2.3 keV) and the selenium peak (Lα = 1.38 keV) [12], [13]. The carbon, oxygen, and copper peaks are attributed to the carbon-formvar copper TEM grid. In addition, a silicon peak is observed at 1.75 keV which can be attributed to contaminations on the TEM grid. The EDX analysis confirms the formation of PbSe NPLs.

5.2. Structural properties of PbSe NPLs analyzed by HAADF-STEM.

In addition to chemical composition, shape, and size are two important parameters that influence the optoelectronic properties of colloidal NPLs. In this work, we employed high-angle annular dark-field scanning transmission electron microscopy (HAADFS-STEM) to investigate the structural properties of PbSe NPLs. Figure 54a shows the presence of NPLs with various shapes and sizes. Analyzing 200 NPLs, the average lateral size is estimated to be 3.5 nm × 4.8 nm (Figure 54d). Atomically resolved HAADF-STEM was employed to investigate the structural characteristics of individual NPLs. Figure 54b presents the HAADF-STEM image of an isolated NPL with high contrast, showing the atomic ordering on the top surface. The corresponding FFT pattern is presented in Figure 54c, exhibiting the characteristic reflections of rock-salt PbSe with [100] in a zone axis, in good agreement with previous reports [2], [10]. The lattice spacing of the (020) plane is calculated to be 3.1 Å.
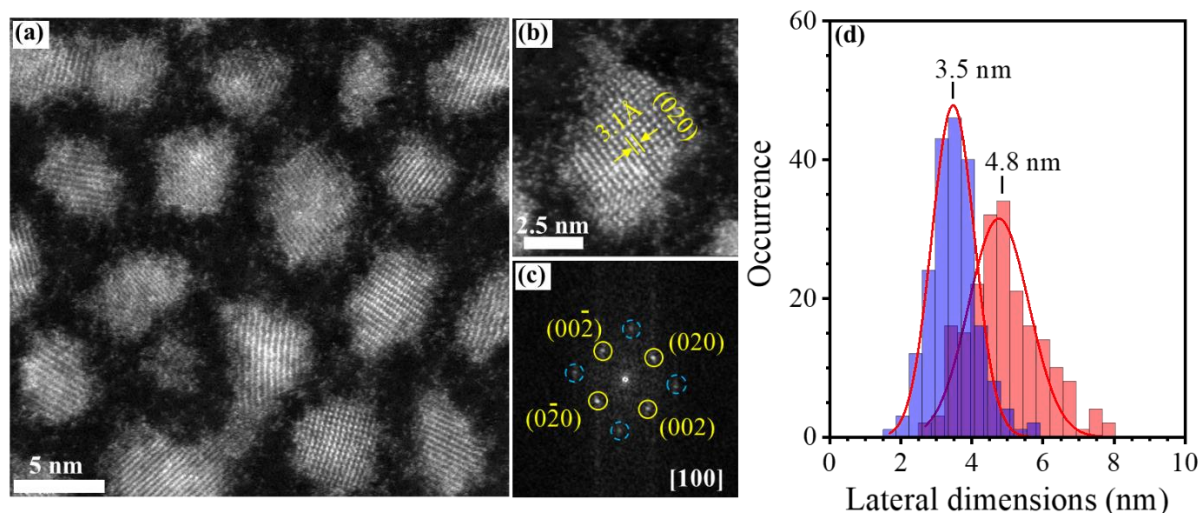
Figure 54: (a) HAADF-STEM image of PbSe NPLs. **(b)** Atomically resolved HAADF-STEM image of an isolated NPL. **(c)** Corresponding FFT pattern. **(d)** Lateral size distribution calculated from 200 NPLs.

5.3. Topography of PbSe NPLs investigated with scanning tunneling microscopy

The HAADF-STEM technique provided detailed information on the structural properties of NPLs, particularly the crystal structure which is important for the electronic properties of NPLs. However, the thickness of NPLs has not been determined yet via the HAADF-STEM images. Here, the LT-STM technique was employed to investigate the shape and thickness of PbSe NPLs. The sample for the STM measurement was prepared by drop-casting the NPL solution on a gold substrate. Figure 55a shows a topographic image of self-assembled layers of PbSe NPLs. The NPLs are very stable under STM imaging conditions (V_s = 4 V, I_t = 30 pA), thus the NPL shape can be observed clearly through the STM image. To determine the thickness exactly, the STM tip was scanned over areas having self-assembled monolayers of NPLs. Figures 55b and c show STM topographic images of isolated PbSe NPLs. The height profile of these NPLs was extracted along the red-dashed lines and presented in Figure 55d. The estimated total height of each NPL is 0.45 nm (for NPL1), and 0.8 nm (for NPL2 and NPL3). These height values are also the thicknesses of NPLs. The statistic

on the NPL thickness is presented in Figure 55e, showing three typical thicknesses of 0.4 nm, 0.8 nm, and 1.6 nm.
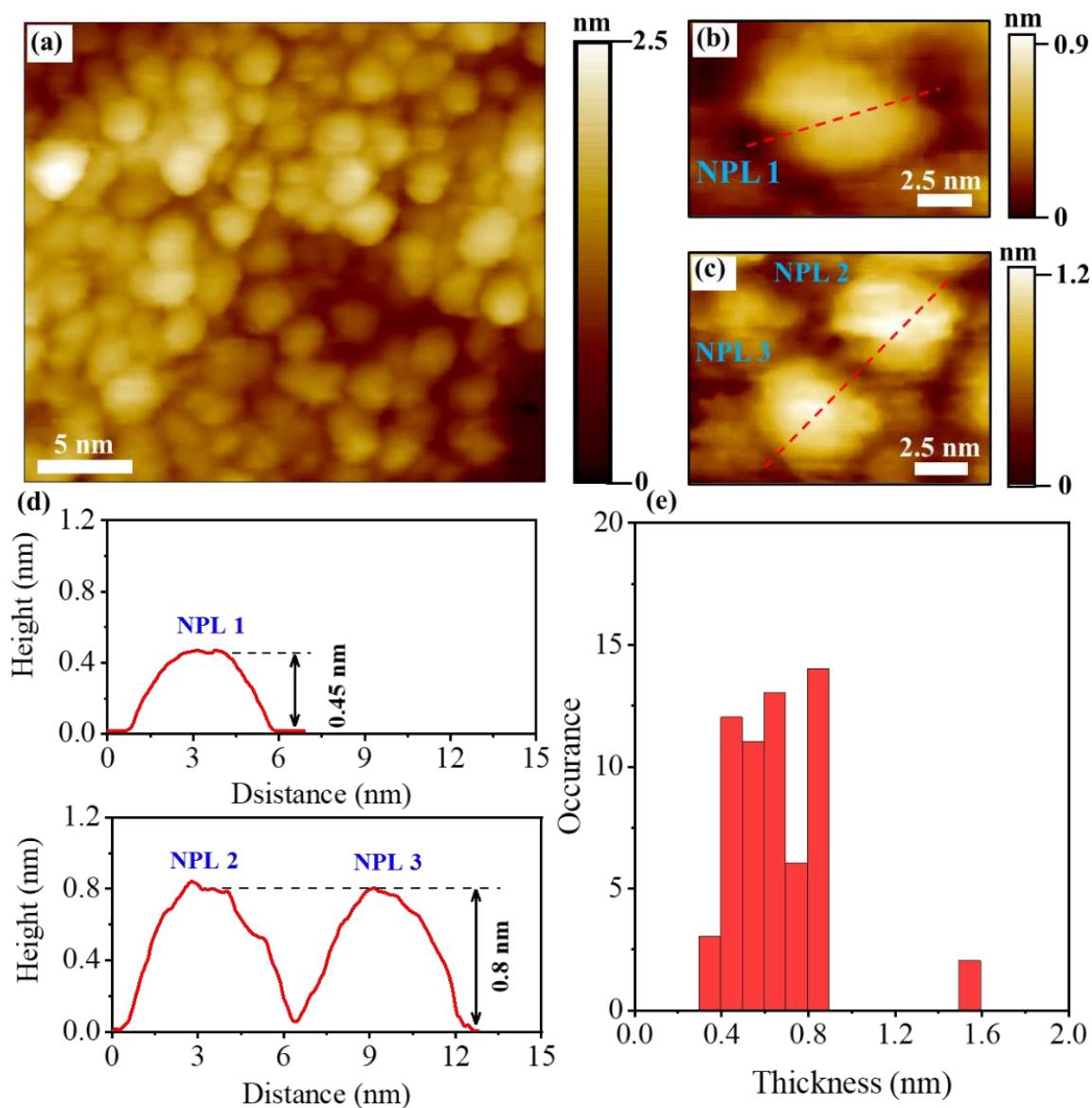

Figure 55: (a) STM topographic image of PbSe multilayers measured at $V_s = 4V$, $I_t = 50$ pA, T = 300 K. **(b-c)** STM topographic images of **(b)** 0.45 nm thick NPL ($V_s = 5$ V, $I_t = 50$ pA, t = 77 K), and **(c)** 0.8 nm thick NPL ($V_s = 3V$, $I_t = 40$ pA, T = 77 K). **(d)** Height profiles extracted along the red dashed lines in Figures **b** and **c**. **(e)** Statistic on the thickness of NPLs.

5.4. Electronic properties of PbSe NPLs probed by scanning tunneling spectroscopy

5.4.1. Spectroscopy of isolated PbSe NPLs

The NPL solution was checked with the PL spectroscopy technique at room temperature to characterize the emission properties. The NPLs give a maximum emission peak at around 0.95 eV, corresponding to the optical gap of NPLs (Figure 56a). While insightful, PL spectroscopy does not provide the detailed electronic band structure of NPLs. Here, we propose low-temperature scanning tunneling spectroscopy (LT-STS) that allows probing the electronic band structure of NPLs at the nanoscale. STS measurements were performed on individual NPLs at T = 77 K. The tunneling process that occurs during resonant tunneling spectroscopy for an isolated NPL on a gold substrate is described in Figure 56b. As the thickness and geometry of NPLs, thus this material is nearly in direct contact with the gold substrate. In this configuration, electrons from the tip are injected into the NPL and then can tunnel out to the substrate (Figure 56b). Figure 56c presents the current-dependent tunneling dI/dV spectra measured at the blue cross on the NPL with 0.45 nm in thickness (see the STM topographic image). At I_{set} = 100 pA, the dI/dV spectroscopy exhibits resonant peaks around a zero-conductance region (ZCR), including the first electron state (e_1) in the CB and the first hole state (h_1) in the VB [14]. The electronic band gap is estimated at 1.6 eV (defined as the spacing between the first electron and hole peaks). When the set-point current is increased to 500 pA, tunneling spectra do not show any significant changes in the position of resonant peaks. Based on previous reports [14], [15], [16], [17], we conclude that our dI/dV spectra are not affected by the tip-NPL distance, which indicates the shell-tunneling regime. In this regime, the Coulomb interaction is absent because electrons from the tip tunnel through the NPL one-by-one, which provides direct access to the quasi-particle band gap of the NPL.
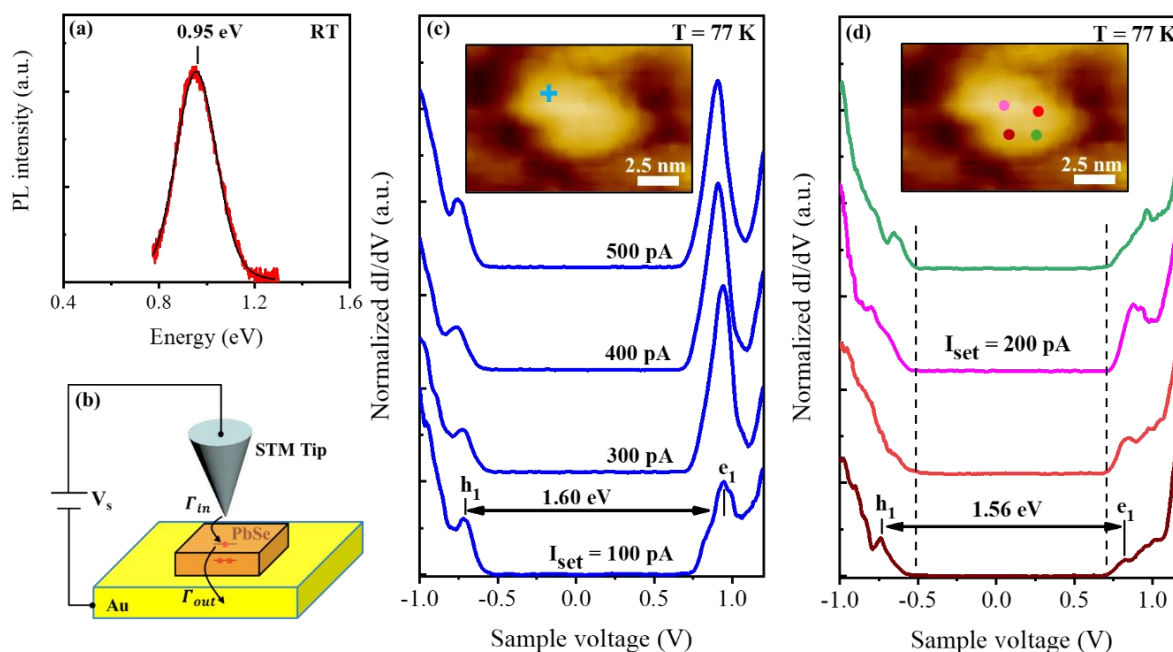
Figure 56: (a) PL spectroscopy of PbSe NPLs at room temperature. **(b)** Schematic illustration of STM/STS measurements on an isolated NPL. Γ_{in} and Γ_{out} are the tip-NPL and NPL-substrate tunneling rates, respectively ($\Gamma_{in} \ll \Gamma_{out}$). **(c)** Current-dependent dI/dV spectra measured at the blue cross on the NPL (see the STM image): $V_s = 1.2$ V. **(d)** Tunneling dI/dV spectra measured at four different positions on the NPL (see the STM image): $V_s = 1.2$ V, $I_t = 200$ pA, T = 77 K.

Figure 56d shows tunneling dI/dV spectra measured at four different positions on the NPL. The dI/dV spectroscopy (brown) exhibits a typical band structure of PbSe NPLs with an electronic band gap of 1.56 eV. At other positions, the density of states (DOS) of the NPL slightly differs from the previous DOS, however, no significant change in the ZCR is observed in the tunneling spectra (Figure 56d, black dashed lines). Based on the STS results, we conclude that the NPL is very stable under STS conditions ($V_s = 1.2$ V, $I_t = 200$ pA), and the electronic band gap is about 1.6 eV for the NPL with 0.45 nm in thickness. These findings provide an overview of the electronic band structure of single NPLs.

5.4.2. Thickness-dependent electronic properties of PbSe NPLs

As mentioned above, the HAADF-STEM and STM images exhibited PbSe NPLs having various thicknesses and lateral sizes in the same sample batch. This raises a question about the correlation between the electronic properties and dimensions of NPLs. Figure 57b shows tunneling dI/dV spectra measured on the 0.45 nm, 0.8 nm, and 1.6 nm thick PbSe NPLs (see the STM topographic images in Figure 57a). For the 0.45-nm thick NPL, the electronic band structure consists of the first electron peak (around +1.0 V) and the first hole peak (around -0.7 V). The electronic band gap (E_g) is about 1.67 eV (Figure 57b, the bottom panel). For thicker NPLs, the DOS is strongly modified because of the quantum confinement effect occurring along the thickness. As a result, the electronic band gap decreases with increasing thickness, specifically E_g = 1.26 nm (for 0.8 nm-thick NPL), and E_g = 1.0 eV (for 1.6 nm-thick NPL) (Figure 57b). To check this conclusion, we used tight-binding (TB) calculations to simulate the band structure of NPL at three different thicknesses (0.4 nm, 0.8 nm, and 1.6 nm). The TB calculations were carried out by Dr. Christophe Delerue at the Institute of Electronics, Microelectronics and Nanotechnology (IEMN – CNRS) – the University of Lille. Figure 57c shows that the band gap energy decreased with increasing NPL thickness, which is consistent with the STS results. By comparing the STM band gap and the optical gap, we conclude that the emission in the NPLs is dominated by the population of 1.6 nm thick NPLs. These STS results indicate the strong dependency of the optoelectronic properties of PbSe NPLs on their thickness, in good agreement with previous reports [3], [10].
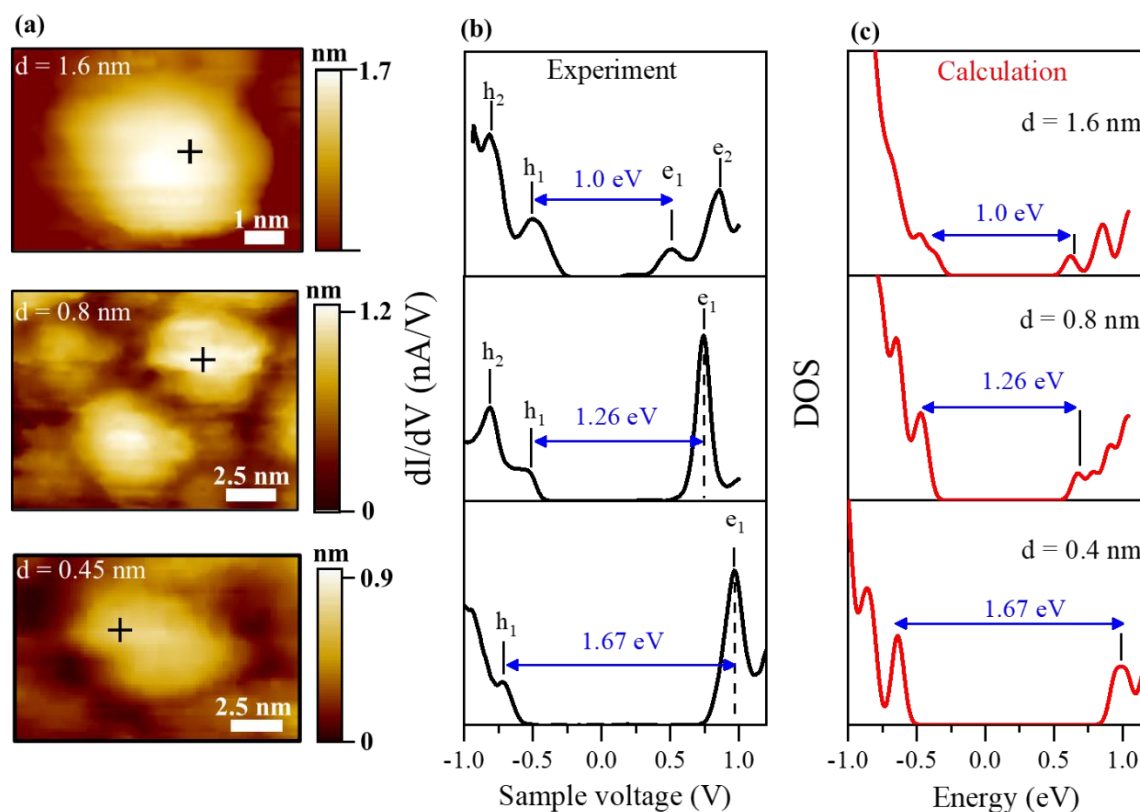
Figure 57: (a) STM topographic images of individual PbSe NPLs with three different thicknesses: 1.6 nm (top), 0.8 nm (middle), and 0.45 nm (bottom). **(b)** Tunneling dI/dV spectra were measured at the black crosses on the 1.6 nm thick-NPL (top, 1 V, 200 pA), 0.8 nm thick-NPL (middle, 1 V, 80 pA), and 0.45 nm thick-NPL (bottom, 1.2 V, 200 pA). All the spectra were performed at T = 77 K. **(c)** Simulated band structures of NPLs by tight-binding calculations.

5.4.3. Lateral size-dependent electronic properties of PbSe NPLs

We now shift to analyze the effect of the lateral size on the electronic properties of PbSe NPLs. Figure 58a presents an average of the thirty consecutive dI/dV curves measured on two different NPLs at the same thickness of 0.8 nm. To compare the two NPLs, tunneling spectra were measured at the same conditions (V_s = 1V, I_t = 80 pA). For the NPL3, the dI/dV spectroscopy exhibits the typical band structure with a band gap energy of 1.28 eV. Meanwhile, the dI/dV spectroscopy measured on the NPL2 shows a band gap energy of 1.23 eV, and we did not observe any significant difference in the electronic band structure of the two NPLs. This is due to the two NPLs having the same lateral size, thus the lateral quantum confinement effect is negligible.
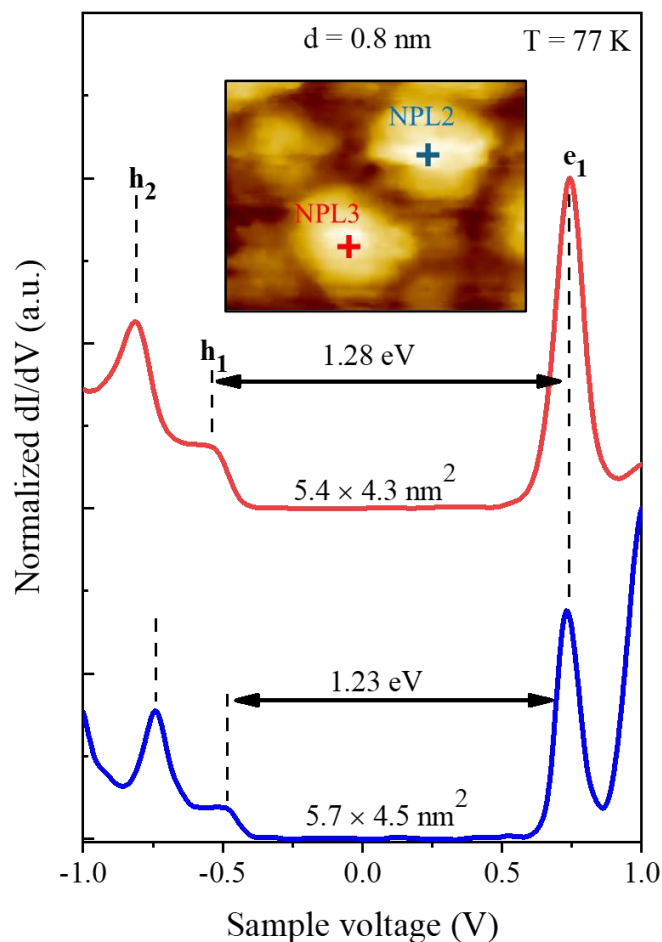
171

Figure 58: Average of thirty consecutive dI/dV curves measured on two different NPLs at the same thickness of 0.8 nm: NPL2 (lateral size: 5.7×4.5 nm^2), and NPL3 (lateral size: 5.4×4.3 nm^2). The spectra were measured at the red and blue crosses: $V_s = 1$ V, I_t = 80 pA, T = 77 K.

To better understand the lateral quantum confinement effect, tight-binding (TB) calculations were employed to calculate the band gap energy of NPLs. In the TB calculations, we assumed that the NPLs have a square shape. Figure 59 exhibits the lateral-size-dependent band gap energy of NPLs at 0.4 nm, 0.8 nm, and 1.6 nm in thickness. The TB calculations demonstrate the band gap energy increased with decreasing the NPL thickness, in good agreement with our experimental STS results. For 1.6 nm thick NPLs, the telecom wavelengths can be achieved in the NPLs with lateral sizes of 4×4 nm^2, 5×5 nm^2, and 6×6 nm^2 (Figure 59, green circles). For all the NPL thicknesses, the band gap energy increased with a decrease in the lateral size of NPLs. These findings indicate the lateral quantum confinement effect occurred in

NPLs, in good agreement with the report of F. Klepzig et al [1]. Based on the STS and simulation results, we conclude that ultrathin PbSe NPLs exhibit their electronic properties dependent on both the thickness and lateral size.
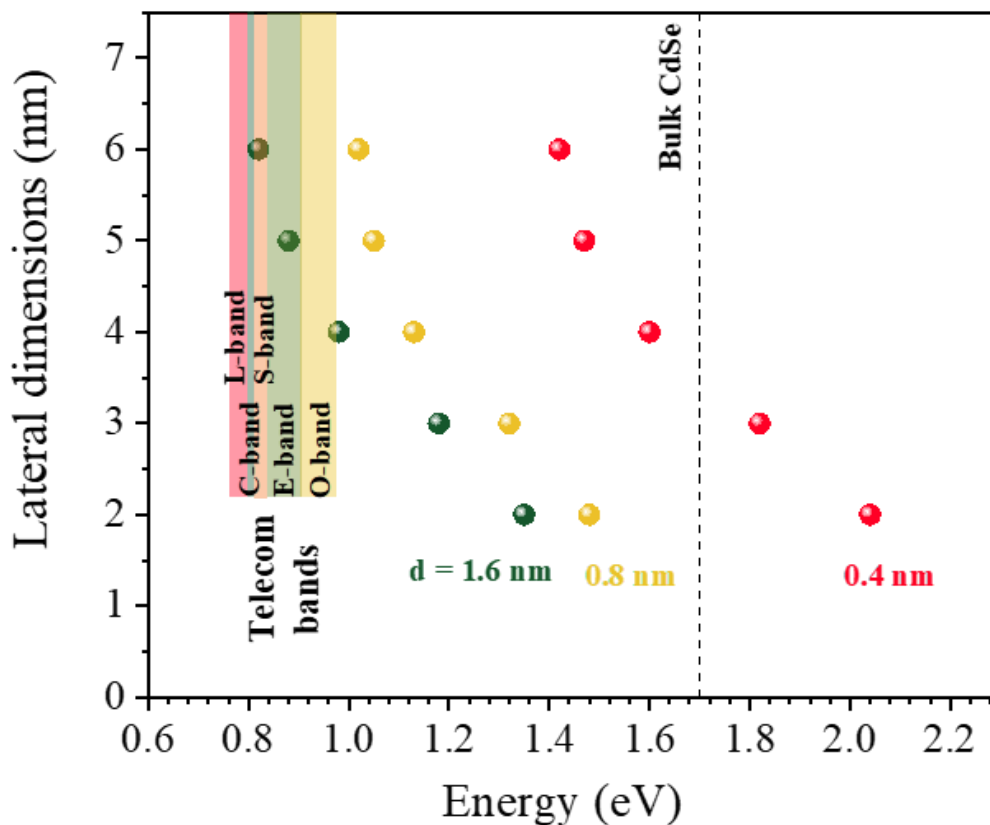

Figure 59: The band gap energy of 0.4 nm, 0.8 nm, and 1.6 nm thick-PbSe NPLs calculated by tight-binding (TB) calculations. The thickness was constant, and the calculated band gap was plotted as a function of the NPL lateral size.

5.5. Conclusions

In summary, the structural and electronic properties of PbSe NPLs prepared via a low-temperature direct colloidal synthesis have been investigated with HAADF-STEM and LT-STM techniques. The HAADF-STEM images provided important information on the shape and crystal structure of NPLs at the atomic scale. The STM topographic images indicated the formation of NPLs with various thicknesses in the same sample batch. The three typical thicknesses of NPLs are determined at 0.4 nm, 0.8 nm, and 1.6 nm. The dI/dV spectra (STS) provided insight into the energy levels of single NPLs, especially the electronic band structure including band gap energy and band edges. Most importantly, the STS measurement performed on single nanoplatelets revealed their thickness-dependent electronic band gap, which implies the 1D quantum confinement effect. Particularly, the electronic band gap of 1.6 nm thick-NPLs is about 1.0 eV, approximately to the optical gap of 0.95 eV. This suitability between the STM and optical band gap confirmed that the emission properties of the NPLs are dominant by the population of 1.6 nm thick-NPLs. Additionally, the STS measured on NPLs with various lateral sizes at the same thickness revealed their lateral size-dependent electronic band gap. On the other hand, the tight-binding calculations confirmed the dependency of the electronic properties of NPLs on both the thickness and lateral size, specifically the telecom wavelengths (e.g., S-, E-, O-bands) can be generated by controlling the lateral size of 1.6 nm thick-NPLs. Our experimental and simulation results demonstrated that colloidal PbSe NPLs are promising nanomaterials with well-controlled shapes and thicknesses for potential applications in the field of telecoms, optoelectronics, and quantum technologies.

Bibliography

[1] L. F. Klepzig *et al.*, "Colloidal 2D PbSe nanoplatelets with efficient emission reaching the telecom O-, E- and S-band," *Nanoscale Adv.*, vol. 4, no. 2, pp. 590–599, 2022, doi: 10.1039/D1NA00704A.

[2] W. Koh, N. K. Dandu, A. F. Fidler, V. I. Klimov, J. M. Pietryga, and S. V Kilina, "Thickness-Controlled Quasi-Two-Dimensional Colloidal PbSe Nanoplatelets," *J. Am. Chem. Soc.*, vol. 139, no. 6, pp. 2152–2155, Feb. 2017, doi: 10.1021/jacs.6b11945.

[3] T. Galle *et al.*, "Colloidal PbSe Nanoplatelets of Varied Thickness with Tunable Optical Properties," *Chem. Mater.*, vol. 31, no. 10, pp. 3803–3811, 2019, doi: 10.1021/acs.chemmater.9b01330.

[4] K. D. Desmet *et al.*, "Clinical and Experimental Applications of NIR-LED Photobiomodulation," *Photomed. Laser Surg.*, vol. 24, no. 2, pp. 121–128, Apr. 2006, doi: 10.1089/pho.2006.24.121.

[5] F. Koch, S. V Chernikov, and J. R. Taylor, "Dispersion measurement in optical fibres over the entire spectral range from 1.1 μm to 1.7 μm," *Opt. Commun.*, vol. 175, no. 1, pp. 209–213, 2000, doi: https://doi.org/10.1016/S0030-4018(99)00763-4.

[6] L. Bakueva *et al.*, "Size-tunable infrared (1000–1600 nm) electroluminescence from PbS quantum-dot nanocrystals in a semiconducting polymer," *Appl. Phys. Lett.*, vol. 82, no. 17, pp. 2895–2897, Apr. 2003, doi: 10.1063/1.1570940.

[7] F. Xu, X. Ma, Q. Zhang, H.-K. Lo, and J.-W. Pan, "Secure quantum key distribution with realistic devices," *Rev. Mod. Phys.*, vol. 92, no. 2, p. 25002, May 2020, doi: 10.1103/RevModPhys.92.025002.

[8] X. Cao, M. Zopf, and F. Ding, "Telecom wavelength single photon sources," *J. Semicond.*, vol. 40, no. 7, p. 71901, 2019, doi: 10.1088/1674-4926/40/7/071901.

[9] I. Skurlov *et al.*, "Temperature-Dependent Photoluminescent Properties of PbSe Nanoplatelets," *Nanomaterials*, vol. 10, no. 12. 2020. doi:

10.3390/nano10122570.

[10] B. B. V Salzmann *et al.*, "Two-Dimensional CdSe-PbSe Heterostructures and PbSe Nanoplatelets: Formation, Atomic Structure, and Optical Properties," *J. Phys. Chem. C*, vol. 126, no. 3, pp. 1513–1522, Jan. 2022, doi: 10.1021/acs.jpcc.1c09412.

[11] L. Biesterfeld, L. F. Klepzig, A. Niebur, M. Rosebrock, and J. Lauth, "Toward Bright Colloidal Near-Infrared Emitters: Surface Passivation of 2D PbSe Nanoplatelets by Metal Halides," *J. Phys. Chem. C*, vol. 126, no. 45, pp. 19277–19285, Nov. 2022, doi: 10.1021/acs.jpcc.2c05850.

[12] E. K. Wujcik, S. R. Aceto, R. Narayanan, and A. Bose, "Lead Selenide Nanostructures Self-Assembled across Multiple Length Scales and Dimensions," *J. Nanomater.*, vol. 2016, p. 9575839, 2016, doi: 10.1155/2016/9575839.

[13] M. Sulaman *et al.*, "High performance solution-processed infrared photodetector based on PbSe quantum dots doped with low carrier mobility polymer poly(N-vinylcarbazole)," *RSC Adv.*, vol. 6, no. 50, pp. 44514–44521, 2016, doi: 10.1039/C5RA25761A.

[14] K. Overgaag, P. Liljeroth, B. Grandidier, and D. Vanmaekelbergh, "Scanning Tunneling Spectroscopy of Individual PbSe Quantum Dots and Molecular Aggregates Stabilized in an Inert Nanocrystal Matrix," *ACS Nano*, vol. 2, no. 3, pp. 600–606, Mar. 2008, doi: 10.1021/nn7003876.

[15] L. Jdira, P. Liljeroth, E. Stoffels, D. Vanmaekelbergh, and S. Speller, "Size-dependent single-particle energy levels and interparticle Coulomb interactions in CdSe quantum dots measured by scanning tunneling spectroscopy," *Phys. Rev. B*, vol. 73, no. 11, p. 115305, Mar. 2006, doi: 10.1103/PhysRevB.73.115305.

[16] P. Liljeroth, K. Overgaag, A. Urbieta, B. Grandidier, S. G. Hickey, and D. Vanmaekelbergh, "Variable Orbital Coupling in a Two-Dimensional Quantum-Dot Solid Probed on a Local Scale," *Phys. Rev. Lett.*, vol. 97, no. 9, p. 96803, Sep. 2006, doi: 10.1103/PhysRevLett.97.096803.

[17]   E. P. A. M. Bakkers *et al.*, "Shell-Tunneling Spectroscopy of the Single-Particle Energy Levels of Insulating Quantum Dots," *Nano Lett.*, vol. 1, no. 10, pp. 551–556, Oct. 2001, doi: 10.1021/nl015572b.

Publications & Manuscripts

✚ Manuscripts during the Ph.D.

1. Pengji Li, Leon Biesterfeld, Lars Klepzig, Jingzhong Yang, **Huu Thoai Ngo**, Ahmed Addad, Tom N Rakow, Ruolin Guan, Eddy P Rugeramigabo, Louis Biadala, Jannika Lauth, Michael Zopf, "*Polarized sub-meV Photoluminescence in 2D PbS Nanoplatelets at Cryogenic Temperatures*"

2. **Huu Thoai Ngo**, Nemanja Peric, Ahmed Addad, Alessio Di Giacomo, Alina Myslovska, Iwan Moreels, Bruno Grandidier*, Louis Biadala*, "*Atomic structure and single traps in CdSe nanoplatelets by low-temperature scanning tunneling microscopy*"

3. **Huu Thoai Ngo**, Alessio Di Giacomo, Alina Myslovska, Elena V Shornikova, Iwan Moreels, Dmitri R Yakovlev, Manfred Bayer, Louis Biadala*, "*Effect of dangling bond spin on the polarized exciton emission from CdSe and CdSe/CdS core/crown nanoplatelets*"

4. **Huu Thoai Ngo**, Leon Biesterfeld, Ahmed Addad, Bruno Grandidier, Jannika Lauth*, Louis Biadala*, "*Thickness-dependent emission wavelength in 2D PbSe (less Se) nanoplatelets studied by low-temperature scanning tunneling microscopy*"

✚ Publications

1. **Huu Thoai Ngo**, Minh Trang Thi Nguyen, Dinh Phuc Do, Kim My Tran, Kieu Hanh Thi Ta, Bach Thang Phan, Kim Ngoc Pham, "*Low operating voltage resistive random-access memory based on graphene oxide–polyvinyl alcohol nanocomposite thin films*", Journal of Science: Advanced Materials and Devices Volume 5, Issue 2, June 2020, Pages 199-206, doi: https://doi.org/10.1016/j.jsamd.2020.04.008

2. Mehdi Bouatou, Cyril Chacon, Aleksander Bach Lorentzen, **Huu Thoai Ngo**, Yann Girard, Vincent Repain, Amandine Bellec, Sylvie Rousset, Mads Brandbyge, Yannick J. Dappe, Jérôme Lagoute, "*Visualizing In-Plane Junctions in Nitrogen-Doped Graphene*", Adv. Funct. Mater. 2022, 32, 2208048, doi: https://doi.org/10.1002/adfm.202208048

Conferences & Summer Schools

1. The *"Nanosciences with Nanocrystals X10 (NaNaX10)"* held by ISTA (Austria), ETH Zurich, CEA (France), and City University of Hong Kong (Poster).
2. Thematic school: "A*dvanced physics of van der Waals heterostructures*" supported by CNRS, Roscoff, France.